

**A Thesis Submitted for the Degree of PhD at the University of Warwick**

**Permanent WRAP URL:**

<http://wrap.warwick.ac.uk/159892>

**Copyright and reuse:**

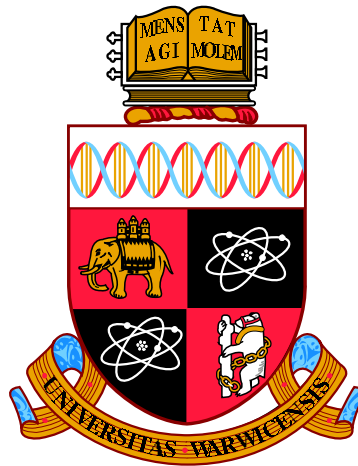
This thesis is made available online and is protected by original copyright.

Please scroll down to view the document itself.

Please refer to the repository record for this item for information to help you to cite it.

Our policy information is available from the repository home page.

For more information, please contact the WRAP Team at: [wrap@warwick.ac.uk](mailto:wrap@warwick.ac.uk)



**Enhanced Polarisation Control and Extreme  
Electric Fields: Advances in Terahertz Spectroscopy  
Applied to Anisotropic Materials and Magnetic  
Phase Transitions**

by

**Connor Devyn William Mosley**

**Thesis**

Submitted to the University of Warwick

for the degree of

**Doctor of Philosophy**

**Department of Physics**

August 2019

THE UNIVERSITY OF  
**WARWICK**

# Contents

<b>Acknowledgments</b>	<b>v</b>
<b>Declarations</b>	<b>vi</b>
<b>Publications</b>	<b>vii</b>
<b>Abstract</b>	<b>ix</b>
<b>Chapter 1 Introduction</b>	<b>1</b>
1.1 Crystal Optics . . . . .	3
1.1.1 The Dielectric Tensor . . . . .	3
1.1.2 Principal Axes and the Index Ellipsoid . . . . .	4
1.1.3 Plane Wave Propagation Through an Anisotropic Medium	7
1.1.4 Effects of an Anisotropic Medium on the Polarisation State of Light . . . . .	10
1.2 Describing the Polarisation State of Electromagnetic Waves . . .	11
1.2.1 Ellipticity and Orientation Angle . . . . .	11
1.2.2 Alternative Descriptions of the Polarisation State . . . .	13
1.3 Electromagnons in Improper Ferroelectrics . . . . .	15
1.3.1 Magnons . . . . .	16
1.3.2 Electromagnons . . . . .	18
1.3.3 Improper Ferroelectricity and Electromagnons in CuO .	21
1.4 Structure of This Thesis . . . . .	26
<b>Chapter 2 Terahertz Time-Domain Spectroscopy</b>	<b>28</b>
2.1 Generation of Broadband Terahertz Radiation . . . . .	28

2.1.1	Photoconductive Emitters . . . . .	29
2.1.2	Optical Rectification . . . . .	32
2.2	Electro-Optic Sampling . . . . .	33
2.2.1	Polarisation-Resolved Electro-Optic Sampling . . . . .	35
2.3	THz-TDS Experimental Setup . . . . .	36
2.3.1	Performing a THz-TDS Experiment . . . . .	38
2.4	Extracting Sample Properties and Polarisation Information from Time-Domain Data . . . . .	40
2.4.1	Complex Refractive Index . . . . .	41
2.4.2	Ellipticity and Orientation Angle . . . . .	43
2.5	Summary . . . . .	44

### **Chapter 3 Rotatable-Polarisation Terahertz Time-Domain Spectroscopy of Anisotropic Media 45**

3.1	Investigating Anisotropy at Terahertz Frequencies . . . . .	46
3.1.1	Disambiguating Spectral Features Using Polarisation-Resolved Detection Methods . . . . .	46
3.1.2	Terahertz Polarimetry and Ellipsometry . . . . .	48
3.1.3	Methods of Terahertz Polarisation Rotation . . . . .	52
3.2	Rotatable-Polarisation Terahertz Time-Domain Spectrometer . .	54
3.2.1	Rotating the Terahertz Polarisation State . . . . .	54
3.2.2	Polarisation-Resolved Detection Method and Alignment .	56
3.2.3	Calibration of the Terahertz Emission Strength . . . . .	57
3.2.4	Polarisation State of the Rotated Terahertz Pulses . . . . .	59
3.3	Comparison of Rotatable Polarisation to Projection via Wire- Grid Polarisers . . . . .	61
3.4	Experimental Implementation of RP-THz-TDS . . . . .	64
3.4.1	Sample Details . . . . .	64
3.4.2	Mapping Birefringence and Identifying Polarisation Eigen- vectors Using RP-THz-TDS . . . . .	66
3.4.3	Extracting the Full Complex Refractive Index Using RP- THz-TDS . . . . .	69
3.4.4	Anisotropic Absorption and Chromatic Dispersion in CuO	74



3.5	Summary . . . . .	78
 <b>Chapter 4 Scalable Interdigitated Photoconductive Emitters for the Electrical Modulation of Terahertz Beams With Arbitrary Linear Polarisation</b>		
		<b>79</b>
4.1	Photoconductive Emitter Geometry and Terahertz Polarisation State . . . . .	80
4.1.1	Electric Dipole Radiation from Photoconductive Emitters	80
4.1.2	Controlling the Terahertz Polarisation State with the Emitter Geometry . . . . .	82
4.2	Multi-Pixel Interdigitated Photoconductive Emitters . . . . .	84
4.2.1	Emitter Concept and Design . . . . .	85
4.2.2	Device Fabrication . . . . .	87
4.2.3	Simulated Device Performance . . . . .	89
4.3	Experimental Device Performance . . . . .	90
4.3.1	Initial Electrical Biasing Tests . . . . .	91
4.3.2	Generating Arbitrary Linear polarisation States Via Electrical Control . . . . .	93
4.4	Rapid Modulation of Circular Polarisation States for Circular Dichroic Spectroscopy . . . . .	96
4.4.1	Converting from Linear to Circular Polarisation via a Prism	97
4.4.2	Stokes Parameters . . . . .	98
4.4.3	Experimental Setup . . . . .	99
4.4.4	Experimental Results . . . . .	101
4.5	Summary . . . . .	103
 <b>Chapter 5 Tracking Disorder Broadening and Hysteresis in First-Order Phase Transitions via the Electromagnon Response in Improper Ferroelectrics</b>		
		<b>105</b>
5.1	First-Order Phase Transitions and Disorder Broadening . . . . .	106
5.1.1	Landau Theory of First-Order Phase Transitions . . . . .	107
5.1.2	Broadening of First-Order Phase Transitions by Disorder	109
5.2	Spin-Disorder in $\text{Cu}_{1-x}\text{Zn}_x\text{O}$ Alloys . . . . .	109

5.2.1	Quenched Spin-Disorder in $\text{Cu}_{1-x}\text{Zn}_x\text{O}$ Alloys . . . . .	110
5.3	Electromagnon Response Over the AF1 - AF2 Phase Transition . . . . .	111
5.3.1	Influence of Zn-Alloying on the Magnetic Interactions . . . . .	114
5.4	Disorder-Broadening of the AF1 - AF2 Phase Transition . . . . .	116
5.5	Hysteresis in the Electromagnon Response . . . . .	117
5.6	Summary . . . . .	120

## **Chapter 6 High-Field Terahertz Time-Domain Spectroscopy of**

### **Single-Walled Carbon Nanotubes and CuO 122**

6.1	Terahertz Spectroscopy using Extreme Electric Fields . . . . .	122
6.1.1	Generating High-Field Terahertz Radiation . . . . .	124
6.1.2	Choosing the Right High-Field THz Source for You . . . . .	125
6.2	High-Field Terahertz Time-Domain Spectrometer . . . . .	126
6.2.1	Tilted Pulse-Front Pumping in $\text{LiNbO}_3$ . . . . .	127
6.2.2	Experimental Setup . . . . .	131
6.2.3	Controlling the Electric Field Strength of Terahertz Pulses . . . . .	134
6.3	A Test Case of Nonlinear THz Transmission: Indium Antimonide . . . . .	136
6.3.1	Experimental Results . . . . .	137
6.4	Nonlinear THz Transmission in Single-Walled Carbon Nanotube Films . . . . .	139
6.4.1	Experimental Results . . . . .	139
6.5	Electric Field-Dependent THz Transmission of CuO . . . . .	143
6.5.1	Electric Field-Dependence of the Electromagnon Response in CuO . . . . .	144
6.5.2	Electric Field-Dependent Absorption Coefficient in CuO . . . . .	146
6.6	Summary . . . . .	148

## **Chapter 7 Conclusions 149**

7.1	Outlook and Future Work . . . . .	150
-----	-----------------------------------	-----

# Acknowledgments

Firstly I would like to express my thanks to my supervisor Dr. James Lloyd-Hughes, for all the support and guidance he has given me during my PhD, and for giving me the opportunity to undertake this research project. It has been a pleasure to work in his group for the past four years. I would similarly like to thank all the members of the THz group at Warwick and those associated with the Warwick Centre for Ultrafast Spectroscopy, past and present, for making it such a nice environment to work in. I would particularly like to thank Dr. Michele Failla and Dr. Michael Staniforth for all the help and advice they have offered me.

I would also like to express my thanks to those who have collaborated with me on parts of the work presented in this thesis. To Dr. Dharmalingam Prabhakaran from the University of Oxford for growing the samples of CuO and  $\text{Cu}_{0.95}\text{Zn}_{0.05}\text{O}$  studied throughout this thesis; to Dr. Mark Ashwin from the University of Warwick for growing the InSb sample studied in chapter 6; and to the group of Prof. Albert Nasibulin from Skoltech and Maria Burdanova from the University of Warwick for growth and preparation of the single-walled carbon nanotube films studied in chapter 6. The work performed in chapter 4 would not have been possible without the clean room training and guidance from Dr. Mark Crouch and Dr. Michele Failla. I would also like to express thanks in this regard to Alan Brunier, in addition to all the coffee breaks and fun chats. I am also grateful to Dr. Arturo Hernandez Serrano for performing the simulations of the device emission presented in chapter 4.

I would like to express my heartfelt thanks to all of the friends I have made during my time at Warwick, and to all the friends I knew from before. To all my bandmates, and everyone associated with Bandsoc, it was a pleasure to share the stage with you. To Charlie Price, Connor White and Trystan Leng for their constant friendship and support. And to Rebecca Swinney, thank you for everything you do, I love you.

Finally, I would like to thank my family, especially my mum and dad, for their unwavering support, encouragement and love. I couldn't have done this without you, so this thesis is dedicated to you.

# Declarations

This thesis is submitted to the University of Warwick in support of my application for the degree of Doctor of Philosophy. It has been composed by myself and has not been submitted in any previous application for any degree.

The work presented (including data generated and data analysis) was carried out by the author except in the cases outlined within the text.

Single crystal samples of CuO and  $\text{Cu}_{0.95}\text{Zn}_{0.05}\text{O}$  used throughout this thesis were grown by Dr. Dharmalingam Prabhakaran from the University of Oxford.

Parts of this thesis (chapters 3, 4 and 5) have been published by the author as specified in the relevant sections.

# Publications

The following is a list of publications to which I have contributed during my PhD, in chronological order of publication:

1. “*Colossal terahertz magnetoresistance at room temperature in epitaxial  $\text{La}_{0.7}\text{Sr}_{0.3}\text{MnO}_3$  nanocomposites and single-phase thin films*”, J. Lloyd-Hughes, **C. D. W. Mosley**, S. P. P. Jones, M. R. Lees, A. Chen, Q. X. Jia, E. M. Choi and J. L. MacManus-Driscoll, *Nano Letters* **17**, 2506 (2017).
2. “*Terahertz spectroscopy of anisotropic materials using beams with rotatable polarization*”, **C. D. W. Mosley**, M. Failla, D. Prabhakaran and J. Lloyd-Hughes, *Scientific Reports* **7**, 12337 (2017).
3. “*Tracking a hysteretic and disorder-broadened phase transition via the electromagnon response in improper ferroelectrics*”, **C. D. W. Mosley**, D. Prabhakaran and J. Lloyd-Hughes, *Journal of Physics D: Applied Physics* **51**, 084002 (2018).
4. “*Conduction properties of thin films from a water soluble carbon nanotube/hemicellulose complex*”, D. Shao, P. Yotprayoosak, V. Saunajoki, M. Ahlskog, J. Virtanen, V. Kangas, A. Volodin, C. Van Haesendonck, M. Burdanova, **C. D. W. Mosley** and J. Lloyd-Hughes, *Nanotechnology* **29**, 145203 (2018).
5. “*Giant negative terahertz photoconductivity in controllably doped carbon nanotube networks*”, M.G. Burdanova, A.P. Tsapenko, D.A. Satco, R.J. Kashtiban, **C.D.W. Mosley**, M. Monti, M. Staniforth, J. Sloan, Y. Gladush, A.G. Nasibulin and J. Lloyd-Hughes, *ACS Photonics* **6**, 1058 (2019).
6. “*Scalable interdigitated photoconductive emitters for the electrical modulation of terahertz beams with arbitrary linear polarization*”, **C.D.W. Mosley**, M. Staniforth, A. I. Hernandez Serrano, E. Pickwell-MacPherson and J. Lloyd-Hughes, *AIP Advances* **9**, 045323 (2019).

The following is a list of conference talks and posters presented by myself during the course of my PhD, in chronological order:

1. Poster: “*Terahertz spectroscopy of anisotropic materials using beams with rotatable polarization*”, OTST 2017, London, UK (April 2017).
2. Talk: “*Tracking a hysteretic and disorder-broadened phase transition via the electromagnon response in improper ferroelectrics*”, APS March Meeting 2018, Los Angeles, USA (March 2018).
3. Talk: “*Broadband, rotatable terahertz polarisation control for the spectroscopy of anisotropic materials*”, Photon 2018, Birmingham, UK (September 2018).
4. Talk: “*Multi-pixel interdigitated photoconductive devices for terahertz polarisation control and imaging*”, CLEO/Europe-EQEC 2019, Munich, Germany (June 2019).
5. Talk: “*Tracking a hysteretic and disorder-broadened phase transition via the electromagnon response in improper ferroelectrics*”, CMQM 2019, St. Andrews, UK (July 2019).

# Abstract

This thesis reports advances in terahertz time-domain spectroscopy, relating to the development of new techniques and components that enhance the experimentalist's control over the terahertz polarisation state produced by photoconductive emitters, and in utilising the dynamic magnetoelectric response at THz frequencies, in the form of electromagnons, to probe material properties at a transition between two magnetically ordered phases.

Two methods of controlling the terahertz polarisation state are reported: The first method is based upon mechanical rotation of an interdigitated photoconductive emitter, and is implemented in a rotatable-polarisation terahertz time-domain spectrometer, the calibration of which is demonstrated to produce a highly uniform polarisation state at all angles. This method is then demonstrated experimentally to identify the orientations of the normal modes of propagation in the plane of birefringent samples, to extract the full complex refractive index along these directions, and to investigate the optical selection rules of an absorbing material. The second method presents a new photoconductive emitter design, based upon separate interdigitated pixel elements for the generation of the horizontally and vertically polarised components of the terahertz pulses, that permits rotation of the polarisation state solely by electrical control. The design, fabrication and experimental verification of the device is reported, demonstrating polarisation control on timescales orders of magnitude faster than those achievable in mechanical rotation methods.

A method of using the electromagnon response in  $\text{Cu}_{1-x}\text{Zn}_x\text{O}$  alloys as a sensitive probe of a phase transition is also demonstrated. Using this method, the phase transition is observed to broaden upon the introduction of spin-disorder when alloying with non-magnetic zinc ions, and the first-order nature of the transition is confirmed by the observation of thermal hysteresis. Additionally, preliminary investigations into the properties of materials exposed to extreme terahertz optical electric fields are performed. Nonlinear terahertz transmission in single-walled carbon nanotube films and evidence for nonlinear behaviour of electromagnons in CuO are observed.

# Chapter 1

## Introduction

The terahertz (THz) region of the electromagnetic spectrum can be approximately defined as the frequency range 0.1 - 10 THz: a frequency of 1 THz corresponds to a photon energy of  $\sim 4$  meV, and therefore THz radiation enables a wide variety of fascinating low energy excitations and intriguing material properties in the far-infrared region of the electromagnetic spectrum to be investigated. Developments in THz generation and detection technology over the past few decades have precipitated an explosion in both research output and potential applications; the advent of femtosecond lasers and novel spectroscopic techniques have widely increased the availability and applicability of THz sources. In particular, terahertz time-domain spectroscopy (THz-TDS) has matured into a powerful tool for characterizing the optical properties of materials at THz frequencies [1, 2, 3]. THz-TDS permits the direct determination of the full complex refractive index  $\tilde{n} = n + i\kappa = \sqrt{\tilde{\epsilon}\tilde{\mu}}$  of the material under study, where  $n$  is the real part of the refractive index,  $\kappa$  is the extinction coefficient,  $\tilde{\epsilon}$  is the complex permeability and  $\tilde{\mu}$  is the complex permittivity of the material, and as such does not require the use of the Kramers-Kronig relations [4].

Many materials demonstrate anisotropic behaviour at THz frequencies, such as birefringence created by anisotropy in the vibrational or electronic response [5, 6], and electro- and magneto-optical effects [7, 8, 9]. One particular class of materials which has attracted much attention in recent years are multiferroics, due to a variety of potential technological applications [10, 11], such as in spintronics [12, 13, 14] and novel electronic components [15, 16]. In the case



of ferroelectric multiferroics in particular the material must be anisotropic, due to the requirement that the material lacks an inversion centre for ferroelectricity to occur. In addition, designs of optical components for polarisation control in the THz region, such as wire-grid polarisers (WGPs) [17] and wave plates [18], depend critically on the optical anisotropy. Therefore the accurate determination of the optical properties of anisotropic materials is crucial for both optical component design and fundamental physical research [19].

Despite the advances made in THz technology thus far, traditionally many tabletop sources of THz radiation have remained weaker than those attainable in other regions of the electromagnetic spectrum. More recently, new THz generation techniques coupled with amplified femtosecond lasers have begun to bridge the gap to high-power, tabletop sources of THz radiation, capable of producing pulses with electric field strengths exceeding  $1 \text{ MVcm}^{-1}$  and a duration of only a few hundred femtoseconds [20]. This extreme THz radiation cannot only provide higher-power sources for applications such as chemical sensing [21], but can also be utilised in the coherent control of collective degrees of freedom in the THz range and nonlinear spectroscopy [22, 23].

The focus of this thesis is on the development of techniques for the spectroscopy of anisotropic materials in the THz region, particularly in terms of enhancing the control of the polarisation state produced by photoconductive emitters, which are perhaps the most common source of THz radiation in both commercially available and custom-made THz spectroscopy and imaging systems. The rest of this chapter will discuss the interaction between light and matter in the linear regime in anisotropic materials, in order to provide the necessary background required to understand the experimental results in future chapters of this thesis. Sections 1.1 and 1.2 will focus on the effect that an anisotropic material structure has on the polarisation state of light propagating through it, and how the polarisation state can be described. Section 1.3 will then discuss the inverse scenario, regarding the effects that the electromagnetic field of light has on anisotropic media, with a particular focus on multiferroics. Section 1.4 will then describe the structure of the rest of this thesis.

## 1.1 Crystal Optics

As a guide to the reader, the following section will provide a theoretical description of the interaction of the electric field of light with an anisotropic dielectric medium. This can then be used to describe the propagation of electromagnetic waves through such an anisotropic medium, and its resulting effects on the polarisation state of the probing light.

### 1.1.1 The Dielectric Tensor

In an optically isotropic, linear medium, such as a gas or an amorphous solid such as glass, the components of the electric displacement field  $\mathbf{D}$  are linearly proportional to the corresponding components of the optical electric field  $\mathbf{E}$ ,

$$\begin{bmatrix} D_x \\ D_y \\ D_z \end{bmatrix} = \epsilon \begin{bmatrix} E_x \\ E_y \\ E_z \end{bmatrix}, \quad (1.1)$$

where the constant of proportionality  $\epsilon$  is the dielectric constant of the medium, which is independent of the orientation and direction of propagation of the wave. However, in an anisotropic medium the structure is no longer the same for any arbitrary direction of propagation, and as such the optical properties will vary depending on the relative orientations of the crystallographic directions and the electric field. Each of the components of  $\mathbf{D}$  will now be made up of a linear combination of the components of  $\mathbf{E}$ , such that

$$D_x = \epsilon_{xx}E_x + \epsilon_{xy}E_y + \epsilon_{xz}E_z, \quad (1.2)$$

$$D_y = \epsilon_{yx}E_x + \epsilon_{yy}E_y + \epsilon_{yz}E_z, \quad (1.3)$$

$$D_z = \epsilon_{zx}E_x + \epsilon_{zy}E_y + \epsilon_{zz}E_z. \quad (1.4)$$

Hence the optical properties of the medium can now be described by a  $3 \times 3$  matrix, the *dielectric tensor*  $\boldsymbol{\epsilon}$ , where

$$\begin{bmatrix} D_x \\ D_y \\ D_z \end{bmatrix} = \begin{bmatrix} \epsilon_{xx} & \epsilon_{xy} & \epsilon_{xz} \\ \epsilon_{yx} & \epsilon_{yy} & \epsilon_{yz} \\ \epsilon_{zx} & \epsilon_{zy} & \epsilon_{zz} \end{bmatrix} \cdot \begin{bmatrix} E_x \\ E_y \\ E_z \end{bmatrix}, \quad (1.5)$$

which can alternatively be written

$$D_i = \sum_j \epsilon_{ij} E_j, \quad (1.6)$$

where  $i, j$  represent the  $x$ ,  $y$  and  $z$  coordinates. The dielectric tensor is symmetric, such that  $\epsilon_{ij} = \epsilon_{ji}$ , and can therefore be described by six independent values. The symmetry of the crystal structure in some materials can further reduce the number of independent components of the dielectric tensor.

### 1.1.2 Principal Axes and the Index Ellipsoid

The particular values of the components of the dielectric tensor depend on the choice of coordinate system relative to the crystal structure. For any given crystal, it is possible to choose a frame of reference such that the off-diagonal components vanish, and the dielectric tensor becomes

$$\boldsymbol{\epsilon} = \begin{bmatrix} \epsilon_1 & 0 & 0 \\ 0 & \epsilon_2 & 0 \\ 0 & 0 & \epsilon_3 \end{bmatrix}, \quad (1.7)$$

where  $\epsilon_1 = \epsilon_{xx}$ ,  $\epsilon_2 = \epsilon_{yy}$  and  $\epsilon_3 = \epsilon_{zz}$ . This coordinate system is known as the *principal axis* system, and defines the directions in which  $\mathbf{D}$  and  $\mathbf{E}$  must be parallel to each other, e.g.  $D_1 = \epsilon_1 E_1$ , and equivalent equations for the other directions. In a non-magnetic, dielectric medium we can assume that the magnetic permeability  $\mu = 1$ , and as such the refractive index is given by  $n = \sqrt{\epsilon/\epsilon_0}$ , where  $\epsilon_0$  is the permittivity of free space. Hence the refractive indices of the principal axes are given by

$$n_1 = \sqrt{\frac{\epsilon_1}{\epsilon_0}}, \quad (1.8)$$

and equivalent equations for the 2 and 3 directions. The relationship between  $\mathbf{D}$  and  $\mathbf{E}$  can also be expressed in the inverse form of Equation 1.5, as

$$E_i = \sum_j (\epsilon^{-1})_{ij} D_j. \quad (1.9)$$

In this case, it is useful to define the *electric impermeability tensor*  $\boldsymbol{\eta}$  as

$$\boldsymbol{\eta} = \epsilon_0 \boldsymbol{\epsilon}^{-1}, \quad (1.10)$$

which is also a symmetric second-rank tensor with the same principal axes as  $\boldsymbol{\epsilon}$ . As such, in the principal axis system  $\boldsymbol{\eta}$  is a diagonal matrix with principal values of

$$\eta_1 = \frac{\epsilon_0}{\epsilon_1} = \frac{1}{n_1^2}, \quad (1.11)$$

and equivalent relations for the 2 and 3 directions.

A symmetric second-rank tensor can be visually represented in three dimensional space by a quadratic surface, such as an ellipsoid [24]; for the impermeability tensor this can be expressed as

$$\sum_{ij} \eta_{ij} x_i x_j = 1, \quad (1.12)$$

for an arbitrary coordinate system  $x_i$ . This surface is invariant to the choice of coordinate system, such that if the frame of reference is rotated the values of  $x_i$  and  $\eta_{ij}$  are altered but the ellipsoid remains unchanged. In the principal axis system this equation simply reduces to

$$\eta_1 x_1^2 + \eta_2 x_2^2 + \eta_3 x_3^2 = 1. \quad (1.13)$$

Using Equations 1.11 and 1.13 we can define the *index ellipsoid* of the system,

$$\frac{x_1^2}{n_1^2} + \frac{x_2^2}{n_2^2} + \frac{x_3^2}{n_3^2} = 1, \quad (1.14)$$

which, along with the principal axes, contains all the information required to completely describe the optical properties of a material. The general form of the index ellipsoid defined in the principal axes of a material system is schematically shown in Figure 1.1, where the half-lengths of the major and minor axes are the principal refractive indices.

If all three principal refractive indices have the same value, e.g.  $n_1 = n_2 = n_3$ , then the index ellipsoid reduces to a sphere and the medium is isotropic. For crystals with certain symmetries two of the principal refractive indices may be

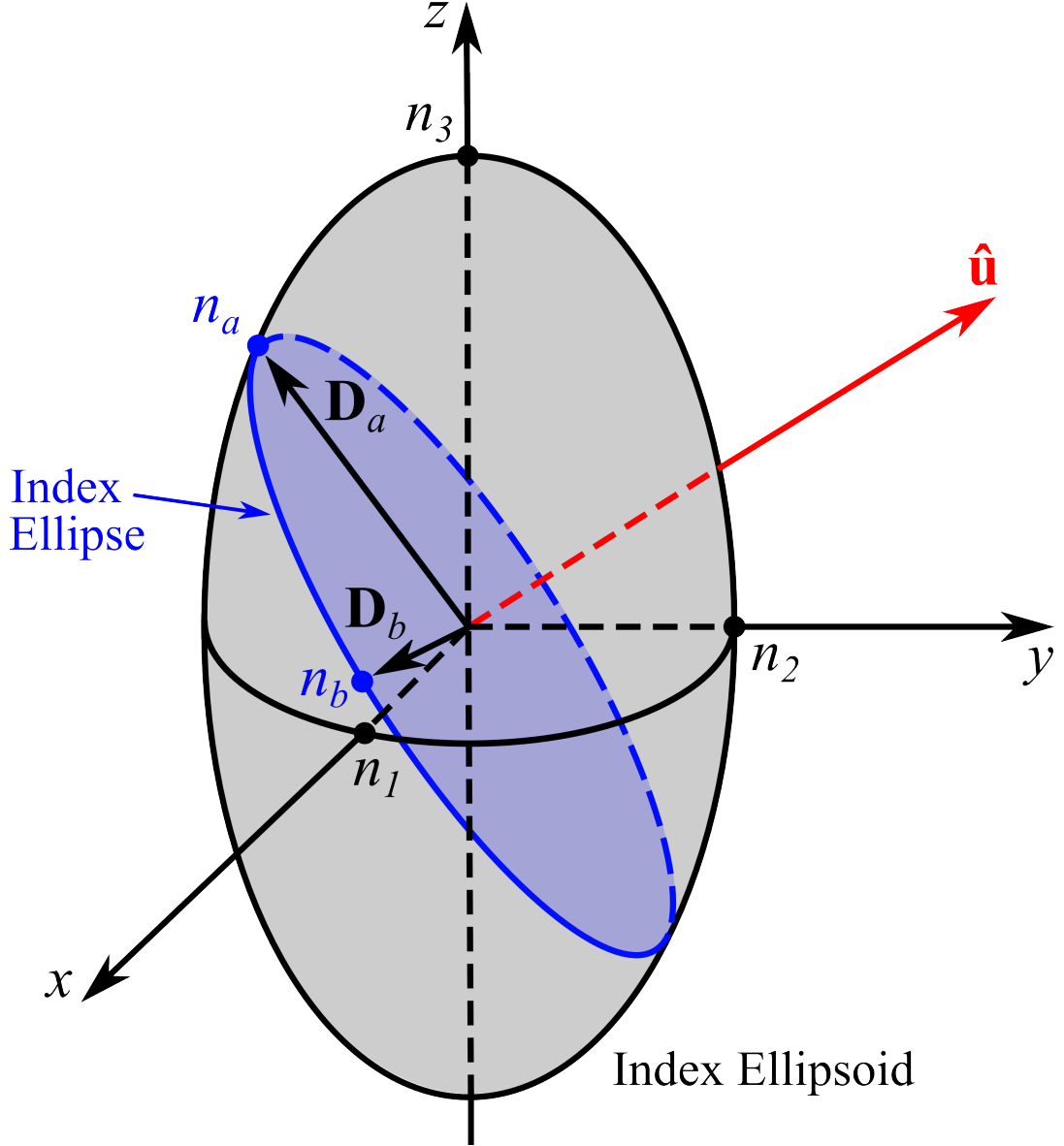


Figure 1.1: Geometrical representation of a general refractive index ellipsoid of an anisotropic medium. The unit vector  $\hat{\mathbf{u}}$  signifies an arbitrary direction of wave propagation through the medium, with the eigenmodes of propagation ( $\mathbf{D}_a$  and  $\mathbf{D}_b$ ) and corresponding eigenvalues ( $n_a$  and  $n_b$ ) in the plane perpendicular to  $\hat{\mathbf{u}}$  represented on the index ellipse. Reproduced and adapted from reference [24].

the same, e.g.  $n_1 = n_2 = n_o$ , but the third is different, e.g.  $n_3 = n_e$ . Here the subscripts o and e denote the *ordinary* and *extraordinary* indices respectively, and the direction corresponding to  $n_e$  is known as the *optical axis*. For a wave propagating along the optical axis the electric field will experience the same refractive index irrespective of the orientation of  $\mathbf{E}$ . Crystals with this type of symmetry are termed *uniaxial*. If all three of the principal refractive indices are different, e.g.  $n_1 \neq n_2 \neq n_3$ , then the crystal exhibits two optical axes (which will not be parallel to the principal axes of the crystal) and is termed *biaxial*.

### 1.1.3 Plane Wave Propagation Through an Anisotropic Medium

In this section we will consider the propagation of electromagnetic waves through anisotropic dielectric media. We will treat the orthogonal electric and magnetic field components of electromagnetic waves as plane waves of the form

$$\begin{aligned}\mathbf{E} &= \mathbf{E}_0 e^{-i(\mathbf{k} \cdot \mathbf{r} - \omega t)}, \\ \mathbf{H} &= \mathbf{H}_0 e^{-i(\mathbf{k} \cdot \mathbf{r} - \omega t)},\end{aligned}\tag{1.15}$$

describing the wave at position  $\mathbf{r}$  with a wavevector  $\mathbf{k} = k\hat{\mathbf{u}}$  oriented along the unit vector  $\hat{\mathbf{u}}$ .

#### Dispersion Relation in an Anisotropic Medium

Maxwell's equations in a dielectric medium can be expressed as

$$\nabla \times \mathbf{E} = -\mu_0 \frac{\partial \mathbf{H}}{\partial t},\tag{1.16}$$

$$\nabla \times \mathbf{H} = -\epsilon \cdot \frac{\partial \mathbf{E}}{\partial t}.\tag{1.17}$$

By considering the electric and magnetic fields as plane waves of the form given in Equation 1.15 and using the relation  $\mathbf{D} = \epsilon \mathbf{E}$ , Equations 1.16 and 1.17 reduce to

$$\mathbf{k} \times \mathbf{E} = \omega \mu_0 \mathbf{H},\tag{1.18}$$

$$\mathbf{k} \times \mathbf{H} = -\omega \mathbf{D}.\tag{1.19}$$

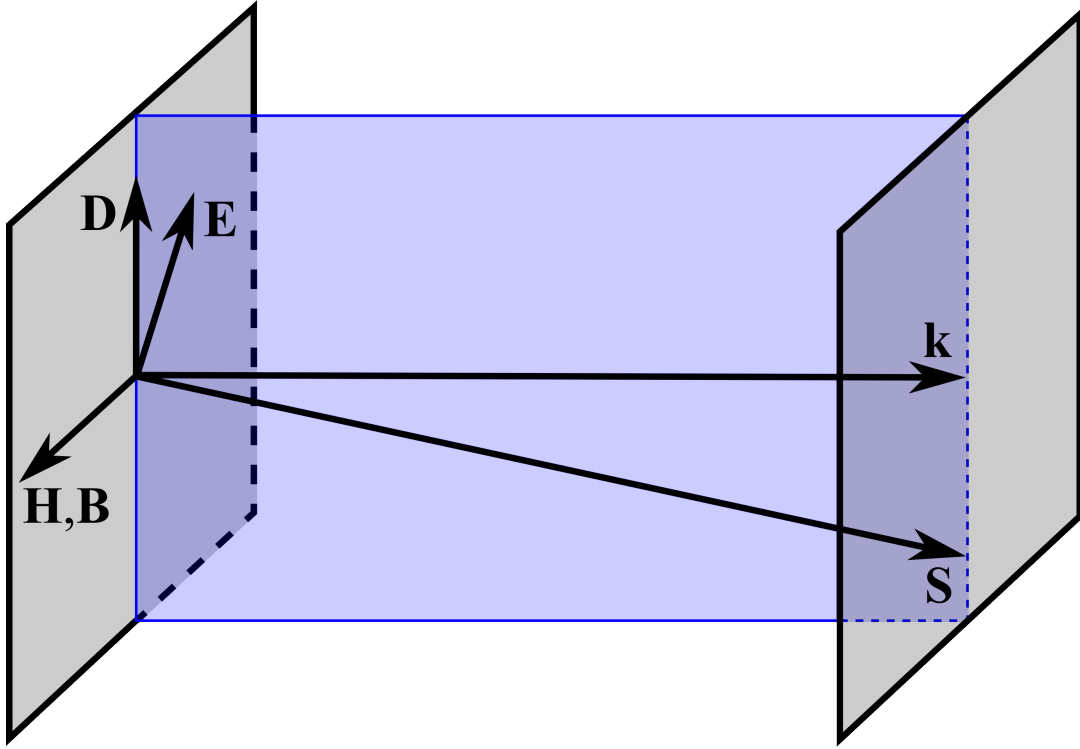


Figure 1.2: Geometrical representation of the vectors describing an electromagnetic wave in a dielectric medium. The vectors  $\mathbf{E}$ ,  $\mathbf{D}$ ,  $\mathbf{k}$  and  $\mathbf{S}$  all lie in the plane perpendicular to  $\mathbf{H}$ ,  $\mathbf{E}$  is perpendicular to  $\mathbf{S}$  and  $\mathbf{D}$  is perpendicular to  $\mathbf{k}$ . Reproduced and adapted from reference [24].

These equations define the geometry of the vectors describing an electromagnetic wave in a dielectric medium, shown schematically in Figure 1.2:  $\mathbf{H}$  is oriented perpendicular to both  $\mathbf{k}$  and  $\mathbf{E}$ , whilst  $\mathbf{D}$  is perpendicular to both  $\mathbf{k}$  and  $\mathbf{H}$ . Defining the direction of energy flow via the Poynting vector  $\mathbf{S} = \mathbf{E} \times \mathbf{H}$  sets it perpendicular to both  $\mathbf{E}$  and  $\mathbf{H}$ . Therefore the vectors  $\mathbf{E}$ ,  $\mathbf{D}$ ,  $\mathbf{k}$  and  $\mathbf{S}$  all lie in the plane perpendicular to  $\mathbf{H}$ ; however, due to Equation 1.5  $\mathbf{E}$  and  $\mathbf{D}$  (and therefore  $\mathbf{k}$  and  $\mathbf{S}$ ) are not necessarily parallel to each other. Rearranging Equation 1.18 for  $\mathbf{H}$  and substituting into Equation 1.19, we obtain

$$\mathbf{k} \times (\mathbf{k} \times \mathbf{E}) + \omega^2 \mu_0 \epsilon \mathbf{E} = 0. \quad (1.20)$$

This vector equation can also be represented in matrix form, which in the principal axis system of the dielectric medium is given by

$$\begin{bmatrix} \omega^2 \mu_0 \epsilon_1 - k_2^2 - k_3^2 & k_1 k_2 & k_1 k_3 \\ k_2 k_1 & \omega^2 \mu_0 \epsilon_2 - k_1^2 - k_3^2 & k_2 k_3 \\ k_3 k_1 & k_3 k_2 & \omega^2 \mu_0 \epsilon_3 - k_1^2 - k_2^2 \end{bmatrix} \cdot \begin{bmatrix} E_1 \\ E_2 \\ E_3 \end{bmatrix} = \begin{bmatrix} 0 \\ 0 \\ 0 \end{bmatrix}. \quad (1.21)$$

Setting the determinant of this matrix equal to zero allows us to solve for  $\omega$  as a function of the principal axis components of  $\mathbf{k} = (k_1, k_2, k_3)$ , and therefore establish the dispersion relation of the anisotropic medium.

### Propagation in an Arbitrary Direction

From Equation 1.19 we know that  $\mathbf{D}$  in a dielectric medium lies in a plane perpendicular to  $\mathbf{k}$ , and therefore is also perpendicular to the direction of propagation  $\hat{\mathbf{u}}$ . Rewriting Equation 1.20 in terms of  $\mathbf{D}$  using  $\mathbf{E} = \boldsymbol{\epsilon}^{-1} \mathbf{D}$ ,  $\boldsymbol{\eta} = \epsilon_0 \boldsymbol{\epsilon}^{-1}$  and  $\mathbf{k} = k \hat{\mathbf{u}}$ , we obtain

$$\frac{k^2}{\epsilon_0} \hat{\mathbf{u}} \times (\hat{\mathbf{u}} \times \boldsymbol{\eta} \mathbf{D}) + \omega^2 \mu_0 \mathbf{D} = 0. \quad (1.22)$$

If we consider the first term in Equation 1.22 as a projection of the vector  $\boldsymbol{\eta} \mathbf{D}$  onto a plane perpendicular to  $\hat{\mathbf{u}}$ , we may define a projection operator  $\mathbf{P}_u$  such that

$$\mathbf{P}_u \boldsymbol{\eta} \mathbf{D} = -\hat{\mathbf{u}} \times (\hat{\mathbf{u}} \times \boldsymbol{\eta} \mathbf{D}). \quad (1.23)$$

By using the relations  $k_0^2 = \omega^2 \mu_0 \epsilon_0$  and  $n = k/k_0$ , we can rewrite Equation 1.22 as an eigenvalue equation of the operator  $\mathbf{P}_u \boldsymbol{\eta}$ ,

$$\mathbf{P}_u \boldsymbol{\eta} \mathbf{D} = \frac{1}{n^2} \mathbf{D}, \quad (1.24)$$

which has two eigenvectors  $\mathbf{D}_a$  and  $\mathbf{D}_b$  corresponding to the normal modes of propagation in the direction of  $\hat{\mathbf{u}}$ , with their corresponding eigenvalues being  $1/n_a^2$  and  $1/n_b^2$ .

The solutions to this eigenvalue equation can be visualised using either the dispersion relation or the index ellipsoid. In the form  $\omega = \omega(k_1, k_2, k_3)$ , the dispersion relation can be considered as the equation of a surface in  $\mathbf{k}$ -space.



For an arbitrary direction of propagation  $\hat{\mathbf{u}}$  there are two intersections with the surface in  $\mathbf{k}$ -space, which correspond to the two normal modes of propagation along  $\hat{\mathbf{u}}$ . These normal modes are demonstrated on the index ellipsoid in Figure 1.1, with the plane perpendicular to  $\hat{\mathbf{u}}$  up to the boundary of the index ellipsoid and passing through the origin known as the *index ellipse*. The major and minor axes of this index ellipse are the directions of the eigenvectors  $\mathbf{D}_{a,b}$ , and the lengths of the semi-major and semi-minor axes are the values of the refractive indices  $n_{a,b}$  along the normal modes of propagation.

#### 1.1.4 Effects of an Anisotropic Medium on the Polarisation State of Light

In an isotropic medium, for any given propagation direction and orientation of  $\mathbf{E}$  of an incident plane electromagnetic wave, the electric field will experience the same refractive index, and so the polarisation state will remain unchanged after propagating through an isotropic medium. So what happens when we consider the case where the principal refractive indices are not all the same? Having established the index ellipsoid and the two orthogonal normal modes of propagation for a given direction, we can now use these concepts to describe how the polarisation state of light evolves upon propagating through an anisotropic medium.

For light with angular frequency  $\omega$  propagating in an anisotropic crystal with an arbitrary wavevector  $\mathbf{k}$  there are two orthogonal normal modes, with polarisation eigenvectors  $\mathbf{D}_{a,b}$ . These normal modes each have different refractive indices. If the incident light is polarised along one of the eigenvectors of a normal mode, then the wave experiences only one refractive index, and the polarisation state remains unchanged after transmission through the medium. However, if the incident light is linearly polarised with components of  $\mathbf{E}$  along  $\mathbf{D}_a$  and  $\mathbf{D}_b$ , then each component will propagate through the crystal with a different velocity. This introduces a relative phase  $\phi_a = \omega dn_a/c$  and  $\phi_b = \omega dn_b/c$  to each component of  $\mathbf{E}$ , depending on the distance  $d$  the wave has propagated through the medium. After transmission through a crystal of thickness  $L$ , the

two components of  $\mathbf{E}$  will have acquired a phase delay

$$\Delta\phi = \phi_b - \phi_a = \frac{\omega L}{c} (n_b - n_a), \quad (1.25)$$

where the difference in refractive index  $n_b - n_a = \Delta n$  is the *birefringence* of the medium. The polarisation state of the transmitted light will therefore depend on the phase delay introduced: a superposition of two orthogonally polarised waves with a phase delay of  $\Delta\phi = \pi/2$  will form a circular polarisation state, whereas for any other value of  $0 < \Delta\phi < \pi/2$  the polarisation state will be elliptical.

## 1.2 Describing the Polarisation State of Electromagnetic Waves

Having established that propagation through an anisotropic medium can alter the polarisation state of light, a crucial consideration in the spectroscopy of anisotropic materials is having a method of describing the polarisation state at a given time or frequency. This section will outline some of the descriptions available which will be used in this thesis: the ellipticity and orientation angle; the ellipsometric parameters; Jones matrices; and Stokes parameters.

### 1.2.1 Ellipticity and Orientation Angle

The polarisation state of an electromagnetic wave can be parameterised by two quantities, the *ellipticity angle*  $\chi$  and the *orientation angle*  $\psi$  [19]. This parameterisation is shown schematically by the *polarisation ellipse* in Figure 1.3, with the viewer oriented such that they are looking into the direction of propagation of the electromagnetic wave. For an arbitrary polarisation state the oscillation of the electric or magnetic field when viewing from this position can be visualised as forming an ellipse. The ellipticity angle is defined as

$$\chi = \tan^{-1} \left( \frac{b}{a} \right), \quad (1.26)$$

where  $a$  and  $b$  are the lengths of the semi-major and semi-minor axes of the polarisation ellipse respectively. An ellipticity angle of zero corresponds to a

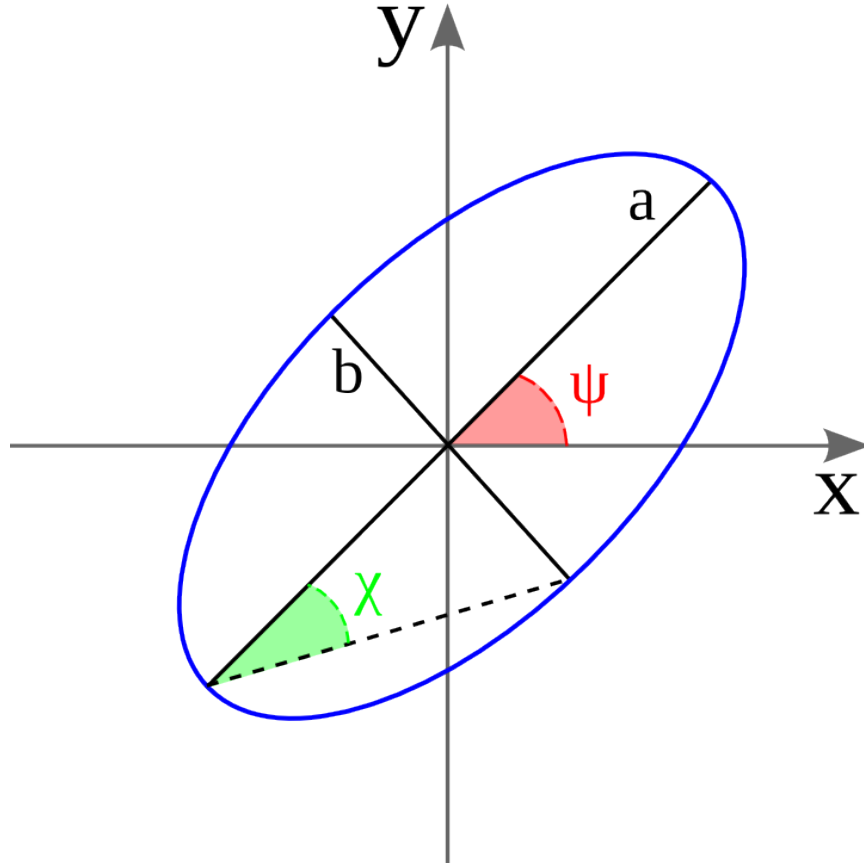


Figure 1.3: Parameterisation of the polarisation state of an electromagnetic wave, using the ellipticity angle  $\chi$  and orientation angle  $\psi$ . The polarisation ellipse (blue curve) is the projection of the oscillation of the electric field onto a plane perpendicular to the direction of propagation.

linear polarisation state, whereas an ellipticity of  $\pm 45^\circ$  corresponds to right- and left-handed circular polarisation, respectively. The orientation angle is defined as the angle of the major axis of the polarisation ellipse away from the  $x$ -axis of the lab coordinate system. A positive orientation angle is defined by the angle formed by an anticlockwise rotation of the polarisation state relative to the  $x$ -axis, e.g.  $\psi = +45^\circ$  occurs in the top right-hand quadrant of the polarisation ellipse as displayed in Figure 1.3.

### 1.2.2 Alternative Descriptions of the Polarisation State

#### Ellipsometric Parameters

The ellipsometric parameters are an alternate parameterisation of the polarisation ellipse. Rather than taking into account the half-lengths of the polarisation ellipse, the ellipsometric parameters consider the s- and p-polarised components of the electromagnetic wave that form the polarisation state. In terms of these components the polarisation state is parameterised by

$$\tan \Psi e^{i\Delta} = \frac{|E_p|}{|E_s|} e^{i(\phi_p - \phi_s)} \quad (1.27)$$

where  $|E_p|$  and  $\phi_p$  are the amplitude and phase of the p-polarised component, respectively, and  $|E_s|$  and  $\phi_s$  are the equivalent values for the s-polarised component.

#### Jones Calculus

Jones calculus is a matrix formulation of polarised light, which makes use of column vectors to describe the polarisation state of light, and  $2 \times 2$  matrices to describe the interaction of light with optical components and materials. The *Jones vector* of an electromagnetic wave is expressed as

$$\mathbf{E} = \begin{bmatrix} E_x \\ E_y \end{bmatrix} = \begin{bmatrix} E_{0x} e^{i\phi_x} \\ E_{0y} e^{i\phi_y} \end{bmatrix}, \quad (1.28)$$

where each component contains information about both the amplitude  $E_0$  and phase  $\phi$ . The *Jones matrix*  $\mathbf{J}$  of an arbitrary polarising element is expressed as

$$\mathbf{J} = \begin{bmatrix} J_{xx} & J_{xy} \\ J_{yx} & J_{yy} \end{bmatrix}, \quad (1.29)$$

and as such the Jones vector describing the resultant polarisation state can be found by  $\mathbf{E}' = \mathbf{J} \cdot \mathbf{E}$ .

### Stokes Parameters

Jones calculus is only applicable to fully polarised light; an alternative description of the polarisation state of light, which can account for partially- and un-polarised light, can be made using the *Stokes parameters*. These are usually given in the form of the *Stokes vector*  $\mathbf{S}_T$ , which can be related to the parameters of the polarisation ellipse  $\chi$  and  $\psi$  by

$$\mathbf{S}_T = \begin{bmatrix} I \\ Q \\ U \\ V \end{bmatrix} = \begin{bmatrix} I_0 \\ I_0 p \cos 2\psi \cos 2\chi \\ I_0 p \sin 2\psi \cos 2\chi \\ I_0 p \sin 2\chi \end{bmatrix}, \quad (1.30)$$

where  $I_0$  is the total intensity of the electromagnetic wave and  $p$  is the *degree of polarisation*, given by

$$p = \frac{\sqrt{Q^2 + U^2 + V^2}}{I}. \quad (1.31)$$

The four components of the Stokes vector in Equation 1.30 can be interpreted as: (i)  $I$  is the sum of the intensities of the purely linearly horizontal and linearly vertical components; (ii)  $Q$  is the difference between the intensities of the purely linearly horizontal and linearly vertical components; (iii)  $U$  is the difference between the intensities of the components purely polarised at  $+45^\circ$  and  $-45^\circ$ ; and (iv)  $V$  is the difference between the intensities of the purely circularly right-hand polarised and circularly left-hand polarised components.

A similar description of the interaction of light with polarising elements to that described by Jones calculus can be made via *Mueller calculus* and the *Mueller matrix*  $\mathbf{M}$ . In this case

$$\mathbf{S}_{\text{out}} = \mathbf{M} \cdot \mathbf{S}_{\text{in}} = \begin{bmatrix} M_{11} & M_{12} & M_{13} & M_{14} \\ M_{21} & M_{22} & M_{23} & M_{24} \\ M_{31} & M_{32} & M_{33} & M_{34} \\ M_{41} & M_{42} & M_{43} & M_{44} \end{bmatrix} \cdot \begin{bmatrix} I \\ Q \\ U \\ V \end{bmatrix}, \quad (1.32)$$

which relates the incident Stokes vector  $\mathbf{S}_{\text{in}}$  to the Stokes vector after interaction with an optical component or a material  $\mathbf{S}_{\text{out}}$ .

### 1.3 Electromagnons in Improper Ferroelectrics

A multiferroic can be defined as a material which exhibits more than one ferroic order parameter, such as ferromagnetism, ferroelectricity or ferroelasticity, in a single phase [25]. While this term encompasses a plethora of different combinations of order parameters, historically the union that has incited the most research interest is that of electricity and magnetism, in so-called magnetoelectric multiferroics [11, 26]. While the intimate link between electricity and magnetism in nature was elucidated by Maxwell’s equations, for a long time their occurrence in condensed matter appeared to be mutually exclusive: conventional ferromagnetism tends to arise due to partially filled  $f$ - or  $d$ -orbitals in rare earth and transition metal ions, whilst conventional ferroelectricity tends to arise due to ‘lone pair’ cations and empty  $d$ -orbitals in transition metal ions [27].

It was only in 1960 that the first magnetoelectric material,  $\text{Cr}_2\text{O}_3$ , was discovered [28] following a prior theoretical prediction [29]. Since this initial experimental observation, a vast number of magnetoelectric materials have been discovered and investigated; just a small selection of the many reviews available on the topic can be found in references [11, 26]. However, broadly speaking the behaviour of many magnetoelectric multiferroics can be typified by the two “poster-boy” materials, bismuth ferrite ( $\text{BiFeO}_3$ ) and terbium manganate ( $\text{TbMnO}_3$ ).  $\text{BiFeO}_3$  is one of the most promising magnetoelectric materials for device applications, owing to its large ferroelectric polarisation ( $\sim 90 \mu\text{C cm}^{-2}$ ) and the persistence of electrical and magnetic ordering at temperatures far above room temperature [30, 31]. Despite these promising properties the magnetoelectric coupling is weak, due to the differing origins of ferroelectricity and magnetism in  $\text{BiFeO}_3$ : ferroelectricity arises due to the  $6s^2$  lone pair in the  $\text{Bi}^{3+}$  ions, while the magnetism has its origins in the spins on the  $\text{Fe}^{3+}$  ions.

Since the discovery of magnetoelectricity in  $\text{BiFeO}_3$ , a variety of other mechanisms giving rise to magnetoelectric multiferroicity in materials have been discovered, including charge ordering [32], magnetic exchange striction [33], and the type of magnetoelectricity typified by  $\text{TbMnO}_3$ , spin-spiral magnetic ordering [34, 35]. Compared to  $\text{BiFeO}_3$ , the ferroelectric polarisation in  $\text{TbMnO}_3$

is small ( $\sim 0.08 \mu\text{C cm}^{-2}$ ) and multiferroicity only occurs at low temperatures ( $\sim 28 \text{ K}$ ), making it a far less practical material for applications. However, the interest in  $\text{TbMnO}_3$  stems from the magnetic origin of the ferroelectricity; the ferroelectricity in such materials is induced by competing magnetic interactions forming a magnetic state that breaks inversion symmetry, for instance an incommensurate spin-cycloid [36, 37]. This so-called “improper” ferroelectricity can result in strong magnetoelectric coupling [38, 39].

Improper ferroelectrics also exhibit dynamic magnetoelectric coupling, whereby an oscillating electric field couples to a spin wave, or magnon. This results in a novel quasiparticle excitation at terahertz frequencies - the electromagnon [8, 40, 41, 42, 43, 44]. This opens up possibilities for a new paradigm in the control of magnetic order, using the electric fields of THz frequency optical pulses [45]. However, the improper ferroelectric phase generally occurs only at low temperatures, typically below  $\sim 70 \text{ K}$  [38]; for many desired technological applications to be realised, room-temperature improper ferroelectrics are strongly desired. A promising material system in the search for room temperature improper ferroelectrics is cupric oxide ( $\text{CuO}$ ), which exhibits a magnetically-induced ferroelectric phase with spin-cycloidal ordering and electromagnons up to  $\sim 230 \text{ K}$  [8, 46].

This section will provide background to the second topic of study presented in this thesis - the behaviour of electromagnons in the improper ferroelectric multiferroic material cupric oxide ( $\text{CuO}$ ). A brief description and theoretical background to spin wave excitations in magnetically ordered materials, magnons, will be provided in Section 1.3.1, before discussing the unique quasiparticle excitation that can occur in improper ferroelectric materials, electromagnons, in Section 1.3.2. Lastly Section 1.3.3 will discuss multiferroicity and electromagnons in the principal multiferroic material system under study in this thesis,  $\text{CuO}$ .

### 1.3.1 Magnons

Having discussed the effect that the properties of a particular material have on the polarisation state of light propagating through it in Section 1.1, we may also consider the converse - what effect do the electric and magnetic fields of

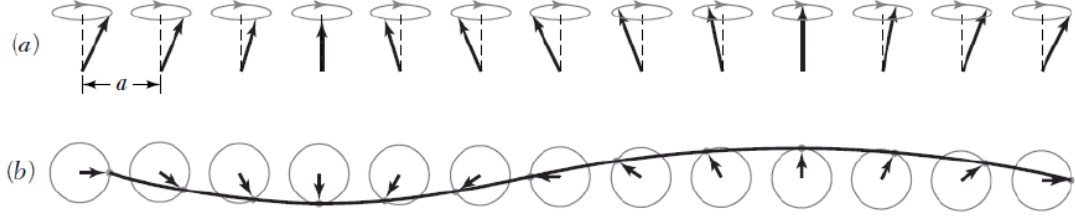


Figure 1.4: Depiction of a magnon, as viewed **(a)** in side profile and **(b)** from a top-down perspective, where the black curve represents the relative phase of the spins. Reproduced from reference [47].

light have on the material? Here we consider the effects of optical electric and magnetic fields in the linear regime only, where the field strengths are small. The effects of large field strength optical pulses on materials will be discussed in further detail in Section 6.1.

A charged particle exposed to an electric and magnetic field is subject to the Lorentz force  $\mathbf{F} = q(\mathbf{E} + \mathbf{v} \times \mathbf{B})$ . When exposed to the electric field of light atoms or ions in a material are displaced from their equilibrium positions, and the interactions between adjacent atoms or ions in the crystalline lattice result in collective vibrational modes, known as phonons. The magnetic field of light can have an analogous effect on the magnetic moments of the ions in the crystal lattice. In a magnetically ordered material, the magnetic torque applied by the optical magnetic field causes displacements of the spins from their equilibrium positions; due to interactions between adjacent spins in the crystal structure, these displacements propagate through the material as a spin wave, the quasiparticle of which is known as a magnon, shown schematically in Fig 1.4.

In order to describe the behaviour of magnons in a material, an equation of motion for the spin angular momentum of the  $i^{\text{th}}$  spin  $\mathbf{S}_i$  can be expressed in terms of an effective magnetic field  $\mathbf{H}_{\text{eff}}$ , used to represent all the interactions felt by a single spin. This is given by the Landau-Lifshitz-Gilbert (LLG) equation

$$\frac{d\mathbf{S}_i}{dt} = \gamma \mathbf{H}_{\text{eff}} \times \mathbf{S}_i - \frac{\lambda}{\hbar} \frac{\mathbf{S}_i \times (\mathbf{H}_{\text{eff}} \times \mathbf{S}_i)}{S^2}, \quad (1.33)$$

where  $\gamma = g|e|/2m$  is the gyromagnetic ratio and  $\lambda$  is the Gilbert damping parameter. The effective field drives the spins to align in its direction, causing



the spins to precess about their equilibrium position. The effective field can be expressed as the partial derivative of the free energy  $F$  of the system with respect to  $\mathbf{S}_i$ . In the condition where the temperature of the system is much lower than the ordering temperature, the free energy can be approximated by the semi-classical spin Hamiltonian  $\mathcal{H}$  of the system, allowing us to define the effective field as

$$\mathbf{H}_{\text{eff}} = \frac{1}{\gamma\hbar} \frac{\partial \mathcal{H}}{\partial \mathbf{S}_i}. \quad (1.34)$$

Using this definition, the spin dynamics in a particular system can be investigated by: defining a specific spin Hamiltonian accounting for all the interactions between spins in the system, calculating the resultant effective field acting on the spins, then solving the LLG equation to find properties of interest, such as the magnon dispersion relation and the nature of the magnetic dynamics.

### 1.3.2 Electromagnons

While the dynamics of magnons may be understood solely by the interaction of the magnetic field of light with the spins in a material, the electric dipole-active nature of electromagnons requires that coupling between the spins and phonons in the material are taken into account in the Hamiltonian. Two distinct mechanisms that give rise to electromagnons have been discussed in the literature: Dzyaloshinskii-Moriya electromagnons, and exchange-striction (ES) electromagnons. The different origins for these mechanisms are shown schematically by Figs. 1.5 (a) for the DM electromagnon and 1.5 (b) for the ES electromagnon.

The static polarisation in an improper ferroelectric phase with spin-cycloidal ordering can be understood as arising from the spin-current or inverse Dzyaloshinskii-Moriya (DM) interaction [33, 36]. The DM interaction can be expressed as

$$\mathcal{H}_{\text{DM}} = \sum_a \mathbf{d}_a(\mathbf{r}_i) \cdot (\mathbf{S}_i \times \mathbf{S}_{i+1}), \quad (1.35)$$

where  $\mathbf{S}_i$  and  $\mathbf{S}_{i+1}$  are adjacent spins in the cycloid. The DM vectors  $\mathbf{d}_a$  are parameterised by

$$\mathbf{d}_a = \gamma(\boldsymbol{\delta}_i \times \mathbf{r}_i), \quad (1.36)$$

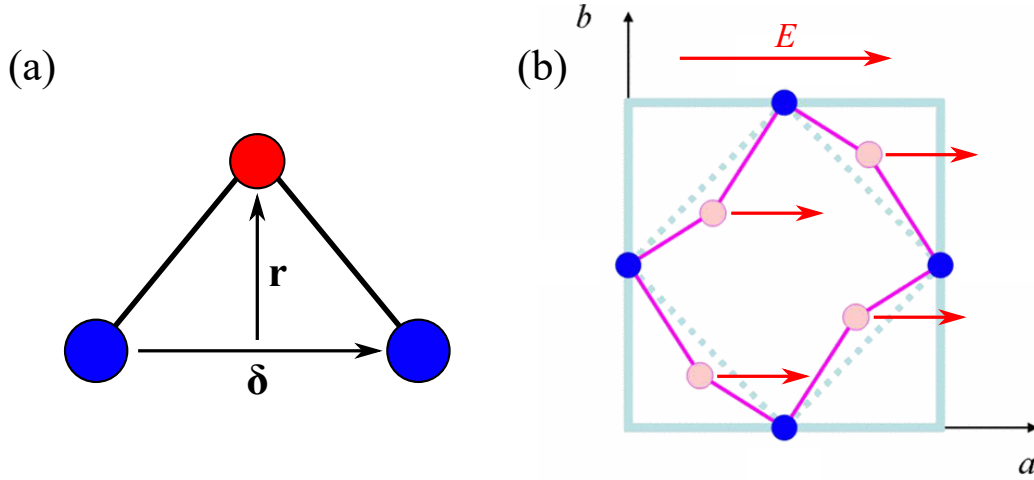


Figure 1.5: **(a)** Schematic diagram of the interactions involved in the Dzyaloshinskii-Moriya interaction, involving the magnetic ions (blue circle) and the superexchange-mediated oxygen ion (red circle), showing the displacement of the oxygen ions  $\mathbf{r}$  away from the vector connecting adjacent spins  $\boldsymbol{\delta}$ . **(b)** Schematic diagram of the exchange-striction mechanism for electromagnons in rare-earth manganites, depicting four Mn ions (blue) and four oxygen ions (pink) in one  $ab$  layer. An electric field applied in the  $a$ -direction causes a uniform displacement of the oxygen ions, which modulates the nearest-neighbour exchange interactions. Panel **(b)** is reproduced and adapted from reference [48].

where  $\gamma$  is the interaction strength,  $\boldsymbol{\delta}$  is the vector connecting two adjacent spins in the cycloid, and  $\mathbf{r}$  is the displacement of the superexchange-mediated oxygen ions from the line connecting the spins, shown schematically in Fig. 1.5 (a). The energy of the DM interaction can therefore be lowered by inducing a polar lattice distortion, resulting in a net polarisation  $\mathbf{P} \propto (\mathbf{S}_i \times \mathbf{S}_{i+1})$ . DM electromagnons result from the dynamic coupling of this polarisation to oscillating electric fields, causing an alteration in the oxygen displacements  $\mathbf{r}$  which in turn alters the magnetic interactions and drives a magnon, and are eigenmodes of the spin-cycloid [43].

Exchange-striction electromagnons, on the other hand, arise from a modulation of the isotropic Heisenberg exchange interaction by lattice vibrations, proportional to a  $(\mathbf{S}_i \cdot \mathbf{S}_j)$  term in the Hamiltonian [48, 49], accounting for interactions between the  $i^{\text{th}}$  and  $j^{\text{th}}$  spins. In  $RMnO_3$  (where  $R$  = rare earth), distortions of the orthorhombic crystal structure cause displacements in the positions of the superexchange-mediated oxygen ions, resulting in a change in the Mn-O-Mn bond angle. According to the Goodenough-Kanamori rules, the

strength of the antiferromagnetic exchange interaction decreases as the Mn-O-Mn bond angle decreases from  $180^\circ$ . The application of an electric field along the  $a$ -direction displaces all the oxygen ions by an equal distance along this direction; this produces an alternating rotation of the  $\text{MnO}_6$  octahedra, changing the Mn-O-Mn bond angles and altering the nearest-neighbour exchange interaction along the spin-spiral propagation vector [48].

The different mechanisms giving rise to electromagnons exhibit separate optical selection rules, which may be used to differentiate between the two experimentally: the DM electromagnon selection rules are directly linked to the plane of the spin-cycloid, hence if the plane of the cycloid is changed (such as by a magnetic field-induced spin flop) the selection rules also change accordingly. The same does not hold for the ES electromagnons, which are linked to the crystal lattice, and as such do not rotate with the plane of the cycloid.

The first experimental observations of electromagnons were made by Pimenov *et al.* in 2006, when they were observed in the rare-earth manganates  $\text{TbMnO}_3$  and  $\text{GdMnO}_3$  [40]. Since this pioneering paper, much progress has been made in understanding electromagnons in rare-earth manganates ( $\text{RMnO}_3$ ) and manganites ( $\text{RMn}_2\text{O}_5$ ) from both experimental [41, 42, 43, 44] and theoretical perspectives [50, 51]. Multiferroic phases, and hence electromagnons, tend to be observed at temperatures below  $\sim 70$  K in these materials. As mentioned previously, electromagnons that occur at higher temperatures would be highly desirable for any potential applications. An IR and Raman-active electromagnon has recently been observed at up to 250 K in a z-type hexaferrite [52]. However the material system focused on in this thesis is  $\text{Cu}_{1-x}\text{Zn}_x\text{O}$  alloys, in which multiferroicity and electromagnons have been observed between 213-230 K in  $x = 0$  [8] and between 159-190 K in  $x = 0.05$  [53]. A particularly intriguing prediction from theoretical investigations is that the introduction of non-magnetic impurities into CuO may stabilize the multiferroic phase at higher temperatures than the pure case [54], and that hydrostatic pressure can broaden the multiferroic phase above room temperature [55]. The following section will explore the current literature on multiferroicity and electromagnons in CuO.

### 1.3.3 Improper Ferroelectricity and Electromagnons in CuO

CuO has a monoclinic crystal structure with space group  $C2/c$ , which can be visualized as zig-zagging Cu-O-Cu chains along the  $[101]$  and  $[10\bar{1}]$  directions, shown in Fig. 1.6 (a). The magnetic phases of CuO have previously been characterized by neutron diffraction [57, 58] and ultrasound velocity measurements [59]. Below 213 K, the dominant magnetic interaction is antiferromagnetic superexchange between spins in  $\text{Cu}^{2+}$  chains in the  $[10\bar{1}]$  direction ( $J_{\text{AFM}} \sim 80 \text{ meV}$ ) [60]. Weaker ferromagnetic superexchange interactions occur between spins in adjacent spin chains along the  $[101]$  ( $J_{\text{FM1}} \sim 5 \text{ meV}$ ) and  $[010]$  ( $J_{\text{FM2}} \sim 3 \text{ meV}$ ) directions [60]. As the ratio of interchain to intrachain interactions is about 0.1, CuO can be described as a quasi-1D collinear Heisenberg antiferromagnet in the low temperature (AF1) phase [61, 62], consisting of two interpenetrating  $\text{Cu}^{2+}$  sublattices with spins aligned along the  $b$ -axis.

At 213 K the spins on one sublattice flop into the  $ac$ -plane [63] and form an incommensurate spin-cycloid phase (AF2) with magnetic ordering vector  $\mathbf{q} = (0.506, 0, -0.483)$  [57, 58], depicted in Figs. 1.6 (b) and 1.6 (c). The first-order nature of the AF1 - AF2 phase transition has been observed in specific heat measurements [64, 65, 66]. A magnetically-induced ferroelectric polarisation  $P_b \sim 100 \mu\text{C m}^{-2}$  in this phase occurs in the  $b$ -direction [46], shown in Fig. 1.6 (d), which also exhibits ferroelectric hysteresis loops [46]. Between 229.3-230 K an intermediate commensurate, collinear magnetic phase (AF3) forms [59], and above 230 K is the paramagnetic phase (PM).

#### Electromagnon in CuO

An electromagnon has been observed in the multiferroic AF2 phase of CuO using THz-TDS by Jones *et al.* [8]. The change in absorption coefficient  $\Delta\alpha$  relative to the absorption at 200 K in the AF1 phase are shown in Figs. 1.7 (a) and 1.7 (b), for various orientations of the electric and magnetic fields of the THz pulse relative to the crystal axes. Representative temperatures chosen were 212 K (AF1 phase), 216 K (AF2 phase), and 246 K (PM phase). The electromagnon is evident as a strong absorption feature at 0.7 THz in the AF2 phase and is active only for THz electric fields parallel to the  $[101]$  direction, regardless of

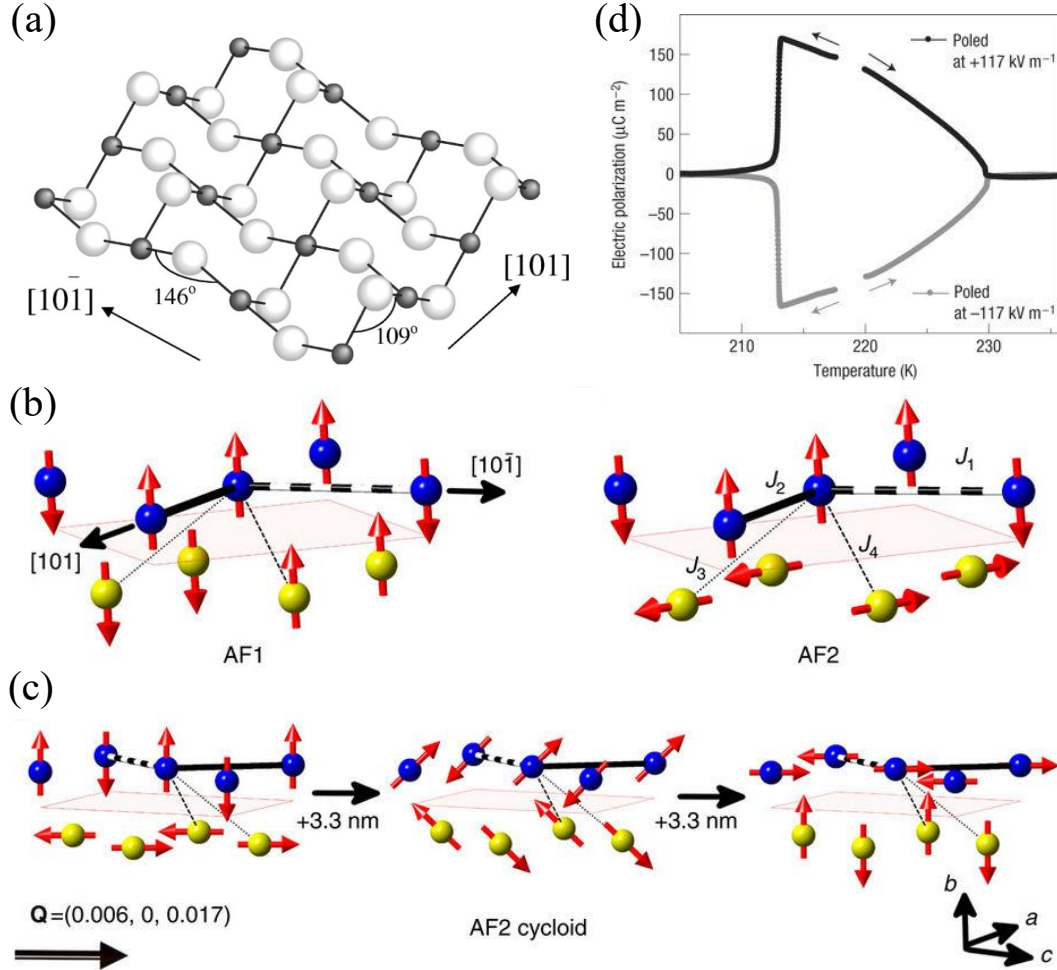


Figure 1.6: (a) Crystal structure of CuO depicting the zig-zagging Cu-O-Cu chains. Copper and oxygen atoms are represented by the light and dark spheres, respectively. (b) Depiction of the spins (red arrows) on copper atoms in the AF1 and AF2 phases of CuO, and (c) a representation of the spin-cycloid in CuO. (d) Ferroelectric polarisation in the AF2 phase of CuO as a function of temperature. Reproduced from references [56] (panel (a)), [8] (panels (b) and (c)), and [46] (panel (d)).

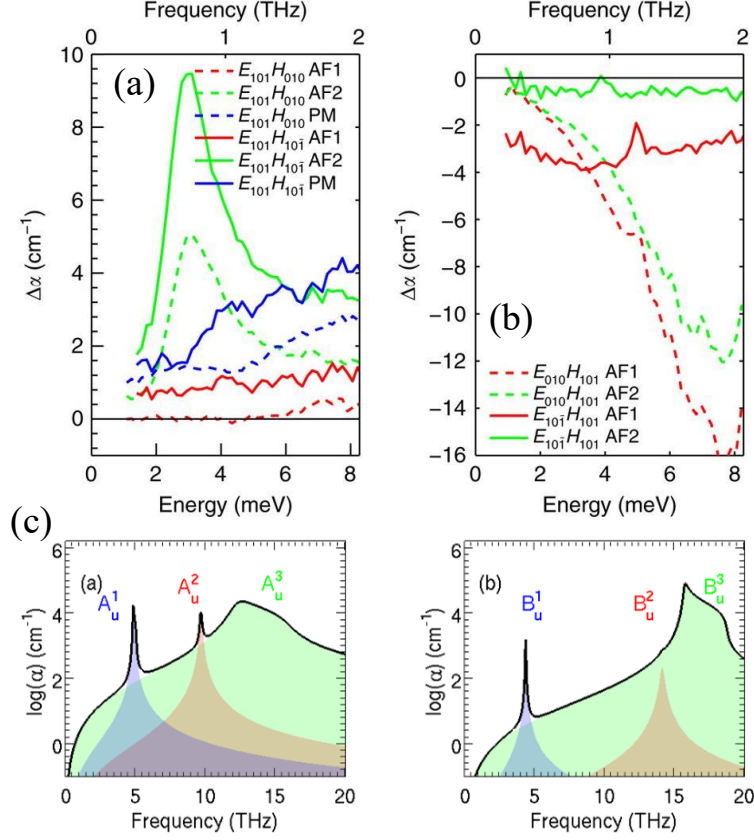


Figure 1.7: **(a)** Spectra for  $E_{\text{THz}} // (101)$  with H along  $(10\bar{1})$  (solid lines) and  $(010)$  (dashed lines) show a strong absorption at 0.7 THz in the AF2 phase (216 K) only. **(b)** Complimentary spectra demonstrating the absence of the 0.7 THz absorption feature when  $E_{\text{THz}}$  is along  $(010)$  and  $(10\bar{1})$ . **(c)** Relative contributions of the phonon modes in CuO to the total absorption coefficient (black lines), calculated from the model and parameters given in reference [56]. The  $A_u$  phonon modes are active when  $E_{\text{THz}} // (010)$ , and the  $B_u$  modes are active when  $E_{\text{THz}} // (101)$ . Reproduced from reference [8].

the orientation of the THz magnetic field, confirming the excitation's electric dipole-active nature. The change in absorption coefficient  $\Delta\alpha$  was presented, rather than the absolute absorption coefficient  $\alpha$ , in order to avoid the influence of the broad  $A_u^3$  phonon mode at 12.4 THz, which dominates the absorption in the THz region due its significant linewidth [8, 56], as shown in Fig. 1.7 (c).

The temperature dependence of the electromagnon was also investigated, and is shown in Fig. 1.8. The electromagnon spectrum consists of the main electromagnon mode at  $\sim 0.7$  THz with a weaker shoulder feature at higher frequencies. The electromagnon emerges rapidly at the AF1-AF2 phase transition, and a decrease in absorption strength and a redshift of the mode frequency are

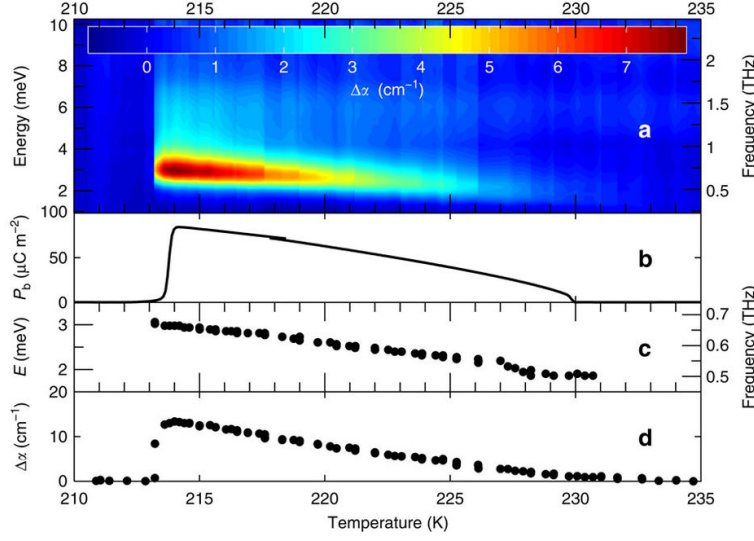


Figure 1.8: **(a)** Temperature evolution of the electromagnon absorption in CuO, demonstrating the sharp onset at the AF1-AF2 phase transition, along with the decrease in strength and redshift with increasing temperature. The static polarisation in the  $b$ -direction (panel **(b)**) is also presented (Reproduced from reference [46]) for comparison with the mode frequency (panel **(c)**) and absorption strength (panel **(d)**). Reproduced from reference [8].

observed as temperature increases. No electromagnon is observed for temperatures above the AF2-AF3 and AF3-PM phase transitions. Both the absorption strength and frequency of the electromagnon closely track the size of the ferroelectric polarisation along [010] in the AF2 phase, which both confirms the identification of this mode as an electromagnon, and intriguingly suggests an intimate link between the strength of the electromagnon and the spin-cycloidal ordering in the AF2 phase. Drude-Lorentz oscillator fits (described in more detail in section 5.3) to the electromagnon spectra in CuO produced an oscillator strength of  $\Delta\epsilon \sim 0.07$ ; this is comparable to the strength of the lower-frequency electromagnon observed in  $\text{TbMnO}_3$  ( $\Delta\epsilon \sim 0.05$ ) which has been assigned to an eigenmode of the spin-cycloid [67], as opposed to the strength of the higher frequency electromagnons ( $\Delta\epsilon \sim 2.0$ ) attributed to the exchange-striction mechanism [48].

A theoretical investigation of electromagnons in CuO was undertaken by Cao *et al.* [68]. Using symmetry analysis they showed that the electromagnon observed by Jones *et al.* could not arise from the exchange-striction mechanism, and was instead compatible with a DM-type electromagnon. The

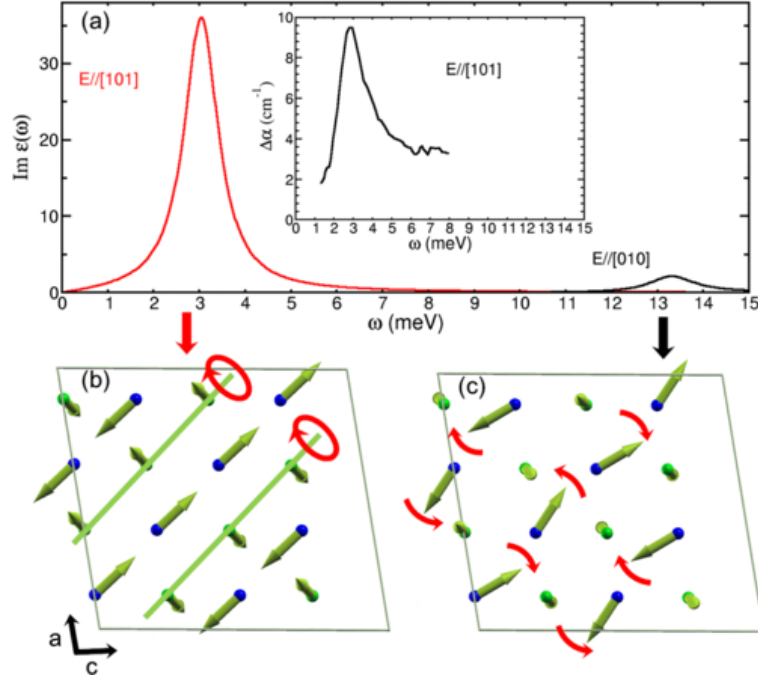


Figure 1.9: **(a)** Theoretical spectrum of the electromagnon in CuO, for  $E_{\text{THz}}$  parallel to [101] (red line) and [010] (black line). Inset is the experimental spectrum, for comparison. Panels **(b)** and **(c)** depict the predicted spin motion of the respective mode. Reproduced from reference [68].

experimentally-observed electromagnon behaviour was reproduced theoretically using *ab initio* calculations and a LLG analysis of the magnetic dynamics. The magnetic properties of CuO were modelled using a spin Hamiltonian of the form

$$\hat{H} = \sum_{ij} J_{ij} \mathbf{S}_i \cdot \mathbf{S}_j + \mathbf{D}_{ij} \cdot (\mathbf{S}_i \times \mathbf{S}_j) - \sum_i (\mathbf{K} \cdot \mathbf{S}_i)^2 + \hat{H}_{\text{me}}, \quad (1.37)$$

where the first term accounts for superexchange interactions between adjacent spins  $\mathbf{S}_i$ , the second term describes the DM interaction, the third term describes single-ion anisotropy, and the final term accounts for magnetoelectric coupling. The theoretical electromagnon spectrum is shown in Fig. 1.9 (a), and the mode was found to correspond to a rigid rotation of the spins in the plane perpendicular to [101], shown in Fig. 1.9 (b). This model of electromagnons in CuO also predicts that an exchange-striction electromagnon should be observed around 3.2 THz for  $E_{\text{THz}} // [010]$ .



## 1.4 Structure of This Thesis

The overarching theme of this thesis is the development of new techniques and components to be employed in terahertz time-domain spectroscopy, and how they may be applied in the study of anisotropic materials. In particular, the work presented here focuses on enhancing the experimentalist's control over the polarisation state of the generated THz radiation for time-domain spectroscopy experiments, while also exploring the applicability of using resonant excitations to probe material properties at a phase transition, and presenting preliminary investigations into the spectroscopy of various condensed matter systems in the nonlinear regime.

Chapter 2 will describe the technique of terahertz time-domain spectroscopy, detailing the methods used in the generation and detection of broadband pulses of THz radiation, and how they may be combined to form the spectrometer constructed as part of this work. The process of extracting the full complex refractive index of a sample under study, and quantitative information about the polarisation state of the THz pulses from the experimental data, will also be described.

Chapter 3 will then describe the development of a rotatable-polarisation terahertz time-domain spectrometer, detailing the adaptations made to the spectrometer described in Chapter 2 which allow the generation and detection of an arbitrarily rotatable, linear THz polarisation state, based upon the mechanical rotation of an interdigitated photoconductive emitter. The optimisation of the setup will be described, then this method of polarisation rotation will be compared to a competing technique - projection of the polarisation state by a wire-grid polariser. Finally, the rotatable-polarisation spectroscopy technique developed in this chapter will be implemented experimentally: demonstrating how the in-plane polarisation eigenvectors of a birefringent sample can be identified, and how the full complex refractive index along each eigenvector can be extracted, then demonstrating how the selection rules of an anisotropic absorption feature can be determined.

Inspired by the work presented in the previous chapter, Chapter 4 will describe the development, fabrication and experimental verification of a novel

photoconductive emitter design, which allows the arbitrary rotation of a linear THz polarisation state using electrical control. As such, this method does not rely on any moving parts, and rotation of the polarisation state may be performed on timescales orders of magnitude faster than those achievable with methods based on rotating emitters or WGP. The characterisation of the devices will be described, before exploring how the emitters may be utilised to modulate between two circular polarisation states for rapid circular dichroism spectroscopy.

Chapter 5 will explore how the electromagnon excitation in  $\text{Cu}_{1-x}\text{Zn}_x\text{O}$  alloys may be used to precisely track a phase transition between two magnetically ordered phases. This technique is utilised to investigate the effects of alloying with non-magnetic zinc ions upon the electromagnons and the phase transition, which is shown to exhibit thermal hysteresis and broaden upon alloying.

Lastly, Chapter 6 will detail the construction and operation of a spectrometer utilising pulses of intense THz radiation to explore nonlinear optical properties of materials at THz frequencies. Nonlinear THz transmission in n-type indium antimonide is used as a test case to explore the performance of the spectrometer. Preliminary investigations are then carried out on two material systems; nonlinear transmission is investigated in single-walled carbon nanotube films, and tantalising hints of nonlinear behaviour of electromagnons are observed in CuO.

## Chapter 2

# Terahertz Time-Domain Spectroscopy

This chapter aims to serve as an overview of the basic technology and experimental techniques that the work presented in later chapters of this thesis expands on and develops. Section 2.1 will introduce and provide background to the main methods of generating broadband pulses of THz radiation used throughout this thesis, while Section 2.2 will describe the detection of these THz pulses. Section 2.3 will then describe how these two aspects are brought together to create a spectrometer, and describe the process of performing a typical THz-TDS experiment. Finally, Section 2.4 will outline the process by which material properties are extracted from the experimental data.

### 2.1 Generation of Broadband Terahertz Radiation

Any THz generation or detection methods used in this work are based upon the use of femtosecond infrared laser pulses, produced by a mode-locked Ti:Sapphire laser. The basic principle used to produce these ultrashort laser pulses is a lasing medium with a broad gain bandwidth: as the time-domain and frequency-domain are inversely related by the Fourier transform, a broad frequency spectrum will produce a pulse with a short temporal profile.

The femtosecond laser used to drive the spectrometer used in the majority of this thesis is a Spectra-Physics Mai Tai Ti:Sapphire oscillator, which

produces 80 fs duration, 800 nm central wavelength pulses at a repetition rate of 80 MHz, resulting in an average optical power of  $\sim 1.5$  W. In the Mai Tai, a semiconductor laser array pumps a Nd:YVO<sub>4</sub> laser, the 1064 nm output of which is frequency-doubled to 532 nm and used to pump the Ti:Sapphire crystal, which produces the output 800 nm laser pulses. The electronic ground states of the Ti<sup>3+</sup> ions are split into two vibrationally broadened energy levels by the sapphire matrix; hence stimulated emission can occur at a wide range of energies, producing the characteristic broadband pulses output by these lasers, with a typical gain bandwidth of 700 - 900 nm.

### 2.1.1 Photoconductive Emitters

The schematic layout of a typical simple photoconductive emitter (PCE) is shown in Fig. 2.1 (a). The PCE consists of a metal electrode structure on top of a semiconducting substrate, acting as a fast optically-activated switch [69, 70, 71]. The active region of the PCE is a small gap between the metal electrodes, typically around 10  $\mu$ m in size. To generate THz radiation from this device, a femtosecond laser pulse is focused onto the gap, which photoexcites charge carriers in this region of the semiconductor. Applying a biasing electric field across the gap causes the electrons and holes to be accelerated in opposite directions, parallel to the applied electric field, and this separation of charges generates a transient photocurrent in the gap. The time-varying photocurrent across the PCE causes the device to act as a transient electric dipole, which generates far-field radiation that can be described by

$$E(t) \propto \frac{dJ(t)}{dt}, \quad (2.1)$$

where  $E(t)$  is the far-field THz electric field produced and  $J(t)$  is the photocurrent density in the gap, both as a function of time  $t$ . The typical behaviour of the charge carrier density and the resultant photocurrent in the PCE as a function of time is demonstrated by Figs. 2.1 (b) - 2.1 (e). The femtosecond pulse photoexcites charge carriers in the semiconductor at a rate proportional to its temporal intensity envelope, which causes a corresponding rise in the photocurrent on a similar timescale. A short time later the applied field is screened

by the dipole formed, and momentum scattering reduces the photocurrent and THz emission. The duration of THz pulses produced by the PCE, hence the bandwidth of the generated radiation, therefore depends on the pump pulse duration and charge carrier dynamics in the substrate material.

A major limitation of this simple PCE design is a saturation of the THz power with increasing pump power due to the screening of the bias voltage by the photoexcited charges [73, 74]. One method used to reduce this effect is to use a larger gap size, on the order of  $\sim 100\ \mu\text{m}$ ; however an order of magnitude increase in gap size also requires a corresponding increase in the bias voltage, and as such requiring the use of high-power voltage supplies. An alternative method of increasing the active area of the device is to employ an interdigitated electrode structure [75, 76]. Such a device is shown schematically in Fig. 2.1 (f). This design consists of alternating electrodes connected to the bias and ground terminals of the device, with a semiconductor gap between each pair of electrodes. Each gap acts as an individual dipole antenna, and the overlap of all the individual dipole radiation in the far-field is the resultant output of the device. The THz radiation produced by the bare electrode geometry in Fig. 2.1 (f) would interfere destructively in the far-field, as the bias field switches direction in adjacent gaps, so a second metallization layer is placed between every second electrode finger to ensure optical excitation only occurs in substrate regions where the electric field points in the same direction, resulting in constructive interference in the far field. If the gap size of the device is  $5\ \mu\text{m}$ , high biasing electric fields of around  $20\ \text{kV cm}^{-1}$  can be produced in the gap by applying a voltage of only  $10\ \text{V}$  to the electrodes, removing the need for high-power voltage supplies. The THz field strength produced by interdigitated emitters can potentially be scaled by increasing the size of the emitting area and exciting them using amplified laser pulses [77].

The PCEs used throughout this thesis were fabricated at the University of Warwick by Michele Failla, with the exception of the work presented in Chapter 4, in which a new PCE design was developed and fabricated by myself as part of this doctoral work, details of which are presented in that chapter. The other PCEs used were interdigitated PCEs consisting of  $5\ \mu\text{m}$  gold wires with a  $5\ \mu\text{m}$  gap between wires, with an active area of  $1.3\ \text{mm} \times 2.0\ \text{mm}$ , and were fabricated

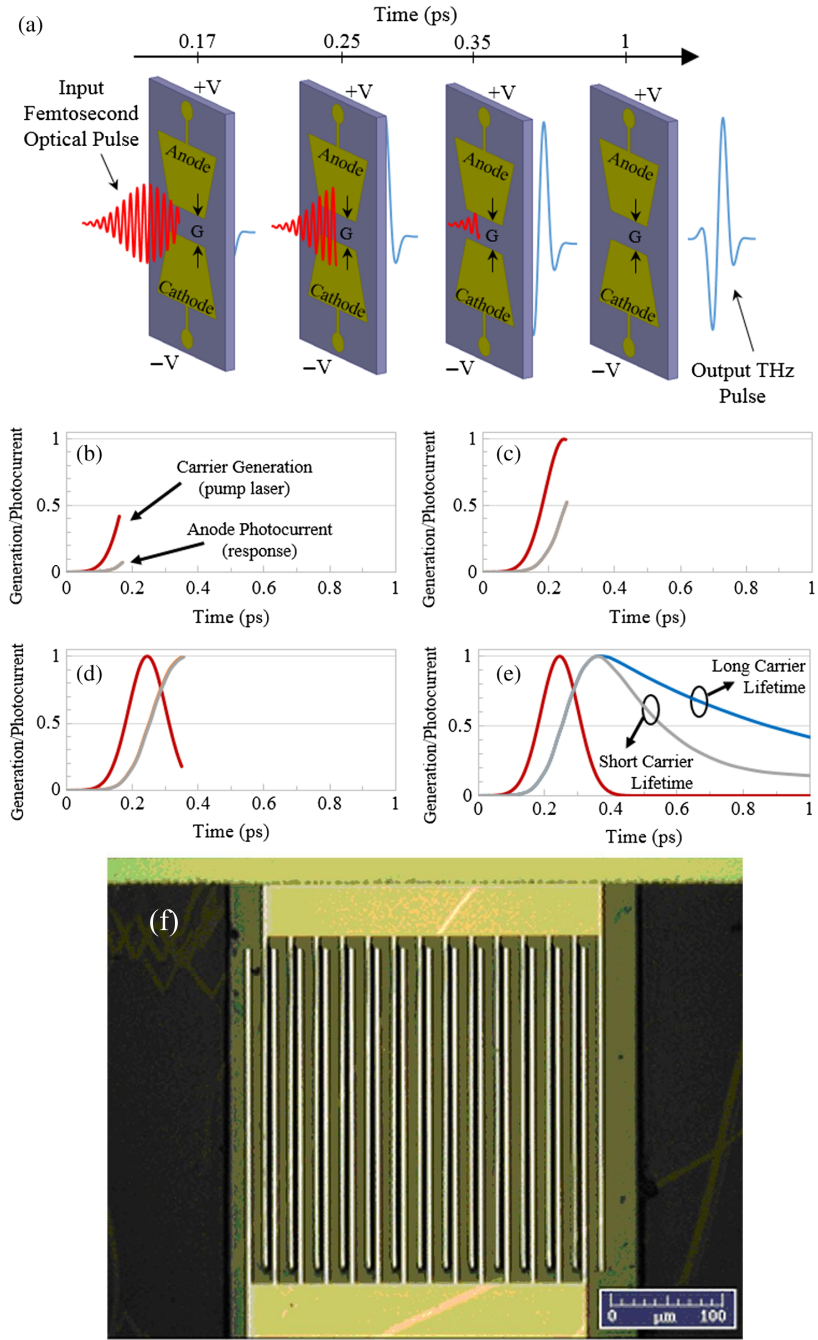


Figure 2.1: **(a)** THz generation from a photoconductive emitter. Panels **(b)** - **(e)** show the pump pulse envelope (red curve) and the photocurrent in the device (grey curve) at each respective step highlighted in panel **(a)**. **(f)** Electrode geometry of an interdigitated photoconductive emitter. Reproduced from reference [71] (panels **(a)** - **(e)**), and reference [72] (panel **(f)**).

on 350  $\mu\text{m}$ -thick semi-insulating gallium arsenide (SI-GaAs) substrates. The bandgap of GaAs (1.42 eV at room temperature) makes it an effective pairing with the peak output wavelength of Ti:Sapphire lasers (800 nm, or 1.55 eV).

### 2.1.2 Optical Rectification

In an optically linear medium the induced electric polarisation  $\mathbf{P}$  has a linear relationship  $\mathbf{P} = \epsilon_0 \chi \mathbf{E}$  with the applied electric field  $\mathbf{E}$ . However, in an optically nonlinear medium the polarisation is described by a series of increasing order terms; in the case of optical rectification (OR) the second order term is important [78],

$$P_i^{(2)} = \epsilon_0 \sum_{j,k=x,y,z} \chi_{ijk}^{(2)} E_j E_k, \quad (2.2)$$

where  $i$ ,  $j$  and  $k$  correspond to the cartesian axes  $x$ ,  $y$  and  $z$  respectively. The electric field components  $E_j$  and  $E_k$  here refer to the components of the incident electric field vector along the corresponding crystal axes. In the case where the electric field is a continuous wave,  $E(t) = E_0 e^{i\omega t}$ , the induced polarisation will be static,  $|\mathbf{P}| \propto |E_0|^2$ . However if the electric field is a time-dependent pulse,  $E(t) = E_0 e^{-at^2} e^{i\omega t}$ , the induced polarisation also has a time dependence,  $|\mathbf{P}| \propto E_0^2 e^{-2at^2}$  [78]. When using an optical pulse to create a time-varying electric field in the nonlinear crystal, the induced polarisation will be proportional to the envelope of the pulse, and this time-varying polarisation will generate electromagnetic radiation. This technique was first demonstrated to generate terahertz radiation using picosecond optical pulses [79, 80] and then adapted to produce higher frequency THz radiation using femtosecond pulses [70, 81].

An important consideration when generating THz radiation by OR is the phase matching condition [82], which can be written as

$$\Delta k = k(\omega_{opt} + \omega_{THz}) - k(\omega_{opt}) - k(\omega_{THz}) = 0, \quad (2.3)$$

where  $k$  is the wavenumber and  $\omega_{opt}$  and  $\omega_{THz}$  are the optical pump and THz frequencies respectively [83]. Taking into account optical dispersion in the ma-

terial, the phase matching condition becomes

$$\frac{k(\omega_{THz})}{\omega_{THz}} \approx \left( \frac{\partial k}{\partial \omega} \right)_{opt}. \quad (2.4)$$

Equation 2.4 states that the best pump-to-THz conversion efficiency is achieved when the group velocity of the optical pump pulse,  $(\partial\omega/\partial k)_{opt} = v_{g,opt}$ , and the phase velocity of the THz pulse,  $\omega_{THz}/k = v_{p,THz}$ , are the same. This allows the generated THz radiation to interfere constructively as the pump pulse moves through the crystal. In order to achieve phase matching the nonlinear crystal must be chosen such that its properties match well with the pump laser pulse, or vice versa. Important properties to consider are the nonlinear coefficient of the crystal, the THz refractive index, the pump frequency group index and the absorption coefficient of the crystal at THz frequencies. The most widely used materials for THz generation via OR are either ZnTe or GaP crystals, as phase matching is approximately satisfied for the 800 nm peak output wavelength of Ti:Sapphire lasers [83, 84].

## 2.2 Electro-Optic Sampling

Detection of THz radiation in all experiments reported in this thesis was performed by electro-optic sampling (EOS). EOS makes use of the Pockels effect [24], whereby an electric field induces birefringence in an electro-optic detection crystal, which is typically ZnTe or GaP. A standard EOS detection scheme is outlined in Fig. 2.2, in which a THz pulse propagates through the detection crystal collinearly with a femtosecond IR pulse. The birefringence created in the detection crystal by the THz electric field induces a change in the polarisation state of the IR pulse. This change in polarisation state can be converted into an intensity difference  $\Delta I$  between the orthogonal components of the IR pulse via the use of a quarter-wave plate (QWP) and a Wollaston prism (WP), and  $\Delta I$  is detected via the change in voltage  $\Delta V$  across a pair of balanced photodiodes. All EOS measurements presented in this thesis were performed using  $\langle 111 \rangle$  surface normal zinc-blende detection crystals, in which  $\Delta V$  is related to



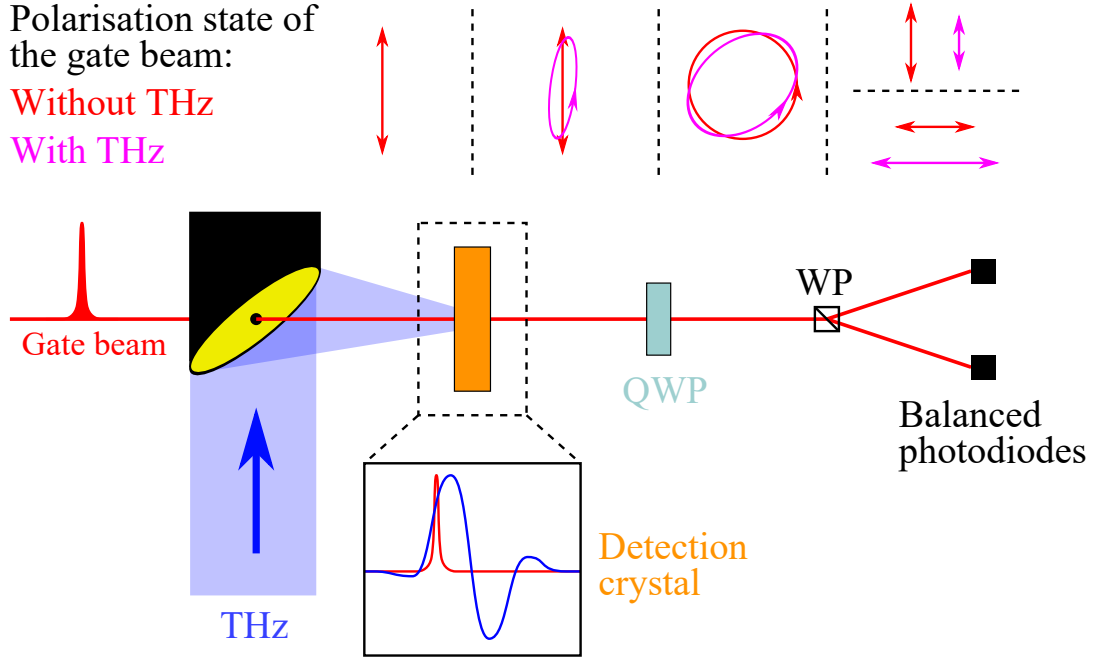


Figure 2.2: Schematic diagram of a standard electro-optic sampling setup. The THz and gate pulses are overlapped in the detection crystal, and the birefringence created in the detection crystal by the THz-induced Pockels effect changes the polarisation state of the gate pulse. The gate beam is separated into two orthogonal components by the use of a quarter-wave plate (QWP) and a Wollaston prism (WP), and the change in polarisation state is measured via the change in intensity of the orthogonal components of the gate beam on a pair of balanced photodiodes.

the THz electric field  $E_{\text{THz}}$  by [85]

$$\frac{\Delta V}{V_{\text{tot}}} = \frac{\sqrt{24}\omega L n^3 r_{41} E_{\text{THz}}}{3c}, \quad (2.5)$$

where  $V_{\text{tot}}$  is the total voltage across the pair of photodiodes,  $L$  is the crystal thickness,  $\omega$  is the frequency of the IR pulse,  $n$  is the refractive index at the IR pulse wavelength, and  $r_{41}$  is the nonlinear coefficient of the detection crystal. Calibration of this detection setup is performed by rotating the QWP to balance the output of the photodiodes without the THz pulse present, resulting in equal intensities of the orthogonal components of the IR pulse after the WP and  $\Delta V/V_{\text{tot}} = 0$ .

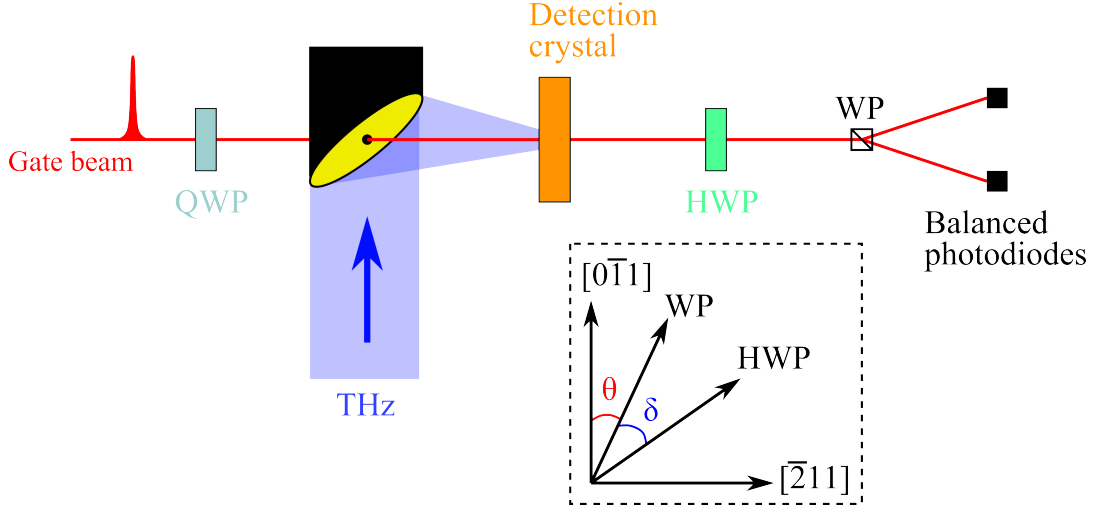


Figure 2.3: Schematic diagram of the polarisation-resolved electro-optic sampling setup used in this thesis. The dashed box represents the relative orientations of the wollaston prism, half-wave plate, and the  $[0\bar{1}1]$  and  $[\bar{2}11]$  directions in the detection crystal.

### 2.2.1 Polarisation-Resolved Electro-Optic Sampling

The standard EOS measurement scheme discussed above is sensitive only to the component of the THz pulse along one of the crystal axes in the detection crystal; as described in Section 1.1.4, anisotropic materials may have an effect on the polarisation state of light propagating through them, which the standard EOS technique will not be able to detect. Therefore a *polarisation-resolved* EOS method is highly desirable when investigating materials which may exhibit anisotropy at THz frequencies. To such ends, various EOS schemes employing a rotation of the detection crystal to determine the THz polarisation state have been demonstrated [86, 87, 88]. However, the polarisation-resolved EOS measurements presented in this thesis were performed using the technique demonstrated by van der Valk *et al.* in reference [85], which changes the detection sensitivity by rotating the polarisation of the gate beam using a half-wave plate (HWP). For a zinc-blende crystal cut with a  $\langle 111 \rangle$  surface-normal, while the absolute maximum electro-optic signal will be around 20 % smaller than a  $\langle 110 \rangle$  crystal, the electro-optic signal has an equal sensitivity for orthogonal polarisations of the gate beam [89], hence no rotation of the electro-optic crystal is required.

The polarisation-resolved EOS detection setup is shown schematically in

Fig. 2.3. Here the gate beam first propagates through a QWP, oriented such that the initially linear polarisation of the gate beam is converted to a circular polarisation state, ensuring that the gate beam will have equal components along two orthogonal directions in the detection crystal. An OAP mirror with a small hole in its centre to pass the gate beam is then used to couple the gate and THz beams together, such that they co-propagate through the detection crystal. For normal propagation through a  $[111]$ -oriented zincblende crystal, the electro-optic response is independent of the gate beam polarisation, which only determines which component of the THz electric field the detection system is sensitive to [85]. The gate beam then propagates through a HWP and is separated into horizontal and vertical components by a WP, before being incident on a pair of balanced photodiodes.

By considering the components of the THz electric field along the  $[0\bar{1}1]$  and  $[\bar{2}11]$  axes of the  $[111]$ -oriented detection crystal as  $E_{0\bar{1}1}$  and  $E_{\bar{2}11}$  respectively, the electro-optic signal  $\Delta V$  can be written [85]:

$$\Delta V \propto [E_{\bar{2}11} \sin(2\theta - 4\delta) + E_{0\bar{1}1} \cos(2\theta - 4\delta)], \quad (2.6)$$

where  $\theta$  is the angle between the WP and  $[0\bar{1}1]$ , and  $\delta$  is the angle between the HWP and the WP. As can be seen from Equation 2.6, for a constant value of  $\theta$ , changing the value of  $\delta$  will alter the polarisation sensitivity of the detection system. If  $\theta = 0$ , having  $\delta = 0$  will result in detection of the  $E_{0\bar{1}1}$  component of the THz pulse only, whilst rotating the HWP by  $22.5^\circ$  will therefore allow detection of the orthogonal  $E_{\bar{2}11}$  component only. Detection of both components allows the resolution of the full THz polarisation state, by considering the two detected waveforms as the projections of the THz pulse onto the lab  $x$ - and  $y$ -planes.

### 2.3 THz-TDS Experimental Setup

This section will describe the constituent parts and operation of the THz time-domain spectrometer used throughout the majority of experimental work presented in this thesis. This spectrometer was designed and constructed by myself as a part of this doctoral research project.

A schematic diagram of the spectrometer is presented in Fig. 2.4. The output of a Ti:Sapphire oscillator (Spectra-Physics Mai Tai) is split into two beams by a 90%-transmission beamsplitter, with the high-power portion used as the THz generation beam. This beam is focussed onto a photoconductive emitter, which generates single-cycle pulses of THz radiation. The THz is generated as a diverging beam, and so is collected and collimated by a  $f = 50.8$  mm gold off-axis parabolic (OAP) mirror, positioned the focal length away from the PCE. OAP mirrors are used to steer and focus the THz pulses to avoid the effects of dispersion on the pulses, which would be introduced by transmissive optics such as lenses. The THz beam is focussed onto the sample position, and then collected and collimated after the focus, by two OAP mirrors each with a focal length  $f = 76.2$  mm. This focal length is required in order to accommodate the size of the optical cryostat the samples will be held in, to facilitate low-temperature measurements. These two mirrors are oriented such as to create a “z-shape” spectrometer, as orienting the mirrors in a “u-shape” (i.e. by rotating the collecting OAP by  $180^\circ$ ) can introduce an ellipticity of around  $5 - 10^\circ$  to the THz beam after collimation. The precise degree of ellipticity induced will depend on the alignment of the OAP mirrors. A final OAP mirror with a focal length  $f = 101.6$  mm focuses the THz beam onto the detection crystal. Atmospheric water vapour has a number of strong absorption features at THz frequencies [90]; to avoid their influence on the measured THz radiation and increase the signal-to-noise of the experiment, the full THz beam path is contained within a sealed box which can be purged with dry nitrogen gas.

The low-power portion of the beam after the beamsplitter is used to detect the THz pulses via electro-optic sampling (EOS). The gate beam is passed through a hole in the final OAP mirror in order for it to propagate collinearly with the THz beam through the detection crystal. The detection crystal used was a [111]-oriented zinc-blende crystal, in order to perform polarisation-resolved EOS; a 0.5 mm-thick ZnTe crystal was used in Chapters 3 and 5, whilst a 0.3 mm-thick GaP crystal was used in Chapter 4. A large EOS signal can be obtained using thick detection crystals with large nonlinear coefficients, while a larger detection bandwidth is generally found for thinner crystals in which the lowest optical phonon frequency is higher. Thus there is a balance to be struck

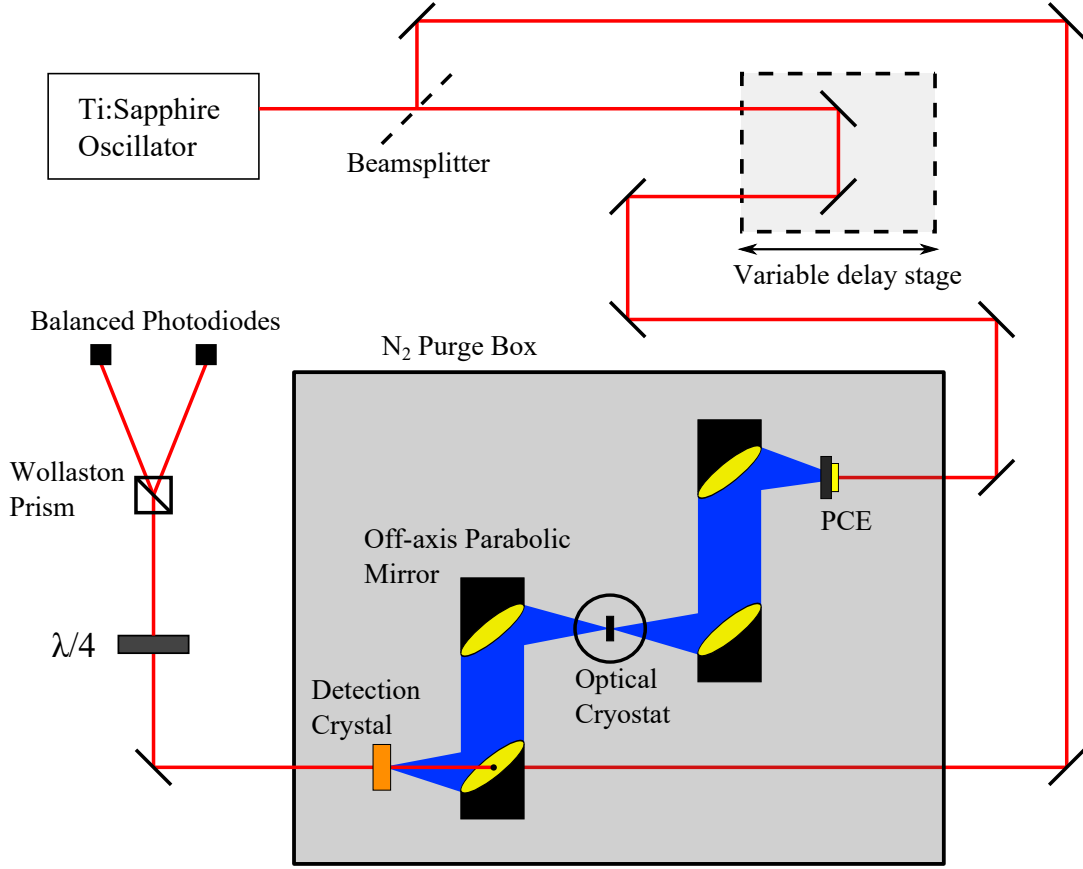


Figure 2.4: Schematic diagram of the THz time-domain spectrometer built to perform the majority of the experimental work presented in this thesis.

between signal size and bandwidth, and the optimal choice of detection crystal will vary depending on the experimental requirements.

### 2.3.1 Performing a THz-TDS Experiment

A THz-TDS experiment is performed by varying the relative arrival times of the gate and THz pulses at the detection crystal, via the mechanical delay stage incorporated into the THz generation beam. The duration of the gate pulse (80 fs) is much shorter than that of the THz pulse (typically a few ps), and as such the gate pulse samples the birefringence created by only a small portion of the THz pulse; thus the temporal profile of the THz electric field can be recorded, by varying the length of the delay line and sampling the instantaneous electric field at each step. To increase the signal-to-noise level of the measurement the

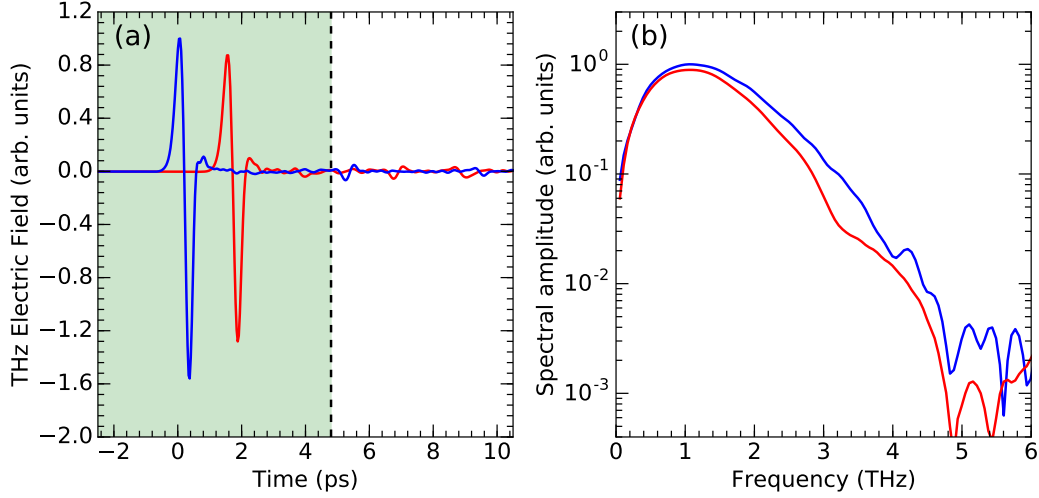


Figure 2.5: **(a)** Time-domain waveforms of THz pulses generated and detected in the spectrometer presented in this thesis, without (blue trace) and after (red trace) transmission through a THz low-pass filter (TYDEX LPF8.8-30). **(b)** The corresponding Fourier transform spectra of the data in the shaded area in panel **(a)**.

THz beam is modulated, by either mechanically chopping the THz generation beam or electrically modulating the PCE bias voltage, and a lock-in amplifier locked to this modulation frequency is used to measure  $\Delta V$ .

A typical time-domain waveform generated and detected in the spectrometer described here, and its corresponding Fourier transformed spectrum, are presented as the blue curves in Figs. 2.5 (a) and 2.5 (b), respectively. The red curves represent the same pulse after transmission through a sample, which in this example was a THz low-pass filter (TYDEX LPF8.8-30). The sample introduces a phase delay in the transmitted pulse, causing it to arrive later in time, and a reduction in amplitude, due to reflection losses at the surfaces or absorptive properties of the material. Sample properties are extracted from the data by comparison of the spectra with and without transmission through the sample, which will be described in Section 2.4.

An important consideration when setting the experimental parameters is the resolution and bandwidth of the measurement. The resolution in the frequency-domain  $\Delta f$  is related to the width of the time-domain  $\Delta t$  by  $\Delta f = 1/\Delta t$ ; similarly the maximum measureable frequency in the measurement is proportional to the reciprocal of the spacing between data points in the time-

domain. As such, to gain the best frequency resolution it is advantageous to measure over the widest time-domain possible. In addition to the main THz pulse, internal reflections of either the THz or gate pulses in the emitter, detection crystal or sample may create artifacts in the EOS signal; two such examples may be observed in the blue trace in Fig. 2.5 (a), around 5 ps for the first internal reflection and 9 ps for the next. Internal reflections in the time-domain introduce periodic oscillations in the frequency-domain, so typically in optically thick samples the time window that the Fourier transform is performed over may be restricted to exclude the internal reflections, as demonstrated in Fig. 2.5. In any THz-TDS experiment, a practical balance must be struck between the desired resolution and bandwidth and the time taken to perform the measurement.

## 2.4 Extracting Sample Properties and Polarisation Information from Time-Domain Data

This section will describe the methods used in this thesis to extract the important sample properties and information about the polarisation state from the measured time-domain waveforms. In particular, this section will describe how the complex transmission function is extracted from the time-domain data, before using it to extract the complex refractive index in Section 2.4.1. The method of extracting the polarisation state of the THz pulses, in terms of  $\chi$  and  $\psi$ , will be described in Section 2.4.2.

The frequency spectra of the THz pulses detected by EOS are obtained by Fourier transforming the time-domain data. We can determine the effect the sample has on the THz pulse by comparing a reference spectrum obtained without the sample in the spectrometer,  $E_r$ , to the spectrum obtained with the sample in the spectrometer,  $E_s$ . The reference spectrum can be expressed as

$$E_r(\omega) = E_i \exp \left[ i \frac{\omega d}{c} \tilde{n}_i \right], \quad (2.7)$$

where  $E_i$  is the electric field at the sample position, and the exponential term describes the relative phase acquired while propagating a distance  $d$ , equal to the thickness of the sample, through either N<sub>2</sub>-purged air or vacuum with a complex

refractive index  $\tilde{n}_i$ . After propagation through the sample the spectrum can be expressed as

$$E_s(\omega) = \tilde{t}_{is}\tilde{t}_{si}E_i \exp \left[ i \frac{\omega d}{c} \tilde{n}_s \right] \text{FP}_{isi}(\omega), \quad (2.8)$$

where  $\tilde{n}_s$  is the complex refractive index of the sample. This expression must take into account the losses in the electric field at the entrance and exit surfaces of the sample, described by the Fresnel transmission coefficients  $\tilde{t}_{ij} = 2\tilde{n}_i/(\tilde{n}_i + \tilde{n}_j)$  for plane waves at normal incidence to a surface. There is an additional contribution from any internal reflections in the sample, described by the Fabry-Perót term  $\text{FP}_{isi}(\omega)$ . This can generally be expressed for light propagating from medium  $i$  to  $j$  to  $k$  by

$$\text{FP}_{ijk}(\omega) = \sum_{p=0}^P \left[ \tilde{r}_{jk}\tilde{r}_{ji} \exp \left( i \frac{2\omega d}{c} \tilde{n}_j \right) \right]^p, \quad (2.9)$$

where  $\tilde{r}_{ij} = (\tilde{n}_i - \tilde{n}_j)/(\tilde{n}_i + \tilde{n}_j)$  are the Fresnel reflection coefficients at the interfaces. If we divide the sample spectrum by the reference spectrum we obtain the complex transmission function,  $\tilde{T}(\omega) = E_s(\omega)/E_r(\omega)$ . This allows us to express  $\tilde{T}(\omega)$  in terms of  $\tilde{n}_s$  as

$$\tilde{T}(\omega) = |\tilde{T}|e^{i\phi(\omega)} = \tilde{t}_{is}\tilde{t}_{si} \exp \left[ i \frac{\omega d}{c} (\tilde{n}_s - \tilde{n}_i) \right] \text{FP}_{isi}(\omega). \quad (2.10)$$

#### 2.4.1 Complex Refractive Index

Whilst Equation 2.10 may always be solved numerically to obtain information about  $\tilde{n}_s$  from the experimentally observed  $\tilde{T}(\omega)$  [91, 92, 93], a general analytical expression cannot be found for  $\tilde{n}_s$  due to its presence in both  $\tilde{t}_{ij}$  and  $\text{FP}_{ijk}$ . However, under certain experimental conditions, the expression for  $\tilde{T}(\omega)$  may be simplified and an analytical expression formed.

The first condition is that in the absence of internal reflections,  $p=0$  and  $\text{FP}_{isi}(\omega) = 1$ ; this may be achieved experimentally by restricting the width of the time-domain to only include data up to just before the first internal reflection, as shown by the shaded area in Fig. 2.5 (a). The second condition is that we make the assumption that the frequency-dependence of the refractive index is weak, hence  $\tilde{t}_{ij}(\tilde{n}) = \tilde{t}_{ij}(\tilde{n}(\omega = 0))$ . Now we may form analytical expres-



sions for the real part of the complex refractive index,  $n$ , and the absorption coefficient,  $\alpha = 2\omega\kappa/c$ , as

$$n(\omega) = 1 + \frac{c}{\omega d} \phi(\omega), \quad (2.11)$$

$$\alpha(\omega) = -\frac{2}{d} \ln \frac{|\tilde{T}(\omega)|}{\tilde{t}_{is}\tilde{t}_{si}}. \quad (2.12)$$

### Differential Measurements

In some cases, changes in a material property of interest can be small compared to the background signal, and as such the interesting processes we want to study may be obscured. Here it is useful to perform a differential measurement, whereby the change in material property as a function of some control variable is studied. For example, for a magnetic field-dependent change in a material, the transmission function becomes  $\tilde{T}(\omega) = E(B)/E(B=0)$ . In this situation, both the reference and sample spectra have propagated through the material under study, and as such are given by

$$E_r(\omega) = \tilde{t}_{is}\tilde{t}_{si}E_i \exp \left[ i \frac{\omega d}{c} \tilde{n}_r \right] \text{FP}_{isi}(\omega), \quad (2.13)$$

$$E_s(\omega) = \tilde{t}_{is}\tilde{t}_{si}E_i \exp \left[ i \frac{\omega d}{c} \tilde{n}_s \right] \text{FP}_{isi}(\omega). \quad (2.14)$$

An analytical solution for  $n_s$  in terms of  $\tilde{T}(\omega)$  can still be found, provided we make the assumption that the change in the refractive index is small,  $\Delta\tilde{n}_{rs} \ll \tilde{n}_r$ . Now we may write the complex refractive index of the sample as

$$\tilde{n}_s = \tilde{n}_r + \Delta\tilde{n}_{rs} = (n + i\kappa) + (\delta n + i\delta\kappa). \quad (2.15)$$

If we disregard higher powers of  $\Delta\tilde{n}$ , then we may derive similar expressions for the change in the real part of the complex refractive index and the change in absorption coefficient,

$$\Delta n_{rs}(\omega) = \frac{c}{\omega d} \phi(\omega), \quad (2.16)$$

$$\Delta\alpha_{rs}(\omega) = -\frac{2}{d} \ln |\tilde{T}(\omega)|. \quad (2.17)$$

#### 2.4.2 Ellipticity and Orientation Angle

When studying birefringent materials, it is important to know the polarisation state of the THz pulse after propagation through the material. In the majority of results presented in this thesis, I will describe the polarisation state of the THz pulses in terms of the ellipticity  $\chi$  and the orientation angle  $\psi$ , defined in Section 1.2.

The frequency-dependent quantities  $\chi(\omega)$  and  $\psi(\omega)$  were obtained from the polarisation-resolved time-domain data by first taking the Fourier transform of the orthogonal  $x$  and  $y$  components, then converting the complex THz spectra obtained  $\tilde{E}_x(\omega)$  and  $\tilde{E}_y(\omega)$  into a circular basis using

$$\tilde{E}_{\pm}(\omega) = |\tilde{E}_{\pm}(\omega)|e^{i\phi_{\pm}} = \frac{\tilde{E}_x(\omega) \pm i\tilde{E}_y(\omega)}{\sqrt{2}}, \quad (2.18)$$

where the circular-basis components  $\tilde{E}_+(\omega)$  and  $\tilde{E}_-(\omega)$  represent the right- and left-hand circularly polarised components of the electromagnetic wave, respectively. In this circular basis the lengths of the semi-major and semi-minor axes of the polarisation ellipse can be regarded as the sum,  $a = |\tilde{E}_+(\omega)| + |\tilde{E}_-(\omega)|$ , and the difference,  $b = |\tilde{E}_-(\omega)| - |\tilde{E}_+(\omega)|$ , of the amplitudes of the circular basis components of the wave, respectively. Using these definitions, along with Equation 1.26, we can extract the ellipticity from the time-domain data using

$$\chi(\omega) = \tan^{-1} \left( \frac{|\tilde{E}_-(\omega)| - |\tilde{E}_+(\omega)|}{|\tilde{E}_+(\omega)| + |\tilde{E}_-(\omega)|} \right). \quad (2.19)$$

The phase term in Equation 2.18 may be calculated using the argument of the complex circular-basis electric field,

$$\phi_{\pm}(\omega) = \tan^{-1} \left( \frac{\text{Im}[\tilde{E}_{\pm}(\omega)]}{\text{Re}[\tilde{E}_{\pm}(\omega)]} \right). \quad (2.20)$$

The orientation angle can then be obtained from the difference between the

phase of the right- and left-hand circular components of the wave, using

$$\psi(\omega) = \frac{\phi_+(\omega) - \phi_-(\omega)}{2}. \quad (2.21)$$

## 2.5 Summary

This chapter has introduced and described the core experimental technique used throughout this thesis, terahertz time-domain spectroscopy. Sections 2.1 and 2.2 detailed the methods of generating and detecting broadband THz radiation that have been used in the work presented in this thesis. Section 2.3 described how these two aspects are brought together to create a spectrometer, and the process of performing a THz-TDS experiment was described. Section 2.4 then explained the process of extracting information from the time-domain data, both about the material properties of samples under study, and the polarisation state of the detected THz pulses.

The rest of this thesis will build on the experimental techniques and concepts introduced in this chapter, developing new THz-TDS methods and components, and applying them to the study of anisotropic materials.

## Chapter 3

# Rotatable-Polarisation Terahertz Time-Domain Spectroscopy of Anisotropic Media

In this chapter I will present a method of performing rotatable polarisation terahertz time-domain spectroscopy (RP-THz-TDS), based on the mechanical rotation of an interdigitated photoconductive emitter, which provides a convenient and powerful probe of the behaviour of anisotropic materials at THz frequencies. Section 3.1 will first explore the current methods of investigating anisotropic properties at THz frequencies, and of rotating the polarisation state of THz radiation, that are available in the literature. Section 3.2 will outline the enhancements that were made to a standard terahertz time-domain spectroscopy system in order to allow the generation of an arbitrarily rotatable linear polarisation state, and to detect the full polarisation state of the THz pulses at the sample position. The performance of the rotatable photoconductive emitter, compared to a polarisation rotation method using a wire-grid polariser, will be explored in Section 3.3. Finally the RP-THz-TDS technique described in this chapter is demonstrated experimentally in Section 3.4 by investigating the anisotropic behaviour of two uniaxial materials, zinc oxide (ZnO) and lanthanum aluminate ( $\text{LaAlO}_3$ ), and the biaxial and absorbing material cupric oxide (CuO). Sections 3.2, 3.3 and 3.4 have been published as C. D. W. Mosley *et al.*, *Scientific Reports* **7**, 12337 (2017).

### 3.1 Investigating Anisotropy at Terahertz Frequencies

In developing experimental methods for investigating the anisotropic properties of materials at THz frequencies, there are two key challenges which must be addressed. The first is the potential for a change in the polarisation state of the probing light after transmission through the sample, as described in Section 1.1.4, for which methods of resolving the full resulting polarisation state are required. The second challenge is having the ability to change the relative orientations of the electric field of the probing light and the polarisation eigenvectors in the plane of the material under investigation. Along with the use of complimentary techniques such as Laue X-ray diffraction, this allows both the nature of the anisotropy and the particular direction in which it occurs in the material to be investigated.

This section will explore the solutions to these two challenges currently available in the literature, to serve as background for the rotatable-polarisation THz-TDS system described later in this chapter.

#### 3.1.1 Disambiguating Spectral Features Using Polarisation-Resolved Detection Methods

Commonly THz-TDS detection methods are sensitive to only one polarisation state, for example along the lab-coordinate  $x$ -axis. The optical properties of a material under study will then be calculated from the transmission along the  $x$ -axis only, as  $T_{xx} = E_{x,\text{sample}}/E_{x,\text{reference}}$ . Whilst this may be suitable for spectroscopy of isotropic materials, it is not sufficient in the study of materials with anisotropic properties; what appear to be absorption peaks, as reduced transmission  $T_{xx}$ , can in fact be frequencies at which the medium is acting as a quarter- or half-wave plate, altering the incident polarisation state and producing some transmitted amplitude in a direction orthogonal to  $x$ . *Polarisation-resolved* detection methods (as discussed in Section 2.2.1) are therefore required, which ideally will measure two orthogonal components of the THz electric field, allowing the full determination of the THz polarisation state.

An example of the requirement for polarisation-resolved detection methods can be found in the study of the birefringent properties of lanthanum alu-

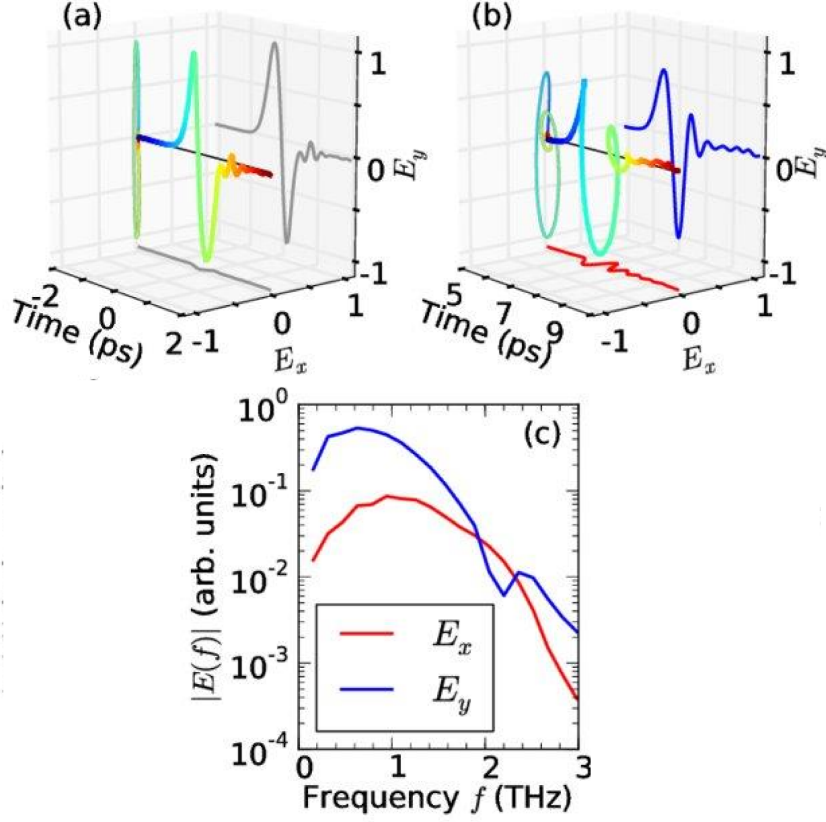


Figure 3.1: Polarisation-resolved THz time-domain waveforms obtained (a) before and (b) after transmission through a [001]-surface normal, 500  $\mu\text{m}$ -thick single crystal of  $\text{LaAlO}_3$ . (c) Fourier-transform spectra of the  $x$  and  $y$  components of the THz electric field displayed in panel (b). Reproduced and adapted from reference [6].

minate ( $\text{LaAlO}_3$ ) in the THz region by Lloyd-Hughes *et al.* [6]. Figs. 3.1 (a) and 3.1 (b) show polarisation-resolved THz pulses before and after, respectively, transmission through a [001]-surface normal, 500  $\mu\text{m}$ -thick single crystal of  $\text{LaAlO}_3$ . In this experiment the incident THz polarisation is not parallel to one of the polarisation eigenvectors in the material, and as such there are components of the incident THz electric field along both eigenvectors. Whilst the polarisation of the incident pulse is linear with a very small  $x$ -component, after transmission through the sample the  $x$ -component of the THz pulse is much larger, forming a complex polarisation state. The THz spectra of the  $x$ - and  $y$ -components of the transmitted pulse are displayed in Figure 3.1(c); if a typical one-dimensional detection method were to have been employed, sensitive to

only  $E_y$ , then the change in the time-domain waveform of  $E_y$  along with the dip in the spectrum around 2.1 THz would make it appear as though there were a resonant absorption feature in  $\text{LaAlO}_3$  around this frequency. However because polarisation-resolved detection was used, it is evident that the change in  $E_y$  occurs due to the alteration of the polarisation state as a result of birefringence, rather than absorption.

### 3.1.2 Terahertz Polarimetry and Ellipsometry

Polarimetry can be defined as the characterisation of materials via the measurement and interpretation of the polarisation state of light after interaction with the material. Ellipsometry is the application of polarimetry to investigate the optical properties of thin films or surfaces [94, 95]. By measuring the change in the polarisation state of light with an initially well-defined polarisation state, the optical properties of the material can be inferred. Anisotropy in the sample can be investigated changing the relative orientations of the THz electric or magnetic fields and the in-plane crystallographic directions; this can be achieved by either rotating the polarisation state of the incident THz radiation, or by rotating the sample [5, 96].

The goal of a typical polarimetry or ellipsometry experiment is to determine components of either the complex Jones transfer matrix,

$$\tilde{\mathbf{T}}(\omega) = \begin{bmatrix} \tilde{t}_{xx}(\omega) & \tilde{t}_{xy}(\omega) \\ \tilde{t}_{yx}(\omega) & \tilde{t}_{yy}(\omega) \end{bmatrix}, \quad (3.1)$$

or the Mueller matrix  $\mathbf{M}$ . The components of the Jones matrix are complex, hence contain information about both the amplitude and phase of the transmitted light, whilst components of the Mueller matrix are based upon components of the Stokes vector, hence are intensity-based only. The Jones matrix is applicable when dealing with purely polarised light, whereas the Mueller matrix can be used when dealing with partially- or un-polarised light. Optical properties of the sample can be calculated from the components of the Jones or Mueller matrices [97, 98, 99].

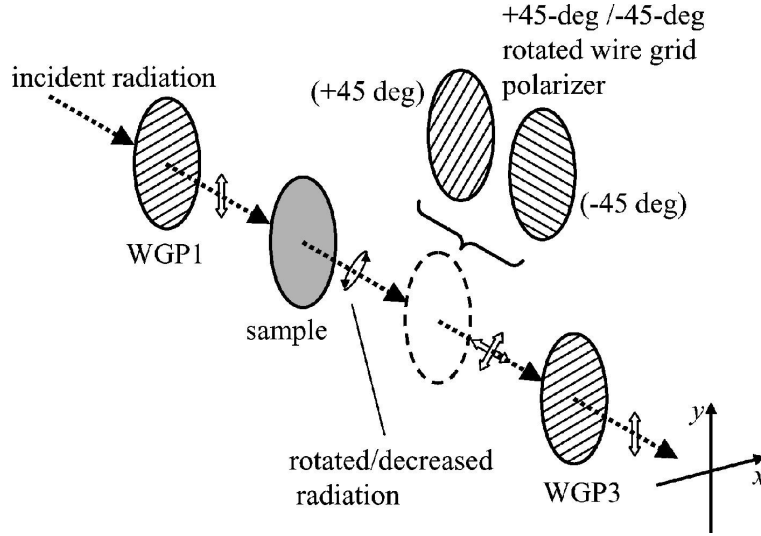


Figure 3.2: Schematic configuration of a polarisation-sensitive detection method utilising static wire-grid polarisers. Reproduced and adapted from reference [101].

### Wire-Grid Polarisers

Linearly polarising optics, which convert unpolarised light or light with an arbitrary polarisation state into a linear polarisation state, are a commonly used component in polarimetry and ellipsometry systems across the electromagnetic spectrum. Due to the broadband nature of many THz sources, linear polarisers that operate over a broad bandwidth are required. At THz frequencies the most commonly used linear polariser is the wire-grid polariser (WGP); a typical WGP consists of an array of parallel metal wires with a width and spacing smaller than the wavelength of light being polarised. The component of the THz radiation parallel to the wires of the polariser will be reflected, whilst the component of the THz radiation perpendicular to the wires will be transmitted through the polariser. The resulting effect is that for a perfect WGP, the transmitted radiation is perfectly linearly polarised perpendicular to the wires. WGP in the THz region can be manufactured as free-standing grids by stretching a metal wires over a frame, or they can be fabricated on a substrate by photolithography processes [100].



## Methods of Terahertz Polarimetry

Static or continuously rotatable WGPs may be used to determine the polarisation state of THz radiation [97, 101, 102], without requiring the direct detection of orthogonal components of the THz electric field using a polarisation-resolved detector. Terahertz polarimetry methods using static WGPs [101, 102] often make use of a geometry such as that shown in Figure 3.2. The generated THz radiation is passed through an initial WGP (WGP 1 in Figure 3.2) to define a linear polarisation state for the THz pulse incident on the sample, i.e. along the  $y$  axis in Figure 3.2. WGP 3 is used to project the THz polarisation state back for efficient detection. After propagation through the sample, a second WGP is placed in the beam, typically at angles of  $\pm 45^\circ$  to WGP 3. Then either the polarisation state of the THz radiation incident on WGP 2 can be reconstructed, or optical properties of the sample under investigation can be obtained, from a number of different time-domain projections obtained with WGP 2 oriented at different angles [101, 103].

A similar method of THz polarimetry replaces the static WGP 2 in Fig. 3.2 with a WGP rotated at a constant frequency, demonstrated at  $\omega \sim 80$  Hz in reference [97]. In this method the optical properties of a sample can be extracted via a lock-in detection scheme [97], which simultaneously measures two components of the complex Jones transfer matrix. This demonstrates an advantage over the static polariser method, which requires two measurements with WGP 2 at different orientations to achieve the same results. However, since the detectors used in these methods are only sensitive to polarisation in one direction, only two components of the transfer matrix can be extracted for a given orientation of the detector, e.g. only the  $\tilde{t}_{xx}$  and  $\tilde{t}_{yx}$  components can be extracted when the detector is oriented along the  $x$ -axis in Fig. 3.2. To extract the other two components,  $\tilde{t}_{xy}$  and  $\tilde{t}_{yy}$ , a rotation of  $90^\circ$  is required in either the sample, or a simultaneous rotation of the THz emitter, detector and WGPs 1 and 3. Using this rotatable WGP method, Morris *et al.* were able to achieve a precision in the measured polarisation angle of  $\sim 0.02^\circ$  for frequencies below 1.5 THz after 20 minutes of measurement time. This is in contrast to detection schemes based on multi-contact PCEs [104, 105, 106] and

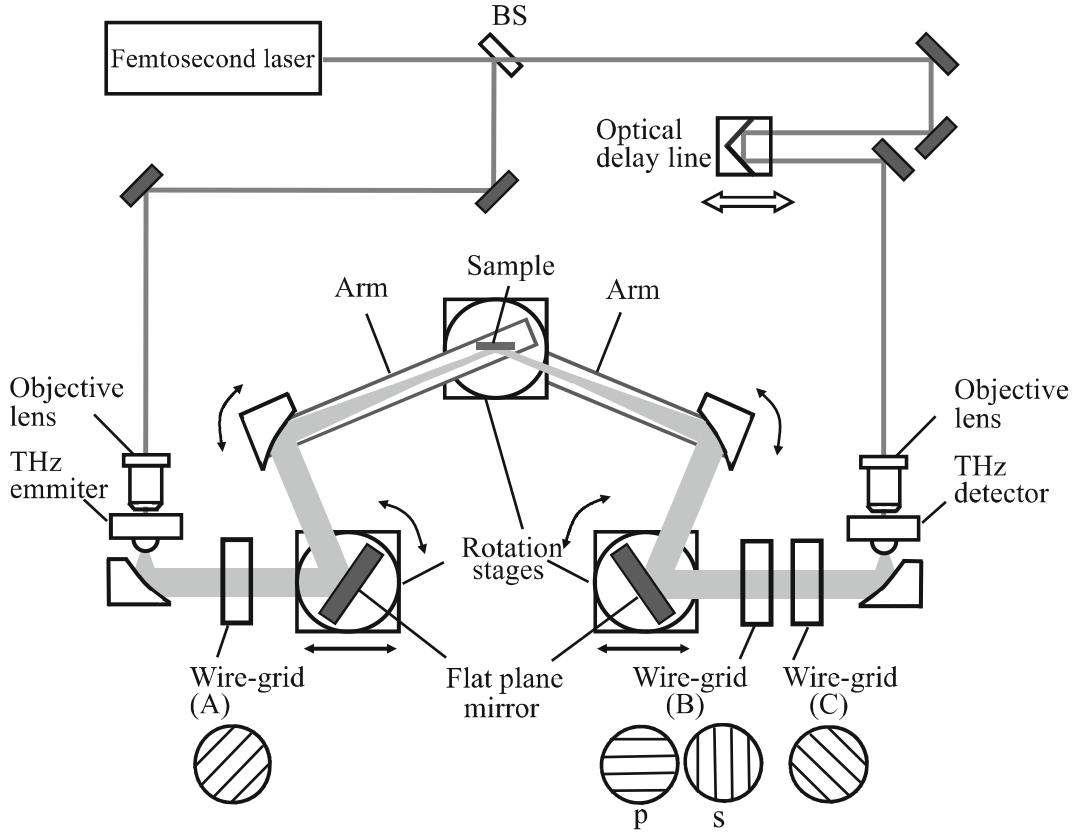


Figure 3.3: Schematic optic configuration for a typical terahertz time-domain ellipsometry system. Reproduced from reference [98].

static wire-grid polarisers [107] which have a precision on the order of  $0.2^\circ$ .

### Terahertz Ellipsometry

A schematic diagram of a typical terahertz time-domain ellipsometry system is displayed in Fig. 3.3. Ellipsometry is often performed in the reflection geometry, and makes use of the different reflectivity of the s- and p-polarised components of light from the surface of, or interface between, materials. As such, a WGP (WGP A in Fig. 3.3) is often used to project the generated THz polarisation to  $45^\circ$ , in order to obtain equal horizontal and vertical components of the THz pulse incident on the sample. A rotatable WGP (WGP B) then selects between sensitivity to the reflected s- or p-component, before a final analyser WGP (WGP C) projects the polarisation state to  $-45^\circ$  before detection.

Many of the experimental techniques used in THz ellipsometry are similar

to those performed in THz polarimetry, except measurements are performed in reflection, rather than transmission. Many methods of rotating the sample or projecting the polarisation state via WGP are similar. Further information can be found in reference [108].

### 3.1.3 Methods of Terahertz Polarisation Rotation

The majority of anisotropic THz spectroscopy methods make use of rotating the sample, changing the directions of  $\mathbf{D}_{a,b}$  relative to  $\mathbf{E}$ , in order to investigate the anisotropy. While simple to perform at room temperature, at cryogenic temperatures or in high external magnetic fields rotating the sample is challenging. Also, if the sample is not perfectly aligned with the axis of rotation, different numbers of grains or domains in the sample may be probed at different angles. This is an important consideration in inhomogeneous materials such as  $\text{LaAlO}_3$ , where the transmitted THz polarization state depends strongly on the size and number of domains probed [6].

Alternatively to rotating the sample, the THz polarization state itself may be rotated, changing the orientation of  $\mathbf{E}$  relative to  $\mathbf{D}_{a,b}$ . A number of methods of achieving this have been reported in the literature: changing the orientation angle of the generated beam during the emission process; rotating the orientation angle using a half-waveplate; and projecting the polarisation state using a wire-grid polariser (WGP). The latter two methods are most commonly used in spectroscopic ellipsometry, with WGP's favored for THz ellipsometry [108]. The low extinction ratio and frequency-dependent response of many THz wire-grid polarizers can have an influence on the detected polarisation state [5, 109]. The use of WGP's also results in a reduction of signal size, and extra data analysis is required to extract the orthogonal electric field components. Further, there is a  $\pi/2$  phase shift between light parallel to and perpendicular to the wires [110] that introduces a finite ellipticity to the transmitted beam, which will be demonstrated later in Section 3.3.

Ideally, a polarization rotation system should satisfy the following criteria: a minimal insertion loss for any components used, minimal change in  $\mathbf{E}$  with rotation angle in terms of the amplitude  $|\mathbf{E}|$  and polarisation state ( $\psi$  and  $\chi$ ), precise and accurate determination of the polarisation state ( $\psi$  and  $\chi$ ), and uni-

form operation over a wide bandwidth. The summary of polarization-rotation methods presented in this section is by no means exhaustive, but is intended to highlight to the reader that currently no scheme meets all the criteria set out above.

### **Terahertz Waveplates**

Half-waveplates made of a single birefringent material [6] and metasurface-based polarization rotators [111] are intrinsically narrowband and have finite loss, and are thus not ideal for broadband THz spectroscopy with arbitrarily rotatable THz pulses. Recently however, efforts have been made to produce metamaterial-based devices that operate over a broader frequency range [112, 113, 114]. Internal reflection within a prism offers broadband polarization rotation: for instance a half-waveplate with retardance close to  $\pi$  and varying by  $\pm 6^\circ$  with frequency was reported [115]. However these components are large and require collimated THz beams to function optimally, and there is an additional loss of signal amplitude due to Fresnel reflection losses on entering and exiting the prism.

### **Rotation During the Emission Process**

A rotation of the generated THz beam has been demonstrated for plasma-based THz emission [116], however this is reliant upon high pulse energy laser amplifiers with lower repetition rates. In terms of the more widely-used THz-TDS systems based on laser oscillators, photoconductive emitters are the THz source of choice for spectroscopy and imaging applications in custom-made and commercial systems. The coarse rotation (to  $0^\circ$ ,  $45^\circ$  and  $90^\circ$ ) of a wide-area photoconductive emitter has been reported, to alternate between vertical and horizontal THz emission [104]. This method produced an accuracy in the orientation angle of  $5^\circ$ , a large ellipticity, and a variation in  $|\mathbf{E}|$  by 40% on rotating the emitter by  $90^\circ$ .

## 3.2 Rotatable-Polarisation Terahertz Time-Domain Spectrometer

As discussed in Section 3.1.3, each method of performing spectroscopy on anisotropic media at THz frequencies comes with its own challenges. The rest of this chapter will propose and demonstrate a solution to these issues, in the form of a *Rotatable-polarisation*-THz-TDS (RP-THz-TDS) system. This section will describe the adaptations made to the THz-TDS system detailed in Section 2.3, in order to generate an arbitrarily-rotatable linear polarisation state, and to resolve the full polarisation state at the detector. The optimisation of the system will also be described, such that all the criteria for an idealised polarisation rotation system outlined in Section 3.1.3 are satisfied.

### 3.2.1 Rotating the Terahertz Polarisation State

A schematic diagram of the method used to produce a rotatable, linear THz polarization state in the spectrometer discussed in this chapter is provided in Fig. 3.4 (a). This method exploits the polarisation state of THz radiation generated by an interdigitated photoconductive emitter; a photoconductive emitter produces THz radiation that is linearly polarised parallel to the electric dipoles generated in the device, hence the polarisation state will be parallel to the biasing electric field applied between the contacts of the device, signified by the red arrows in Fig. 3.4 (a). By mounting such a THz emitter in a motorised rotation stage the *orientation of the emitter*  $\psi_{\text{em}}$ , and hence the orientation angle of the generated THz radiation, can be reliably and repeatably varied to any arbitrary angle.

For results presented in this chapter, the 800 nm pump beam (red waveform in Fig. 3.4 (a)) had a power of 200 mW, and the photoexcited charge carriers in the GaAs substrate were accelerated under an applied bias voltage of  $\pm 10$  V. The interdigitated emitter was fabricated (as described below) in the centre of a 25 mm  $\times$  25 mm semi-insulating GaAs (SI-GaAs) wafer, which was securely glued over the middle of the clear aperture of a Newport PR50CC motorised rotation stage. The angular range of the emitter's rotation was limited to 180°, to ensure the THz generation beam was never obscured by the emitter's

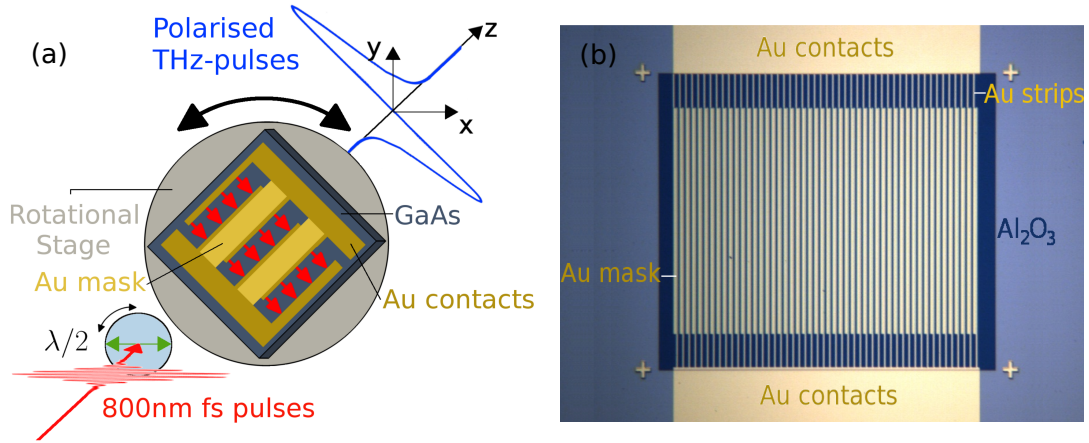


Figure 3.4: (a) Schematic (not to scale) of the interdigitated photoconductive emitter mounted on a motorised rotation stage. The THz pulse (blue waveform) has a linear polarization parallel to the direction of the applied electric field (red arrows). (b) Optical microscopy image of the interdigitated photoconductive emitter.

wiring.

#### Emitter Layout and Fabrication

The photoconductive emitter used in this spectrometer was fabricated by Michele Failla, using UV photolithography and metal evaporation procedures. An optical microscopy image of the device is provided in Fig. 3.4 (b). The photoactive area was  $2.0\text{ mm} \times 1.3\text{ mm}$  and consisted of a  $350\text{ nm}$ -thick SI-GaAs substrate covered by gold strips with a  $5\text{ }\mu\text{m}$  width and a  $5\text{ }\mu\text{m}$  spacing, which act as the electrical bias contacts. In order to avoid destructive interference in the far-field, a masking layer of gold strips covered every other gap between the contacts. To prevent short circuiting, a  $110\text{ nm}$  layer of insulating  $\text{Al}_2\text{O}_3$  vertically separated the mask and bias contacts, the thickness of which was chosen in order to maximize the transmission of the  $800\text{ nm}$  photoexcitation beam. A similar fabrication procedure to this one, used to create the pixel-based interdigitated photoconductive emitters presented in Chapter 4, will be explained in greater detail in Section 4.2.2 of this thesis, where it has been adapted by myself to improve reproducibility and increase the yield of devices.

### 3.2.2 Polarisation-Resolved Detection Method and Alignment

Polarisation-resolved detection in the RP-THz-TDS setup was performed using the polarisation-resolved electro-optic sampling variant proposed by van der Valk *et al.* [85], as described in Section 2.2.1 and shown schematically by Figure 2.3. In the RP-THz-TDS system alignment of the detection optics was performed by setting the values of  $\theta$  and  $\delta$  from Equation 2.6 to well-defined values, such that two orthogonal components of an incident THz pulse can be obtained by simply changing the value of one of these parameters. A 0.5 mm-thick  $\langle 111 \rangle$ -oriented ZnTe was used as the detection crystal, and the  $x$ -axis of the lab coordinate system, and thus the orientation which defines  $\psi = 0$ , is defined by the orientation of the  $[\bar{2}11]$ -axis of the ZnTe detection crystal. Both the QWP and HWP were mounted in high-precision motorised rotation stages to facilitate repeatable and remotely-controllable rotation of these optics.

The initial step in the alignment procedure is to define  $\delta = 0$ ; since the output of the laser and therefore the gate beam is horizontally polarised, this is achieved by rotating the HWP to find the orientation  $\theta_{\text{HWP}}^{\text{V}}$  which minimises the intensity of the vertically-polarised arm of the gate beam after the WP, *without* the QWP present in the gate beam path. The next step was to place the QWP and ZnTe into the gate beam path, and rotate the QWP to find the angle  $\theta_{\text{QWP}}^{\text{V}}$  at which the output of the photodiode circuit is balanced. The rotatable emitter was then set at  $\psi_{\text{em}} = 0$ , and the ZnTe crystal was rotated about its surface normal to find the maximum electro-optic signal, which defines  $\theta = 0$ . By referring to Equation 2.6 and Figure 2.3, we see that when both  $\delta = 0$  and  $\theta = 0$  the detection system is only sensitive to the  $E_{0\bar{1}1}$  component of the THz electric field, corresponding to vertically polarised THz radiation parallel to the lab  $y$ -axis,  $E_y$ . The  $x$  component of the THz radiation,  $E_x$ , was then obtained by setting  $\delta = 22.5^\circ$  by precisely rotating the HWP to  $\theta_{\text{HWP}}^{\text{H}}$ , and the photodiode output was balanced again by rotating the QWP to  $\theta_{\text{QWP}}^{\text{H}}$ .

This alignment procedure therefore allows the detection sensitivity to be easily switched between two orthogonal components of the THz pulse; by rotating the HWP and QWP to known values of  $\theta_{\text{HWP}}^{\text{V}}$  and  $\theta_{\text{QWP}}^{\text{V}}$  to detect the vertical component, and to  $\theta_{\text{HWP}}^{\text{H}}$  and  $\theta_{\text{QWP}}^{\text{H}}$  to detect the horizontal component.

### 3.2.3 Calibration of the Terahertz Emission Strength

As defined in Section 3.1.3, an ideal polarisation rotation system should have a minimal variation in the amplitude of the electric field  $|\mathbf{E}| = \sqrt{E_x^2 + E_y^2}$ . Therefore in the RP-THz-TDS system we want to achieve a minimal variation in  $|\mathbf{E}|$  with  $\psi_{\text{em}}$ , in order to achieve the most consistent operation of the spectrometer possible for all orientation angles. On initially rotating the emitter it was apparent that its center was close to, but not exactly on, the axis of the rotation stage. Thus under rotation the emitter was no longer centered on the THz generation beam, altering the radiated THz power. To overcome this problem the centre of the emitter was found at a range of different  $\psi_{\text{em}}$  from  $\psi_{\text{em}} = 0$  to  $\psi_{\text{em}} = 180^\circ$ , which allowed us to re-centre and photoexcite the same area on the emitter at each angle. The rotation stage holding the emitter was mounted on a motorized  $x$ - $y$  translation stage to facilitate precisely controllable adjustment of the emitter position in the  $xy$ -plane. The device was then raster scanned, under illumination by the photoexcitation beam, and the device resistance was measured at each  $\psi_{\text{em}}$  in steps of  $10^\circ$ . When the photoexcitation beam is incident on the active area of the device, the generated photocurrent causes the resistance of the device to decrease; in comparison when the beam is incident on an area of the substrate outside of the active area, the resistance will remain at a higher value. Example maps at a few select angles are shown in Figs. 3.5 (a) - 3.5 (e), together with the centre of the device (white dots).

The centre of the emitter was obtained by performing a *centre of mass*-type calculation on the resultant resistance maps; the centre coordinates  $x_c$  and  $y_c$  are found using

$$x_c(\psi_{\text{em}}) = \frac{1}{R_{\text{tot}}(\psi_{\text{em}})} \sum_{i,j} \frac{1}{R(\psi_{\text{em}}, x_i, y_j)} x_i(\psi_{\text{em}}), \quad (3.2)$$

$$y_c(\psi_{\text{em}}) = \frac{1}{R_{\text{tot}}(\psi_{\text{em}})} \sum_{i,j} \frac{1}{R(\psi_{\text{em}}, x_i, y_j)} y_i(\psi_{\text{em}}), \quad (3.3)$$

where  $R_{\text{tot}} = \sum_{i,j} R(\psi_{\text{em}}, x_i, y_j)$ , and  $i, j$  are the map coordinates. The coordinates of the emitter's centre are shown in Fig. 3.5 (f) for all  $10^\circ$  steps of  $\psi_{\text{em}}$  over the full  $180^\circ$  range, revealing that the emitter was off-centred from the stage's rotation axis by about 0.3 mm. For higher precision scans, i.e. scans



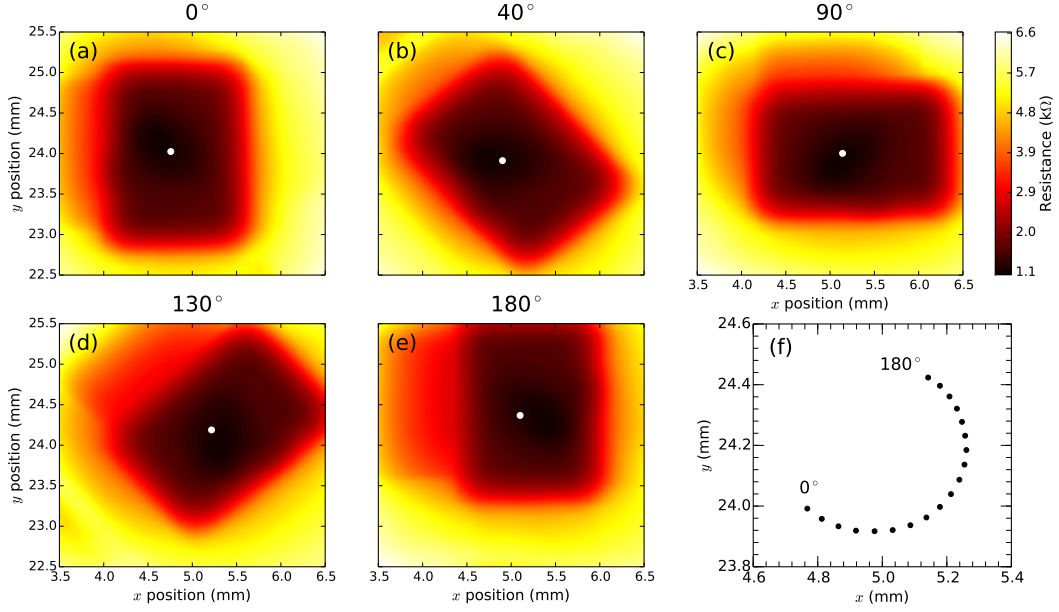


Figure 3.5: **(a) - (e)** Resistance of the interdigitated photoconductive emitter as it is raster scanned, under illumination, relative to the photoexcitation beam. The angle the emitter was rotated to in each scan is displayed above the panel. **(f)** Centre of the device at  $10^\circ$  steps over a  $180^\circ$  rotation of the emitter.

with a smaller angular step size than  $10^\circ$ , the centre position was found by interpolating the data in Fig. 3.5 (f). A larger emitter area or more precise mounting on the rotation stage's axis could avoid this  $x$ - $y$  calibration step.

The amplitude of the horizontal and vertical components of the THz electric field are shown in Fig. 3.6 versus  $\psi_{\text{em}}$  by the red and blue data points, respectively. When the applied electric field in the emitter was vertical, close to  $\psi_{\text{em}} = 0$  and  $180^\circ$ , the amplitude of  $E_y$  was a maximum, while  $E_x$  was greatest near  $\psi_{\text{em}} = 90^\circ$ . A small offset in the emitter angle compared to the orientation angle can be identified, for instance by the small  $E_x$  component at  $\psi_{\text{em}} = 0$ . The total amplitude of the THz electric field  $|\mathbf{E}|$  is shown by the green data points, and initially varied by 20% across the full range of rotation (as shown by the data points connected by the dashed lines). A motorised HWP was then added to the 800 nm pump beam, to co-rotate the pump polarization along with the emitter, keeping the pump's polarization parallel to the gold contacts. This optional step reduced the variation in  $|\mathbf{E}(\psi_{\text{em}})|$  to less than 7%, as shown by comparison between the solid lines (with HWP) and the dashed lines (without

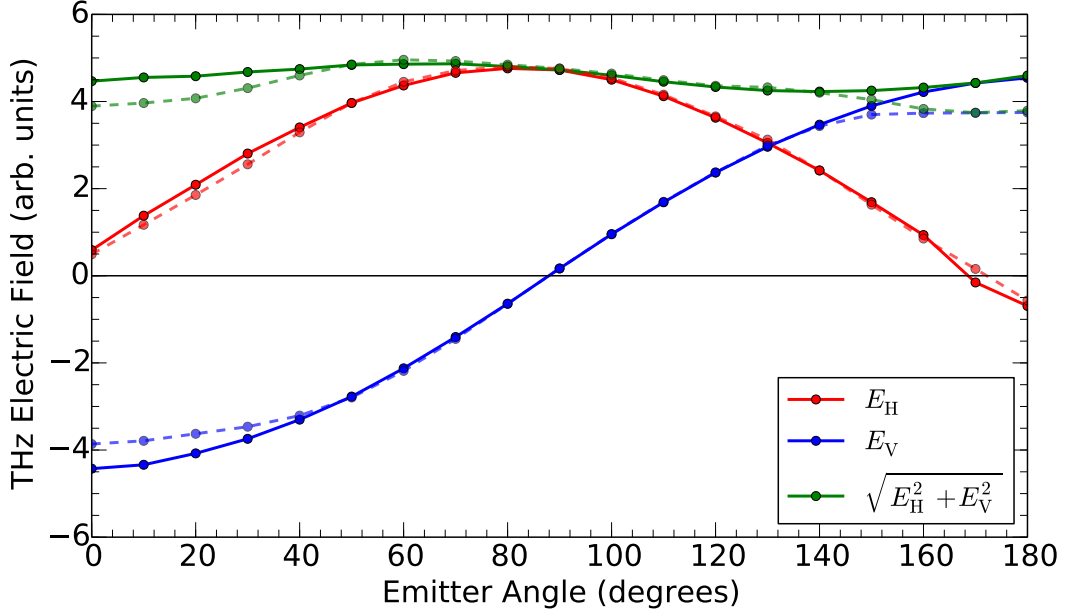


Figure 3.6: Dependence on  $\psi_{\text{em}}$  of the time-domain peak amplitude of the horizontal component (red data), vertical component (blue data) and total amplitude  $|\mathbf{E}| = \sqrt{E_{\text{H}}^2 + E_{\text{V}}^2}$  (green data), of the THz electric field, which is vertically polarized close to  $\psi_{\text{em}} = 0$  and  $\psi_{\text{em}} = 180^\circ$ , while it is horizontal close to  $\psi_{\text{em}} = 90^\circ$ . Solid lines represent data taken in the presence of a HWP to co-rotate the THz generation beam with the emitter, whilst dashed lines represent data in the absence of the HWP.

HWP) in Fig. 3.6, ensuring that a good signal-to-noise can be obtained for all orientation angles.

### 3.2.4 Polarisation State of the Rotated Terahertz Pulses

Further to a uniform electric field amplitude, an ideal RP-THz-TDS setup would exhibit minimal variation in the ellipticity of the generated THz pulses with  $\psi_{\text{em}}$ , and facilitate precise and accurate knowledge of the ellipticity and orientation angle. To investigate the polarisation state of the generated THz pulses with  $\psi_{\text{em}}$ , polarisation-resolved time-domain waveforms of THz pulses were recorded at each  $\psi_{\text{em}}$  in  $2.5^\circ$  steps over a  $180^\circ$  rotation of the emitter. A selection of time-domain waveforms can be seen in Figs. 3.7 (a) - 3.7 (e), at the corresponding angles to those of the resistance maps in Figs. 3.5 (a) - 3.5 (e). The ellipticity and orientation angle of the pulses was then extracted using the method described in Section 2.4.2.

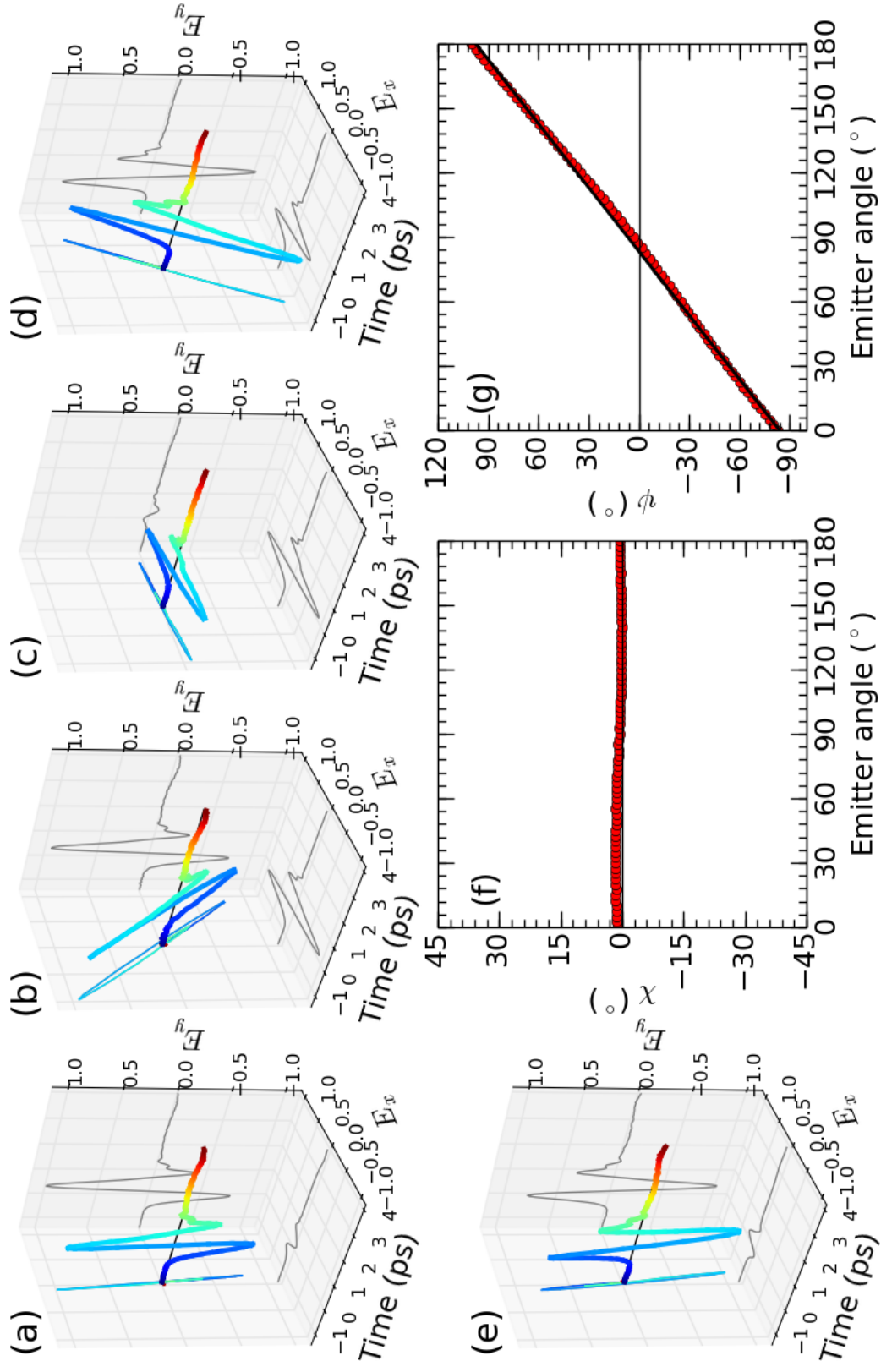


Figure 3.7: Polarisation-resolved time-domain waveforms of THz pulses generated at (a)  $\psi_{\text{em}} = 0^\circ$ , (b)  $\psi_{\text{em}} = 40^\circ$ , (c)  $\psi_{\text{em}} = 90^\circ$ , (d)  $\psi_{\text{em}} = 130^\circ$ , and (e)  $\psi_{\text{em}} = 180^\circ$ . (f) Ellipticity and (g) orientation angle of the THz pulses as the emitter is rotated in  $2.5^\circ$  steps over a  $180^\circ$  rotation.

The ellipticity of the pulses at 1.0 THz as a function of  $\psi_{\text{em}}$  is reported in Fig. 3.7 (f). The average  $\chi$  of THz pulses from the emitter was  $0.925^\circ$ , which varied by  $0.75^\circ$  over a  $180^\circ$  rotation, demonstrating that the polarisation remained close to linear for all  $\psi_{\text{em}}$ . The small measured ellipticity may be an artifact of a slight misalignment of the gate and THz beams while propagating through the detection crystal [89], or it may arise from some slight misalignment of optics in the THz beam path. However, this small ellipticity, reported here for the first time for an interdigitated THz emitter, is much smaller than the ellipticity  $\chi \sim 10^\circ$  of wide-area emitters [104] and dipole antennas [117]. While a small quadrupole moment may contribute to the finite ellipticity in those two cases [117], the small ellipticity in this case may result from the gold fingers, which in essence act as a wire-grid polarizer within the near-field of the generated THz radiation.

The precise orientation of  $\psi = 0$  relative to a sample under investigation will be an important factor in applications of this rotatable polarisation technique, for example in optical component design and material characterisation. In order to determine precisely which  $\psi_{\text{em}}$  corresponded to purely horizontally polarised pulses, where  $\psi = 0$ , the orientation angle of the incident pulse at 1.0 THz was measured as a function of  $\psi_{\text{em}}$ , shown in Fig. 3.7 (g). A linear fit to the data gives an emitter angle of  $83.85^\circ$  for  $\psi = 0$ . Thus the *incident orientation angle*  $\psi_{\text{in}}$  of the THz pulses that will be incident on the sample in the RP-THz-TDS system was calibrated precisely for each  $\psi_{\text{em}}$ . Zero  $\psi_{\text{in}}$  corresponds to a horizontally polarized incident pulse and  $\psi_{\text{in}} = \pm 90^\circ$  corresponds to vertically polarized incident pulses of opposite polarity.

### 3.3 Comparison of Rotatable Polarisation to Projection via Wire-Grid Polarisers

To illustrate the advantages of the RP-THz-TDS method over other methods of anisotropic spectroscopy, a relevant comparison is to that of polarisation projection via WGP. The polarization state of THz pulses projected to a certain angle using a WGP was compared to that achieved when the polarisation state is directly rotated using the rotatable emitter method described in this

chapter. To explore this, a WGP was fabricated by Michele Failla, using a similar UV photolithography process used to create the THz emitter described in Section 3.2.1, which consisted of 300 nm thick gold wires with 8  $\mu\text{m}$  width and 20  $\mu\text{m}$  period deposited onto a SI-GaAs substrate.

A schematic diagram of the experiment is shown in Figs. 3.8 (a) and 3.8 (b). The WGP was held in a manual rotation mount at the sample position of the spectrometer, and was rotated to an arbitrary angle. This angle at which the THz polarisation is perpendicular to the wires was precisely identified as  $\psi_{\text{in}} = -35.0^\circ$ , by scanning  $\psi_{\text{in}}$  over a range of  $20^\circ$  in  $0.625^\circ$  steps around the approximate direction perpendicular to the wires and determining the angle at which the transmitted THz amplitude  $|\mathbf{E}|$  was a maximum. The emitter was then rotated by  $45^\circ$  such that the THz pulse incident on the WGP would have equal components parallel and perpendicular to the wires. This simulates the action of projecting a linear THz pulse at an angle of  $45^\circ$  using a WGP. The frequency-dependent ellipticity and orientation angle of the projected pulse are shown by the blue lines in Figs. 3.8 (c) and 3.8 (d), respectively. The WGP produces a highly frequency-dependent elliptical pulse, which is approaching circular polarisation for frequencies above 3.0 THz. This ellipticity occurs due to the finite transmission of the component of the THz electric field parallel to the wires; this component is the first time derivative of the incident field [110], and is therefore phase-shifted by a factor of  $\pi/2$  with respect to the orthogonal component perpendicular to the wires. The orientation angle also deviates significantly from the intended angle of  $\psi = -35.0^\circ$ , by  $2.0^\circ$  in the best case at low frequency, and with larger change as the transmitted pulse becomes more elliptical.

As demonstrated in Fig. 3.8 (b), the WGP was then removed and the emitter rotated to  $\psi_{\text{in}} = -35.0^\circ$ , the same angle as that discovered to be perpendicular to the wires of the WGP in the first section of this experiment. This simulates rotating the polarisation state by  $45^\circ$  by rotating the emitter, allowing direct comparison of rotating the polarisation state and projecting it to the same angle. The frequency dependence of the ellipticity and orientation angle of THz pulses in this case is shown by the red lines in Figs. 3.8 (c) and 3.8 (d), respectively. The rotatable polarization method produces a linear THz

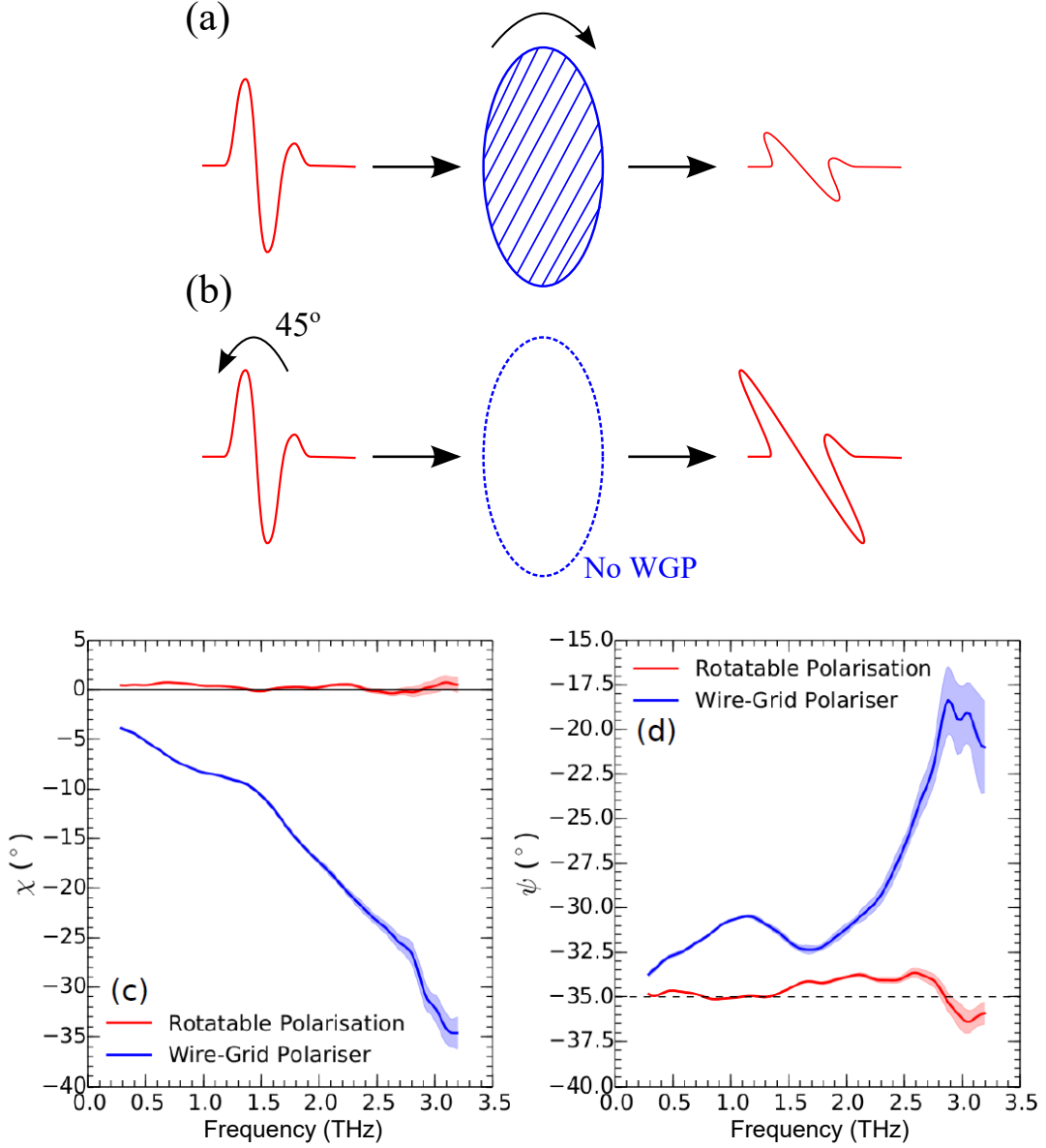


Figure 3.8: Schematic diagram of the experiment comparing **(a)** projection of the THz polarisation state by a WGP and **(b)** rotation of the polarisation state using a rotatable emitter. **(c)** Ellipticity and **(d)** orientation angle of THz pulses after transmission through a WGP acting on the incident pulse at an angle of  $45^\circ$  (blue lines), and without transmission through the WGP after the incident polarization state has been rotated  $45^\circ$  by rotating the emitter (red lines). Shaded regions show the standard deviation after 20 repeated scans. The dashed line in **(d)** represents the direction perpendicular to the wires of the WGP.

pulse over the whole experimental bandwidth when rotated to an arbitrary angle, with an ellipticity of  $\leq 0.75^\circ$  and a statistical error (the precision) in the ellipticity of  $< 0.05^\circ$  over the  $0.3 - 1.5$  THz range ( $< 0.1^\circ$  from  $0.3 - 2.5$  THz) after 20 repeated measurements. The accuracy of the orientation angle was defined as the variation of  $\psi(\omega)$  away from the mean [97], and was  $< 1.0^\circ$  between  $0.3 - 2.5$  THz. The statistical error in the orientation angle was  $< 0.05^\circ$  between  $0.3 - 1.5$  THz ( $< 0.1^\circ$  from  $0.3 - 2.5$  THz).

The above demonstrates the drawbacks in using WGP in polarization-resolved detection or in ellipsometric schemes to study anisotropic materials. While the above WGP may not be competitive with some of the best commercial WGP (which have smaller periods), any WGP will introduce uncertainty into the identification of optical properties. Comparatively, RP-THz-TDS does not suffer from this issue, and has an accuracy and precision comparable to the best ellipsometric methods [97].

### 3.4 Experimental Implementation of RP-THz-TDS

To demonstrate how RP-THz-TDS can be utilised to investigate anisotropic media, case studies were made of birefringence in two uniaxial crystals, ZnO and LaAlO<sub>3</sub>, and anisotropic absorption and birefringence in the biaxial crystal CuO. This section will demonstrate how the RP-THz-TDS technique may be used to identify the orientations of polarisation eigenvectors and extract their complex optical properties, and also how the orientations of anisotropic absorption features may be investigated.

#### 3.4.1 Sample Details

##### ZnO

The first test case material under study is ZnO, which is a wide-gap semiconductor of interest in optoelectronics. With a hexagonal structure (space group C6mc), ZnO consists of alternating hexagonal stacks of Zn<sup>2+</sup> and O<sup>2-</sup> ions along the *c*-axis, with each Zn<sup>2+</sup> ion coordinated tetrahedrally with the O<sup>2-</sup>, and vice versa. Measurements presented in this section were performed on a 0.6 mm thick single crystal of ZnO, oriented with the *a*-axis as the surface normal and

the  $c$ -axis in the plane. The birefringence in the THz range can be linked to the differences in phonon mode frequency and strength for directions parallel to and perpendicular to  $c$  [118], and also to any additional anisotropy in the electronic contribution to the dielectric function. The dielectric tensor for a uniaxial crystal can be expressed as

$$\boldsymbol{\epsilon} = \begin{bmatrix} \epsilon_{xx} & 0 & 0 \\ 0 & \epsilon_{xx} & 0 \\ 0 & 0 & \epsilon_{zz} \end{bmatrix}, \quad (3.4)$$

where  $\epsilon_{xx}$  and  $\epsilon_{zz}$  are the components of the dielectric tensor along the mutually orthogonal principal axes of the material  $x$ ,  $y$  and  $z$ ,  $\epsilon_{xx} = \epsilon_{yy}$ , and  $z$  is the optical axis.

### **LaAlO<sub>3</sub>**

The second test case material is LaAlO<sub>3</sub>, which is a useful substrate for epitaxial growth of complex oxides. At room temperature LaAlO<sub>3</sub> is a rhombohedrally-distorted perovskite with space group  $R\bar{3}c$  [119]. The optical axis is in the [111] pseudocubic direction [6]. While ZnO forms a homogeneous single crystal, LaAlO<sub>3</sub> is inhomogeneous with twin domains bounded along the [010] direction. The size of these twin domains has been shown to sensitively influence the apparent birefringence in the THz region [6]. Here, measurements were performed on a 0.5 mm thick [001]-oriented single crystal of LaAlO<sub>3</sub>, with twin domains that were small in comparison to the THz spot size. The in-plane crystallographic directions were oriented arbitrarily with respect to the incident THz polarization.

### **CuO**

Having a monoclinic crystal structure with space group  $C2/c$ , CuO is a biaxial crystal. Due to its monoclinic crystal structure, the dielectric tensor in CuO is

$$\boldsymbol{\epsilon} = \begin{bmatrix} \epsilon_{xx} & 0 & \epsilon_{xz} \\ 0 & \epsilon_{yy} & 0 \\ \epsilon_{zx} & 0 & \epsilon_{zz} \end{bmatrix} \quad (3.5)$$



where  $x \parallel a$ ,  $y \parallel b$  and  $c \parallel c^*$  [56]. Measurements in this chapter were performed on a 1.3 mm thick single crystal of CuO that was aligned by Laue X-ray diffraction to have a  $(10\bar{1})$  surface normal. Thus, the  $[101]$  and  $[010]$  directions are in-plane.

### 3.4.2 Mapping Birefringence and Identifying Polarisation Eigenvectors Using RP-THz-TDS

As discussed previously in Section 1.1.3, for an arbitrary direction of propagation there are two eigenmodes of propagation  $\mathbf{D}_{a,b}$  with refractive indices  $n_{a,b}$ . For light propagating along an optical axis the refractive index is independent of the polarization direction, and hence there is no birefringence. When light propagates along any other direction the polarization eigenmodes will have different propagation speeds, and hence the material is birefringent. When  $\psi_{\text{in}}$  is midway between the two polarisation eigenvectors the ellipticity  $\chi$  of the pulse transmitted through the sample will be a maximum, while conversely  $\chi = 0$  when  $\psi_{\text{in}}$  is parallel to a polarization eigenvector. Therefore by rotating the incident THz polarization state and measuring  $\chi$  at each angle, the orientation of the in-plane polarization eigenvectors can be accurately determined.

#### ZnO

As a demonstration of how the phase delay between the components of the THz electric field propagating along each of the polarisation eigenvectors in a birefringent material produces an elliptical polarization state, polarization-resolved time-domain waveforms before and after transmission through ZnO are reported in Figs. 3.9 (a) and 3.9 (b), both at  $\psi_{\text{in}} = 56.15^\circ$ . Fig. 3.10 (a) shows the evolution of  $\chi(\omega)$  after transmission through ZnO, as  $\psi_{\text{in}}$  is varied over  $180^\circ$  in  $2.5^\circ$  steps, and Fig. 3.10 (b) shows slices through the contour at a few fixed frequencies. Zero  $\chi$  occurs around  $\psi_{\text{in}} = 4^\circ$  and  $\psi_{\text{in}} = 94^\circ$ , identifying the orientation of the polarization eigenvectors. Tracing the evolution of  $\chi$  with frequency, right- and left-handed circularly polarized states can be observed for certain  $\psi_{\text{in}}$  at 0.75 and 2.25 THz, where the ZnO is acting as a quarter-wave plate, and between these frequencies the polarization state becomes linear again at 1.5 THz, where the ZnO is acting as a half-wave plate.

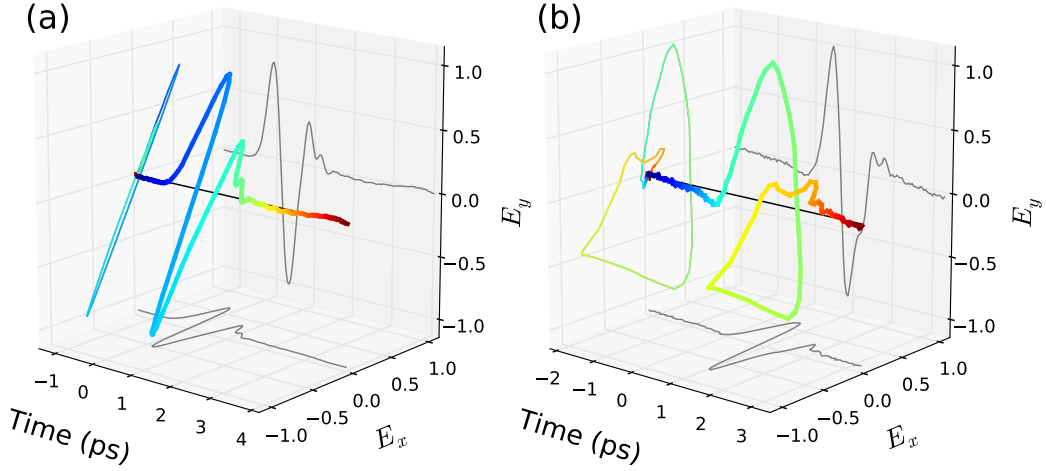


Figure 3.9: Polarisation-resolved time-domain waveforms measured (a) without and (b) after transmission through ZnO, initially polarised at  $\psi_{\text{in}} = 56.15^\circ$ . The grey curves on the bottom and righthand planes of each panel are the projections of the polarisation state onto the  $x$ - and  $y$ -axis, respectively. The multicoloured curve on the lefthand plane is the projection of the polarisation state as viewed looking against the direction of propagation, and the multicoloured curve in the centre of each panel is the full 3D polarisation state.

Fig. 3.10 (c) shows the frequency dependence of  $\chi$  for  $\psi_{\text{in}} = 56.0^\circ$  (red dots),  $\psi_{\text{in}} = 71.0^\circ$  (orange dots) and  $\psi_{\text{in}} = 26.0^\circ$  (yellow dots). The solid black lines are the calculated ellipticity, at each angle, of an initially linearly polarized pulse transmitted through ZnO of the same thickness as the experimental sample. The birefringence  $\Delta n = n_a - n_b$  of ZnO was assumed to be frequency dependent and was empirically modelled as  $\Delta n = \Delta n_0 + \alpha f$ , where  $f$  is the frequency in THz. A quadratic component to the birefringence was also considered, but was found to be negligible in the experimental frequency range. Using this model and fitting to the experimental data gave  $\Delta n_0 = 0.14$  and  $\alpha = 0.011 \text{ THz}^{-1}$ . A linear fit to  $\Delta n$  over the experimental frequency range  $0.5 - 2.5 \text{ THz}$  is reasonable, as the lowest infrared active phonon modes in ZnO occur at 11.5 and 12.5 THz for the  $A_1$  and  $E_1$  modes respectively [118].

### LaAlO<sub>3</sub>

The variation of the change in ellipticity  $\Delta\chi(\omega) = \chi_{\text{sample}}(\omega) - \chi_{\text{reference}}(\omega)$  with  $\psi_{\text{in}}$  of pulses after transmission through LaAlO<sub>3</sub> is presented in Fig. 3.11 (a),

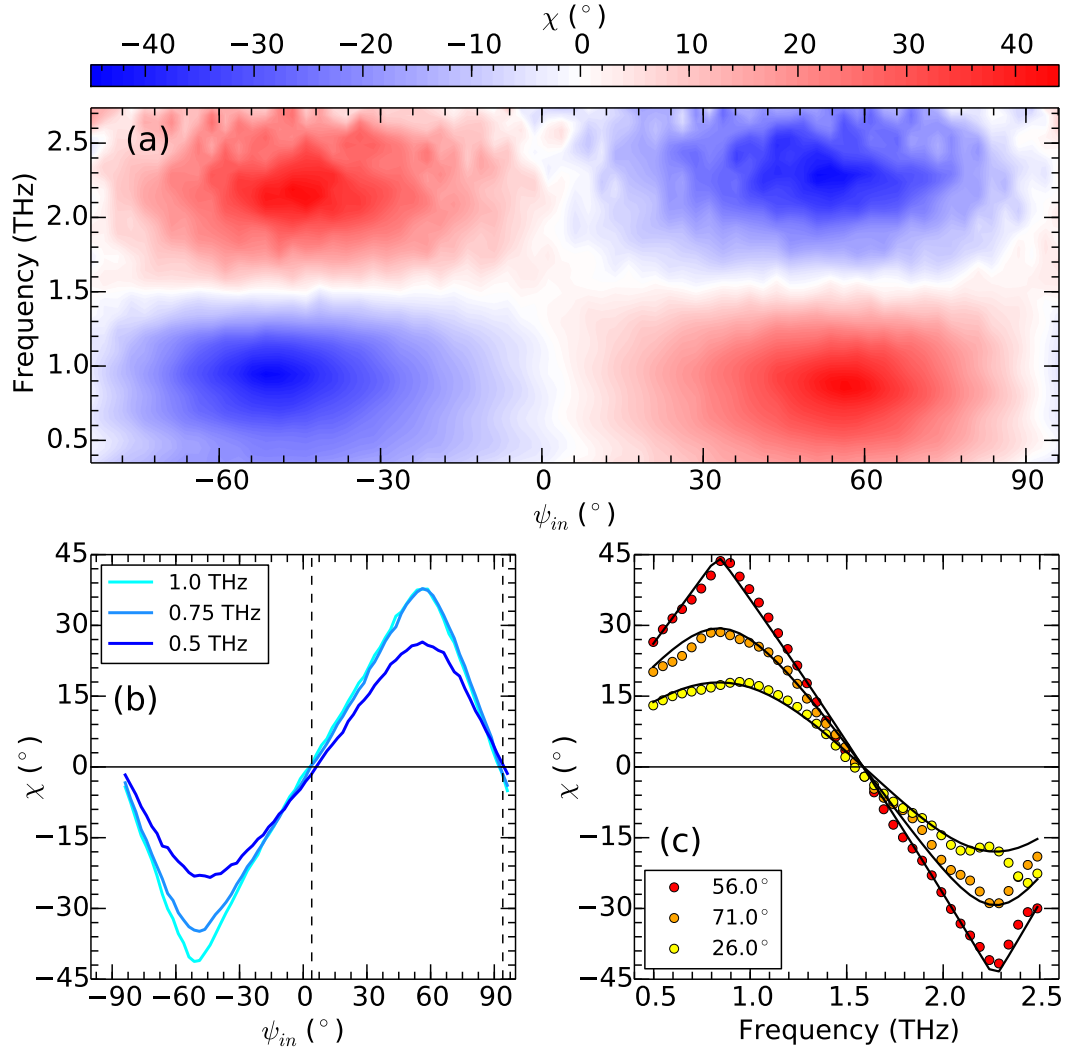


Figure 3.10: (a) Ellipticity of THz pulses after transmission through ZnO as a function of incident orientation angle and frequency. (b) Ellipticity of THz pulses after transmission through ZnO at a few fixed frequencies. (c) Ellipticity as a function of frequency after transmission through ZnO, at three values of  $\psi_{in}$ . Dots are experimental data and solid lines are calculated fits.

and in Fig. 3.11 (b) at a few fixed frequencies. By considering  $\Delta\chi$  rather than  $\chi$  the influence of the finite ellipticity of the reference pulses is removed, and only the influence of the sample on the ellipticity remains. This allows greater sensitivity when investigating materials in which the birefringence is small, as it is at low frequency in this particular sample of  $\text{LaAlO}_3$ .  $\Delta\chi$  was fit to a cosine model (solid lines),  $A \cos(B(\psi_{\text{in}} + \phi)) + C$ , where  $A$ ,  $B$  and  $C$  are constants and  $\phi$  is a phase offset, which gave  $\Delta\chi = 0^\circ$  at  $\psi_{\text{in}} = -16.5^\circ$  and  $\psi_{\text{in}} = 76.0^\circ$ , corresponding to the directions of the polarization eigenvectors. The directions of the eigenvectors measured here are given to a precision of  $\pm 1.25^\circ$ , limited by the angular step size of the scan.

The change in ellipticity at a few fixed values of  $\psi_{\text{in}}$  is presented in Fig. 3.11 (c). As in the case of  $\text{ZnO}$  discussed previously, the solid black lines are the calculated ellipticity, at each angle, of an initially linearly polarized pulse transmitted through  $\text{ZnO}$  of the same thickness as the experimental sample. The birefringence of  $\text{LaAlO}_3$  was calculated similarly to the method used previously for  $\text{ZnO}$ , by assuming a frequency dependent model  $\Delta n = \Delta n_0 + \beta f^2$  and calculating the frequency dependent change in ellipticity for certain  $\psi_{\text{in}}$ , giving  $\Delta n_0 = 0.0045$  and  $\beta = 0.0065 \text{ THz}^{-2}$ . As with  $\text{ZnO}$ , a linear term to  $\Delta n$  was considered, but was found to be negligible for  $\text{LaAlO}_3$ . The difference in the frequency dependence to the birefringence in  $\text{LaAlO}_3$  compared to  $\text{ZnO}$  is due to its lower frequency infrared active phonon modes, at 5.0 and 5.5 THz for the  $A_1$  and  $E_1$  modes respectively [6], which occur closer to the experimental frequency range: Hence both  $n_a$  and  $n_b$ , and therefore  $\Delta n$ , vary more rapidly with frequency.

### 3.4.3 Extracting the Full Complex Refractive Index Using RP-THz-TDS

One of the major advantages of time-domain spectroscopic techniques, compared those based solely on measuring the intensity of radiation, is that the phase information allows the direct determination of both the real and imaginary part of the complex refractive index, as described in Section 2.4. Having determined the orientations of the in-plane principal axes of the two samples of  $\text{ZnO}$  and  $\text{LAO}$  in the previous section, this section will demonstrate how

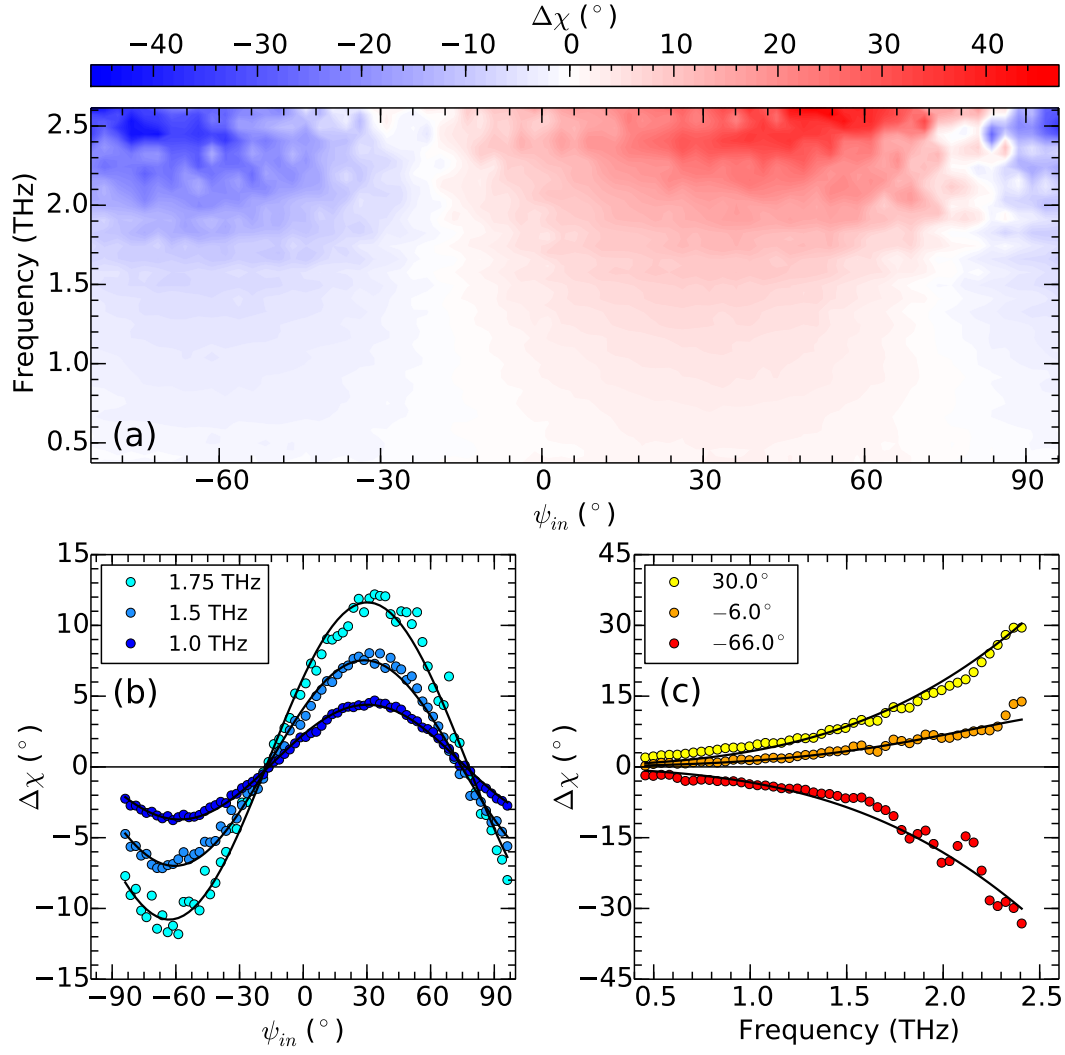


Figure 3.11: (a) Ellipticity of THz pulses after transmission through  $\text{LaAlO}_3$  as a function of incident orientation angle and frequency. (b) Ellipticity of THz pulses after transmission through  $\text{LaAlO}_3$  at a few fixed frequencies. (c) Ellipticity as a function of frequency after transmission through  $\text{LaAlO}_3$ , at three values of  $\psi_{in}$ . Dots are experimental data and solid lines are calculated fits.

the RP-THz-TDS technique may be used to extract the full complex refractive index for both principal axes for an arbitrary orientation of the sample.

### Rotating the Frame of Reference

As Figs. 3.10 and 3.11 have shown, the polarisation state of the THz pulses experiences no change when the electric field is parallel to a polarisation eigenvector in the sample. The transmitted THz pulse therefore has the same orientation angle as the incident pulse; if the frame of reference of the sample and reference pulses can be rotated to match that of the polarisation eigenvector, then the usual one-dimensional data analysis to extract  $n(\omega)$  and  $\alpha(\omega)$  as described in Section 2.4.1 can be applied.

The rotation matrix  $\mathbf{R}$  representing points in the cartesian  $x$ - $y$  plane being rotated anticlockwise about the origin of the coordinate system by an angle  $\theta_R$  is

$$\mathbf{R} = \begin{bmatrix} \cos \theta_R & -\sin \theta_R \\ \sin \theta_R & \cos \theta_R \end{bmatrix}. \quad (3.6)$$

Applying this rotation matrix to the complex frequency-domain electric field vector  $\tilde{\mathbf{E}}(\omega)$  will obtain the electric field vector in the rotated coordinate system  $\tilde{\mathbf{E}}^R(\omega)$ ; in terms of the horizontal and vertical components in the respective coordinate systems this is

$$\begin{bmatrix} \cos \theta_R & -\sin \theta_R \\ \sin \theta_R & \cos \theta_R \end{bmatrix} \cdot \begin{bmatrix} \tilde{E}_H(\omega) \\ \tilde{E}_V(\omega) \end{bmatrix} = \begin{bmatrix} \tilde{E}_{x'}(\omega) \\ \tilde{E}_{y'}(\omega) \end{bmatrix}. \quad (3.7)$$

The rotated coordinate system is oriented such that the majority of the THz electric field now lies parallel to the  $x'$  axis, with only a very small orthogonal component in the  $y'$  direction. The complex transmission function is then simply the ratio of the sample and reference electric field  $x'$  components,  $\tilde{T}(\omega) = \tilde{E}_{x'}^s(\omega)/\tilde{E}_{x'}^r(\omega)$ , and  $n(\omega)$  and  $\alpha(\omega)$  are obtained via Equations 2.16 and 2.17.

### ZnO

As demonstrated in Fig. 3.10, the polarisation eigenvectors in the ZnO sample investigated here occur around  $\psi = 4^\circ$  and  $\psi = 94^\circ$ . As the angular step size

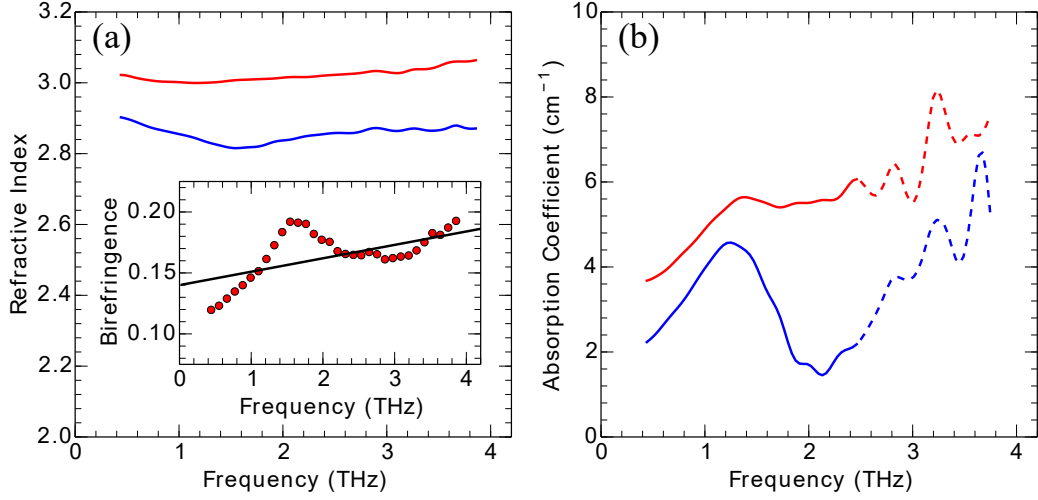


Figure 3.12: **(a)** Refractive index and **(b)** absorption coefficient of the in-plane polarisation eigenvectors  $\mathbf{D}_a$  at  $\psi_{\text{in}} = 3.65^\circ$  (red lines) and  $\mathbf{D}_b$  at  $\psi_{\text{in}} = 93.65^\circ$  (blue lines) in ZnO. Dashed lines represent frequencies at which the experimental signal-to-noise is low, but the data are included to demonstrate the overall trend. The birefringence  $\Delta n = n_a - n_b$  is shown in the inset of panel **(a)**, with the red dots representing the experimental data and the solid black line representing the empirical fit determined in Section 3.4.2.

between scans was  $2.5^\circ$  the closest datasets to these polarisation eigenvectors, at  $\psi_{\text{in}} = 3.65^\circ$  and  $\psi_{\text{in}} = 93.65^\circ$  respectively, were used in the following analysis. The average  $\psi$  of the THz pulses between 0.3-2.5 THz was obtained from the data and used as the value of  $\theta_R$  when applying the rotation matrix in equation 3.7 to find  $\tilde{E}_{x'}$ .

The refractive index and absorption coefficient along each polarisation eigenvector in ZnO obtained by this method are presented in Figs. 3.12 (a) and 3.12 (b), respectively. Red lines represent  $n$  and  $\alpha$  for the eigenvector  $\mathbf{D}_a$  at  $\psi = 4^\circ$ , and blue lines represent  $n$  and  $\alpha$  for the eigenvector  $\mathbf{D}_b$  at  $\psi = 94^\circ$ . The values of  $n_a = 3.02$  and  $n_b = 2.85$  at 1 THz are in agreement with those observed previously [118]. The data in reference [118] demonstrate a monotonic increase in the refractive index with increasing frequency over the 0.25-1.35 THz range for both ordinary and extraordinary axes, consistent with the behaviour observed along  $n_a$  here, however the data in reference [118] does not exhibit the behaviour observed here in  $n_b$  at 1.2 THz, potentially due to this being on the edge of their experimental bandwidth. Here, a peak in  $\alpha$  and

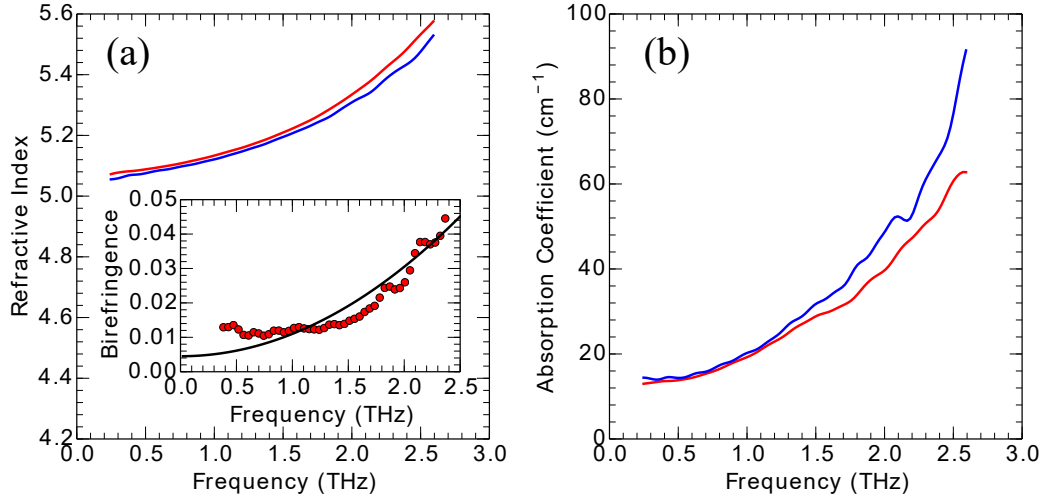


Figure 3.13: (a) Refractive index and (b) absorption coefficient of the in-plane polarisation eigenvectors  $\mathbf{D}_a$  at  $\psi_{\text{in}} = -16.5^\circ$  (red lines) and  $\mathbf{D}_b$  at  $\psi_{\text{in}} = 76.0^\circ$  (blue lines) in ZnO. The birefringence  $\Delta n = n_a - n_b$  is shown in the inset of panel (a), with the red dots representing the experimental data and the solid black line representing the empirical fit determined in section 3.4.2.

a dip in  $n$  are observed along  $\mathbf{D}_b$  at 1.2 THz. This weak absorption feature may be associated with a difference mode between the  $A_1$  and  $E_1$  modes, as the energy difference between them is around 1 THz [118]. Anisotropy in the phonon band structure of ZnO [120] could cause a weak optically active mode to occur along one crystallographic direction; similar weak phonon modes have previously been observed in ZnTe [121, 122]. The experimentally obtained birefringence is presented in the inset of Fig. 3.12(a), along with the empirical fit to the birefringence obtained in Section 3.4.2. The fit can be seen to reproduce the general trend of the data, but cannot reproduce the observed fine structure caused by the feature at 1.2 THz. The value of  $\Delta n = 0.15$  at 1 THz is consistent with the experimentally measured value of 0.18 and the theoretically calculated value of 0.17 reported by the authors of reference [118].

### LaAlO<sub>3</sub>

The polarisation eigenvectors in the sample of LAO under study were observed to be  $\psi_{\text{in}} = -16.5^\circ$  for  $\mathbf{D}_a$  and  $\psi_{\text{in}} = 76.0^\circ$  for  $\mathbf{D}_b$  from Fig. 3.11. Using the same procedure described for ZnO, the refractive index and absorption coefficient for



the two eigenvectors were extracted from the data, and are presented in Figs. 3.13 (a) and 3.13 (b), respectively. As before, red lines represent  $n$  and  $\alpha$  for the eigenvector  $\mathbf{D}_a$  at  $\psi_{\text{in}} = -16.5^\circ$ , and blue lines represent  $n$  and  $\alpha$  for the eigenvector  $\mathbf{D}_b$  at  $\psi_{\text{in}} = 76.0^\circ$ . Both refractive indices increase monotonically with frequency, with values of  $n_a = 5.15$  and  $n_b = 5.14$  at 1 THz, in agreement with previous observations [6]. As with ZnO, the empirical fit to the birefringence reproduces the general trend of the data. Fig. 3.13 (b) demonstrates a monotonic increase in the absorption coefficient along both eigenvectors.

#### 3.4.4 Anisotropic Absorption and Chromatic Dispersion in CuO

To demonstrate how RP-THz-TDS can be used to investigate the absorptive properties of anisotropic media, the dependence of the electromagnon absorption on the incident THz orientation angle was investigated in CuO. From previous experimental and theoretical work [8, 68], it has been shown that the electromagnon present in the AF2 phase of CuO absorbs light only for electric fields oriented close to the [101] direction. Since a cryostat is required to access the temperature range at which the electromagnon is active, rotating the THz polarization state, rather than the sample, is a highly convenient method to probe its anisotropic optical properties. RP-THz-TDS was performed at 210 K, in the AF1 phase, and at 215 K, in the AF2 phase, and the sample was oriented in the spectrometer such that the [101] direction is close to  $\psi_{\text{in}} = 0^\circ$ .

##### Anisotropy of the Electromagnon Absorption in CuO

To examine the absorption of the electromagnon and to precisely determine its selection rule, we examined the temperature-dependent change in absorption coefficient between the AF1 and AF2 phase, expressed as

$$\Delta\alpha(\omega, \psi_{\text{in}}) = -\frac{2}{d} \ln |\tilde{T}(\omega, \psi_{\text{in}})|, \quad (3.8)$$

where  $d$  is the sample thickness and  $|\tilde{T}(\omega, \psi_{\text{in}})|$  is the absolute part of the complex transmission function. The transmission function at each value of  $\psi_{\text{in}}$  was

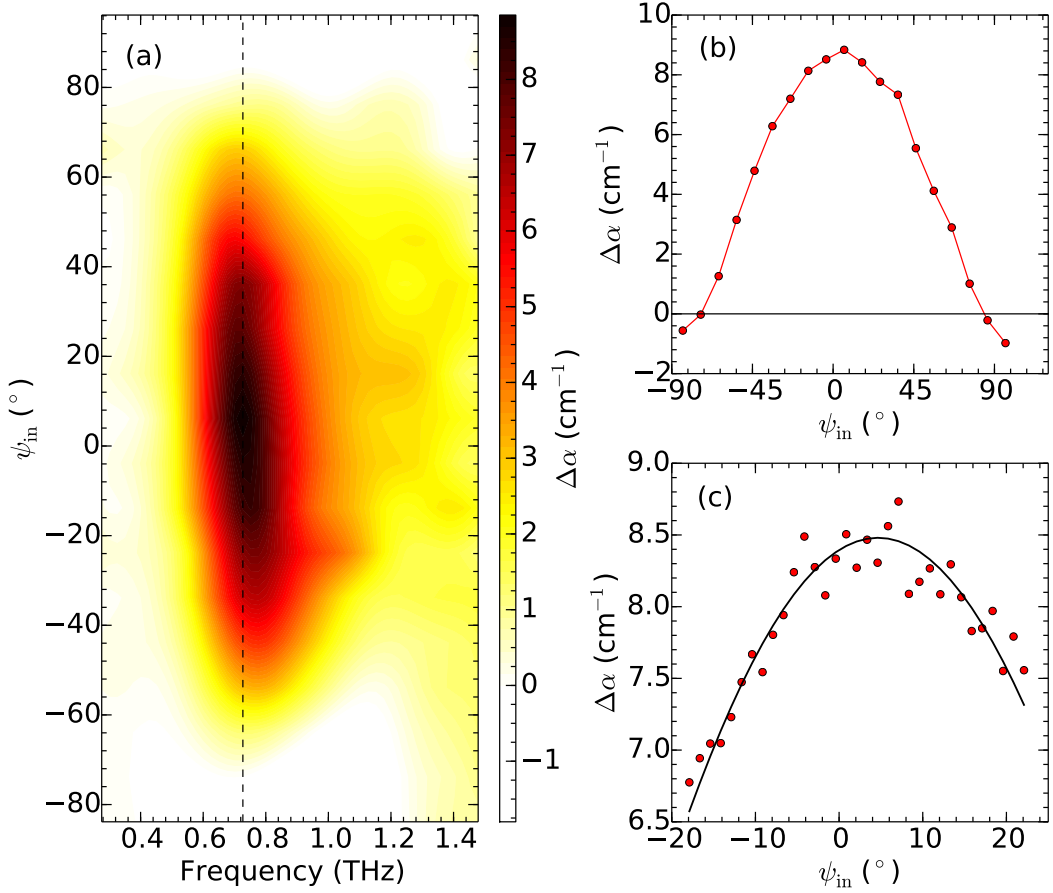


Figure 3.14: **(a)** Change in the terahertz absorption coefficient  $\Delta\alpha$  of CuO due to multiferroicity versus incident orientation angle and frequency. The dashed line represents the maximum absorption at 0.72 THz. **(b)** Evolution of  $\Delta\alpha$  with incident orientation angle at 0.72 THz. **(c)** shows the experimental data (red dots) and fit (solid line) for a scan over the peak of the absorption with a smaller angular step size.

found from the ratio of the total transmitted THz intensity, using

$$|\tilde{T}(\omega)| = \frac{\sqrt{|\tilde{E}_x^s(\omega)|^2 + |\tilde{E}_y^s(\omega)|^2}}{\sqrt{|\tilde{E}_x^r(\omega)|^2 + |\tilde{E}_y^r(\omega)|^2}}, \quad (3.9)$$

where the superscripts s and r denote the sample (at 215 K) and reference (at 210 K) spectra, and the subscripts  $x$  and  $y$  denote the horizontally and vertically polarized components, respectively.

The change in absorption induced by multiferroicity,  $\Delta\alpha(\omega)$ , as  $\psi_{\text{in}}$  is varied is reported in Fig. 3.14 (a). The electromagnon is evident as a peak in

$\Delta\alpha$  around 0.7 THz with a weaker tail at higher frequencies, and a strength that decreases as  $\psi_{\text{in}}$  moves away from [101] (close to  $\psi_{\text{in}} = 0^\circ$ ) towards [010] (close to  $\psi_{\text{in}} = \pm 90^\circ$ ). This verifies that the electromagnon is only excited when applying a THz electric field along the [101] direction, as reported by Jones *et al.* [8] using measurements at only a few fixed angles. A cut through the peak of the absorption at 0.72 THz is shown in Fig. 3.14 (b), represented by the dashed line in Fig. 3.14 (a). The maximum change in absorption occurs when  $\psi_{\text{in}} = 6^\circ$ , with a precision of  $5^\circ$  defined by half the angular step size of the scan. To more precisely determine the orientation of maximum absorption, an angular range of  $40^\circ$  containing the peak of the absorption was scanned with a smaller angular step size, shown in Fig. 3.14 (c). The experimental data (dots) were fit (solid line) to a cosine model,  $A \cos(2(\psi_{\text{in}} + \phi)) + C$ , where  $A$  and  $C$  are constants and  $\phi$  is a phase offset. From this fit the angle of maximum absorption occurs at  $\psi_{\text{in}} = 5^\circ$ .

An additional feature that can be observed in Fig. 3.14 (a) is that as  $\psi_{\text{in}}$  approaches  $\pm 90^\circ$ , where it is close to the [010] direction,  $\Delta\alpha$  is observed to become negative, corresponding to a larger transmission in the AF2 phase than in the AF1 phase. This can be attributed to the static polarization along [010] that arises in the multiferroic phase altering the absorption of the higher-lying phonon modes [53].

### Birefringence Mapping and Chromatic Dispersion in CuO

The ellipticity of THz pulses after transmission through CuO at 215 K is shown in Fig. 3.15. The region where  $\chi \approx 0$  occupies a range of around  $6^\circ$  centered on  $\psi_{\text{in}} = 4^\circ$ , represented by the dashed line in Fig. 3.15. This is in agreement with the angle of maximum  $\Delta\alpha$  determined from Fig. 3.14 (c), suggesting that this polarization eigenvector coincides with the [101] direction. The birefringence in CuO was calculated using the same method as in Section 3.4.2 for ZnO and LaAlO<sub>3</sub>, and was found to be linearly dependent on frequency,  $\Delta n = \Delta n_0 + \alpha f$  with  $\Delta n_0 = 0.14$  and  $\alpha = 0.03 \text{ THz}^{-1}$ .

From Fig. 3.15 it can be observed that the polarisation eigenvector along [101] demonstrates chromatic dispersion, i.e. a frequency dependence to its direction. This can be seen as a deviation in the  $\psi_{\text{in}}$  for which  $\chi = 0^\circ$  away

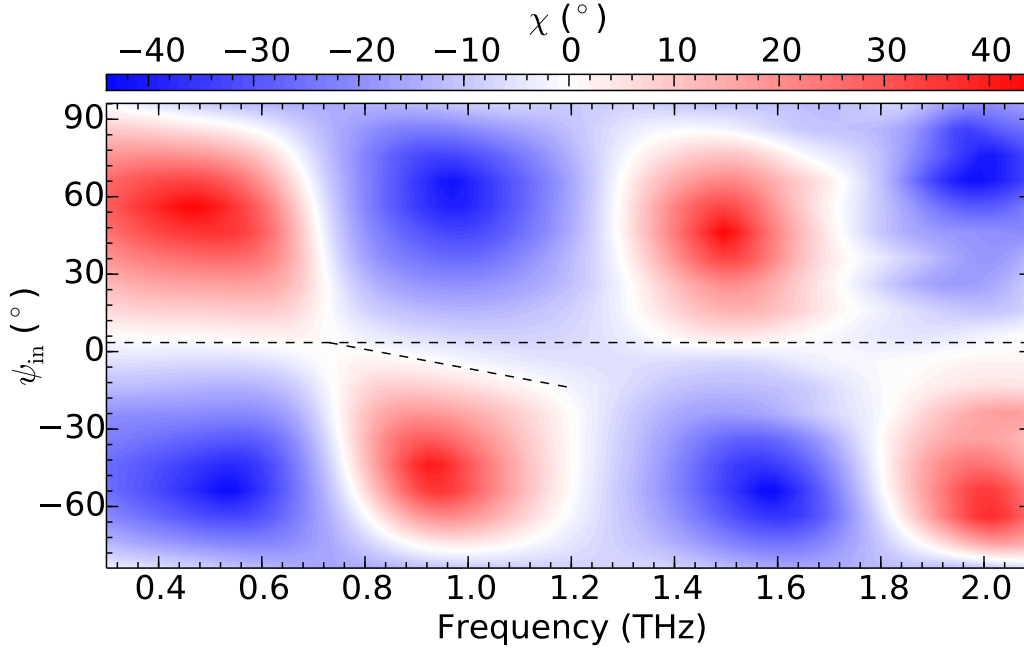


Figure 3.15: Ellipticity of THz pulses after transmission through CuO as a function of incident orientation angle and frequency. The long dashed line at  $\psi_{\text{in}} = 4^\circ$  represents the approximate orientation of the [101] direction. The short dashed line is a guide to the eye highlighting chromatic dispersion.

from the dashed line at  $\psi_{\text{in}} = 4^\circ$ , highlighted by the shorter dashed line. The rotation of the polarization eigenvector away from [101] as a result of chromatic dispersion is almost  $20^\circ$  at 1.2 THz. For comparison, Fig. 3.10 shows that the polarization eigenvectors in ZnO occur at a constant  $\psi_{\text{in}}$ . In a monoclinic crystal, a preferential triplet of orthogonal directions is not compatible with the crystalline symmetry [123]. The frequency dependence of the complex components of the dielectric tensor causes the principal axes of the crystal, and hence the propagation eigenvectors  $\mathbf{D}_{a,b}$ , to also vary with frequency. In monoclinic crystals two of the principal axes are colour dispersive, while one principal axis has a fixed direction [123]. From Equation 3.5, since there are no off-diagonal components to the dielectric tensor involving  $y$ , the fixed principal axis will occur along the  $b$  direction, and the two colour dispersive axes will lie in the  $ac$ -plane. In this particular case, light propagates along the  $(10\bar{1})$  surface normal, which has been found previously to be a principal axis of the dc dielectric tensor [56]. The observation of birefringence for this  $\mathbf{k}$  means that  $(10\bar{1})$  is not an optical axis.

### 3.5 Summary

This chapter has presented a method of rotatable-polarisation THz-TDS, in which the polarisation state of the generated THz radiation was arbitrarily rotated via the use of an interdigitated PCE mounted in a motorised rotation stage. Polarisation-resolved EOS was used to obtain  $E_x$  and  $E_y$  directly, resolving the full THz polarization state without requiring the extra components, assumptions and data analysis required by other polarimetry or ellipsometry methods. This approach allows broadband polarization rotation, with linearly polarized THz pulses that can be rotated to arbitrary angles (accuracy  $< 1.0^\circ$ , precision  $< 0.1^\circ$ ) over a frequency range of 0.3-2.5 THz. The optimisation of the setup was reported, resulting in a variation in amplitude of only  $\sim 7\%$  over the  $180^\circ$  range of the device, and the polarisation state exhibits only a very small intrinsic ellipticity (accuracy  $< 0.75^\circ$ , precision  $< 0.1^\circ$ ). This method of polarisation rotation was also shown to perform favourably compared to WGP, which were shown to introduce large variations in the polarisation state of projected THz pulses.

RP-THz-TDS was also experimentally implemented, demonstrating how the technique may be used to identify the in-plane polarisation eigenvectors of birefringent materials, and to determine the full complex refractive index along each of these directions. A demonstration of how RP-THz-TDS may be used to investigate the selection rules of an anisotropic absorption feature was also provided, by studying the electromagnon absorption in CuO.

The polarisation rotation method presented here does not require WGP, circumventing the problem of their poor extinction ratio, and is performed during the generation of the THz pulses, avoiding reflection losses associated with transmissive components like wave plates. Rotating the THz polarization state not only allows convenient access to the anisotropic optical properties at cryogenic temperatures or other situations in which rotating the sample may be challenging, but also ensures that the same area on the sample is probed at each angle, solving many issues related to rotating the sample.

## Chapter 4

# Scalable Interdigitated Photoconductive Emitters for the Electrical Modulation of Terahertz Beams With Arbitrary Linear Polarisation

Photoconductive emitters are a crucial component for terahertz (THz) radiation sources and detectors, being the most commonly used in commercially available and custom-built spectroscopy and imaging systems based on oscillator and fibre lasers [71, 124]. A recent development in THz generation from photoconductive emitters is the creation of complex polarisation states [125, 126, 127, 128], and the ability to control the polarisation state of the emitted radiation [104, 129, 130]. These advances in THz polarisation control may permit otherwise inaccessible excitations, and the anisotropic properties of materials, to be probed in the THz region.

In this chapter, a multi-element interdigitated photoconductive emitter for broadband THz polarisation rotation, consisting of separate pixels for the emission of horizontally and vertically polarised THz radiation, is proposed and experimentally verified. The device is scalable in design, and with its simple method of polarisation rotation it allows the modulation of the generated THz

polarisation at rates significantly faster than those achievable in ellipsometry systems based on mechanically rotating components. Section 4.1 gives a short overview of the generation of electromagnetic radiation by electric dipoles, and of the generation of THz pulses with various polarisation states via photoconductive emitters with novel geometries. The design and fabrication of the multi-element device proposed in this thesis is outlined in Section 4.2, accompanied by simulations of the radiation pattern the device is expected to produce. Section 4.3 details the experimental verification of the multi-pixel photoconductive emitters, which demonstrates the broadband nature of the device and the control of the polarisation angle of the generated far-field THz radiation by varying the relative bias voltage applied to the horizontally and vertically emitting pixels. Finally, Section 4.4 details an experimental setup for the investigation of circular dichroic properties of materials, based on a silicon prism converting the linear polarisation produced by the multi-pixel emitters into left- and right-handed circularly polarised states, which allows for rapid modulation between the two chiralities. Sections 4.2 and 4.3 of this chapter have been published as C.D.W. Mosley *et al.*, *AIP Advances* **9**, 045323 (2019).

## 4.1 Photoconductive Emitter Geometry and Terahertz Polarisation State

Starting with a description of the radiation produced by a small dipole, this section will provide a brief overview of how pulses of THz radiation with complex polarisation states can be created using PCEs with novel geometries.

### 4.1.1 Electric Dipole Radiation from Photoconductive Emitters

The source of THz radiation emitted by PCEs is the transient photocurrent in the device, generated by the time-varying electric dipoles created in the semiconductor as free carriers are photoexcited, accelerated away from each other and then recombined on sub-picosecond timescales. In a PCE these can be approximated as Hertzian dipoles, as the dipole size is much smaller than the wavelength of light generated; a frequency of 1 THz corresponds to a wavelength of  $300\text{ }\mu\text{m}$ , whereas the dipole size in an interdigitated PCE is restricted to a few

$\mu\text{m}$  by the size of the gaps between electrodes. The components of the electric field radiated by such a dipole can be given in spherical coordinates  $r$ ,  $\theta$  and  $\phi$  as

$$E_r = Z_0 \frac{I_0 l \cos(\theta)}{2\pi r^2} \left[ 1 + \frac{1}{ikr} \right] e^{-ikr}, \quad (4.1)$$

$$E_\theta = iZ_0 \frac{kI_0 l \sin(\theta)}{4\pi r} \left[ 1 + \frac{1}{ikr} - \frac{1}{(kr)^2} \right] e^{-ikr}, \quad (4.2)$$

$$E_\phi = 0, \quad (4.3)$$

where  $l$  is the length of the dipole,  $I_0$  is the photocurrent,  $k$  is the wavenumber and  $Z_0 = \sqrt{\mu_0/\epsilon_0}$  is the impedance of free space [131].

Equations 4.1 and 4.2 describe the *near-field* and *far-field* radiation pattern of a small dipole, which has components in both the radial  $\hat{\mathbf{r}}$  and polar  $\hat{\boldsymbol{\theta}}$  directions. If we consider the *far-field* case, where the distance from the dipole is much larger than the wavelength ( $r \gg \lambda$ ), then terms on the order of  $1/r^2$  or greater powers tend to zero and the far-field electric field  $\mathbf{E}_{\text{ff}}$  can be described by

$$\mathbf{E}_{\text{ff}} = i\zeta_0 \frac{kI_0 l \sin(\theta)}{4\pi r} e^{-ikr} \hat{\boldsymbol{\theta}}. \quad (4.4)$$

As such, the electric field generated by a small dipole oscillates only in the polar direction in the far-field regime. A similar expression for the far-field magnetic field  $\mathbf{H}_{\text{ff}}$  can be obtained, with its only component in the azimuthal  $\hat{\boldsymbol{\phi}}$  direction; this demonstrates that a small dipole radiates transverse electromagnetic (TEM) waves, as the electric and magnetic fields are orthogonal to each other and the direction of propagation.

An important concept in the physics of antennas is that of the dipole array. A single dipole generates radiation over a wide range of angles. By positioning a number of dipoles in close proximity, the radiation they produce may be designed to interfere constructively in the far-field; this increases the efficiency and power output of the array compared with a lone dipole, as well as improving the directionality of the generated radiation. Some PCE designs, such as arrays of individual dipole antennas [132, 133] and interdigitated photoconductive emitters [75, 134], utilise this emission geometry to improve the generation efficiency of linearly polarised THz radiation.



#### 4.1.2 Controlling the Terahertz Polarisation State with the Emitter Geometry

The generation of complex polarisation states from PCEs can be performed by utilising emitter geometries that create a pattern of individual dipoles with different orientations, which then interact in the far-field to create the desired polarisation state. Radially polarised THz beams have been generated by circularly-shaped large-gap emitters [127, 128], whilst both radially- and azimuthally-polarised beams have been produced using interdigitated PCEs with suitable electrode geometries [125, 126]. Examples of some of these interdigitated PCE geometries are shown schematically in Figs. 4.1 (a) - 4.1 (f).

A design for PCEs that emit radially-polarised THz pulses is demonstrated in Figs. 4.1 (a) - 4.1 (c). The electrode layout in these devices will cause the photoexcited charge carriers to be accelerated radially outwards or inwards, depending on the polarity of the the bias voltage applied; this causes the orientation of the THz electric field generated by a small segment of the device to vary depending on the position of that segment around the device circumference. After interaction in the far-field, the THz radiated by the device will produce a radially symmetric pulse, with the electric field oriented as demonstrated by the arrows in Fig. 4.1 (c). The time-domain waveforms in Fig. 4.1 (g) demonstrate the radial symmetry of the emission from the device: as a detector sensitive only to horizontally polarised THz radiation is scanned in the  $x$ -direction (orthogonally to the direction of propagation), the THz transient flips in polarity about the beam axis, while showing a similar decrease in strength as the detector is moved in either the positive or negative  $x$ -direction. An analogous design for an interdigitated PCE producing azimuthally polarised THz pulses is shown by Figs. 4.1 (d) - 4.1 (f), with the acceleration of carriers and hence the THz polarisation of a small section of the device this time oriented azimuthally, with a strength depending on the radial position of that particular section. These two device designs, amongst the others reported in the literature, demonstrate the applicability of overlapping the radiation generated by dipoles with different orientations to create a coherent beam with a complex polarisation state in the far-field.

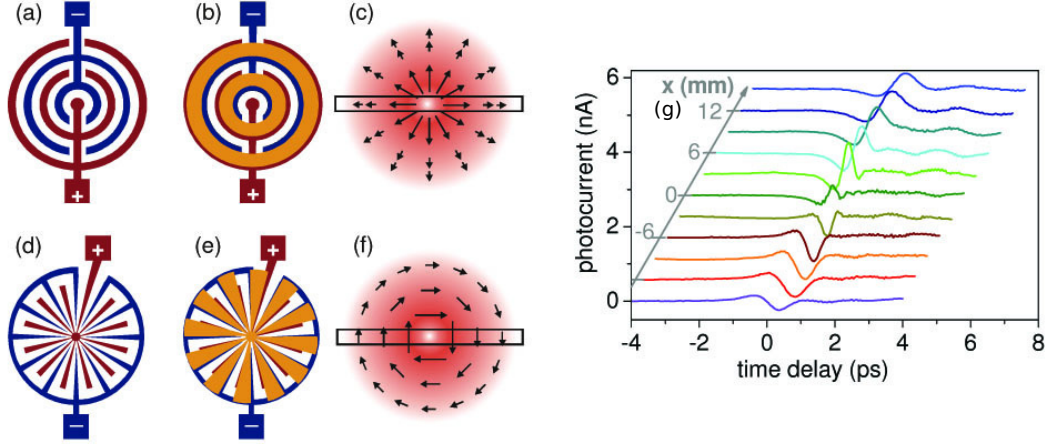


Figure 4.1: Schematic diagram demonstrating the layout of photoconductive emitters for the emission of (a-c) radially and (d-f) azimuthally polarised THz pulses. (a) and (d) represent the electrode geometry, (b) and (e) the device with the masking layer, and (c) and (f) the electric field generated by the device (orientation of the electric field is represented by the arrows). (g) THz time-domain waveforms of the horizontally polarised component of the THz radiation emitted by the radial emitter. Reproduced from reference [125].

The ability to variably control the THz polarisation state has been demonstrated via the rotation of PCEs; previously in the literature by rotating a wide-gap photoconductive emitter to a few fixed angles [104], whilst a rotatable-polarisation THz-TDS system making use of the rotation of an interdigitated PCE to arbitrary angles was reported in Chapter 3 of this thesis. Electrical modulation between two orthogonal polarisation states has also been achieved [129], using the four-contact large area emitter shown in Fig. 4.2 (c). When the entire central area of the device, shown by the zoom-in in Fig. 4.2 (c), is illuminated by femtosecond optical pulses, the THz polarisation state produced by the device can be altered by changing which of the contacts are electrically biased and which are grounded. For example if the quadrants (1) and (2) are electrically biased, whilst (3) and (4) are grounded, the device will produce a THz pulse linearly polarised at  $\psi = +45^\circ$ ; alternatively biasing quadrants (2) and (3) whilst grounding (1) and (4) will produce a THz pulse linearly polarised at  $\psi = -45^\circ$ . The electrical nature of this polarisation switching allows rapid modulation of the THz polarisation state. However, the polarisation state produced by this emitter demonstrated significant deviations from a pure linear state, with an ellipticity of up to  $4.5^\circ$  at 1 THz, which was attributed to asym-

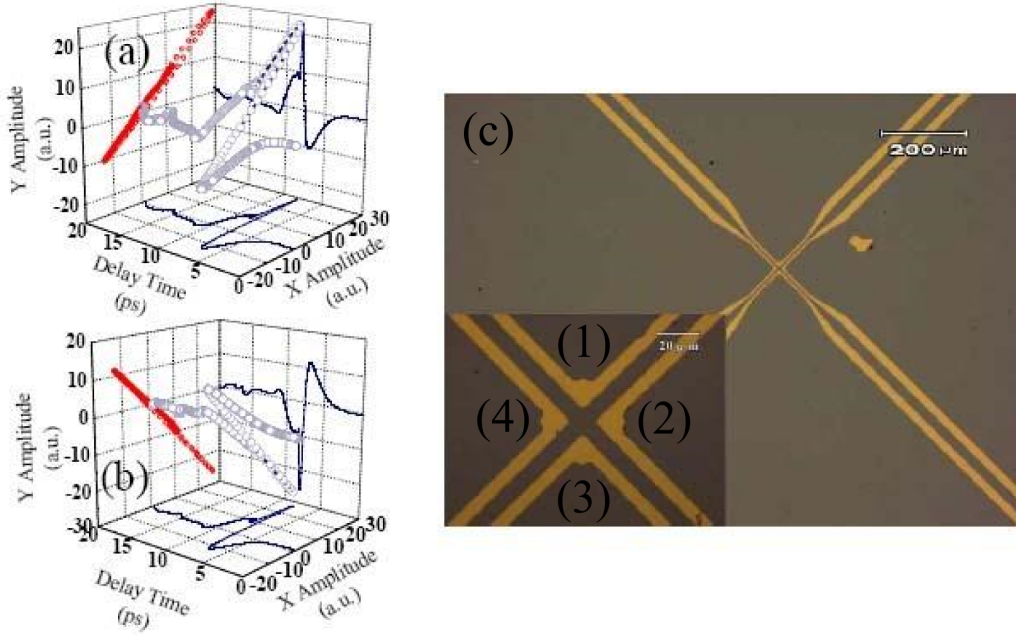


Figure 4.2: Polarisation-resolved time-domain waveforms produced at (a)  $\psi = +45^\circ$  and (b)  $\psi = -45^\circ$  by the four-contact wide-area emitter shown in panel (c). Numbers (1 – 4) label different quadrants of the device. Reproduced from reference [129].

metries in the pump beam profile and in the bias fields generated in the device. The authors of reference [129] also utilise this four-contact PCE to produce and modulate between different-handed circularly polarised THz pulses, which will be discussed in further detail in Section 4.4.

## 4.2 Multi-Pixel Interdigitated Photoconductive Emitters

In this section I will report the design and fabrication of interdigitated photoconductive emitters consisting of separate pixels for the generation of horizontally and vertically polarised THz radiation, making use of a combination of the electrical modulation and overlapping dipole concepts discussed in the previous section. This photoconductive emitter design has the benefit of allowing the direct control of the polarisation angle of the emitted THz beam, without requiring any additional or mechanically moving components, via the applied bias voltage on the pixels.

### 4.2.1 Emitter Concept and Design

In Chapter 3 of this thesis a method of rotating a linear polarisation state to arbitrary angles has been demonstrated, using the mechanical rotation of an interdigitated PCE. The results presented in Section 3.2.4 demonstrate that an interdigitated PCE produces highly linearly polarised THz pulses with an intrinsic ellipticity of less than  $1^\circ$ ; the direction of the bias field applied between the electrodes defines the direction of acceleration of the photoexcited charge carriers, and therefore the polarisation state of the generated THz radiation. Hence the orientation of the interdigitated PCE itself can be used to define the polarisation of the generated THz radiation.

The results presented in Section 3.2.3 highlight improvements that could be made relative to this method of polarisation rotation: it is based upon mechanically rotating components, and additional alignment steps were required in order to optimise the signal-to-noise ratio of the THz emission at all angles. A source of inspiration for an alternative method of polarisation rotation can come from the both the results of Chapter 3, and the concept of sub-wavelength sources interacting in the far-field. An electromagnetic wave with an arbitrary polarisation state can be resolved into two orthogonally polarised components, and the polarisation state produced by an interdigitated PCE can be varied between two orthogonal polarisations by changing its orientation by  $90^\circ$ . By positioning small interdigitated structures with orientations that vary by  $90^\circ$  in close proximity, and photoexciting both orientations with the same pump beam, the resulting polarisation state of the THz in the far-field may be controlled if the emission strength of the orthogonally oriented interdigitated PCEs can be controlled.

The geometry of the multi-pixel interdigitated PCE reported in this thesis is shown schematically in Figs. 4.3 (a) and 4.3 (b). The layout of the device is a  $2 \times 2$  grid of pixels, with the electrodes in each pixel arranged orthogonally to those in the adjacent pixels. The direction of the bias voltage in each gap, and therefore the orientation of the THz polarisation that will be produced by that gap, is demonstrated by the arrows in Fig. 4.3 (b). The pixels producing horizontally polarised radiation share a common set of bias and ground elec-

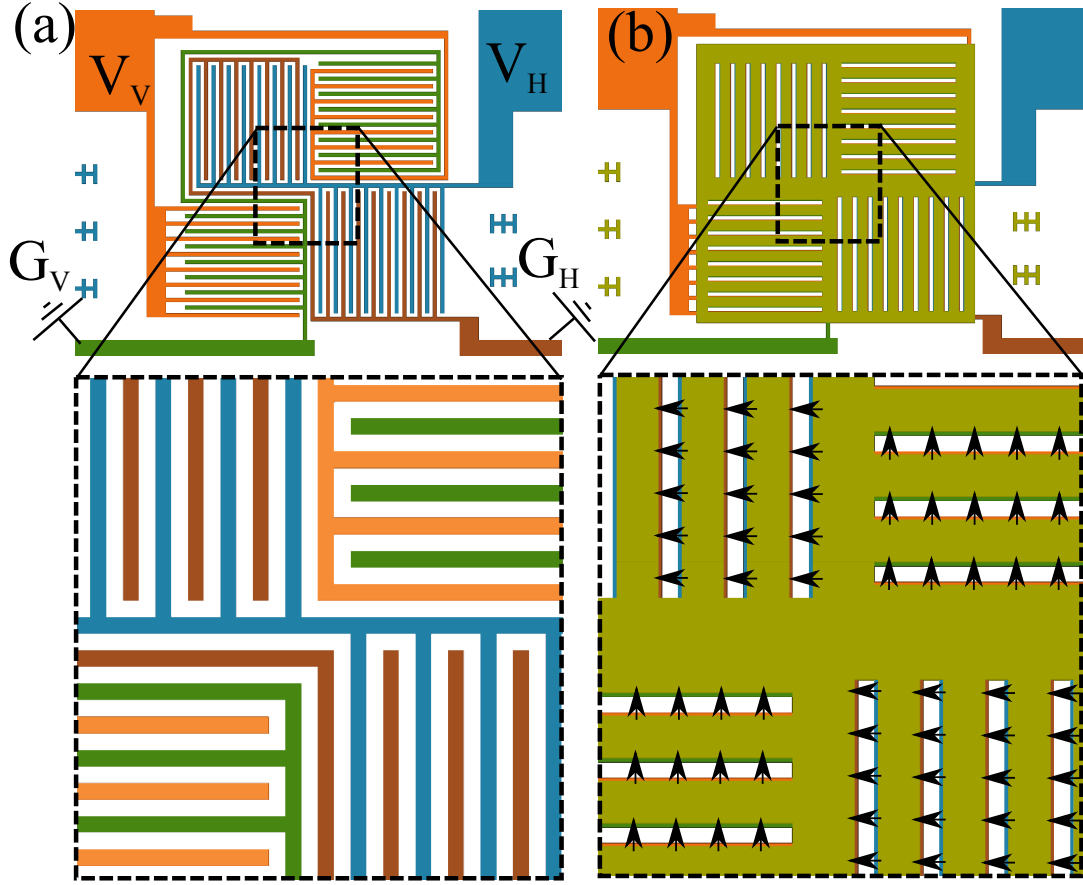


Figure 4.3: Schematic diagram of the multi-pixel interdigitated photoconductive emitter, showing (a) the interdigitated electrodes and (b) the completed device with the masking layer.  $V_H$  ( $G_H$ ) and  $V_V$  ( $G_V$ ) signify the biased (grounded) contacts for horizontally and vertically polarised emission, respectively. The direction of the bias field, and therefore polarisation state of the emitted THz pulse, is demonstrated by the arrows in (b) for emission at a target polarisation angle of  $135^\circ$ .

trodes, indicated in Fig. 4.3 (a) by  $V_H$  and  $G_H$  respectively, as do the vertically emitting pixels ( $V_V$  and  $G_V$  in Fig. 4.3 (a)). Photoexciting the entire active area of the device and varying the relative strengths of  $V_H$  and  $V_V$  will vary the relative strengths of the horizontally and vertically polarised components of the generated THz radiation; hence the orientation of the polarisation state of the far-field THz pulse generated by the device can be defined by simply varying the relative bias voltage on the horizontal and vertical contacts.

#### 4.2.2 Device Fabrication

The multi-pixel interdigitated photoconductive emitter was fabricated by performing UV photolithography, metal evaporation and lift-off processes on a 500  $\mu\text{m}$ -thick semi-insulating GaAs (SI-GaAs) substrate. The bottom layer of the device, shown in Fig. 4.4 (b), consists of an interdigitated pattern of 5  $\mu\text{m}$ -wide electrodes, with a 5  $\mu\text{m}$  gap between adjacent electrodes. Initially a thin layer of AZ5214-E image-reversal photoresist was spin-coated onto the SI-GaAs substrate at 8000 rpm for 35 seconds, which was then pre-baked for 2 minutes at 115 °C. The AZ5214-E resist was chosen as it produces an ideal negative wall profile in the developed photoresist in order to facilitate easier lift-off [135]. The electrode pattern in Fig. 4.3 (a) was transferred to the photoresist from a photomask via exposure to UV light with a fluence of 90 mJ/cm<sup>2</sup>. The exposed resist was baked at 120 °C for 4 minutes, before a second exposure to UV light with a fluence of 250 mJ/cm<sup>2</sup> without the photomask present. The photoresist was then developed in MF-319 developer for 50 s, which removed part of the resist to leave a negative image of the photomask pattern. Electron-beam metal evaporation was then used to deposit an initial 5 nm-thick layer of Ti onto the substrate and photoresist, before depositing a 300 nm-thick layer of Au. The Ti layer was used in order to improve adhesion to the substrate. The bottom layer of the device was finalised by removing the unwanted portions of gold via lift-off of the photoresist in acetone.

The generation of THz radiation from the bare bottom layer of the device would be subject to destructive interference in the far-field, as the bias voltage in adjacent gaps has the opposing polarity, hence the THz pulses produced in adjacent gaps will be  $\pi$  out of phase. To avoid this destructive interference, a 300 nm-thick Au masking layer was deposited on top of the metal electrodes, shown in Fig. 4.4 (d), to block the photoexcitation beam in every other gap. To avoid short circuiting, the electrodes and masking layer were vertically separated by first depositing a 110 nm-thick insulating layer of Al<sub>2</sub>O<sub>3</sub> over the bottom layer electrodes, shown in Fig. 4.4 (c), with such a thickness chosen in order to maximize the transmission of the 800 nm photoexcitation beam. Both the insulating and masking layers were produced by an identical photolithography

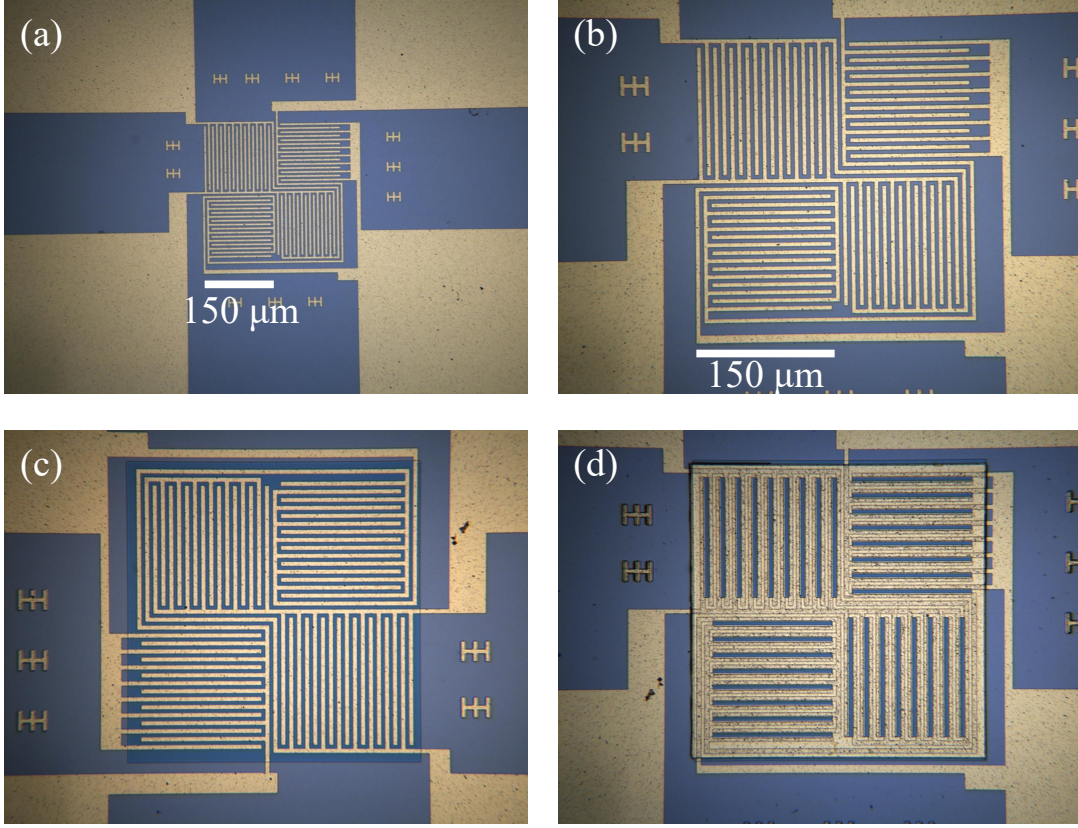


Figure 4.4: Optical microscopy images of the multi-pixel interdigitated photoconductive emitter. The device after the first set of photolithography, metal evaporation and lift-off procedures is displayed in panel (a) including the electrical contacting pads, and a zoomed-in view of the active area only is shown in panel (b). Panel (c) shows the device after the second step, with the active area covered by the insulating layer of  $\text{Al}_2\text{O}_3$ . Panel (d) shows the finished device containing the gold masking layer.

procedure as detailed for the bottom layer. The active area of each pixel is defined by the masking layer, and is  $150\,\mu\text{m} \times 150\,\mu\text{m}$  for these devices. The photomask for the bottom layer also contained four  $2\,\text{mm} \times 2\,\text{mm}$  gold pads, of which only a small portion can be seen in Fig. 4.4 (a), to facilitate easy contact with the voltage source and ground. One gold pad is connected to each set of gold electrodes, signified by the different colours in Fig. 4.3. This fabrication method is scalable to larger or smaller pixel sizes, or to a higher number of pixels, simply by using alternative UV photolithography masks.



### 4.2.3 Simulated Device Performance

To explore the expected far-field performance of the device, the radiation pattern of an array of dipoles arranged with the same spatial distribution as the active semiconductor area of the device was calculated. All calculations presented in this section were performed by Arturo Hernandez Serrano. Small dipoles of length  $l = 5 \mu\text{m}$  were placed at  $5 \mu\text{m}$  intervals along each active finger, as indicated in Fig. 4.5 (a) by the small arrows. For an individual dipole, the electric field vector can be calculated analytically at an arbitrary location using Equations 4.1, 4.2 and 4.4. After performing a coordinate transform from spherical coordinates to cartesian coordinates, the total THz electric field amplitude

$$E(x, y, z) = \sum_n \sqrt{E_{x,n}^2 + E_{y,n}^2} \quad (4.5)$$

was then calculated at each position  $x, y$  (in an image plane a distance  $z$  from the emitter) by summing over the array of small dipoles, each with index  $n$ . Each dipole was assumed to have the same strength, corresponding to uniform excitation of the emitter.

Here, calculations are presented for two frequencies representative of the broadband spectrum produced by a typical photoconductive emitter, which peaks around 1 THz. In Fig. 4.5 (b)  $E(x, y)$  is shown at 300 GHz at a distance  $z = 50 \text{ mm}$  away from the device, for the case of vertical emission only (as indicated by the inset). This  $z$  position corresponds to the effective focal length of the first (collimating) off-axis parabolic mirror in the experiment. The radiation pattern in the far-field has Gaussian cross-sections in  $x$  and  $y$  (white lines), is close to circular, and becomes more circular when both horizontal and vertical pixels are excited (panel (c)). In contrast, in panel (d) the near-field  $E(x, y, z = 5 \mu\text{m})$  at 3 THz and for vertical emission is shown, where each photoexcited dipole line can be seen. As the radiation evolves into the far-field, the individual lines are no longer visible, and the radiation pattern becomes more beam-like for vertical (panel (e)) and combined (panel (f)) emission, with a beam width below 40 mm at  $z = 50 \text{ mm}$ . However as the divergence of a higher frequency beam is lower, the beam profiles at 3 THz are more non-uniform than at 300 GHz, and exhibit some destructive interference. Further calculations may



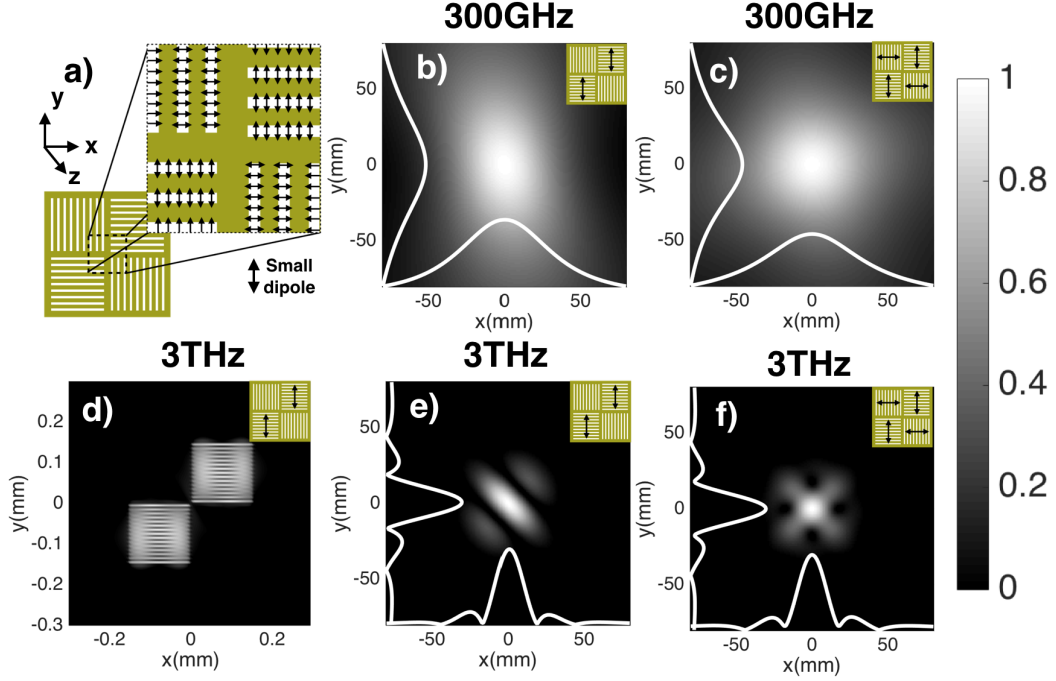


Figure 4.5: Calculated radiation patterns in the  $x - y$  plane for the multi-pixel interdigitated emitter. **(a)** Diagram of the simulation geometry. **(b)** Far-field ( $z = 50$  mm) THz electric field amplitude  $E$  at 300 GHz when only the vertically-emitting pixels on. **(c)** As **(b)**, but with both vertical and horizontal pixels on. **(d)** Near-field  $E$  at 3 THz with only the vertical pixels on ( $z = 5$   $\mu\text{m}$ ). **(e)** Far-field ( $z = 50$  mm)  $E$  at 3 THz with vertically-emitting pixels on. **(f)** As **(e)**, with both vertical and horizontal pixels on.

suggest design improvements to mitigate against these effects, for instance using a smaller pixel size.

### 4.3 Experimental Device Performance

The performance of the fabricated device was investigated using terahertz time-domain spectroscopy, by using the multi-pixel photoconductive emitter as the THz generation source in the spectrometer described in Section 2.3. The emitter was photoexcited by optical pulses with a peak wavelength of 800 nm with an average optical power of 350 mW at the emitter. The photoexcitation beam was found to have a full-width at half-maximum (FWHM) spot size of 320  $\mu\text{m}$  by a knife-edge measurement, resulting in photoexcitation of the entire 300  $\mu\text{m} \times 300 \mu\text{m}$  active area of the device. The electrical contacts produced by

photolithography were connected to the voltage source and ground as displayed in Fig. 4.3. The bias voltages applied to the horizontal and vertical contacts were varied independently from zero to a maximum voltage of  $\pm 10$  V, with the voltage source modulated at a frequency of 50 kHz.

The generated THz pulses were detected via polarisation-resolved electro-optic sampling [85, 89] in a  $200\text{ }\mu\text{m}$ -thick,  $[111]$ -surface normal GaP crystal. Measurements were performed under a dry nitrogen purge, in order to avoid atmospheric absorption of the THz radiation. The polarisation state of the generated THz pulses was parameterised by their ellipticity,  $\chi$ , and orientation angle,  $\psi$ , which were obtained from the experimental data by the method described previously in Section 2.4.2. As described previously in Section 3.2.2, the orientation angle is the relative angle between the polarisation state and the  $x$ -axis of the lab reference frame, which is defined by the  $[\bar{2}11]$  axis of the detection crystal using an identical calibration procedure to the one described in Section 3.2.2.

#### 4.3.1 Initial Electrical Biasing Tests

To initially verify that the pixel emitter works as intended, three cases of emitter bias were tested: biasing the horizontally emitting pixels only, to produce a THz pulse with a target polarisation angle  $\psi_T = 0^\circ$ ; applying the same bias voltage to both sets of pixels, for  $\psi_T = 45^\circ$ ; and biasing the vertically emitting pixels only, for  $\psi_T = 90^\circ$ . Polarisation-resolved time-domain traces are shown in Fig. 4.6 (a) - 4.6 (c), respectively. In each case, the emitter produced linearly polarised pulses of THz radiation, and the polarisation state of the pulses was rotated as intended by changing the bias voltage applied to the device.

The corresponding Fourier transform spectra of the time-domain traces are shown in Fig. 4.6(d). In each of the three cases, the generated THz pulses demonstrate broadband frequency components from  $0.3 - 5.0$  THz. To quantify the polarisation state of the generated THz pulses, their frequency-dependent ellipticity and orientation angle were extracted from the spectra using Equations 2.18 - 2.21, and are shown in Figs. 4.6 (e) and 4.6 (f) respectively. In the  $0^\circ$  and  $90^\circ$  cases, the orientation angle of the pulses remains close to the target values (represented by the dashed lines) and the ellipticity remains less than

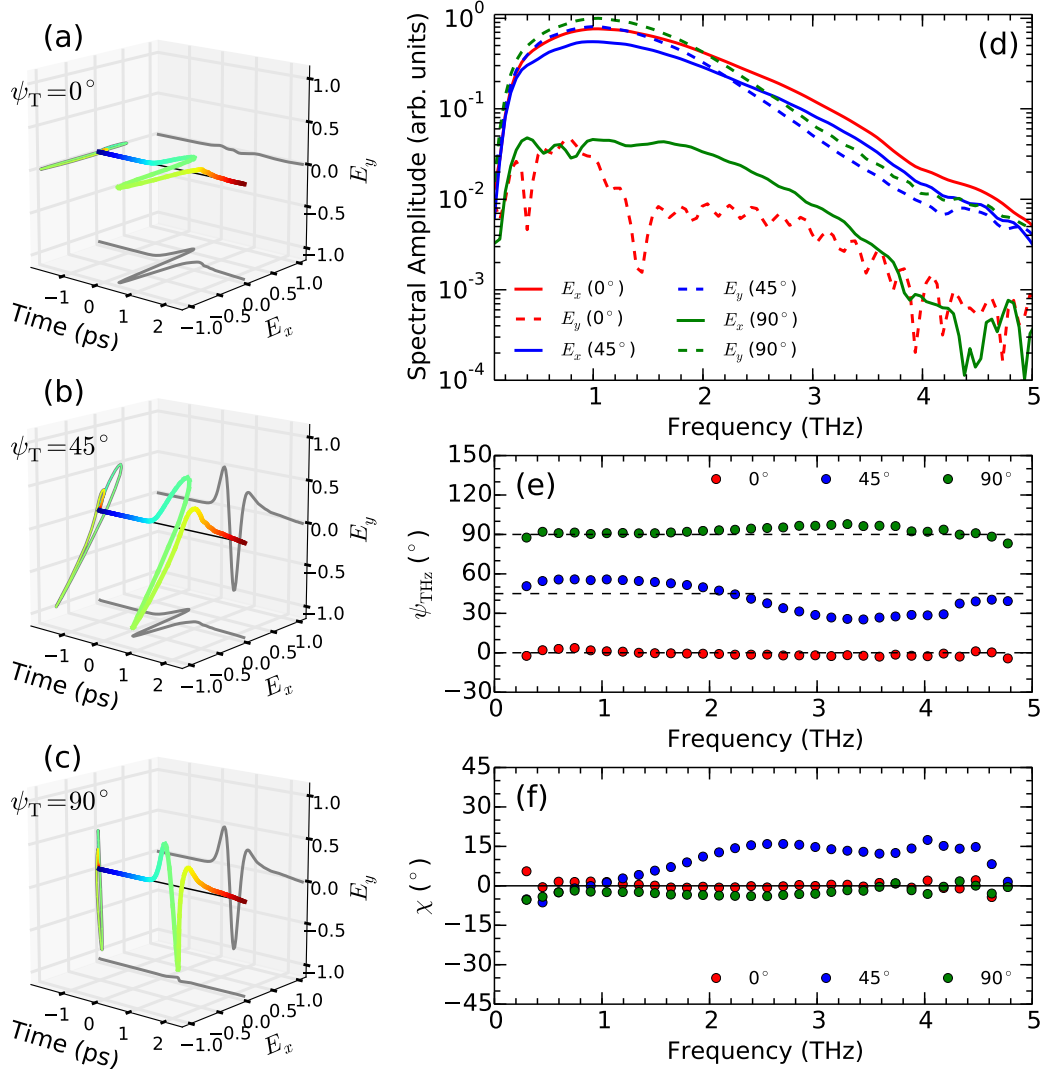


Figure 4.6: polarisation-resolved time-domain traces for THz pulses emitted from the multi-pixel interdigitated photoconductive emitter at target polarisation angles of (a)  $\psi_T = 0^\circ$ , (b)  $\psi_T = 45^\circ$  and (c)  $\psi_T = 90^\circ$ . (d) The corresponding Fourier transform spectra of each component to the time-domain traces in (a)-(c). (e) and (f) show the orientation angle and ellipticity, respectively, at each target angle.

4° between 0.6 - 4.5 THz, demonstrating that the generated pulses are linearly polarised over the entire broadband frequency range. In the 45° case, there is more variation in both the ellipticity and the orientation angle, particularly at higher frequencies, however the polarisation state has clearly been rotated in between the 0° and 90° cases.

The peak THz electric field strength obtained from electro-optic sampling was  $3.4 \text{ kVm}^{-1}$ , using Equation 2.5. This is in agreement with the average power of  $1 \mu\text{W}$  measured by a calibrated pyroelectric detector. Comparable emission strengths were obtained from reference devices with one large pixel, which have the same layout as the device used in Section 3.2.1. This demonstrates that these multi-pixel devices have a comparable efficiency to the standard interdigitated PCE design, which suggests they do not suffer from any significant destructive interference of the radiation emitted from separate pixels.

#### 4.3.2 Generating Arbitrary Linear polarisation States Via Electrical Control

Having proved the principle of rotating the polarisation state of the emitted THz pulses by varying the relative bias voltage applied to each set of contacts, the characteristics of the emitted THz radiation were investigated as the orientation angle of the polarisation state was varied over a 360° range. In order to rotate the polarisation state, the bias voltages applied to the horizontally and vertically emitting pixels were varied according to

$$V_H = V_{\max} \cos(\psi_T), \quad (4.6)$$

$$V_V = V_{\max} \sin(\psi_T), \quad (4.7)$$

where  $V_{\max} = 10 \text{ V}$  and  $\psi_T$  is the target orientation angle. The bias voltages applied to produce each  $\psi_T$  are shown in the inset of Fig. 4.7 (a). The target polarisation angle was varied in 22.5° steps and polarisation-resolved time-domain traces taken at each step.

The maximum amplitude,  $E_{\max} = \sqrt{E_x^2 + E_y^2}$ , at the time-domain peak of the THz pulse at each target angle is reported in Fig. 4.7 (a), normalised to the mean value. The variation in amplitude is less than  $\pm 15\%$  over the

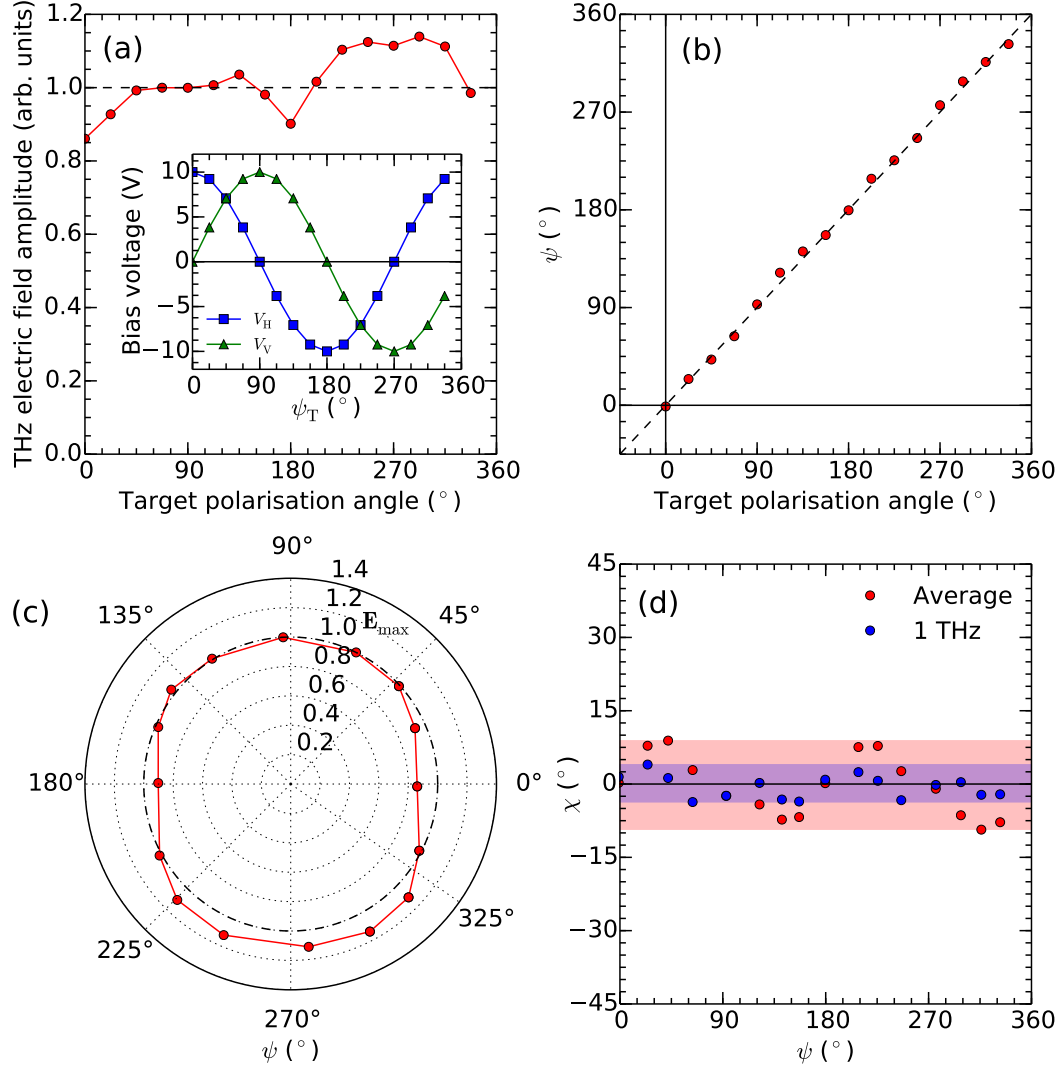


Figure 4.7: **(a)** Maximum THz electric field amplitude, normalised to the mean value, as the polarisation angle is varied over a 360° range by changing the relative bias voltages between horizontal and vertical pixels. The inset shows the bias voltage applied for each target polarisation angle. **(b)** Comparison of the experimentally measured orientation angle to the target angle at each step. The dashed line represents an exact match between the two. **(c)** Polar representation of the orientation angle and amplitude of the THz pulses at each step. **(d)** Ellipticities of the generated THz radiation at each orientation angle, at 1 THz (blue) and averaged from 0.3-5.0 THz (red). The shaded areas represent the variation over the 360° rotation.

360° range, demonstrating that the device maintains a fairly consistent THz emission strength at all angles. Fig. 4.7 (b) shows the orientation angle of the emitted THz pulses, averaged over their 0.3 – 5.0 THz bandwidth, versus the target orientation angle. The measured orientation angle remains close to the target angle for all points, with the ideal case represented by the dashed line, demonstrating that the orientation angle of the emitted radiation can be reliably varied by changing the relative bias voltage on the horizontally and vertically emitting pixels.

The combined data from Figs. 4.7 (a) and 4.7 (b) are presented in Fig. 4.7 (c). The THz amplitude is observed to be larger for vertical emission than for horizontal emission, and also to increase when the bias voltage applied to the contacts is negative rather than positive. The increase in THz emission strength when negatively biasing the contacts occurs due to the well-known effect in photoconductive antennas whereby exciting the device closer to the anode increases the THz emission strength [136, 137, 138]. In the case of negative bias on the multi-pixel emitter, excitation over the entire device acts as being close to the anode, producing more efficient THz emission than with a positive bias. The difference in response between the horizontal and vertical emission may occur due to the polarisation of the pump pulse relative to the geometry of the pixels; it has been previously shown that orienting the polarisation state of the pump pulse parallel to the wires of an interdigitated photoconductive emitter increases the THz emission strength [130]. In the setup used in this work, the polarisation of the pump was parallel to the wires in the vertically emitting pixels, enhancing their emission strength relative to the horizontally emitting pixels. The amplitude of the THz pulses emitted by the device presented here may therefore be made more uniform during rotation of the polarisation state by: using a half-wave plate to rotate the polarisation of the pump pulses to 45°, to ensure a similar response from both sets of pixels; and by using only negative bias voltages and swapping the biased and grounded contacts to change the polarity of the generated THz pulses.

The ellipticities of the generated THz radiation at each orientation angle are reported in Fig. 4.7 (d). The red points represent the ellipticity averaged over the 0.3 – 5.0 THz bandwidth of the pulses, whilst the blue points show the

ellipticity at 1 THz. At 1 THz, the ellipticity remains small at all angles, varying less than  $4^\circ$  over the full  $360^\circ$  rotation. When the higher frequency components are taken into account, the variation in ellipticity becomes larger, particularly when the polarisation state is between a purely horizontal or vertical state. One reason for the increase in ellipticity at these angles may be due to the different response of the pixels due to their geometry relative to the polarisation of the pump pulse. The grating created by the interdigitated wires of the emitter has a different reflectivity for an s- or p-polarised pump beam, and hence different pump beam powers are coupled to the photoconductor, giving a different carrier density in each set of pixels. Such an effect may be observed in Fig. 4.6 (d), where the horizontal and vertical components of the electric field in the  $\psi_T = 45^\circ$  case have slightly different spectral shapes, as a result of small differences in the time-domain waveforms for the two components. Another reason for the larger variation at higher frequencies may be due to the higher frequencies having a smaller beam divergence, and as such creating a slightly asymmetrical beam profile in the far-field if the high frequency components generated from each pixel do not overlap fully; an example of this is demonstrated by the simulations of the expected radiation pattern at 3 THz in Figs. 4.5 (e) and 4.5 (f). One possible solution would be to use a smaller pixel size, which would position the pixels closer together and increase the overlap of the high frequency components in the far-field.

#### 4.4 Rapid Modulation of Circular Polarisation States for Circular Dichroic Spectroscopy

Following from the method used to convert linear THz polarisation states into circular THz polarisation states by Hirota *et al.* in reference [129], this section will outline a similar setup making use of the multi-pixel PCEs reported earlier in this chapter. As will be shown, the advantage of the multi-pixel PCE in such a setup is the ability to arbitrarily change the polarisation angle of the linear THz pulse, allowing optimisation of the circular THz polarisation state.

#### 4.4.1 Converting from Linear to Circular Polarisation via a Prism

The use of a prism as a waveplate is based upon the phase delay introduced between the s- and p-polarised components by total internal reflection at the rear internal surface. The Fresnel reflection coefficients for a linear, homogeneous and isotropic medium for the p-component  $r_p$  and s-component  $r_s$  of an electromagnetic wave are given by

$$r_s = \frac{n_1 \cos(\theta_i) - n_2 \cos(\theta_t)}{n_1 \cos(\theta_i) + n_2 \cos(\theta_t)}, \quad (4.8)$$

$$r_p = \frac{n_2 \cos(\theta_i) - n_1 \cos(\theta_t)}{n_2 \cos(\theta_i) + n_1 \cos(\theta_t)}, \quad (4.9)$$

where  $n_1$  and  $n_2$  are the refractive indices of the media before and after the interface, and  $\theta_i$  and  $\theta_t$  are the angles of the incident and transmitted waves, respectively. In the case of total internal reflection, the angle  $\theta_t$  does not have a conventional definition, however we can represent it as a complex number. Using a trigonometric identity and Snell's law,  $n_1 \sin(\theta_i) = n_2 \sin(\theta_t)$ , we can express

$$\cos(\theta_t) = \sqrt{1 - \sin^2(\theta_t)} = \sqrt{1 - \left(\frac{n_1}{n_2}\right)^2 \sin^2(\theta_i)}. \quad (4.10)$$

For angles greater than the critical angle for total internal reflection the value under the square root becomes negative, and

$$\cos(\theta_t) = \pm i \sqrt{\left(\frac{n_1}{n_2}\right)^2 \sin^2(\theta_i) - 1}. \quad (4.11)$$

Substituting Equation 4.11 into Equations 4.8 and 4.9, and defining the *relative refractive index* between the internal and external media at the interface as  $n_r = n_1/n_2$ , gives

$$r_s = \frac{n_r \cos(\theta_i) - i \sqrt{n_r^2 \sin^2(\theta_i) - 1}}{n_r \cos(\theta_i) + i \sqrt{n_r^2 \sin^2(\theta_i) - 1}}, \quad (4.12)$$

$$r_p = \frac{\cos(\theta_i) - i n_r \sqrt{n_r^2 \sin^2(\theta_i) - 1}}{\cos(\theta_i) + i n_r \sqrt{n_r^2 \sin^2(\theta_i) - 1}}. \quad (4.13)$$

The argument of these two complex numbers allows us to define the *phase*



*advance*  $\delta_{s,p}$  of the two components upon reflection as

$$\delta_s = 2 \tan^{-1} \left( \frac{\sqrt{n_r^2 \sin^2(\theta_i) - 1}}{n_r \cos(\theta_i)} \right), \quad (4.14)$$

$$\delta_p = 2 \tan^{-1} \left( \frac{n_r \sqrt{n_r^2 \sin^2(\theta_i) - 1}}{\cos(\theta_i)} \right). \quad (4.15)$$

This allows us to determine the total phase delay between the s- and p-components as  $\delta = \delta_p - \delta_s$ . Thus the choice of material the prism is made from, hence the refractive index, and the angle of incidence can be chosen such that  $\delta = \pi/2$ ; this will cause a linearly polarised plane wave at  $45^\circ$  (e.g. it has equal s- and p-components) to become circularly polarised after reflection inside the prism.

#### 4.4.2 Stokes Parameters

Previously in this thesis, the polarisation state of light has been described using the polarisation ellipse and the values  $\chi$  and  $\psi$ , which provides us with an instantaneous description of the polarisation state at a given frequency. In this section, we are simply interested in the purity of the circularly right- and left-hand polarised components produced by the prism waveplate; as such, the Stokes parameter  $V$  provides us with a more convenient measure of the purity of circular polarisation states. The components of  $\mathbf{S}_T$  can be related to the experimentally observed  $x$  and  $y$  components of the THz intensity obtained from polarisation-resolved electro-optic sampling by

$$\begin{bmatrix} I \\ Q \\ U \\ V \end{bmatrix} = \begin{bmatrix} |E_x|^2 + |E_y|^2 \\ |E_x|^2 - |E_y|^2 \\ 2\text{Re}[E_x E_y^*] \\ -2\text{Im}[E_x E_y^*] \end{bmatrix}, \quad (4.16)$$

or in the circular basis defined by  $\tilde{E}_\pm = |\tilde{E}_\pm| \exp(i\phi_\pm) = (\tilde{E}_x \pm i\tilde{E}_y)/\sqrt{2}$  as

$$\begin{bmatrix} I \\ Q \\ U \\ V \end{bmatrix} = \begin{bmatrix} |E_+|^2 + |E_-|^2 \\ 2\text{Re}[E_+ E_-^*] \\ -2\text{Im}[E_+ E_-^*] \\ |E_+|^2 - |E_-|^2 \end{bmatrix}. \quad (4.17)$$

After normalisation by the total intensity  $I$ , when  $V/I = \pm 1$  the polarisation state is either purely right- or left-handed circular, whilst for  $V = 0$  there is an equal amount of both chiralities present and the polarisation state is linear. There is some ambiguity in the sign of  $V$ , as for a right-handed circularly polarised beam  $V/I$  may be  $+1$  or  $-1$  depending on whether the handedness is defined by viewing the beam against or with the direction of propagation, respectively. For the results presented in this section, we will define the polarisation state by observing *against* the direction of propagation, such that for a right-handed circular polarisation  $V/I = +1$ .

#### 4.4.3 Experimental Setup

Silicon has a very low dispersion at THz frequencies [139], and as such is an appropriate choice of material for creating an achromatic quarter-wave plate in the THz range via the mechanism described in Section 4.4.1. Using a refractive index  $n = 3.425$  for silicon and Equations 4.14 and 4.15, the phase advances and total phase delay between the s- and p-polarised components of the THz pulses after total internal reflection at the rear face of a silicon prism can be calculated as a function of  $\theta_i$ , and are shown in Fig. 4.8 (a). A phase delay of  $\delta = \pi/2$  was observed for an incidence angle  $\theta_i = 41.9^\circ$ . This sets the dimensions of the prism in order to achieve optimal performance as a quarter-wave plate; a high-resistivity floating-zone grown silicon prism cut with two angles of  $41.9^\circ$  and one of  $96.2^\circ$  was used in this setup, in order to achieve an optimal  $\theta_i$  for light travelling through the entrance face at normal incidence onto the rear face of the prism.

A schematic diagram of the setup used to produce and measure the circularly polarised THz pulses is shown in Fig. 4.8 (b). Conversion from a linear polarisation state to a circular polarisation state was achieved by mounting a multi-pixel interdigitated PCE directly onto the entrance face of the silicon prism. The multi-pixel interdigitated PCE was mounted at an angle of  $45^\circ$  relative to the entrance face of the prism, which permits linearly polarised THz pulses with orientation angles of  $\pm 45^\circ$  to be generated by biasing only the horizontally or only the vertically emitting pixels, respectively. As with previous results presented in this chapter, the voltage was varied independently from

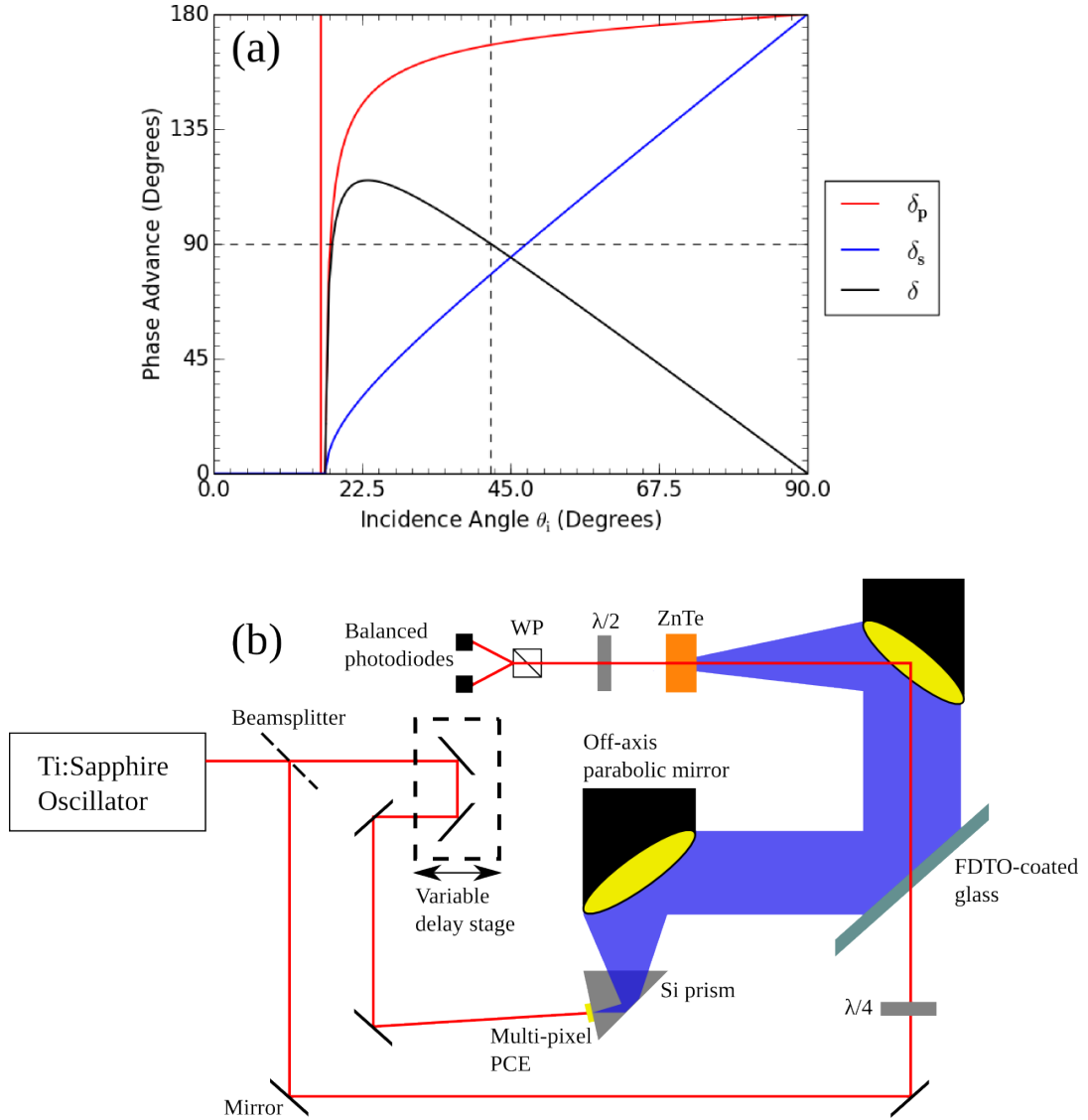


Figure 4.8: **(a)** Phase advances  $\delta_s$  and  $\delta_p$  of s- and p-polarised light, respectively, along with the phase shift between the s and p components  $\delta$ , upon reflection inside a silicon prism as a function of incidence angle  $\theta_i$ . The refractive index of the silicon is taken to be  $n = 3.425$ . **(b)** Schematic diagram of the THz-TDS setup used to convert linearly polarised THz pulses produced by the multi-pixel PCE into circularly polarised pulses, and then detect them in a polarisation-resolved manner.

zero to a maximum voltage of  $\pm 10$  V, with the voltage source modulated at a frequency of 50 kHz. After transmission through the prism, the THz pulses were collimated by a  $f = 50.8$  mm off-axis parabolic gold mirror, before being reflected by a fluorine-doped tin oxide (FDTO)-coated-glass THz mirror and focused onto a  $500\text{ }\mu\text{m}$ -thick,  $\langle 111 \rangle$ -surface normal ZnTe detection crystal by a second  $f = 50.8$  mm off-axis parabolic gold mirror. The FDTO-coated glass has a high reflectivity at THz frequencies but is transparent in the visible range, allowing the gate and THz beams to be coupled together for EOS.

#### 4.4.4 Experimental Results

Upon measuring some initial polarisation-resolved time-domain waveforms, it was clear that biasing the horizontally emitting or vertically emitting pixels only did not produce fully circularly polarised pulses as intended, due to the device being misaligned from  $45^\circ$  when it was mounted onto the prism. However the design and operation of the multi-pixel devices allows for easy rectification of any device misalignment; a small bias voltage can be applied to the orthogonally emitting pixels to correct for any error in the original orientation angle. To find the optimal voltages to produce circularly polarised THz pulses, the bias voltages on the two contacts were varied according to Equations 4.6 and 4.7. This calibration procedure identified an  $8^\circ$  misalignment of the device from its intended  $45^\circ$  orientation. The optimal voltages were found to be  $V_H = 9.903$  V and  $V_V = 1.392$  V to produce a right-hand circularly polarised THz pulse, corresponding to a linear THz pulse being emitted at an angle relative to the orientation of the emitter of  $\psi_R = 8^\circ$ , and  $V_H = -1.392$  V and  $V_V = 9.903$  V to produce a left-hand circularly polarised THz pulse, corresponding to a relative emission angle of  $\psi_R = 98^\circ$ .

The resulting optimised right-hand circularly polarised and left-hand circularly polarised THz pulses are presented in Figs. 4.9 (a) and 4.9 (b), respectively. The purity of the circular polarisation states were analysed using the Stokes parameter  $V$  normalised by the total intensity  $I$ , as described in Section 4.4.2. Fig. 4.9 (c) shows  $V/I$  for both circular THz pulses in Figs. 4.9 (a) and 4.9 (b) over the experimental bandwidth of  $0.3 - 2.5$  THz. Bandwidth was limited in this setup due to transmission losses on entering and exiting the

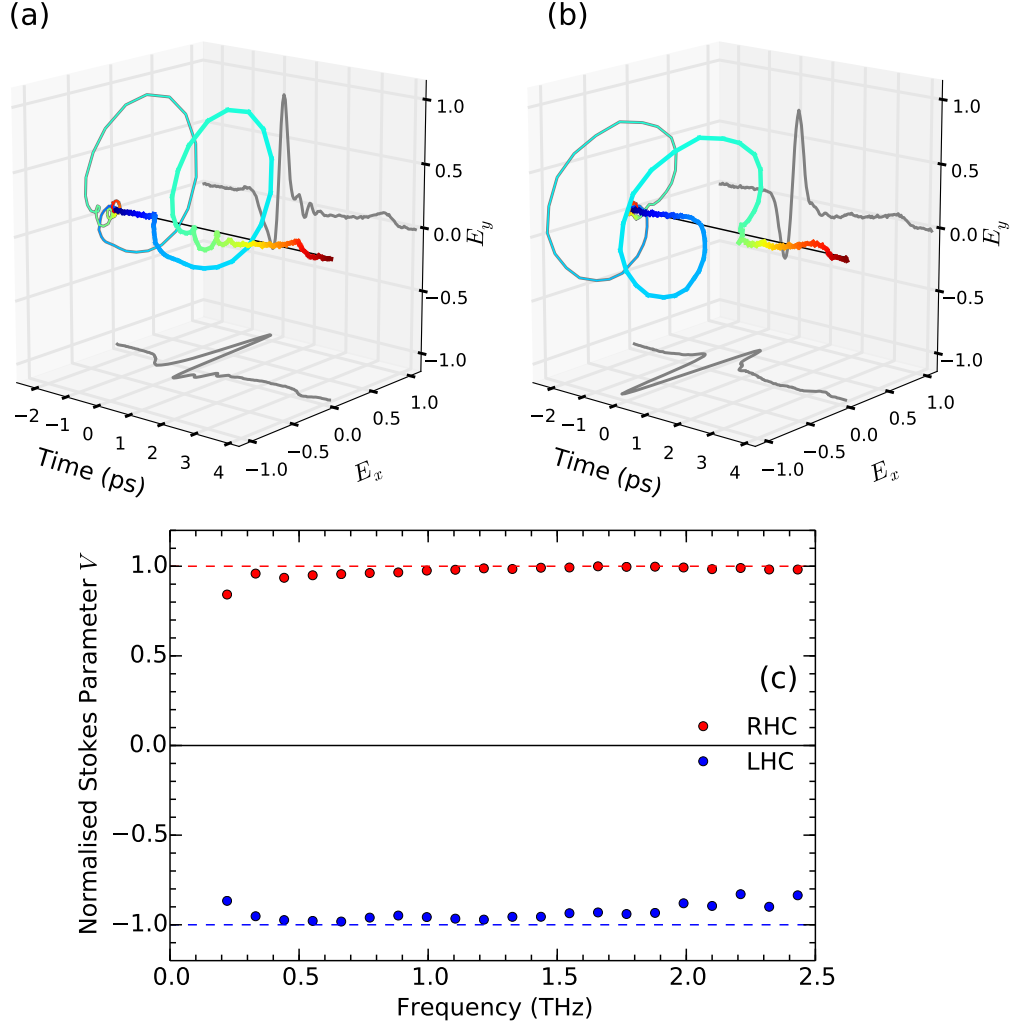


Figure 4.9: Polarisation-resolved time-domain traces for THz pulses emitted from the multi-pixel interdigitated photoconductive emitter mounted on a Si prism, in order to generate (a) right-hand circularly polarised pulses ( $\psi_R = 8^\circ$ ) and (b) left-hand circularly polarised pulses ( $\psi_R = 98^\circ$ ). (c) Frequency-dependent Stokes parameter  $V$  for the right- and left-hand circularly polarised pulses, normalised by the Stokes parameter  $I$  of each pulse.

silicon prism. For both chiralities,  $V/I$  remains close to the target values of  $\pm 1$ , demonstrating the purity of the circular states created by this method. Small deviations away from  $V/I = \pm 1$  at different frequencies may occur because of the different divergence at different frequencies giving a small frequency dependence to  $\theta_i$ ; this could be avoided by collimating the THz emission from the device before the prism. As in the linear emitting case presented in Section 4.3 the purely electrical nature of the polarisation state switching allows rapid modulation between the two states, which will permit fast broadband circular dichroism spectroscopic measurements to be performed at THz frequencies using these multi-pixel devices.

## 4.5 Summary

To summarise, a novel photoconductive emitter geometry for broadband THz polarisation rotation, consisting of separate interdigitated pixels for emission of horizontal and vertical polarisation states, has been proposed and tested. The generated orientation angle of the THz pulse was shown to be controllable by varying the relative bias voltages applied to the horizontally and vertically emitting contacts, and remained close to the target values over a  $360^\circ$  rotation of the polarisation state. Simulations of the emitted radiation pattern showed that in the far-field beams from the individual pixels have overlapped, and demonstrated that the calculated gaussian beam quality of the emitter is higher at lower frequency. The wide bandwidth (0.3 – 5.0 THz), scalable design, and simple polarisation rotation method (varying the applied bias voltage to each contact) make this emitter geometry an attractive concept for applications in spectroscopy and imaging systems, in which the THz polarisation state may be rotated arbitrarily without resorting to any physically moving parts. Since the polarisation angle of the THz radiation generated by this device depends only upon the applied bias voltages, the THz polarisation can be modulated at speeds much faster than systems relying on mechanically rotating components, such as polarizers, which are limited to low frequencies (e.g. 15 Hz) [140]. In addition, an experimental scheme for converting the linear pulses produced by the multi-pixel devices into circular polarisation states was presented, which

would allow rapid spectroscopic measurements of circular dichroic properties of materials at THz frequencies due to the fast electrical polarisation modulation capabilities of the multi-pixel devices.

In future work, a combination of simulation and experiment may allow the device layout to be further optimised, by possibly reducing the pixel size and scaling up to a higher number of pixels. This optimisation may allow the next generation of devices to produce more uniform Gaussian beams, and to reduce the ellipticity of the THz pulses, at high frequencies. The general concept of pixel-based photoconductive devices also has further applications in polarisation-resolved THz detection, for spectroscopy, imaging and THz beam profiling. Detection using a device with the same layout as the one presented in this chapter would allow the simultaneous measurement of two orthogonal components of THz radiation. A similar device consisting of a large number of smaller pixels may allow the spatial extent of a THz beam to be determined simultaneously in a polarisation-resolved manner.

## Chapter 5

# Tracking Disorder Broadening and Hysteresis in First-Order Phase Transitions via the Electromagnon Response in Improper Ferroelectrics

In this chapter, THz-TDS is used to examine the behaviour of electromagnons in  $\text{Cu}_{1-x}\text{Zn}_x\text{O}$  ( $x = 0, 0.05$ ) alloys during the AF1-AF2 phase transition. I demonstrate that the strength of the electromagnon can be used as a sensitive probe of the magnetic state of the material during the phase transition, and can be used to confirm the first-order nature of this phase transition via the observation of thermal hysteresis in the electromagnon strength.

The chapter begins with some background on first-order phase transitions, and the effects of disorder upon them, in Section 5.1. Section 5.2 describes the effect of Zn-alloying on the multiferroic phase and electromagnons in  $\text{Cu}_{1-x}\text{Zn}_x\text{O}$  ( $x = 0, 0.05$ ) alloys, in terms of the spin-disorder introduced by the non-magnetic zinc ions. The behaviour of the electromagnons during the AF1-AF2 phase transition is reported in Section 5.3. The electromagnon response is then used to probe broadening of the AF1-AF2 phase transition due to spin-disorder in Section 5.4, before finally being utilised to confirm the first-



order nature of this phase transition via the observation of thermal hysteresis in the electromagnon response in Section 5.5. All sections of this chapter have been published as C. D. W. Mosley *et al.*, *Journal of Physics D: Applied Physics* **51**, 084002 (2018).

## 5.1 First-Order Phase Transitions and Disorder Broadening

The change in magnetic or lattice structure at a first-order phase transition is associated with many functional properties that emerge in the ordered phases [141, 142]. First-order phase transitions are characterized by a latent heat, due to a difference in entropy between the two phases requiring the system to absorb a fixed amount of energy in order for the transition to occur. This leads to phase coexistence, where some parts of the material have undergone the transition and others have not. Experimentally, a phase transition can be classified as first-order by the observation of a discontinuous change in the order parameter and a latent heat, phase coexistence, or hysteresis with respect to a control variable (such as temperature or external magnetic field). It is not necessary to observe hysteresis in the order parameter, as many experimental observables can be hysteretic over a first-order phase transition, exemplified by the observation of hysteresis in magneto-optical properties during the melting of a superconducting vortex-solid [143].

Ideally when investigating a phase transition in a multiferroic material, such as the AF1-AF2 transition in CuO, one should look for changes in an experimental observable that is uniquely linked to the multiferroic state (e.g. the ferroelectric polarization), rather than observables that only change marginally across the transition (e.g. ultrasound velocity, magnetization). The pyroelectric current method is commonly used to study the polarization of magnetically-induced ferroelectrics: a large electric field is applied while in the multiferroic state, which is then removed and the pyroelectric current on cooling or heating through the ferroelectric/paraelectric phase transition is recorded and integrated to yield the polarization. This method often only measures the polarization as the temperature is swept out of the multiferroic state, and it is therefore

challenging to study phenomena such as thermal hysteresis.

### 5.1.1 Landau Theory of First-Order Phase Transitions

Here we consider a simple phenomenological description of the free energy with reference to Landau theory for a first-order phase transition, in order to describe the observed hysteretic behaviour. Advanced treatments more suitable for multiferroics have been reported, for instance including the magnetoelectric coupling between a uniform polarization and incommensurate magnetic order [144], or non-local Landau theories that describe spin-lattice coupling [59, 145]. However these descriptions are beyond the scope of this work, and reference to Landau theory is made purely to aid in the qualitative understanding of the results presented in this chapter.

The free energy density of the system with respect to a control variable, here taken to be the temperature  $T$ , can be expressed in terms of the order parameter  $\phi$ . One possibility by which a first-order phase transition can occur is if the free energy density has a third-order term in  $\phi$ , such as

$$f(T, \phi) = \frac{r(T)}{2}\phi^2 - w\phi^3 + u\phi^4, \quad (5.1)$$

where  $w$  and  $u$  are positive and temperature-independent. In many systems third-order terms in  $\phi$  are forbidden by symmetry. In such a case, a first-order phase transition can still occur if the free energy has a negative quartic term with a positive sixth-order term for stability, such as

$$f(T, \phi) = \frac{r(T)}{2}\phi^2 - w\phi^4 + u\phi^6. \quad (5.2)$$

Fourth- and sixth-order terms can arise in magnetoelectrics, for instance as a result of strong spin-lattice coupling [145], and such Landau models have been developed for CuO [59, 146]. Substantial spin-lattice coupling has been reported in  $\text{Cu}_{1-x}\text{Zn}_x\text{O}$  as the phonon modes alter across the AF1-AF2 transition [53]. Note that the order parameter can be complex, to allow for non-collinear magnetic states [146].

A schematic diagram of the form of the free energy density around a first-order phase transition with respect to  $\phi$  is presented in Fig. 5.1. Here we

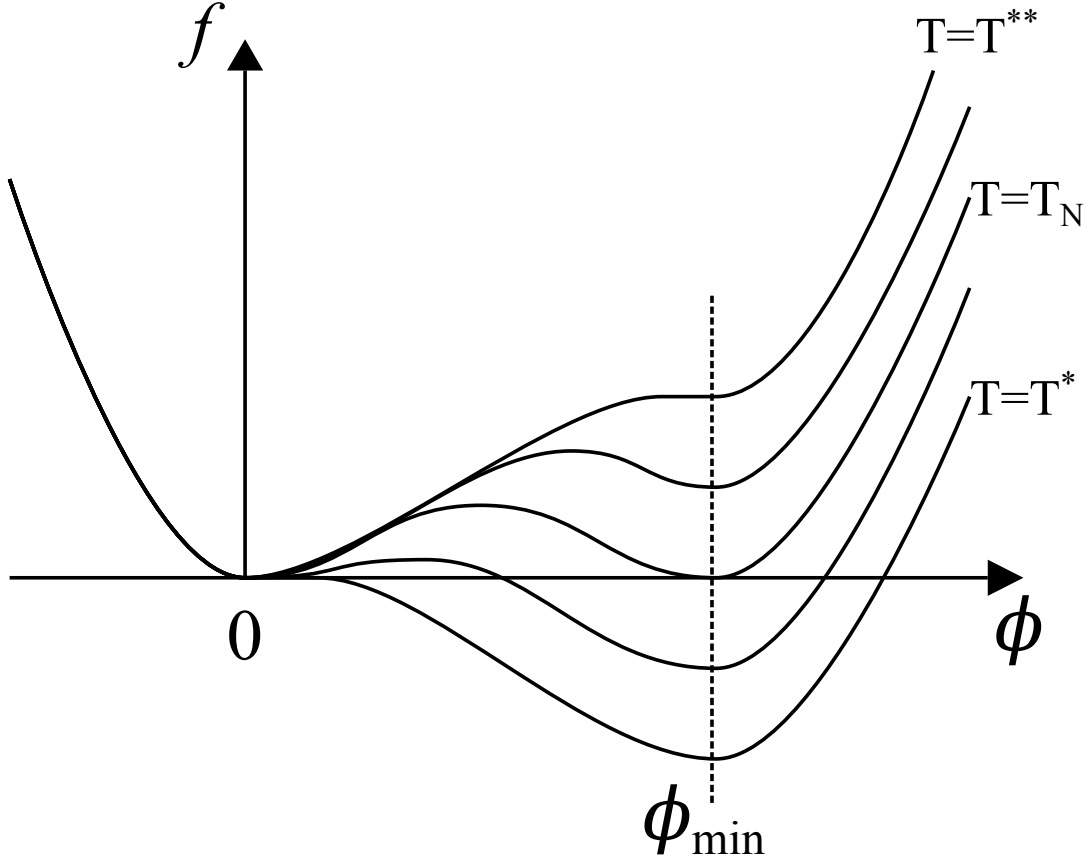


Figure 5.1: Schematic diagram of the free energy  $f$  as temperature is increased and decreased across a first-order phase transition, with respect to the order parameter  $\phi$ .  $T_N$  is the thermodynamic transition temperature,  $T^*$  is the metastable limit of supercooling, and  $T^{**}$  is the metastable limit of superheating.

assume the order parameter for CuO to be represented by the magnetisation along  $b$  for one magnetic sublattice, which is zero in the spin-cycloid phase (AF2) and a finite value  $\phi_{\min}$  in the antiferromagnetic AF1 phase. When the temperature is higher than the thermodynamic transition temperature  $T_N$  the free energy has one global minimum, at  $\phi = 0$ , corresponding to the AF2 phase. At  $T = T_N$  there are two minima to the free energy and the AF1 and AF2 phases can coexist. These minima are located at  $\phi = 0$  and  $\phi = \phi_{\min}$  and separated by an energy barrier. When the temperature drops below  $T_N$  the global minimum of the system shifts to  $\phi_{\min}$ , corresponding to the AF1 phase; however  $\phi = 0$  remains a local minimum of the system, with the two phases still separated by an energy barrier, which will reduce in height with decreasing

temperature. Eventually the height of the energy barrier will reduce to zero at the limit of metastability for supercooling  $T = T^*$ , the temperature at which  $d^2f/d\phi^2 > 0$  at  $\phi = 0$  and none of the AF2 phase can exist. An analogous process occurs for increasing temperature, where  $\phi_{\min}$  continues to be a local minimum of the system until the limit of metastability for superheating  $T = T^{**}$ , the temperature at which  $d^2f/d\phi^2 < 0$  at  $\phi_{\min} = 0$  and none of the AF1 phase can exist. Hysteresis in experimental observables with respect to the control parameters can be explained by these superheating and supercooling effects.

### 5.1.2 Broadening of First-Order Phase Transitions by Disorder

In alloys, the dopant concentration can influence the nature of both the phase transition and the functional properties of interest [141, 142]. Imry and Wortis demonstrated that a first-order phase transition can be broadened by the introduction of quenched random disorder into the system [147]. The correlation length of interactions can be reduced by local impurities, causing different parts of the material to undergo a first-order phase transition at different temperatures, appearing to round off the discontinuity in the order parameter or other related experimental observables. Broadening of first-order phase transitions by disorder may obscure discontinuities in experimental observables, making the latent heat of the transition difficult to determine [142, 147]. As such, hysteresis or phase coexistence are required to observe the first-order nature of the transition.

## 5.2 Spin-Disorder in $\text{Cu}_{1-x}\text{Zn}_x\text{O}$ Alloys

The occurrence of the AF1-AF2 phase transition in CuO can be understood using the mechanism proposed by Yablonskii [63], whereby a biquadratic exchange term stabilizes the low temperature AF1 state. The free energy of a system is given by  $F = E - TS$ , where  $T$  is temperature and  $S$  is entropy. The energy of the interactions between the spin chains in the  $[10\bar{1}]$  direction is given

by Yablonskii as [63]:

$$E = \sum_n [J_1 \mathbf{S}_n \cdot \mathbf{S}_{n+1} + J_2 \mathbf{S}_n \cdot \mathbf{S}_{n+2} + I(\mathbf{S}_n \cdot \mathbf{S}_{n+1})(\mathbf{S}_n \cdot \mathbf{S}_{n+2})], \quad (5.3)$$

where  $J_1$  is the nearest-neighbour ferromagnetic exchange interaction,  $J_2$  is the next-nearest-neighbour antiferromagnetic exchange interaction, and  $I$  is the bi-quadratic exchange interaction. Taking a mean-field approximation with the spatially averaged value of the spins as  $S_{\text{av}}$ , the AF1 state will have a lower energy for  $S_{\text{av}}^2 > J_1^2/8IJ_2$ . As temperature increases, the value of  $S_{\text{av}}$  decreases, therefore at some point the AF2 state has a lower energy and the system undergoes a phase transition. The value of  $S_{\text{av}}$  is effectively controlled by disorder, which can be influenced in a number of ways, the simplest being a change in temperature changing the form of  $F$  and driving the phase transition. Analogously a change in the entropy of the system will also change the form of  $F$ ; evidence for this has been provided by optical-pump X-ray probe measurements on CuO [148]. With the system held just below the phase transition at 207 K, electrons were excited above the charge-transfer bandgap by 800 nm femtosecond pulses, introducing spin-disorder into the system and thus changing the entropy. A larger reduction in the intensity of the X-ray peak associated with the AF1 phase compared to the peak associated with the AF2 phase was observed, hinting at an ultrafast phase transition driven by the introduction of spin-disorder.

### 5.2.1 Quenched Spin-Disorder in $\text{Cu}_{1-x}\text{Zn}_x\text{O}$ Alloys

An alternative method of introducing spin-disorder into the system which may be more desirable for technological applications is by alloying with non-magnetic ions: theoretical investigations predict that the introduction of non-magnetic impurities may stabilize the multiferroic phase at higher temperatures than the pure case [54], and that hydrostatic pressure can broaden the multiferroic phase above room temperature [55]. Alloying of  $\text{Cu}_{1-x}\text{M}_x\text{O}$  with a non-magnetic ion  $M$  has been demonstrated to broaden the multiferroic phase, for  $M = \text{Zn}$ , Co by studying the static ferroelectric polarization along  $b$  [149], and for  $M = \text{Zn}$  using

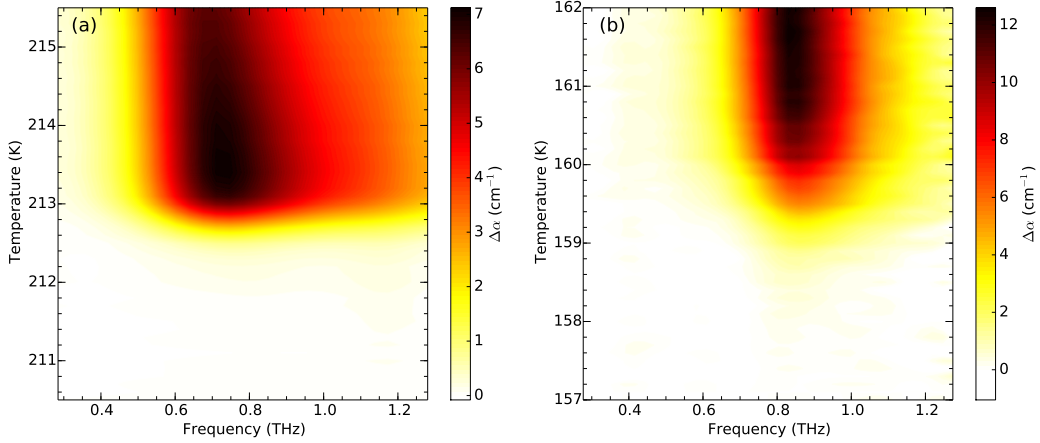


Figure 5.2: Change in terahertz absorption coefficient  $\Delta\alpha$  with respect to the low temperature phase over the AF1 - AF2 phase transition in  $\text{Cu}_{1-x}\text{Zn}_x\text{O}$  alloys, with (a)  $x = 0$  and (b)  $x = 0.05$ .

the electromagnon response [53]. Spin-disorder introduced by the non-magnetic ions breaks up long-range correlations between spins and suppresses the Néel temperatures [150], reducing the AF1 - AF2 transition to  $\sim 159$  K and the AF2 - paraelectric transition to  $\sim 190$  K for  $M = \text{Zn}$  and  $x = 0.05$  [53]. This equates to broadening the multiferroic phase from 17 K to 30 K. The electromagnon is preserved in the AF2 phase of  $\text{Cu}_{0.95}\text{Zn}_{0.05}\text{O}$ , with the same  $E \parallel [101]$  selection rule as in the pure case [8, 53].

### 5.3 Electromagnon Response Over the AF1 - AF2 Phase Transition

To investigate the effects of zinc alloying on the AF1 - AF2 phase transition in  $\text{Cu}_{1-x}\text{Zn}_x\text{O}$ , the change in terahertz absorption coefficient  $\Delta\alpha$  over the AF1 - AF2 phase transition is presented in Fig. 5.2 (a) for  $x = 0$  and Fig. 5.2 (b) for  $x = 0.05$ . Samples were heated over a 5 K range around the AF1 - AF2 transition temperatures ( $\sim 213$  K for  $x = 0$  and  $\sim 160$  K for  $x = 0.05$ ), and  $\Delta\alpha$  measured at each step. The electromagnon is observable in both samples as a peak in  $\Delta\alpha$ , at 0.72 THz for  $x = 0$  and at 0.85 THz for  $x = 0.05$ , consistent with previous observations [8, 53]. In the case of pure CuO, the electromagnon onset is rapid, with  $\Delta\alpha$  rising from zero to a maximum in around 1.5 K. Com-

paratively in the Zn-alloyed sample the onset is much slower, with the rise in absorption occurring in around 3.5 K. At higher frequencies, a broad shoulder to the electromagnon around 1.2 THz is also visible in the  $x = 0$  sample, and has a similar temperature-dependent onset as the main electromagnon. Intriguingly, this higher-frequency shoulder is not observed in the  $x = 0.05$  sample, suggesting that this mode may be either shifted in energy, suppressed or even disrupted entirely upon alloying with zinc.

The electromagnon strength is intimately linked to the incommensurate magnetic order in the multiferroic phase, and therefore can give insight into the nature of the magnetic ordering. To evaluate the properties of the observed electromagnons in the  $\text{Cu}_{1-x}\text{Zn}_x\text{O}$  alloys, and to allow comparison with each other and others reported in the literature, a Drude-Lorentz oscillator model was used to fit the data. This gives the temperature-dependent change in dielectric function  $\Delta\epsilon(\omega) = \epsilon(\omega, T_2) - \epsilon(\omega, T_1)$  as

$$\Delta\epsilon(\omega) = \frac{\Delta\epsilon \cdot \omega_0^2}{\omega_0^2 - \omega^2 - i\omega\Gamma}, \quad (5.4)$$

where  $\Delta\epsilon$  is the oscillator strength,  $\omega_0$  is the oscillator frequency and  $\Gamma$  is the linewidth. Fits to the experimentally measured change in dielectric function  $\Delta\epsilon(\omega)$  of  $\text{Cu}_{1-x}\text{Zn}_x\text{O}$  with respect to the low-temperature phase are presented in Fig. 5.3 (a) for  $x = 0$  at 213 K, and in Fig. 5.3 (b) for  $x = 0.05$  at 161 K. A combination of two oscillators was required when fitting  $\Delta\epsilon(\omega)$  for  $x = 0$ , due to the oscillator frequency of the fit being shifted to a noticeably incorrect, higher value than the peak in the experimental data when a single oscillator was used, as a result of the high frequency data. The main electromagnon (blue) has strength  $\Delta\epsilon = 0.065$ , frequency  $f = 0.71$  THz and linewidth  $\Gamma = 2.0$  THz, while the broader shoulder mode (green) has  $\Delta\epsilon = 0.025$  and linewidth  $\Gamma = 8.0$  THz. In order to correctly model the high-frequency features, the frequency of the shoulder mode was fixed at 1.2 THz. Comparatively  $\Delta\epsilon(\omega)$  for  $x = 0.05$  was well fit by a single oscillator (red), with strength  $\Delta\epsilon = 0.072$ , frequency  $f = 0.84$  THz and linewidth  $\Gamma = 2.0$  THz. Experimental bandwidth was limited to 1.3 THz in the zinc-alloyed sample due to the softening and broadening of the phonon modes upon alloying with zinc [53] increasing absorption in the THz region. All

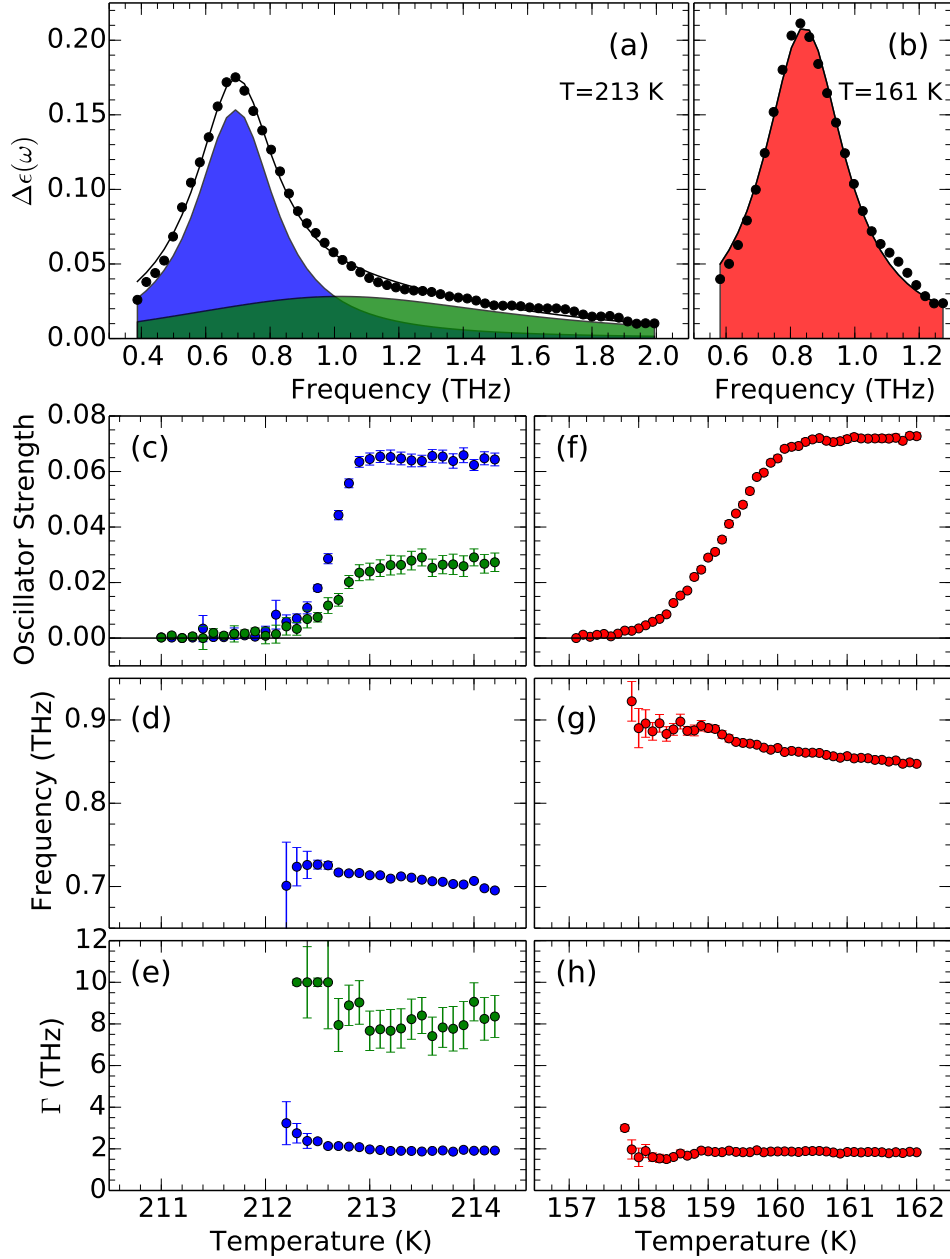


Figure 5.3: **(a)** and **(b)** are the temperature-induced change in dielectric function  $\Delta\epsilon(\omega)$  (black dots) across the AF1-AF2 phase transition in  $\text{Cu}_{1-x}\text{Zn}_x\text{O}$  alloys with  $x = 0$  and  $x = 0.05$ , respectively. Black lines are Drude-Lorentz fits comprised of two oscillators (blue and green shaded areas) for pure CuO (shown in panel **(a)**), and a single oscillator (red shaded area) for the zinc-alloyed sample (shown in panel **(b)**); a single oscillator was used in this case due to the reduced experimental bandwidth as a result of the softening and broadening of the higher lying phonon modes upon alloying with zinc. **(c)**, **(d)** and **(e)** are the best fit parameters of the oscillator strength, frequency and linewidth  $\Gamma$ , respectively, over the phase transition for  $x = 0$ . **(f)**, **(g)** and **(h)** are the corresponding best fit parameters over the phase transition for  $x = 0.05$ . The colour of the data points corresponds to the oscillator they refer to in **(a)** and **(b)**.



values are consistent with those reported previously in the literature [8, 53].

To quantify the evolution of the electromagnon across the phase transition in both samples, similar Drude-Lorentz fits to those in Fig. 5.3 (a) and 5.3 (b) were performed at each temperature step on cooling the samples over the AF1-AF2 phase transition. For the pure CuO data, fits at all temperatures were performed using the two oscillator model, demonstrated at a single temperature by Fig. 5.3 (a). Fit parameters of oscillator strength, oscillator frequency and linewidth for  $x = 0$  are presented in Figs. 5.3 (c)-5.3 (e). The strength of both oscillators begins increasing sharply at 212.2 K, reaching a maximum in around 1.2 K. The frequency of the main electromagnon mode continually red-shifts with increasing temperature over the phase transition, decreasing from 0.73 THz at 212.2 K to 0.69 THz at 214.2 K. The linewidth of both oscillators remains constant over the majority of the phase transition, decreasing slightly in width from when the excitation first begins to emerge. For the  $\text{Cu}_{0.95}\text{Zn}_{0.05}\text{O}$  data, fits at all temperatures were performed using the single oscillator model, demonstrated at a single temperature by Fig. 5.3 (b). Fit parameters for  $x = 0.05$  are presented in Figs. 5.3 (f) - 5.3 (h). The strength of the oscillator shows a gentler, broader increase with temperature, starting to increase around 157.8 K and reaching a maximum after around 3.5 K. Both frequency and linewidth demonstrate the same trends seen for  $x = 0$ , with the frequency red-shifting from 0.9 THz at 158 K to 0.85 THz at 162 K, and the linewidth remaining constant except for initially when the oscillator strength was very small. Values of frequency and linewidth are presented for temperatures at which the oscillator strength was large enough to provide a meaningful fit.

### 5.3.1 Influence of Zn-Alloying on the Magnetic Interactions

Theoretical investigations of electromagnons in CuO [68] have modelled the magnetic properties using a spin Hamiltonian of the form

$$\hat{H} = \sum_{ij} J_{ij} \mathbf{S}_i \cdot \mathbf{S}_j + \mathbf{D}_{ij} \cdot (\mathbf{S}_i \times \mathbf{S}_j) - \sum_i (\mathbf{K} \cdot \mathbf{S}_i)^2 + \hat{H}_{\text{me}}, \quad (5.5)$$

where the first term accounts for superexchange interactions between adjacent spins  $\mathbf{S}_i$ , the second term describes the DM interaction, the third term describes single-ion anisotropy, and the final term accounts for magnetoelectric coupling. Increases to the magnitude of  $\mathbf{D}$  and  $\mathbf{K}$ , the DM and anisotropic coupling constants respectively, were found to enhance the electromagnon energy, directly linking the electromagnon energy to the strength of the interactions responsible for the AF2 phase. An electromagnon frequency of 0.73 THz (energy  $\sim 3$  meV) as observed at 212.3 K in Fig. 5.3(d) corresponds to  $|\mathbf{D}| = 0.4$  meV and  $|\mathbf{K}| = 0.6$  meV [68]. The frequency of the electromagnon mode in  $\text{Cu}_{1-x}\text{Zn}_x\text{O}$  is observed to increase considerably upon alloying of  $x = 0.05$ , suggesting that zinc alloying alters the interactions between spins. From reference [68], an increase in electromagnon frequency to 0.9 THz (energy  $\sim 3.7$  meV) as observed at 158.1 K in Fig. 5.3 (g) corresponds to either an increase in  $|\mathbf{D}|$  to 0.65 meV, or an increase in  $|\mathbf{K}|$  to 0.95 meV, or a smaller simultaneous increase in both.

This alteration of magnetic interactions may be understood with reference to the “order-by-disorder” mechanism proposed by Henley [151], which describes the stabilization of a non-collinear spin state with respect to a collinear spin state, as quenched disorder favors spins in different sublattices to be oriented perpendicular to each other. Simulations have shown that the multiferroic phase in CuO can be stabilized by alloying with non-magnetic ions [149]. Density functional theory (DFT) calculations for pure CuO give a difference in energy between the AF2 and AF1 phase  $\Delta E = E_{\text{AF2}} - E_{\text{AF1}} = 2.15$  meV per Cu, parameterised by  $\Delta E = 4IS^4$  where  $S = 1/2$  and  $I$  is the biquadratic exchange coupling constant. Similar DFT calculations for alloyed CuO show a reduction in the energy difference between the AF1 and AF2 states, estimating a reduction to  $\Delta E = 1.94$  meV per Cu for 5% zinc alloying. Two contributions to this reduction in energy were determined, with similar sized contributions for Zn alloying: modification of the biquadratic exchange interactions between the non-magnetic impurity and spins on the other sublattice, and an alteration of the local Weiss field around the non-magnetic impurities which acts to orient spins on the same sublattice perpendicular to those on the other sublattice by the Henley mechanism. This change in the Weiss field around the non-magnetic ions will alter the value of the anisotropic coupling constant  $\mathbf{K}$ . A change in

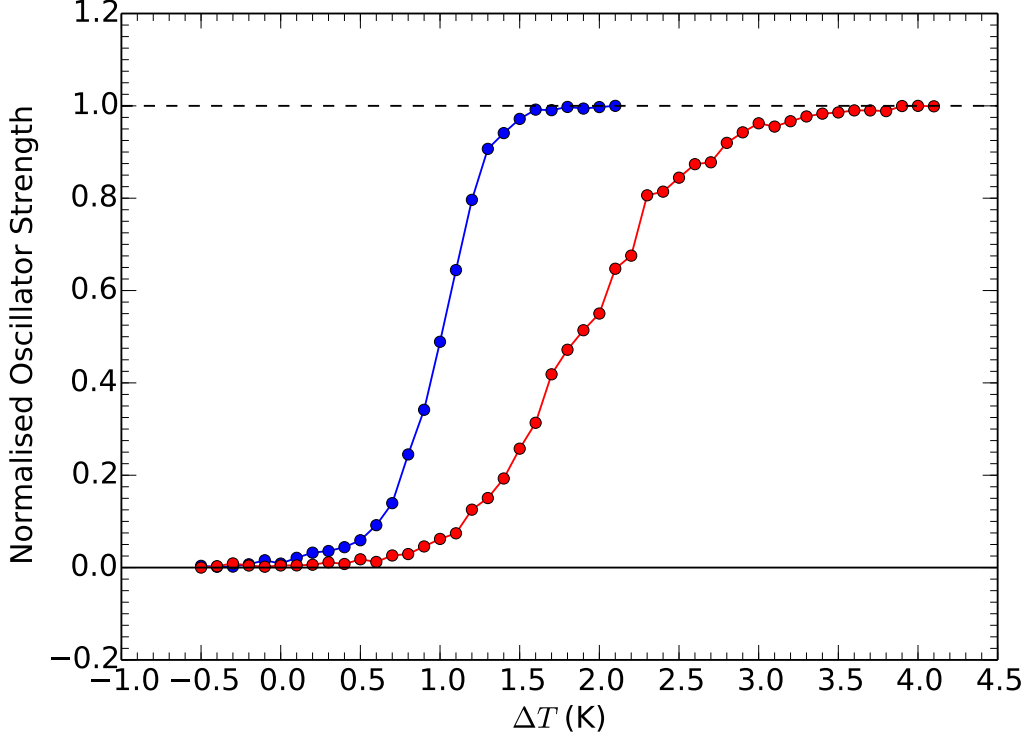


Figure 5.4: Temperature dependent change in the oscillator strength of the electromagnon, over the AF1-AF2 phase transition, in  $\text{Cu}_{1-x}\text{Zn}_x\text{O}$  alloys with  $x = 0$  (blue points) and  $x = 0.05$  (red points).

the DM coupling constant  $\mathbf{D}$  can also occur as the DM interaction is sensitive to the Cu-O-Cu bond angle [36], which changes on alloying with zinc [8].

#### 5.4 Disorder-Broadening of the AF1 - AF2 Phase Transition

For a direct comparison of the width of the AF1-AF2 phase transition for  $x = 0$  and  $x = 0.05$ , Fig. 5.4 presents the oscillator strength of the two main modes from Figs. 5.2 (a) and 5.2 (b), normalized by their maximum value. The change in temperature  $\Delta T$  is defined relative to the temperature at which the oscillator strength increases continuously from zero. The oscillator strength rises from zero to maximum in around  $\Delta T_1 = 1.6 \text{ K}$  for  $x = 0$  and  $\Delta T_2 = 3.9 \text{ K}$  for  $x = 0.05$ . Thus a broadening of 2.3 K occurs for the AF1 - AF2 phase transition

upon alloying with 5% zinc, a ratio of  $\Delta T_2/\Delta T_1 = 2.6$ .

This broadening of the phase transition occurs due to the quenched random spin-disorder introduced upon alloying with non-magnetic zinc ions. As mentioned previously, CuO can be regarded as a quasi-1D colinear Heisenberg antiferromagnet in the commensurate AF1 phase, consisting of spin chains along the  $[10\bar{1}]$  direction. Alloying of  $x = 0.05$  has been shown to suppress the Néel temperatures in  $\text{Cu}_{1-x}\text{Zn}_x\text{O}$  [53] due to spin disorder breaking communication along the spin chains, which reduces the correlation length to the average impurity separation. During formation of the alloy, the local impurity density in the melt will vary slightly around an average value, and this variation becomes frozen-in as the alloy crystallizes. The correlation length of interactions therefore varies depending on the local impurity density, and hence so does the local Néel temperature. In local regions where the impurity density is higher than average the Néel temperature will be lower than average, and vice versa. This causes the AF1-AF2 phase transition to occur over a range of temperatures depending on the local impurity density [147].

The electromagnon excitation cannot be observed without the presence of the AF2 phase, as its strength is strongly linked to the size of the magnetically-induced static polarization in the AF2 phase [8]; as such the normalised oscillator strength in Fig. 5.4 can be interpreted as the ratio of the amount of AF2 to AF1 phase present in the sample. The emergence of the electromagnon upon heating the sample through the phase transition therefore corresponds to initial nucleation of the AF2 phase. The local variation in Néel temperature resulting from quenched spin-disorder in the  $x = 0.05$  sample causes nucleation to occur at different temperatures in different regions of the sample, evidenced by the broader increase in electromagnon strength with temperature.

## 5.5 Hysteresis in the Electromagnon Response

Temperature-dependent hysteresis is one of the experimental signatures of a first-order phase transition, and should be present in many experimental observables related to an order parameter involved in the phase transition. As a natural extension to the analysis of Fig. 5.4, we show here that the strength of

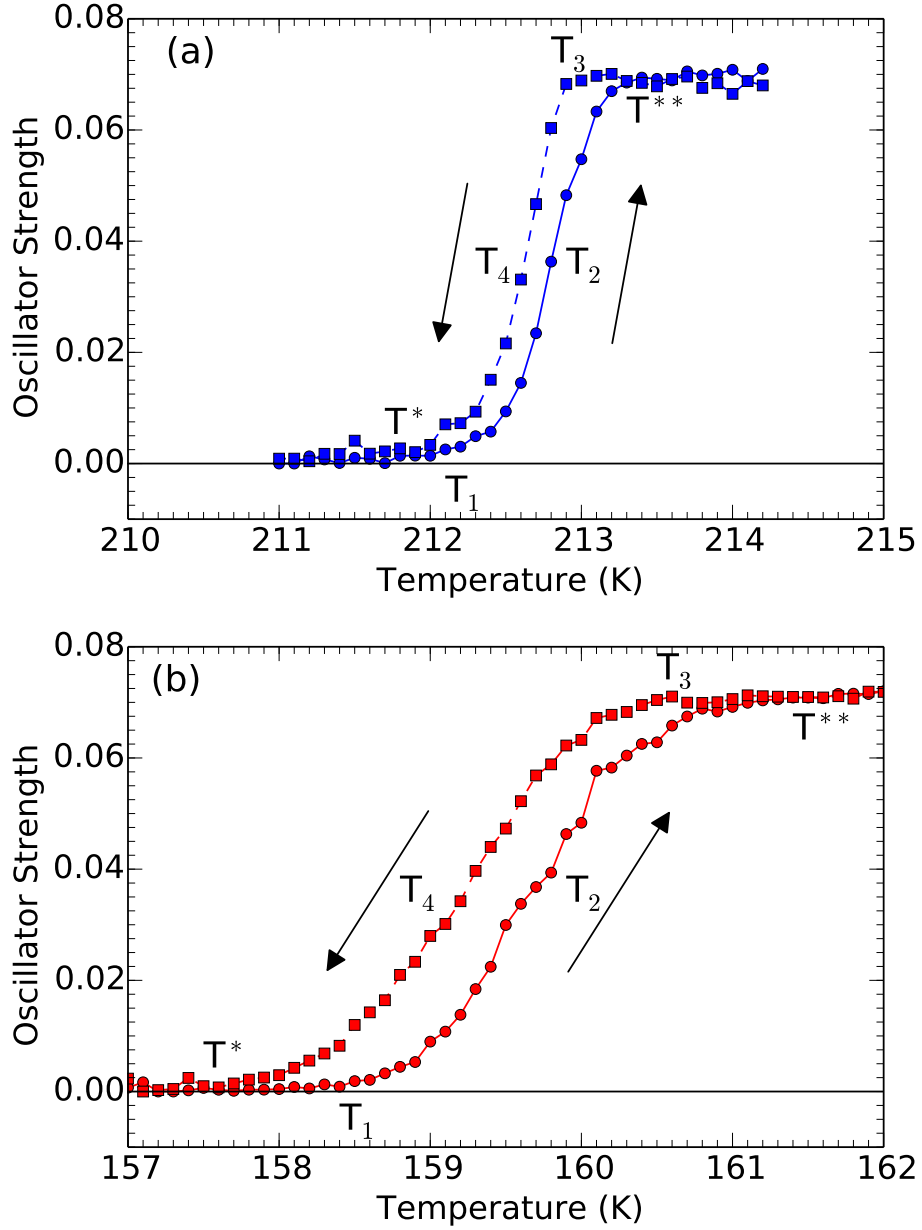


Figure 5.5: Temperature-dependent hysteresis observed in the electromagnon response across the AF1-AF2 phase transition in  $\text{Cu}_{1-x}\text{Zn}_x\text{O}$  alloys with (a)  $x = 0$  and (b)  $x = 0.05$ . Upwards facing arrows denote increasing temperature (also denoted by solid circles) and downwards facing arrows denote decreasing temperature (solid squares).  $T_1$  and  $T_3$  are the temperatures at which the oscillator strength begins to deviate significantly from zero or the maximum, respectively.  $T_2$  and  $T_4$  are the mid-points of the phase transition during heating and cooling, respectively.  $T^{**}$  and  $T^*$  are the limits of metastability for superheating and supercooling, respectively.

the electromagnon can be used to observe hysteretic behaviour at the AF1 - AF2 phase transition on heating and cooling of the sample.

The electromagnon response in  $\text{Cu}_{1-x}\text{Zn}_x\text{O}$  alloys as the temperature is first increased and then decreased across the AF1 - AF2 phase transition is presented in Fig. 5.5 (a) for  $x = 0$  and in Fig. 5.5 (b) for  $x = 0.05$ . Hysteresis is clearly visible in both pure and zinc alloyed samples, with the centre of the phase transition occurring at higher temperatures when temperature was increased over the phase transition compared to when it was decreased. The centre points of the increasing and decreasing temperature measurements,  $T_2$  and  $T_4$  respectively, are separated by 0.2 K in the  $x = 0$  sample and 0.5 K in the  $x = 0.05$  sample. The ratio between these values of 2.5 is similar to the degree of disorder-induced broadening of the phase transition observed in Fig. 5.4. Subsequent heating and cooling measurements reproduced the same hysteretic behaviour.

The hysteretic evolution of the oscillator strength with temperature for both pure and zinc alloyed samples can be explained with reference to the free energy diagram in Fig. 5.1, and the nomenclature used to describe hysteresis of disorder-broadened first-order phase transitions outlined in reference [142]. In the case of an ideally pure compound and in the absence of temperature fluctuations, the high or low temperature states can be taken to the limit of metastability at  $T^*$  and  $T^{**}$  respectively, where the phase transition occurs as a sharp discontinuity in the hysteretic parameter being observed.

In any real system, temperature fluctuations will perturb the system and destroy the metastable state at some intermediate temperature between  $T_N$  and  $T^*$  or  $T^{**}$ . The small amount of disorder present in any real crystal from impurities or defects will also cause a slight rounding of the transition. Both of these effects are observable in the hysteresis of pure CuO in Fig. 5.5 (a). On heating, the electromagnon excitation emerges at temperature  $T_1$ , signifying the onset of nucleation of the AF2 phase, and grows in strength until reaching a maximum at 213.4 K. On cooling, the electromagnon strength begins to differ from that observed during heating around 213.4 K, signifying this temperature as  $T^{**}$ , and begins to decrease in strength at temperature  $T_3$  signifying the onset of nucleation of the AF1 phase. The temperature at which the electromagnon

strength reduces to zero on cooling can therefore be identified as  $T^*$ . The system is observed to be in the metastable state for superheating and supercooling over a temperature range of 0.4 K in both cases. Similar trends can be seen for the zinc alloyed sample in Fig. 5.5 (b), however in this case the phase transition is broadened by spin-disorder. The metastable phases for superheating and supercooling are also broadened upon zinc alloying, with both increasing to a width of 1 K.

As discussed previously, simulations of the magnetic interactions in alloyed CuO showed a decrease in the energy difference between the AF1 and AF2 states relative to pure CuO [149]. However, the metastable phase observed in the zinc alloyed sample is wider than the pure sample. This may be partially due to smaller thermal fluctuations at the lower Néel temperatures of the alloyed sample, but could also be due to modifications to the exchange coupling parameters on alloying altering the form of the free energy barrier between the two phases. Modification of the biquadratic exchange and higher order coupling terms by the non-magnetic ions, as discussed in terms of the “order-by-disorder” mechanism above, could therefore possibly alter the free energy barrier height and increase the stability of the metastable phases in the zinc alloyed sample.

## 5.6 Summary

Here, it has been reported for the first time that the dynamic magnetoelectric response at terahertz frequencies can be used to probe hysteresis and spin-disorder broadening at magnetic phase transitions. The oscillator strength  $\Delta\epsilon$  of the electromagnon in  $\text{Cu}_{1-x}\text{Zn}_x\text{O}$  ( $x = 0, 0.05$ ) alloys was taken to represent the fraction of the magnetically-induced ferroelectric phase, AF2. By precisely tracking  $\Delta\epsilon$  on cooling or heating across the phase transition between the commensurate AF1 phase and the spin-spiral, ferroelectric AF2 phase we observed thermal hysteresis, indicating the first-order nature of this transition. The limits of metastability for superheating and supercooling were identified, and the metastable region was found to broaden for the alloy with greater spin-disorder. Alloying also enhanced the electromagnon energy from 3.0 meV to 3.7 meV, potentially as a result of enhanced DM interaction or greater single-ion anisotropy.

The results were discussed within the context of a simple Landau theory of a first-order phase transition, with reference to recent advances in phenomenological and first-principles theoretical models of CuO.

This technique may not be limited to observing the change in an electromagnon using temperature as the control variable; multiferroic materials typically display a wealth of different phases with respect to other parameters such as electric and magnetic fields [152, 153, 154] or pressure [155]. For example, CuO exhibits a number of additional magnetic phases under an applied magnetic field [154], and a similar method to the one outlined in this chapter could potentially be used to probe the nature of some of these phase transitions. Other resonant excitations such as magnons could also be used to test for hysteresis at a phase transition.



## Chapter 6

# High-Field Terahertz Time-Domain Spectroscopy of Single-Walled Carbon Nanotubes and CuO

Section 6.1 of this chapter gives a brief overview of some techniques utilised to generate high-field THz pulses and their applications in spectroscopy. Section 6.2 then describes the setup and operation of the high-field THz-TDS system developed as a part of this doctoral work. Section 6.3 then explores the use of indium antimonide (InSb) as a test material for the high-field THz-TDS system, before Sections 6.4 and 6.5 present some preliminary results on high-field THz spectroscopy of highly-conductive single-walled carbon nanotube (SWCNT) films and electromagnons in CuO.

### 6.1 Terahertz Spectroscopy using Extreme Electric Fields

When the electric field strength of the THz radiation is sufficiently large, the THz pulse can induce nonresonant effects in materials by the ponderomotive force applied to charges via the intense, oscillating electric field. A measure of

this can be gained using the *ponderomotive potential*  $U_p$ , given by

$$U_p = \frac{e^2 E^2}{4m\omega^2}, \quad (6.1)$$

where  $e$  is the electronic charge,  $m$  is the mass,  $\omega$  is the angular frequency of the oscillating electric field and  $E$  is the electric field amplitude. Since  $U_p \propto E^2/\omega^2$ , the greatest effects are observed for large electric fields with long wavelengths, hence THz pulses can induce very large ponderomotive effects in materials. In a driving 1 THz field of  $\sim 300 \text{ kVcm}^{-1}$ , the energy applied to free electrons in a half-cycle of the THz pulse can approach 1 eV, comparable to the size of the bandgap in many semiconductor materials. Examples of nonresonant effects induced by THz pulses are the field-ionisation of impurities [156] and excitons [157], ballistic electron transport [158, 159], intervalley scattering [160, 161, 162], and impact ionisation [163, 164] in semiconductors. The hot-carrier dynamics induced by strong THz pulses have also been studied in graphene [165, 166] and carbon nanotube films [167].

Intense THz pulses can also be used to exert coherent control over materials, by directly coupling to a resonant excitation such as a phonon mode. Examples of this have been demonstrated by driving the soft mode of  $\text{SrTiO}_3$  [168, 169]. Resonant control over electronic degrees of freedom have also been demonstrated, over Cooper pairs in superconductors by ultrafast suppression of superconductivity [170] and by the excitation of Josephson plasmons [171].

In addition to the electric field of the intense THz pulses, the magnetic field of the THz pulse can effect the spins in materials by the application of a Zeeman torque  $\mathbf{T} = \mathbf{m} \times \mathbf{B}$ , where  $\mathbf{m}$  is the magnetic dipole moment. The time-varying magnetic field of the THz pulse deflects the spins from their equilibrium position, and induces a precession of the spins about their equilibrium position. The high-field dynamics of magnetic excitations in ferromagnets have been explored in Fe [172] and Co [173] thin films, the results of which indicate that the magnetic dynamics are phase-locked to the incident THz pulse [173]. THz control over spin dynamics can also be performed on antiferromagnets, by making use of resonant excitation of magnons. Kampfrath *et al.* used intense THz transients of maximum magnetic field amplitudes 0.13 T to excite the 1

THz magnon in NiO [174]. By using 2 pulses with a suitable time delay between them, it was found that the magnon could either be excited further by a factor of two by an in-phase pulse, or the spin precession could be almost completely stopped by an out-of-phase pulse. Subsequently coherent spin control over THz frequency magnons has been demonstrated in YFeO<sub>3</sub> [175, 176].

### 6.1.1 Generating High-Field Terahertz Radiation

The intense optical pulses produced by amplified femtosecond lasers offer new routes to efficient generation of high-field THz pulses, both by a scaling-up of established techniques such as photoconductive emission and optical rectification, and by enabling new THz generation techniques to be developed.

By focusing femtosecond laser pulses with energies greater than  $\sim 10 \mu\text{J}$  onto a gas target the ionisation intensity of the gas molecules ( $\sim 10^{14} \text{ W/cm}^2$ ) can be exceeded, creating a plasma. Because the femtosecond pulse is short enough to inertially confine the ions, an ultrafast charge density separation is created in the plasma due to the ponderomotive motion of the electrons, causing broadband THz emission from the plasma [177, 178, 179, 180]. Subsequently, a number of other methods of THz generation from gas plasmas have been devised in an attempt to increase the THz field strength. Single-cycle THz pulses can be generated by electrically biasing the gaseous target as it is photoionized by the amplified laser pulses [181, 182] or by using few-cycle optical pump pulses [183], however the most common method uses a superposition of the fundamental and second harmonic of the femtosecond laser to produce THz radiation [184, 185]. THz generation by gas plasmas may be used to produce extremely broad bandwidth pulses, as there is no absorption of the generated radiation in the target material. More in-depth reviews of the generation of THz radiation from gas plasmas, including generation mechanisms, can be found in references [180] and [186].

Recently, an upscaling to amplified laser systems has been demonstrated for metallic spintronic emitters [187], in which electric fields of  $300 \text{ kVcm}^{-1}$  were achieved, with a peak frequency around 2 THz and a broad bandwidth between 0.1 - 10 THz. The potential for creating longitudinally-polarised high-field THz radiation at a focus has also been demonstrated using spintronic emitters, by

patterning the magnetic field applied to the device [188]. Photoconductive emitters also have the potential for upscaling to produce higher field strengths, by increasing the size of the emitting area and exciting it using amplified laser pulses. THz electric fields of  $36 \text{ kVcm}^{-1}$  have been achieved using a pump laser fluence of  $20 \text{ } \mu\text{J/cm}$ , bias electric field of  $70 \text{ kV/cm}$  and a large active emitter region of  $1 \text{ mm}^2$  [77].

High-field THz radiation can be generated by optical rectification in materials that possess a large nonlinear coefficient, such as organic crystals like DAST and DSTMS [189, 190]. Emission strength from these organic crystals is limited by their low damage threshold. An alternative method to produce THz radiation by optical rectification is by using the tilted pulse-front pumping (TPFP) technique. The TFPF technique was first demonstrated in a proof-of-principle experiment using (111)-oriented GaP [191], and has since been utilised with materials such as lithium niobate ( $\text{LiNbO}_3$ ), in which THz electric fields of up to  $1.2 \text{ MVcm}^{-1}$  have been achieved at a diffraction-limited focus [20]. The TFPF technique forms the basis of the high-field generation technique utilised in the spectrometer described in Section 6.2, and as such will be discussed in further detail in Section 6.2.1.

### 6.1.2 Choosing the Right High-Field THz Source for You

An important consideration when choosing which method of high-field THz generation to employ is the spectral bandwidth it covers, and the material systems one is interested in. Fig 6.1 presents a comparison of different sources and their typical frequency spectra. Examining the sources, we see that plasma generation produces ultrabroadband, gapless THz emission over a broad range of frequencies. However, its spectrum is peaked around  $8 \text{ THz}$ , so whilst this technique provides emission over a broad range of frequencies, the spectral weight around  $1 \text{ THz}$  is quite low. By comparison, optical rectification in  $\text{LiNbO}_3$  and organic crystals have a lot of spectral weight at low frequencies, with a narrower bandwidth. As such optical rectification will be the best choice for investigating material properties at low THz frequencies, and plasma generation for higher THz frequencies.

The choice of high-field source used in the spectrometer presented in this

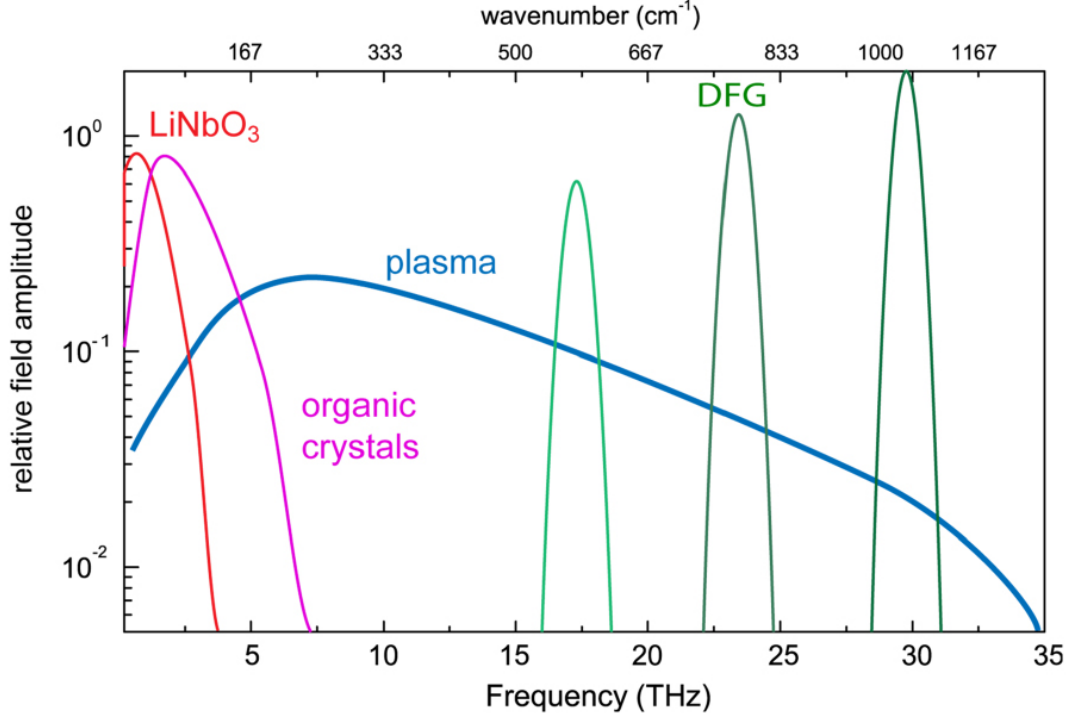


Figure 6.1: Comparison of typical spectra produced by different high-field THz generation techniques. Reproduced from reference [192].

chapter was motivated by the research interests of the THz group at the University of Warwick. Much of the fundamental physics of interest, such as charge transport dynamics in carbon nanotubes [193, 194], metal halide perovskites [195, 196], semiconductors [197], and nanomaterial heterostructures [198], alongside low-energy collective excitations such as electromagnons [8, 53, 130], all occur at low THz frequencies. As such, optical rectification in  $\text{LiNbO}_3$  was the generation scheme of choice, rather than an organic crystal; the lower spectral peak frequency of  $\sim 1$  THz makes it the more applicable method for much of the interesting physics, particularly the Drude and plasmon conductivity peaks in SWCNTs [194] and the resonant frequency of the electromagnon in  $\text{CuO}$ .

## 6.2 High-Field Terahertz Time-Domain Spectrometer

This section will describe the high-field THz-TDS system used to perform the experiments described in Sections 6.3, 6.4 and 6.5 of this chapter, starting with

a description of the high-field generation technique of choice, tilted pulse-front pumping in LiNbO<sub>3</sub>, in Section 6.2.1, before moving on to describe the optical setup of the spectrometer in Section 6.2.2, and finally characterising the performance of the spectrometer and describing the method of varying the THz electric field strength in Section 6.2.3.

### 6.2.1 Tilted Pulse-Front Pumping in LiNbO<sub>3</sub>

As described in Section 2.1.2, the greatest efficiency is obtained for THz generation via optical rectification in a nonlinear material where  $v_{p,THz} = v_{g,opt}$ . In materials in which this velocity matching condition is satisfied, the generated THz radiation is emitted collinearly with the direction of propagation of the pump pulse, so constructive interference of the generated THz radiation occurs as the pump pulse propagates through the material. Some materials such as LiNbO<sub>3</sub> have a very high nonlinear coefficient, but velocity matching is not satisfied because  $v_{p,THz} < v_{g,opt}$ . In this case the THz radiation is emitted in a Cherenkov-like cone [70, 199], as shown in Fig. 6.2 (a), at an angle  $\theta_C$  to the direction of propagation of the pump pulse, defined by the ratio of the optical group index and the THz phase index as

$$\cos \theta_C = \frac{n_{g,opt}}{n_{p,THz}} = \frac{v_{p,THz}}{v_{g,opt}}. \quad (6.2)$$

This conical emission profile makes the THz radiation difficult to collect and collimate, and therefore the usefulness of the Cherenkov geometry as a source of THz radiation is limited.

However, by using the technique of *tilted pulse-front pumping* (TPFP), intense THz pulses can be generated in materials that have good nonlinear properties but cannot meet the collinear velocity matching condition [191]. TFPF makes use of a tilt in the the pulse front of the pump laser beam with respect to the phase front, causing the geometry seen in Fig. 6.2 (b). The velocity matching condition now becomes

$$v_{g,opt} \cos \gamma_c = v_{p,THz}, \quad (6.3)$$

where  $\gamma_c$  is the tilt angle of the pump pulse front; now the most efficient THz

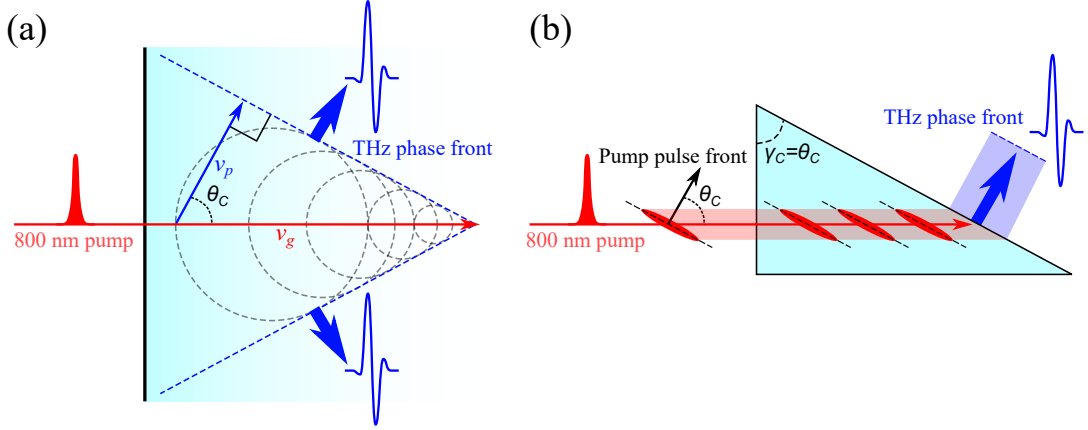


Figure 6.2: **(a)** Velocity-mismatched generation of THz radiation in a nonlinear material, exhibiting a Cherenkov-like emission geometry. The THz phase velocity is lower than the IR group velocity, hence the phase front of the generated THz radiation is at an angle  $\theta_C$  to that of the pump pulse. **(b)** Tilted pump pulse pumping geometry in LiNbO<sub>3</sub>. The pump pulse front is tilted to match the angle of the THz phase front, resulting in constructive interference of the generated THz radiation throughout the LiNbO<sub>3</sub> crystal.

generation is achieved when  $\gamma_c = \theta_C$ , the angle at which the THz radiation would be generated at in the Cherenkov geometry. In this way, the generated THz radiation interferes constructively as the pump pulse propagates through the crystal, and exits the crystal at a face cut at the same angle,  $\theta_C$ .

#### Obtaining the Pulse Front Tilt

A number of methods are available for obtaining a tilt to the pulse front of the optical pulse, which include using a diffraction grating and one [200] or two [201] lenses, or by patterning a grating structure directly onto the generation crystal [202]. The method used here consists of a diffraction grating and two cylindrical lenses to create the pulse front tilt, shown schematically in Fig. 6.3.

To calculate the pulse front tilt inside the LiNbO<sub>3</sub> crystal, we start from the equation for diffraction from a grating,

$$\sin \theta_i + \sin \theta_d = mN\lambda_0, \quad (6.4)$$

where  $\theta_i$  and  $\theta_d$  are the angles of incidence and diffraction, respectively,  $m$  is the diffraction order,  $N$  is the groove density of the grating, and  $\lambda_0$  is the wavelength of the pump pulse. The pulse front tilt  $\gamma$  after diffraction from a grating can be

shown to be [203]

$$\tan \gamma = \frac{\sin \theta_i + \sin \theta_d}{\cos \theta_d}, \quad (6.5)$$

which when combined with Equation 6.4 can be expressed as

$$\tan \gamma = \frac{mN\lambda_0}{\cos \theta_d}. \quad (6.6)$$

The pair of cylindrical lenses apply a horizontal demagnification  $\beta_1$  to the pump pulse, which changes the tilt angle according to

$$\tan \gamma_{\text{CL}} = \frac{\tan \gamma}{\beta_1}, \quad (6.7)$$

where  $\gamma_{\text{CL}}$  is the pulse front tilt angle after the pair of cylindrical lenses. As the pulse propagates into the LiNbO<sub>3</sub> crystal, refraction at the interface causes an alteration in the pulse length  $l_c = l/n_{\text{g,opt}}$ , causing a corresponding change in the pulse front tilt angle of

$$\tan \gamma_c = \frac{\tan \gamma_{\text{CL}}}{n_{\text{g,opt}}} \quad (6.8)$$

where  $\gamma_c$  is the pulse front tilt inside the LiNbO<sub>3</sub> crystal. Combining Equations 6.6 - 6.8, we obtain the equation describing the pulse front tilt angle inside the LiNbO<sub>3</sub> crystal as

$$\tan \gamma_c = \frac{mN\lambda_0}{n_{\text{g,opt}}\beta_1 \cos \theta_d}. \quad (6.9)$$

Finally, by rearranging Equations 6.9 and 6.4, we can obtain the expressions for the angles of diffraction and incidence which produce the required pulse tilt as

$$\theta_d = \cos^{-1} \left( \frac{mN\lambda_0}{n_{\text{g,opt}}\beta_1 \tan \gamma_c} \right), \quad (6.10)$$

and

$$\theta_i = \sin^{-1} \left( mN\lambda_0 - \sin \left[ \cos^{-1} \left( \frac{mN\lambda_0}{n_{\text{g,opt}}\beta_1 \tan \gamma_c} \right) \right] \right). \quad (6.11)$$

### Optimising the Pulse Front Tilt for THz Generation Efficiency

For efficient generation of THz radiation by this scheme, an important factor is having the pulse front tilt angle  $\gamma_c$  match the angle of the grating image  $\theta_g$  created in the LiNbO<sub>3</sub> [200]. The grating image created in the LiNbO<sub>3</sub> can be



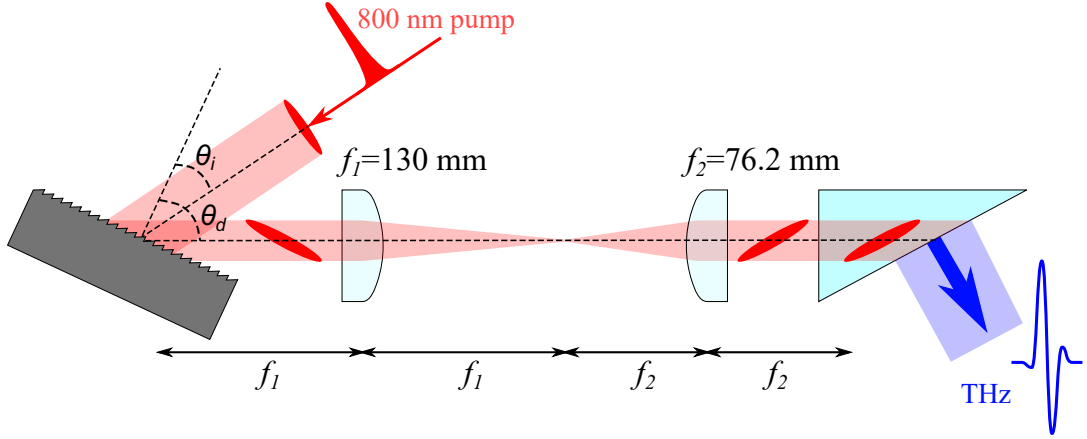


Figure 6.3: Schematic diagram of the tilted pulse front pumping scheme used to generate high-field THz pulses in LiNbO<sub>3</sub>. A grating and two cylindrical lenses are used to tilt the pulse front of the 800 nm pump beam to satisfy the velocity matching condition in the LiNbO<sub>3</sub> crystal.

shown to be [200]

$$\tan \theta_g = n\beta_2 \tan \theta_d, \quad (6.12)$$

where  $\beta_2$  is the demagnification factor of the cylindrical lens pair. As such, the greatest THz generation efficiency occurs when  $\beta_1 = \beta_2$ .

The THz generation crystal used in this thesis was a 0.6 mol% MgO-doped stoichiometric LiNbO<sub>3</sub> crystal, which has dimensions of 5 mm × 5 mm × 9.81 mm, with the crystal cut at an angle of  $\theta_{\text{LN}} = 63^\circ$  between the pump beam entrance and THz beam exit face. The pump beam entrance face was anti-reflection coated for 800 nm. To find the optimal optics for the pulse front tilting setup, the demagnification factors  $\beta_1$  and  $\beta_2$  were calculated as a function of  $\theta_d$  from Equations 6.9 and 6.12. In these calculations, various grating groove densities were used,  $m = 1$ ,  $\lambda_0 = 800$  nm,  $n_{\text{g,opt}} = 2.23$  and  $n = 2.16$  [204], and the pulse front tilt and grating image angles were set to match the cut angle of the LiNbO<sub>3</sub> crystal  $\gamma_c = \theta_g = 63^\circ$ . Using an 1800 lines mm<sup>-1</sup> grating the optimal value of  $\beta_1, \beta_2 = 0.6$ . The cylindrical lenses chosen had focal lengths of  $f_1 = 130$  mm and  $f_2 = 75.6$  mm which give a demagnification factor  $\beta = f_2/f_1 = 0.582$ , close to the optimum value. This then allows us to calculate the optimal angles of incidence and diffraction from Equations 6.10 and 6.11, which give values of  $\theta_i = 38.0^\circ$  and  $\theta_d = 55.6^\circ$  for this system.

### 6.2.2 Experimental Setup

The experimental setup of the high-field THz-TDS system used in this chapter is shown schematically in Fig 6.2 (a). A quarter of the output of a regeneratively amplified Ti:Sapphire laser system (Spectra-Physics Spitfire Ace-PA-40) was used to produce pulses with a central wavelength of 800 nm (40 nm bandwidth at FWHM) with pulse energies of 3 mJ and duration of 40 fs at a repetition rate of 1 kHz. The pulses from the laser were then split by a 70/30 beamsplitter, with 70% of the laser output being used for the high-field THz generation. This high-field THz pump portion of the beam passes through a variable delay stage, in order to change the relative arrival times of the THz and gate beams at the detection crystal. The pump beam is then reduced in size from  $\sim 12$  mm to  $\sim 4$  mm in diameter by an  $f = 200$  mm plano-convex lens and  $f = -50$  mm convex mirror beam telescope, in order to match the size of the LiNbO<sub>3</sub> THz generation crystal. This smaller beam is then incident upon a diffraction grating and 4- $f$  cylindrical lens setup, in order to generate high-field THz radiation via the tilted-pulse-front-pumping technique in LiNbO<sub>3</sub> (discussed in detail in Section 6.2.1).

Using the 4- $f$  cylindrical lens scheme to create the grating image inside the LiNbO<sub>3</sub> causes the generated THz radiation to be produced in a roughly collimated beam [20], hence the generated THz radiation was collected after a short distance of  $\sim 25$  mm by a 12.7 mm diameter,  $f_{\text{OAP1}} = 15$  mm off-axis parabolic mirror (OAP1 in Fig. 6.2). This first OAP focuses the THz radiation, and constitutes the first mirror in a telescope system; the expanding beam of THz radiation after the focus is collected by a second OAP mirror (OAP2 in Fig. 6.2) with 50.8 mm diameter and  $f_{\text{OAP2}} = 152.4$  mm. This second OAP was positioned a distance  $f_{\text{OAP1}} + f_{\text{OAP2}} = 167.4$  mm away from OAP1 in order to expand the THz beam by a factor  $f_{\text{OAP2}}/f_{\text{OAP1}} = 10.16$ , to better fill the focussing optics and create a smaller spot size at the sample focus. This step is important to achieve the highest possible THz electric fields, since the electric field strength is inversely proportional to the THz spot size, which will be discussed further in Section 6.2.3. The expanded beam is focused onto the sample space then collected and collimated by a pair of 50.8 mm diameter,  $f = 76.2$  mm

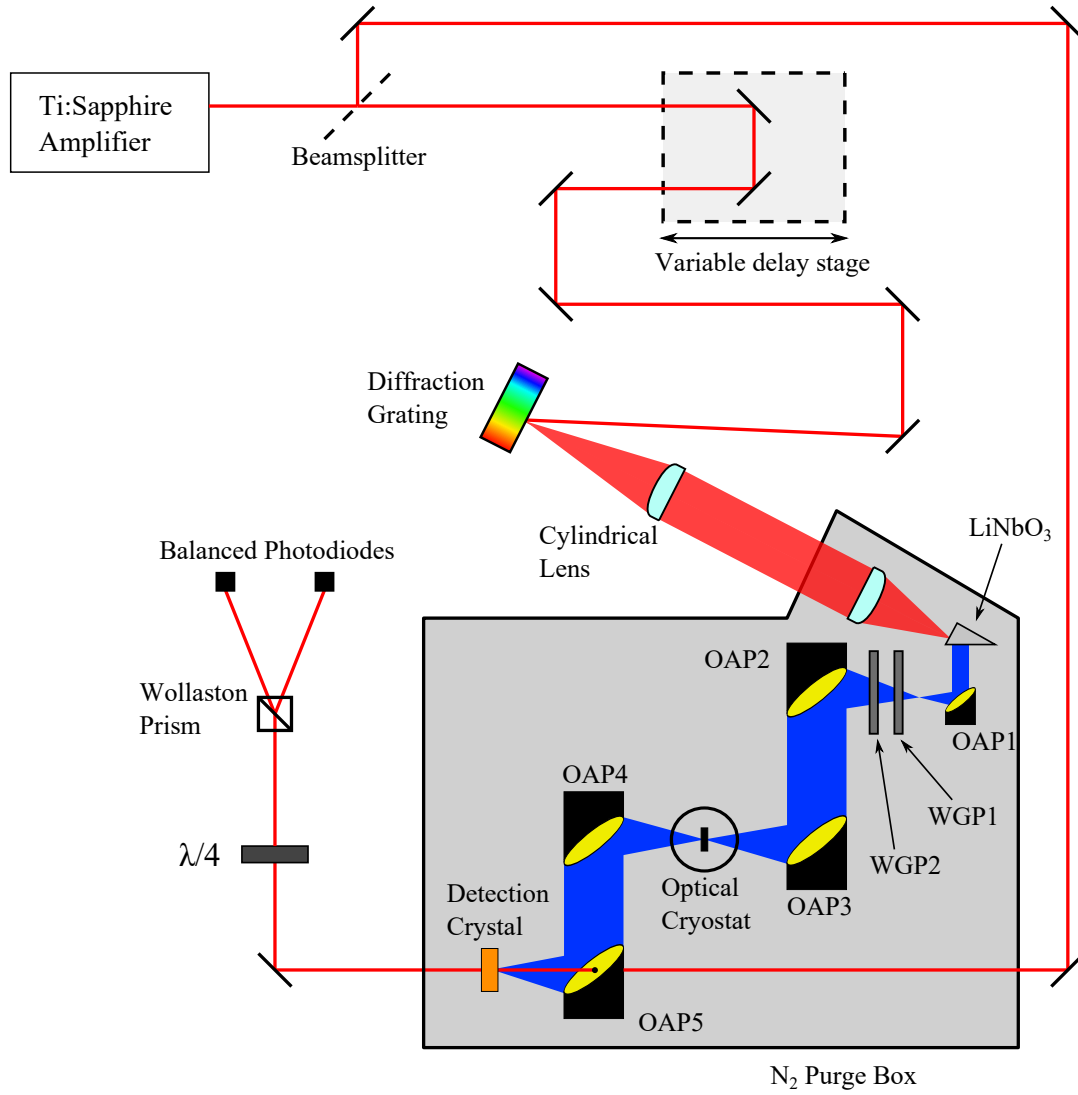


Figure 6.4: Schematic diagram of the terahertz time-domain spectrometer used to perform high-field THz transmission measurements.

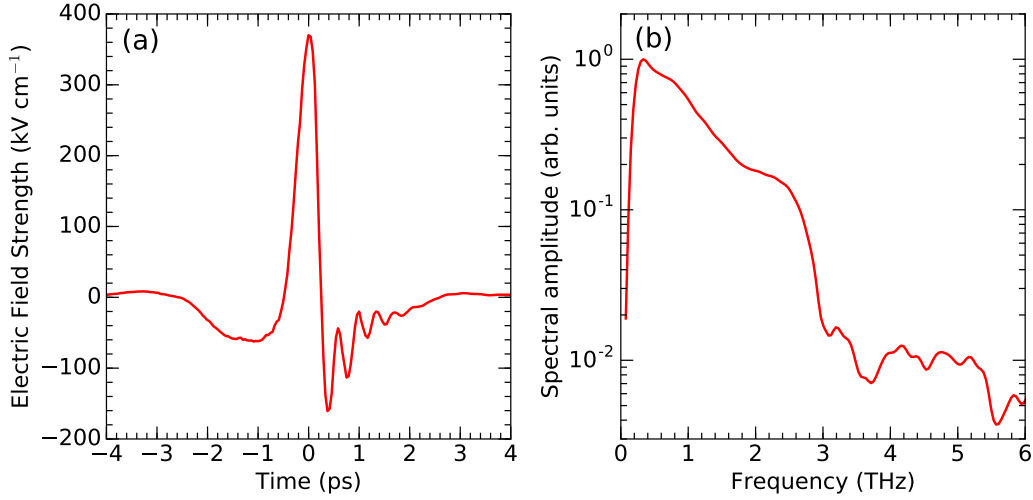


Figure 6.5: **(a)** Time-domain waveform of a typical high-field THz pulse generated by TPF in  $\text{LiNbO}_3$  in the spectrometer presented in this thesis, and **(b)** its corresponding Fourier transform spectrum.

OAPs (OAP3 and OAP4 in Fig. 6.2). The 76.2 mm focal length of these optics is not the shortest possible, which would achieve the smallest possible THz spot size, but is required in order to accommodate the size of the optical cryostat (Oxford Instruments Optistat DN-V) to be used for low-temperature measurements. Finally, the THz beam is focused onto the detection crystal by a 50.8 mm diameter,  $f = 50.8$  mm OAP (OAP5 in Fig 6.2). The entire THz beam path is encased in a box that can be purged with dry  $\text{N}_2$  gas, in order to remove the influence of water vapour absorption from the THz spectra.

Of the remaining 30% of the laser output after the beamsplitter, a second beamsplitter with a 90/10 ratio was used, in order to have 10% of this beam to be used for the gate beam. For experiments presented in this chapter, the remaining 90% of the beam was not used and instead directed onto a beamdump, however in the future this beam may be utilised as an additional, low-field THz generation beam to create a THz pump-THz probe setup. Detection of THz radiation in the high-field THz-TDS system was performed by the standard EOS method (described in Section 2.2) using a 300  $\mu\text{m}$ -thick,  $\langle 111 \rangle$ -oriented GaP detection crystal. An example THz pulse and its corresponding Fourier-transform spectrum generated and detected by this spectrometer are presented in Figs.

6.5 (a) and 6.5 (b), respectively. The spectrum shows frequency components between 0.2 - 2.5 THz, and the THz electric field strength was controlled by a pair of wire-grid polarisers in the THz beam and calibrated by the method discussed in Section 6.2.3.

### 6.2.3 Controlling the Electric Field Strength of Terahertz Pulses

The method used to vary the THz electric field strength in the spectrometer is demonstrated schematically in Fig. 6.6 (a), and consists of two gold WGP (5  $\mu\text{m}$  width wires, 10  $\mu\text{m}$  period) fabricated on 25.4 mm diameter, 2 mm thick substrates of z-quartz by a single-step UV photolithography process identical to that used in Section 4.2.2. An optical microscopy image of the fabricated WGP is shown in Fig 6.6 (b). WGP1 is mounted in a Newport PR50CC motorised rotation stage, and WGP2 is mounted in a manual rotation mount. To calibrate the field strength adjustment, a time domain scan is taken with only WGP2 present in the beam, and WGP2 is rotated to maximise the electro-optic signal, then fixed in place. WGP1 is then placed in the THz beam and similarly rotated to maximise the electro-optic signal. This sets the wires in WGP1 parallel to those in WGP2. By rotating WGP1 by an angle  $\theta_{\text{WGP}}$  the THz electric field strength may be adjusted as

$$E_{\text{THz}} = E_0 \cos^2 \theta_{\text{WGP}}, \quad (6.13)$$

where  $E_0$  is the maximum THz electric field strength achieved when the WGP are aligned. Both WGP are mounted on magnetic bases, to allow them to be removed to increase the THz electric field strength further.

The THz electric field strength in the high-field setup is calculated using

$$E_{\text{THz}} = \sqrt{\frac{Z_0 W}{\pi r^2 \int A^2(t) dt}}, \quad (6.14)$$

where  $W$  is the THz pulse energy,  $r$  is the radius of the THz spot at the sample focus,  $A(t)$  is the temporal profile of the THz pulse, and  $Z_0 = 376.7 \Omega$  is the impedance of free space. Integrating the temporal profile of the pulse in Fig. 6.5 (a) gives  $\int A^2(t) dt = 400 \text{ fs}$ . The spot size of the THz beam, shown in Fig.

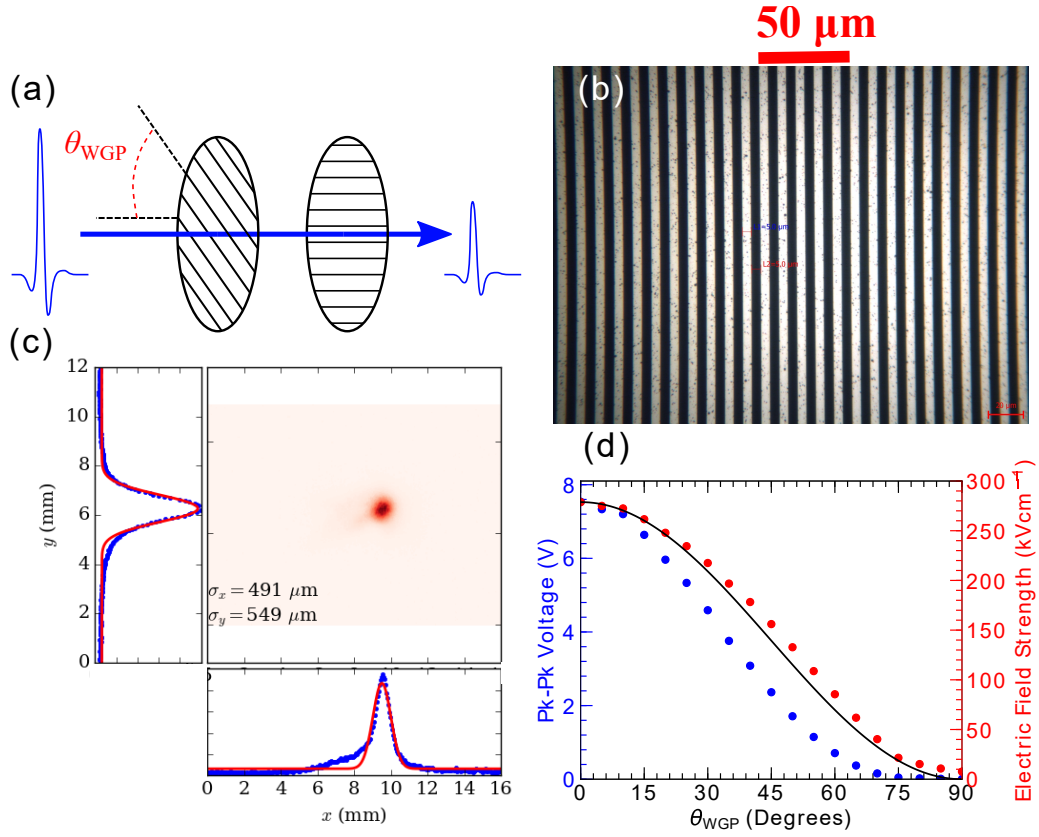


Figure 6.6: (a) Schematic diagram of the method used to vary the electric field strength, consisting of two wire-grid polarisers. (b) Optical microscopy image of the fabricated wire-grid polariser, consisting of  $5 \mu\text{m}$  thick,  $5 \mu\text{m}$  spaced gold wires on top of a z-quartz substrate. (c) Spot size of the THz beam at the sample focus, measured by an uncooled bolometer array THz camera. (d) Measured voltage and THz electric field strength as a function of the angle between wire-grid polarisers  $\theta_{\text{WGP}}$ . The solid black line represents  $\cos^2 \theta_{\text{WGP}}$ .

6.6 (c), was measured at the sample focus by an uncooled bolometer array THz camera, which gave an intensity FWHM of  $\pi r^2 = 1.17 \text{ mm}^2$ . A pyroelectric detector (Gentec-EO QS5-THZ-BL) was positioned at the sample focus and used to measure the average THz power. With the THz pump beam optically chopped at 5 Hz, the peak-to-peak voltage  $V$  obtained from the pyroelectric detector was read off from an oscilloscope, and is plotted against  $\theta_{\text{WGP}}$  in Fig. 6.6 (d). The pyroelectric detector has a calibrated voltage responsivity  $R_V = 2.44 \times 10^5 \text{ VW}^{-1}$  for 632 nm light chopped at  $f_c = 5 \text{ Hz}$ , with the stated absorption of the BL coating at 1 THz being  $\alpha_{\text{BL}} = 0.08$  of that at 632 nm. The THz pulse energy is therefore obtained from the voltage measurements using

$$W = \frac{V}{R_V \alpha_{\text{BL}} t_F N_p f_c}, \quad (6.15)$$

where  $t_F = 0.80$  accounts for the transmission of a THz low-pass filter (TYDEX LPF8.8-30) placed in front of the pyroelectric detector, and  $N_p = 100$  is the number of pulses hitting the pyroelectric detector in one on/off cycle of the optical chopper. Using Equations 6.14 and 6.15 the THz electric field strength can be calculated from the measured voltage, and is also plotted in Fig. 6.6 (c). This therefore allows the THz electric field strength to be varied between  $8 \text{ kV cm}^{-1}$  and  $279 \text{ kV cm}^{-1}$ , with two additional higher field strengths available,  $308 \text{ kV cm}^{-1}$  when WGP1 is removed, and  $373 \text{ kV cm}^{-1}$  when both WGPs are removed.

### 6.3 A Test Case of Nonlinear THz Transmission: Indium Antimonide

In many experimental setups, a test case or material is a valuable resource; a comparison of a well-known material response from other systems to that obtained from the system in question can either be used for calibration purposes, or to explore the effectiveness of the experiment. For THz systems employing pulses with large electric field strengths, a test material can be found in the form of indium antimonide (InSb). InSb is a direct-gap III-V semiconductor with a zinc-blende crystal structure, and exhibits both a narrow bandgap of  $\sim 0.17 \text{ eV}$

[205, 206] and a high electron mobility of  $\sim 7 \times 10^4 \text{ cm}^2 \text{ V}^{-1} \text{ s}^{-1}$  [207] at 300 K. The low bandgap leads to a high intrinsic carrier concentration, on the order of  $10^{16} \text{ cm}^{-3}$  at room temperature, which coupled with the high carrier mobility results in a large absorption coefficient in the THz region.

Previous investigations of InSb using THz-TDS with high electric field strength THz pulses have been performed by Hoffmann *et al.* [163], who observed a reduction in the absorption of THz radiation with increasing electric field strength in both n-type InSb and GaAs. This effect was attributed to electron heating by the intense THz pulses and strong intervalley scattering: the energy supplied to the electrons by the electric field of the THz pulse is sufficient for many of them to scatter out of the lowest energy conduction band and into side valleys, wherein they have reduced mobilities, and since the free-carrier absorption is linked to the carrier concentration and mobility, the THz absorption is reduced. The THz absorption in both InSb and GaAs was observed to reduce monotonically with increasing electric field strength, without saturation, up to fields of  $150 \text{ kVcm}^{-1}$ .

The following section will utilise this effect in InSb as a test of the high-field THz-TDS system outlined in Section 6.2, to ensure it operates as intended, and to provide context for the results presented in Sections 6.4 and 6.5.

### 6.3.1 Experimental Results

The transmission of THz pulses through InSb are presented in Fig. 6.7 (a), for THz electric field strengths ranging from  $8 \text{ kV cm}^{-1}$  and  $373 \text{ kV cm}^{-1}$ . The sample used in these measurements was produced by Mark Ashwin at the University of Warwick, and consisted of a  $6.5 \mu\text{m}$ -thick layer of n-type InSb grown by molecular beam epitaxy on top of a  $350 \mu\text{m}$ -thick SI-GaAs substrate. The reference scan in these measurements was taken as the THz pulse transmitted through the bare SI-GaAs substrate. Electric field strengths of  $8 \text{ kVcm}^{-1}$  and  $15 \text{ kVcm}^{-1}$  are represented by dashed lines in Fig. 6.7 (a) due to the low signal-to-noise in these measurements creating some artifacts in the data, however the data at these field strengths have been included for completeness. The transmission at  $0.52 \text{ THz}$  as a function of electric field strength is displayed in Fig. 6.7 (b) in order to demonstrate the general trend of the data.



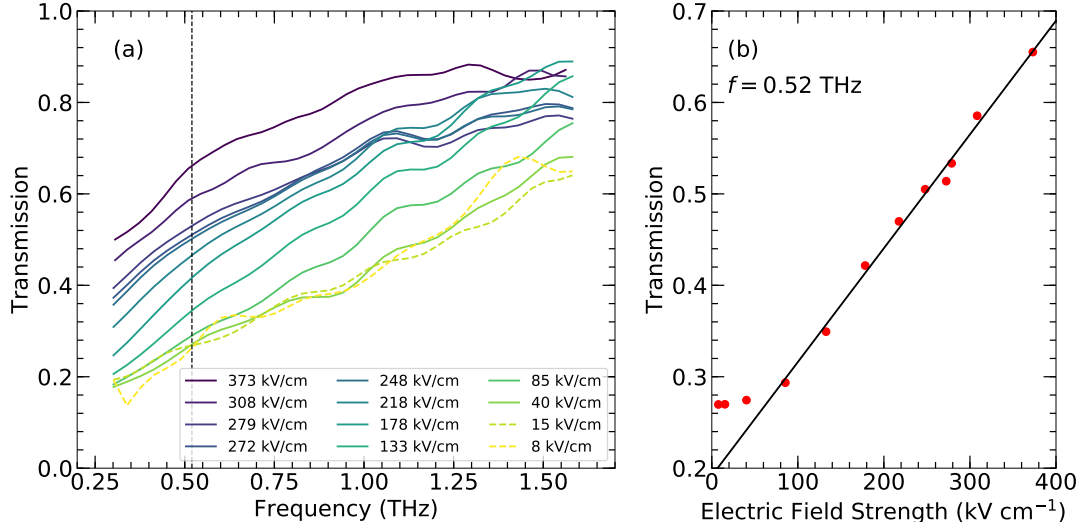


Figure 6.7: Nonlinear THz transmission of InSb using THz pulses with electric field strengths ranging between  $8 \text{ kV cm}^{-1}$  and  $373 \text{ kV cm}^{-1}$ . Displayed in panel (a) are the transmission curves for each value of electric field strength, and panel (b) displays the value of the transmission at a frequency of  $0.52 \text{ THz}$  (signified by the dashed line in panel (a)) as a function of electric field strength, in order to show the general trend. The solid line in panel (b) is an empirical fit to the data.

Figs. 6.7 (a) and 6.7 (b) both demonstrate the expected electric field-dependent behaviour in InSb. For each individual value of electric field strength, the transmission increases monotonically as expected for Drude-like free carrier conduction. As the electric field strength is increased, the transmission of the THz pulses increases, consistent with the previous observations in the literature [163]. An increase in transmission of around 40% is observed for the highest electric field strength of  $373 \text{ kV cm}^{-1}$ . The data at field strengths higher than  $85 \text{ kV cm}^{-1}$  have been fit to a straight line in Fig. 6.7 (b), with a gradient of  $0.00125 \text{ cm kV}^{-1}$ . Saturation of the THz transmission has not been observed up to electric fields of  $373 \text{ kV cm}^{-1}$ , and the data at high field strengths show no deviation from the linear increase in transmission.

The consistency of the observed behaviour with other reports in the literature demonstrates that the high-field THz-TDS system operates as intended, and InSb may be used as an effective test material for high-field THz systems. Future experiments may extend these measurements to higher field strengths, in order to observe saturation behaviour in InSb.

## 6.4 Nonlinear THz Transmission in Single-Walled Carbon Nanotube Films

The unique optical and electronic properties of single-walled carbon nanotubes (SWCNTs), such as 1D ballistic conduction, large exciton binding energies and strong many-body interactions [208, 209], has driven much recent research into their applicability for use in device applications [210, 211], and in THz devices [212, 213]. THz spectroscopy provides a non-contact method of probing the motion of charges in nanomaterials [2, 3], and has previously been utilised to explore the conductivity of SWCNT films [214].

In a SWCNT film, both the conductivity of a single nanotube and the conductive network of intertube contacts play an important role in defining the overall macroscopic properties of the film [215, 216, 217]. The conductivity of SWCNT films at THz frequencies can be described by a Drude-plasmon model [193, 194, 218], in which there is a combination of a Drude-type free-carrier response, whereby charges are transported over long intertube distances throughout the nanotube network, and a plasmon-type resonance, describing the collective contribution of charges confined to individual nanotubes.

As CNTs gain popularity in device applications, their properties in the high-field regime are becoming of greater interest, and as such experimental insight is vital to their use in future device applications. The following section will describe preliminary results into the high-field behaviour of SWCNT films, which show promise for future investigations into their behaviour in this regime.

### 6.4.1 Experimental Results

The SWCNTs studied were produced by the floating-catalyst aerosol chemical vapour deposition method [219], and a dry-transfer technique was used to create a 1 cm×1 cm cross-section, 40 nm-thick free-standing thin film comprised of a network of both individual and bundled SWCNTs, with around 5 CNTs per bundle. The creation and characterisation of these films has been performed by Maria Burdanova and is reported in reference [194]. A mean diameter of 2.1  $\mu\text{m}$  and lengths of  $> 10 \mu\text{m}$  were observed by transmission electron microscopy, and the films were found to contain a mixture of one-third metallic to two-thirds

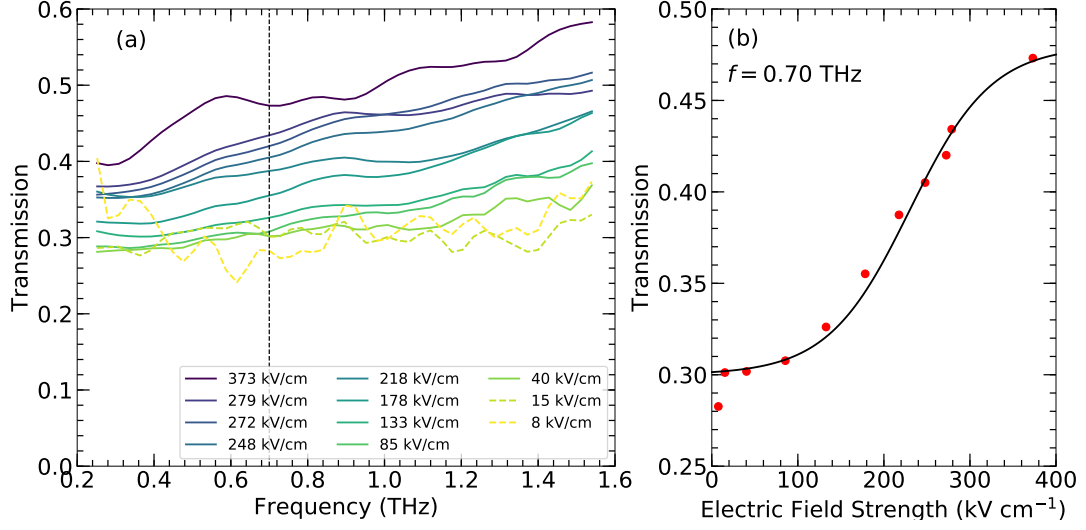


Figure 6.8: Nonlinear THz transmission of highly-conductive SWCNT films using THz pulses with electric field strengths ranging between  $8 \text{ kV cm}^{-1}$  and  $373 \text{ kV cm}^{-1}$ . Displayed in panel (a) are the transmission curves for each value of electric field strength, and panel (b) displays the value of the transmission at a frequency of  $0.70 \text{ THz}$  (signified by the dashed line in panel (a)) as a function of electric field strength, in order to show the general trend. The solid line in panel (b) is an empirical fit to the data.

semiconducting nanotubes.

The transmission of THz pulses through the SWCNT film are presented in Fig. 6.8 (a), for THz electric field strengths ranging from  $8 \text{ kV cm}^{-1}$  and  $373 \text{ kV cm}^{-1}$ . As before in Section 6.3, electric field strengths of  $8 \text{ kV cm}^{-1}$  and  $15 \text{ kV cm}^{-1}$  are represented by dashed lines due to the low signal-to-noise in these measurements creating some artifacts in the data, however the data at these field strengths have been included for completeness. The transmission at  $0.70 \text{ THz}$  as a function of electric field strength is displayed in Fig. 6.7 (b) in order to demonstrate the general trend of the data. The transmission data have been empirically fit to a logistic function of the form

$$T = \frac{L_{\max}}{1 + e^{-m(E_{\text{THz}} - E_{\text{mid}})}} + T_{\text{LF}}, \quad (6.16)$$

where  $L_{\max}$  is the maximum value of the logistic function,  $m$  is the logistic growth rate,  $E_{\text{mid}}$  is the midpoint of the logistic function, and  $T_{\text{LF}}$  is a constant offset to the logistic function accounting for the low-field limit of the transmission. The fit produced values of  $L_{\max} = 0.18$ ,  $T_{\text{LF}} = 0.3$ ,  $m = 0.021 \text{ cm kV}^{-1}$ ,

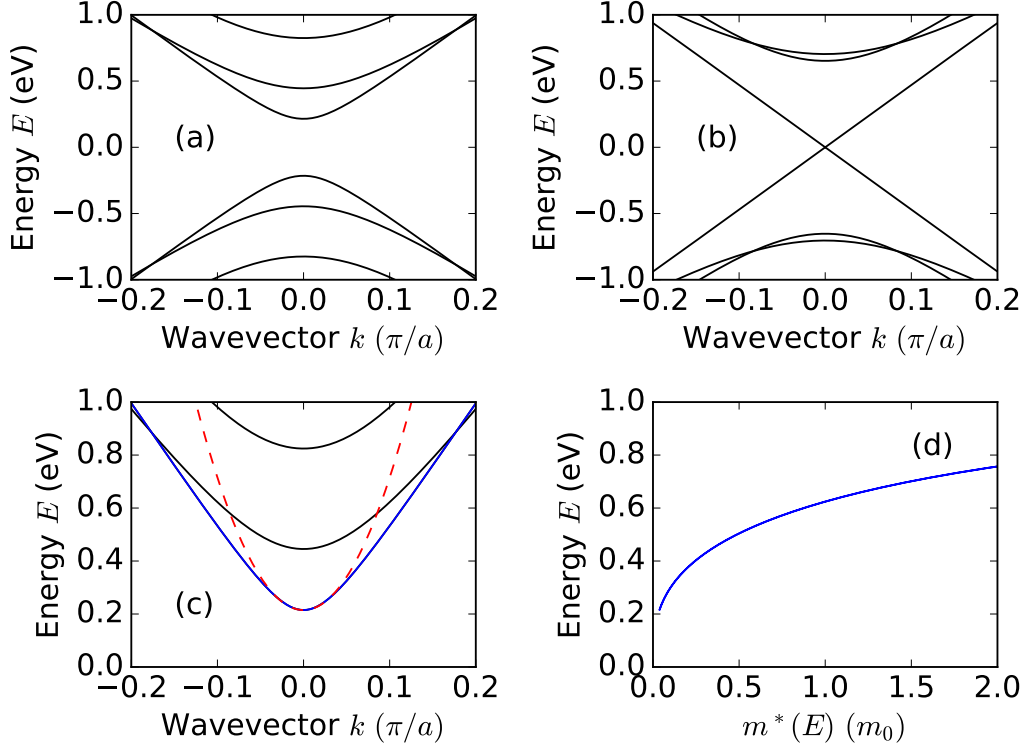


Figure 6.9: **(a)** Bandstructure of a (25,0) semiconducting nanotube, in units of  $\pi/a$  ( $a = 0.426$  nm). **(b)** Bandstructure of (24,0) metallic nanotube. **(c)** Bandstructure of (25,0) nanotube around the lowest conduction band (solid blue line). The dashed red line indicates a fit using a parabolic dispersion with effective mass  $m^* = 0.2 m_0$ . **(d)** Energy-dependent effective mass  $m^*(E)$  calculated from  $m^* = \hbar^2/(d^2E/dk^2)$ .

and  $E_{\text{mid}} = 230 \text{ kV cm}^{-1}$ . This fit suggests that the transmission of the SWCNT film saturates at a value of  $T_S = T_{\text{LF}} + L_{\text{max}} = 0.48$ , under an electric field strength of  $460 \text{ kV cm}^{-1}$ .

A phenomenological interpretation of these experimental results can be obtained by reference to the bandstructure of the two types of CNTs comprising the film. Bandstructure calculations presented here were performed by James Lloyd-Hughes (who also provided Fig. 6.9), using the methods outlined in reference [220] and tools from reference [221]. The calculated bandstructure of a single (25,0) semiconducting CNT is shown in Fig. 6.9 (a), and the bandstructure of a single (24,0) metallic nanotube is shown in Fig. 6.9 (b). These are representative examples of the semiconducting and metallic nanotubes which make up the thin film. A zoom-in on the lowest conduction band in the semi-

conducting nanotubes (blue line) is presented in Fig. 6.9 (c), demonstrating its nonparabolic nature; defining the effective mass as  $m^* = \hbar^2 / (d^2 E / dk^2)$ , an energy-dependent effective mass can be calculated for the lowest conduction band, and is presented in Fig. 6.9 (d). From Fig. 6.9 (d) we can see that for even modest ponderomotive energies on the order of a few hundred meV (easily achievable at the field strengths of the THz pulses used in this study), the effective mass will experience a significant change; as such, as the THz electric field strength increases, we can expect that the effective mass also increases and thus conductivity decreases. For the highest THz electric field strength used in this study of  $373 \text{ kV cm}^{-1}$ , the ponderomotive potential calculated from Equation 6.1 applied to electrons at the bottom of the conduction band would be 0.7 eV, assuming an effective mass of  $m^* = 0.2 m_0$  from the lowest energy in Fig. 6.9 (d). From Fig. 6.9 (d) an energy of 0.7 eV would result in an increase in effective mass to  $1.5 m_0$ . Therefore the increasing transmission with increasing electric field strength observed in Fig. 6.8 can be explained as the higher electric fields giving more ponderomotive energy to the charge carriers, which moves them higher in the conduction band where they have an increased effective mass, leading to lower mobility and conductivity which is observed as an increase in the transmission at THz frequencies. A similar effect may occur in the metallic nanotubes, although due to their Dirac cone-shaped lowest conduction band a more in-depth treatment than the one used here for the semiconducting nanotubes is required.

The potential saturation observed in Fig. 6.8 (b) may be due to the conducting behaviour exhibited by the metallic nanotubes, and due to interband scattering and hot carrier dynamics in both the semiconducting and metallic nanotubes that make up the thin film. At higher energies the charge carriers may scatter into adjacent conduction bands, which changes their effective mass. Additionally, as the charge carriers gain energy from the THz pulse they thermalise, which produces a non-equilibrium carrier distribution; as such there are always some carriers with low energy, which in turn means low mass and high conductivity, and hence the transmission in the THz region remains at a finite value less than one, as seen at high field strengths in Fig. 6.8 (b).

## 6.5 Electric Field-Dependent THz Transmission of CuO

Multiferroic materials are of great interest for new applications in data storage and sensor devices [222, 223], and direct optical switching of magnetic or electric domains by intense pulses of electromagnetic radiation may allow the dynamics of the domain reorientation process in such devices to occur on faster timescales [224]. Direct manipulation of the magnetic order, using direct excitation via the magnetic field of electromagnetic pulses, has been demonstrated in a number of magnetic materials [173, 174, 175, 225]. However, since many of these excitations occur at THz frequencies, the field strengths achievable in the currently available experimental techniques are not yet sufficient to achieve domain switching.

An alternate route to domain control may be found in multiferroic materials, particularly those which exhibit strong magnetoelectric coupling, such as improper ferroelectrics. The magnetic origin of the ferroelectricity in these materials, along with the dynamic magnetoelectric coupling exemplified by electromagnons, suggests that the magnetic order and domain switching may instead be controlled by a strong electric field of a THz pulse. Ultrafast magnetic dynamics have been theoretically predicted to occur via excitation of an electromagnon in  $R\text{MnO}_3$  at electric field strengths  $\sim 14 \text{ MVcm}^{-1}$  [50]. Experimentally, modification of the magnetic structure in  $\text{TbMnO}_3$  by excitation of an electromagnon by THz pulses with electric fields of  $300 \text{ kVcm}^{-1}$  has been demonstrated [45]; in this work the authors suggest that THz pulses with an electric field on the order of  $1 - 2 \text{ MVcm}^{-1}$  may be sufficient to cause a  $90^\circ$  rotation of the spin-cycloid in  $\text{TbMnO}_3$ , an order of magnitude lower than the theoretical prediction in reference [50].

As discussed previously in Section 1.3.3 and Chapter 5,  $\text{CuO}$  is a magnetically-induced multiferroic that exhibits electromagnons at significantly higher temperatures than rare-earth manganates such as  $\text{TbMnO}_3$ ; hence understanding the behaviour of  $\text{CuO}$  during interaction with intense THz electric fields may be an important step towards room temperature, optical electric field control of magnetic order and domain switching for device applications. The coercive field of  $\text{CuO}$ , around  $55 \text{ kVm}^{-1}$  at 220 K in the multiferroic phase [46],

is also considerably lower than the coercive field of  $\text{TbMnO}_3$ , around  $2 \text{ MVm}^{-1}$  at 24 K in the multiferroic phase [226]; a lower coercive field could suggest that CuO will be more susceptible to control by electric fields and nonlinear processes could be induced at lower electric field strengths. The following sections will present results of preliminary investigations into the interaction of strong THz electric fields with CuO and its electromagnons, and suggest future experimental avenues of research.

### 6.5.1 Electric Field-Dependence of the Electromagnon Response in CuO

As an initial exploration into the electric field control of magnetic order in CuO, the dependence of the electromagnon response on the driving electric field strength was investigated. A single crystal sample of CuO oriented with the [101]- and [010]-directions in-plane, identical to that used in Chapters 3 and 5, was mounted in an optical cryostat in the sample space of the high-field THz spectrometer shown in Fig 6.2. The electric field strength was varied using the same method as in Sections 6.3 and 6.4, with the electric field strength incident on the sample varying from  $38 \text{ kV cm}^{-1}$  to  $354 \text{ kV cm}^{-1}$  due to the  $\sim 95\%$  THz transmission of the TPX cryostat windows.

The change in absorption coefficient due to multiferroicity  $\Delta\alpha$  is presented in Fig. 6.10 (a) for various THz electric field strengths. The same method as described in Section 5.3 is used to extract  $\Delta\alpha$  from the time-domain waveforms, with reference scans taken at 210 K in the AF1 phase and sample scans taken at 216 K in the AF2 phase for all electric field strengths. All field strengths demonstrate the expected form of the electromagnon from previous results presented in the literature [8] and in previous chapters of this thesis, with the main electromagnon mode occurring around 0.7 THz at 216 K and the higher frequency shoulder still present. For field strengths between  $38 \text{ kV cm}^{-1}$  and  $265 \text{ kV cm}^{-1}$  the shape of the absorption curve remains constant, however for the highest two field strengths of  $293 \text{ kV cm}^{-1}$  and  $354 \text{ kV cm}^{-1}$  the main electromagnon mode appears to strengthen, with a corresponding decrease in the strength of the higher frequency shoulder feature.

To quantify the electromagnon response at each electric field strength,

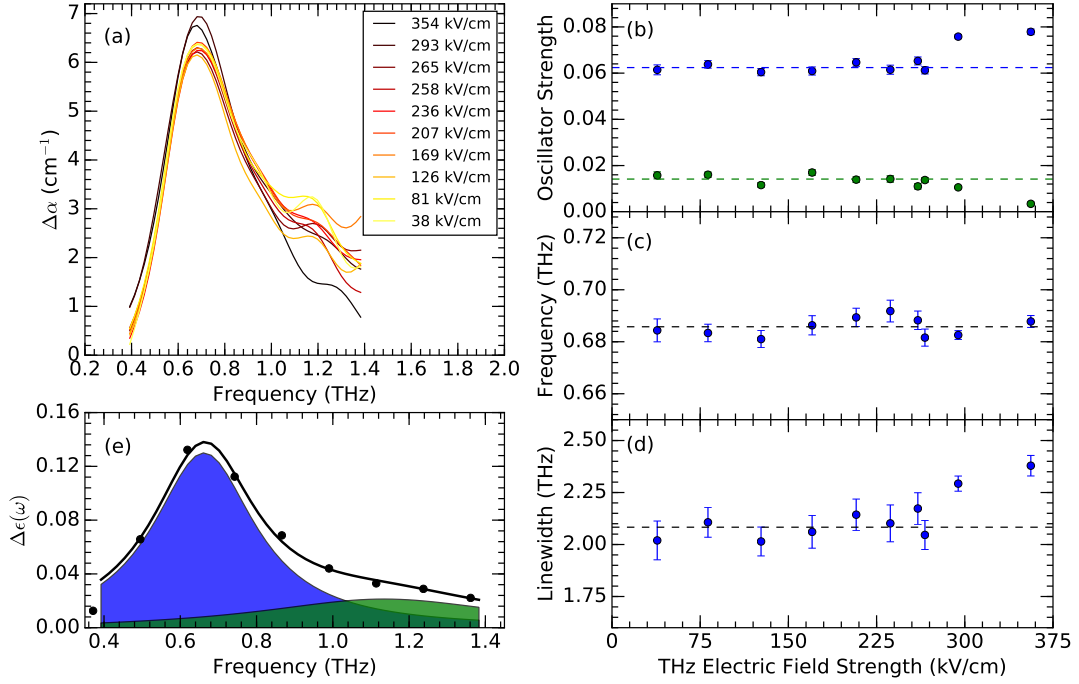


Figure 6.10: **(a)** Change in the THz absorption coefficient due to multiferroicity in CuO for THz pulses with electric field strengths ranging between  $7.6 \text{ kV cm}^{-1}$  and  $354 \text{ kV cm}^{-1}$ . The change in dielectric function  $\Delta\epsilon$  calculated from the data in panel **(a)** is modelled with two Drude-Lorentz oscillators and presented in panels **(b)**, **(c)** and **(d)**, for the oscillator strength, centre frequency and linewidth, respectively. Blue data correspond to the oscillator representing the main electromagnon mode, whilst the green data correspond to the oscillator representing the higher frequency shoulder feature. Errors in panels **(b)**, **(c)** and **(d)** are uncertainties in the fit, and some error bars may be too small to see. An example fit at an electric field strength of  $265 \text{ kV cm}^{-1}$  is shown in panel **(e)**, where the black points are the experimental data, the black line is the best fit, the blue curve represents the electromagnon mode and the green curve represents the shoulder mode.

the change in dielectric function  $\Delta\epsilon(\omega)$  was calculated at each field strength and fit to the same dual Drude-Lorentz oscillator model used in Section 5.3. An example fit at  $265 \text{ kV cm}^{-1}$  is shown in Fig. 6.10 (e), where the black points are the experimental data, the black line is the best fit, the blue curve represents the electromagnon mode and the green curve represents the shoulder mode.. The fit parameters of oscillator strength, mode frequency and linewidth are presented in Figs. 6.10 (b), 6.10 (c) and 6.10 (d), respectively. To produce these fits the resonant frequency of the oscillator corresponding to the shoulder feature was fixed at  $1.2 \text{ THz}$  and its linewidth was fixed at  $10 \text{ THz}$ , which are values consistent with those in Chapter 5 of this thesis and the literature [8]. Errors in Figs.



6.10 (b) - (d) are taken from errors in the fit. All values of the fit parameters below  $E_{\text{THz}} = 265 \text{ kV cm}^{-1}$  remain around a constant value (averages of the parameters between  $E_{\text{THz}} = 38 \text{ kV cm}^{-1}$  and  $265 \text{ kV cm}^{-1}$  are represented by the dashed lines in Fig. 6.10). However above  $E_{\text{THz}} = 265 \text{ kV cm}^{-1}$ , while the resonant frequency of the electromagnon remains the same, an increase in the oscillator strength of the main electromagnon can be observed, accompanied by an increase in linewidth, along with a corresponding decrease in the oscillator strength of the shoulder mode.

The results presented here could be indicative of a nonlinear enhancement in the electromagnon absorption strength in CuO at high THz electric field strengths. However the results are not conclusive, as they consist of only one dataset, with only a single time-domain scan used for each sample and reference measurement at each field strength; as such, it is difficult to provide an accurate estimation of the uncertainty in the absorption data and fit parameters, which are required to conclusively prove a field-dependent change in the electromagnon absorption strength. Further experimental investigations are required to prove that these observations are reproducible, and to extend them to higher electric field strengths.

### 6.5.2 Electric Field-Dependent Absorption Coefficient in CuO

As described in Section 1.3.3 and shown in Fig. 1.7 (c), while the resonant frequency of the  $A_u^3$  and  $B_u^3$  phonon modes in CuO (12.5 THz and 16 THz, respectively) are outside the bandwidth of the high-field THz pulses generated in this spectrometer, due to their broad linewidth both make a significant contribution to the absorption at low THz frequencies [8, 56]. As such, it could be assumed that the intense THz pulses may have some nonresonant driving effect on these phonon modes, which may be apparent in a change in the THz absorption coefficient as the electric field strength of the incident THz pulse is increased.

To explore this, the THz absorption coefficient of CuO at room temperature is presented in Fig. 6.11, at high fields ( $354 \text{ kV cm}^{-1}$ ) with  $E_{\text{THz}}//[101]$  represented by the blue solid line, and with  $E_{\text{THz}}//[010]$  represented by the red solid line. The dashed lines represent the absorption with  $E_{\text{THz}}$  parallel to the

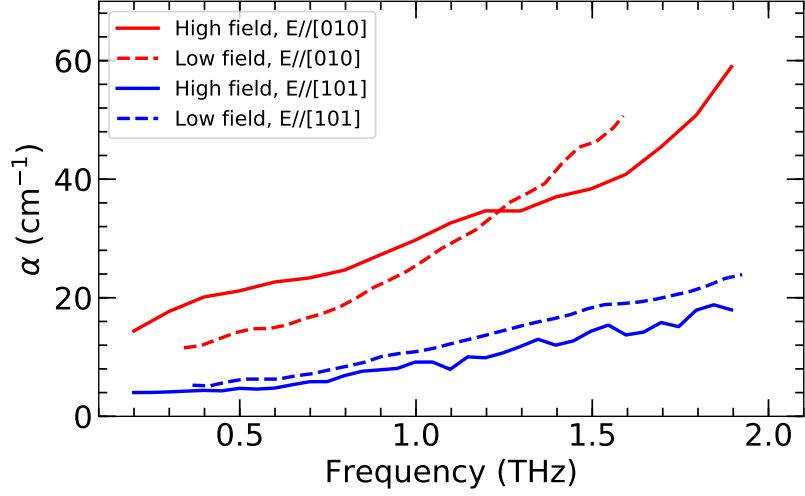


Figure 6.11: Room temperature absorption coefficient in CuO for THz radiation polarised parallel to the [010] direction (red lines) and parallel to the [101] direction (blue lines). Solid lines represent data obtained using high-field THz pulses ( $E_{\text{THz}} = 354 \text{ kV cm}^{-1}$ ), while dashed lines represent data obtained using low-field THz pulses from a standard THz-TDS system. Low field data is reproduced from reference [8].

same direction in the low-field limit, reproduced from reference [8]. The same sample of CuO was used in both the high-field measurements I performed and the low-field data reproduced from reference [8]. Whilst  $\alpha$  for  $E_{\text{THz}}//[101]$  displays a very similar trend in both the high- and low-field cases, the lineshape of  $\alpha$  when  $E_{\text{THz}}//[010]$  changes more significantly, with an increase at low frequencies and a decrease at high frequencies relative to the low-field regime, which hints at a THz field-induced change in the  $A_u^3$  phonon mode. Whilst the results presented here represent a potentially exciting avenue of research, in the first instance these results must be repeated to collect the high- and low-field data in the same experiment, to ensure the results are reproducible and to perform a more detailed field-dependent study. Since the electromagnon strength is linked to the size of the static polarisation induced in the [010]-direction in CuO, exciting this phonon mode with a strong THz pulse may induce some dynamic behaviour in the electromagnon. To explore this, future experiments utilising a high-field THz pump polarised with  $E_{\text{THz}}//[010]$  and a low-field THz probe polarised with  $E_{\text{THz}}//[101]$  may be performed to investigate the dynamic effects of this nonresonant excitation of the phonon modes on the electromagnon in

CuO.

## 6.6 Summary

This chapter has presented the design and operation of a THz-TDS system capable of producing pulses of high electric field strength THz radiation, for use in the spectroscopic study of material properties in the nonlinear regime. The spectrometer performance was characterised, and was found to be capable of producing THz pulses with electric fields of up to  $370 \text{ kV cm}^{-1}$ . The nonlinear THz transmission of InSb was used as a test material for the spectrometer, and the observed behaviour was consistent with that reported previously in the literature, demonstrating that the spectrometer works as intended.

Preliminary investigations into the nonlinear behaviour of SWCNT films and electromagnons in CuO were also reported. A nonlinear increase in the THz transmission with increasing field strength was observed in the SWCNT film, which also exhibited evidence of saturation for electric fields above  $\sim 400 \text{ kV cm}^{-1}$ . The nonlinear increase in transmission can be explained by similar processes of electron heating and intervalley scattering as observed in InSb, whilst the saturation may arise due to the differing responses of the metallic and semiconducting nanotubes that comprise the film. No unusual behaviour was observed in the electromagnon response in CuO up to electric fields of  $\sim 280 \text{ kV cm}^{-1}$ , however higher field strengths provide tantalising evidence of a field-dependent increase in the oscillator strength of the electromagnon. The room-temperature absorption coefficient along the  $[010]$  direction was also observed to change when probed with high field strength pulses, hinting at non-resonant driving of the  $A_u^3$  phonon mode in CuO. Results presented here on these two systems are very much in the preliminary stage, however they provide sufficient evidence to suggest future investigations into their nonlinear properties may prove fruitful.

## Chapter 7

# Conclusions

This thesis has reported advances in terahertz spectroscopy relating to new techniques and components that enhance the control of THz polarisation produced by photoconductive emitters, and the use of electromagnons to probe material properties at a phase transition. In addition, preliminary investigations have been opened into the nonlinear behaviour of SWCNTs and electromagnons in CuO under exposure to extreme electric fields. This chapter will summarise the key results and findings presented in this thesis, and Section 7.1 will put these results into context with the current state-of-the-art in THz-TDS technology and suggest future avenues of research.

Chapter 3 presented a method of rotatable-polarisation-THz-TDS, in which an arbitrarily rotatable THz polarisation state was produced by the mechanical rotation of an interdigitated photoconductive emitter. The optimisation of the system was reported, resulting in a highly uniform, broadband electric field over a  $180^\circ$  rotation of the polarisation state, with only a variation of  $< 7\%$  in amplitude and  $< 1^\circ$  in ellipticity. This technique was implemented experimentally, investigating both birefringent and absorbing anisotropic media. The orientations of the polarisation eigenvectors were identified in the uniaxial materials ZnO and LaAlO<sub>3</sub>, and the full complex refractive index along each eigenvector was extracted. The optical selection rule of the electromagnon absorption in CuO was also precisely mapped using this technique.

The layout, fabrication and experimental verification of a new design of photoconductive emitter, based on separate interdigitated pixel elements for

the emission of horizontally and vertically polarised THz radiation, is presented in Chapter 4. Both theoretical and experimental results demonstrate that the radiation produced by the device interacts constructively in the far-field; the THz pulses generated by the device have been shown to be linear, and the orientation angle of the THz polarisation state has been demonstrated to be arbitrarily rotatable simply by changing the bias voltage applied to each set of pixels. The purely electrical nature of the polarisation rotation in this device permits control of the THz polarisation state on timescales orders of magnitude faster than those achievable by mechanical rotation methods. An experimental technique permitting rapid modulation between two circular polarisation states was also reported, utilising these pixel emitters in combination with a silicon prism.

Chapter 5 demonstrated a method of using the dynamic magnetoelectric response at THz frequencies, in the form of an electromagnon, to probe a phase transition between two magnetically ordered phases. The oscillator strength of the electromagnon in  $\text{Cu}_{1-x}\text{Zn}_x\text{O}$  alloys was used to track the relative amounts of the multiferroic AF2 phase and antiferromagnetic, paraelectric AF1 phase present in the sample. Using this method, the phase transition was observed to broaden under spin-disorder introduced by the non-magnetic Zn ions, and the first-order nature of the transition was confirmed by the observation of thermal hysteresis upon heating and cooling through the transition.

Chapter 6 described the design and operation of a high-field THz-TDS system. The spectrometer performance was characterised by the use of non-linear THz transmission in InSb as a test case; similar behaviour to that reported previously in the literature was observed, confirming the effectiveness of the spectrometer. Preliminary investigations into the behaviour of SWCNTs and electromagnons in CuO in the high-field regime were reported, suggesting promising areas of future work.

## 7.1 Outlook and Future Work

The results presented in Chapter 6 represent the very early stages of the investigations into the nonlinear behaviour of these material systems. Firstly, the

results must be proven to be reproducible, and then may be extended to higher field strengths. The spectrometer described in Section 6.2 may be adapted to include an additional delay line and low-field THz generation optics, to create a THz-pump-THz-probe system. This would permit the dynamics of these non-linear processes to be studied, which may help to elucidate their nature. The work presented in Chapter 5 may have an immediate impact by providing a new way to study the nature of magnetic phase transitions in multiferroics. In the longer term the increased understanding of multiferroics yielded by ultrafast spectroscopic methods, including THz-TDS, may help develop new magneto-electric and multiferroic materials for applications such as spintronics.

There is much scope to investigate the optimisation of the devices presented in Chapter 4, and the implementation of the design in THz detectors. Future work, both theoretical and experimental, may explore the effects of the number, size and arrangement of pixels in the device on the resultant far-field radiation produced; this may lead to improvements in the polarisation purity and a more uniform electric field amplitude from these devices.

The results presented in Chapters 3 and 4 may have immediate impacts on the study of anisotropic media at THz frequencies. Photoconductive emitters and detectors are the most commonly used components for commercially available THz spectroscopy and imaging systems, and interdigitated photoconductive emitters (such as Laser Quantum’s Tera-SED device) have been available commercially for a number of years; as such, the technology currently exists to allow straightforward implementation of the techniques and components presented in this thesis in commercially available systems. A particularly exciting future prospect would be in combining the techniques and components presented in this thesis with fibre-coupled THz-TDS systems; their increased portability may permit the anisotropic properties of materials to be investigated outside of a laboratory setting, bridging the gap to a myriad of potential applications in industry and beyond.

# Bibliography

- [1] P. Jepsen, D. Cooke, and M. Koch, *Laser & Photonics Reviews* **5**, 124 (2011).
- [2] R. Ulbricht, E. Hendry, J. Shan, T. F. Heinz, and M. Bonn, *Reviews of Modern Physics* **83**, 543 (2011).
- [3] J. Lloyd-Hughes and T.-I. Jeon, *Journal of Infrared, Millimeter, and Terahertz Waves* **33**, 871 (2012).
- [4] V. Lucarini, Kramers-Kronig Relations and Sum Rules in Linear Optics, in *Kramers-Kronig Relations in Optical Materials Research*, pages 27–48, Springer-Verlag, Berlin/Heidelberg.
- [5] K. Wiesauer and C. Jördens, *Journal of Infrared, Millimeter, and Terahertz Waves* **34**, 663 (2013).
- [6] J. Lloyd-Hughes, S. P. P. Jones, E. Castro-Camus, K. I. Doig, and J. L. MacManus-Driscoll, *Optics letters* **39**, 1121 (2014).
- [7] T. Arikawa, Q. Zhang, L. Ren, A. A. Belyanin, and J. Kono, *Journal of Infrared, Millimeter, and Terahertz Waves* **34**, 724 (2013).
- [8] S. P. Jones et al., *Nature Communications* **5**, 3787 (2014).
- [9] M. Failla et al., *New Journal of Physics* **18**, 113036 (2016).
- [10] M. Fiebig, T. Lottermoser, D. Meier, and M. Trassin, *Nature Reviews Materials* **1**, 16046 (2016).
- [11] N. A. Spaldin and R. Ramesh, *Nature Materials* **18**, 203 (2019).

- [12] M. P. Kostylev, A. A. Serga, T. Schneider, B. Leven, and B. Hillebrands, *Applied Physics Letters* **87**, 153501 (2005).
- [13] W. Tong, Y. Fang, J. Cai, S. Gong, and C. Duan, *Computational Materials Science* **112**, 467 (2016).
- [14] Z. Zanolli, *Scientific Reports* **6**, 31346 (2016).
- [15] M. Gajek et al., *Nature Materials* **6**, 296 (2007).
- [16] S. Y. Yang et al., *Nature Nanotechnology* **5**, 143 (2010).
- [17] P. Ade et al., *Infrared Physics* **19**, 599 (1979).
- [18] J.-B. Masson and G. Gallot, *Optics Letters* **31**, 265 (2006).
- [19] E. Castro-Camus and M. B. Johnston, *J. Opt. A-Pure Appl. Opt.* **11**, 105206 (2009).
- [20] H. Hirori, A. Doi, F. Blanchard, and K. Tanaka, *Applied Physics Letters* **98**, 091106 (2011).
- [21] B. Fischer, M. Hoffmann, H. Helm, G. Modjesch, and P. U. Jepsen, *Semiconductor Science and Technology* **20**, S246 (2005).
- [22] M. C. Hoffmann and J. A. Fülöp, *Journal of Physics D: Applied Physics* **44**, 083001 (2011).
- [23] T. Kampfrath, K. Tanaka, and K. A. Nelson, *Nature Photonics* **7**, 680 (2013).
- [24] B. E. A. Saleh and M. C. Teich, *Polarization and Crystal Optics*, in *Fundamentals of Photonics*, pages 193–237, John Wiley & Sons, Inc., New York, USA, 1991.
- [25] H. Schmid, *Ferroelectrics* **162**, 317 (1994).
- [26] S. Dong, H. Xiang, and E. Dagotto, *National Science Review* (2019).
- [27] N. A. Hill, *J. Phys. Chem. B* **104**, 6694 (2000).
- [28] D. N. Astrov, *Sov. Phys. JETP* **11**, 708 (1960).



- [29] I. E. Dzyaloshinskii, Sov. Phys. JETP **10**, 628 (1960).
- [30] J. Wang et al., Science **299**, 1719 (2003).
- [31] G. Catalan and J. F. Scott, Advanced Materials **21**, 2463 (2009).
- [32] D. V. Efremov, J. van den Brink, and D. I. Khomskii, Nature Materials **3**, 853 (2004).
- [33] I. A. Sergienko, C. Şen, and E. Dagotto, Physical Review Letters **97**, 227204 (2006).
- [34] M. Mostovoy, Physical Review Letters **96**, 067601 (2006).
- [35] S.-W. Cheong and M. Mostovoy, Nature Materials **6**, 13 (2007).
- [36] H. Katsura, N. Nagaosa, and A. V. Balatsky, Physical Review Letters **95**, 057205 (2005).
- [37] M. Kenzelmann et al., Physical Review Letters **95**, 087206 (2005).
- [38] T. Kimura et al., Nature **426**, 55 (2003).
- [39] K. Wang, J.-M. Liu, and Z. Ren, Advances in Physics **58**, 321 (2009).
- [40] A. Pimenov et al., Physical Review B **74**, 100403 (2006).
- [41] A. Pimenov et al., Nature Physics **2**, 97 (2006).
- [42] A. B. Sushkov, R. V. Aguilar, S. Park, S.-W. Cheong, and H. D. Drew, Physical Review Letters **98**, 027202 (2007).
- [43] H. Katsura, A. V. Balatsky, and N. Nagaosa, Physical Review Letters **98**, 027203 (2007).
- [44] N. Kida et al., Journal of the Optical Society of America B **26**, A35 (2009).
- [45] T. Kubacka et al., Science (New York, N.Y.) **343**, 1333 (2014).
- [46] T. Kimura, Y. Sekio, H. Nakamura, T. Siegrist, and A. P. Ramirez, Nature Materials **7**, 291 (2008).
- [47] C. Kittel, *Introduction to Solid State Physics*, Wiley, 1953.

- [48] R. Valdés Aguilar et al., Physical Review Letters **102**, 047203 (2009).
- [49] A. B. Sushkov, M. Mostovoy, R. Valdés Aguilar, S.-W. Cheong, and H. D. Drew, Journal of Physics: Condensed Matter **20**, 434210 (2008).
- [50] M. Mochizuki, N. Furukawa, and N. Nagaosa, Physical Review Letters **104**, 177206 (2010).
- [51] K. Cao, G.-C. Guo, and L. He, Journal of Physics: Condensed Matter **24**, 206001 (2012).
- [52] F. Kadlec et al., Physical Review B **94**, 024419 (2016).
- [53] S. P. P. Jones et al., Physical Review B **90**, 064405 (2014).
- [54] G. Giovannetti et al., Physical Review Letters **106**, 026401 (2011).
- [55] X. Rocquefelte, K. Schwarz, P. Blaha, S. Kumar, and J. van den Brink, Nature Communications **4**, ncomms3511 (2013).
- [56] A. B. Kuz'menko et al., Physical Review B **63**, 094303 (2001).
- [57] J. B. Forsyth, P. J. Brown, and B. M. Wanklyn, Journal of Physics C: Solid State Physics **21**, 2917 (1988).
- [58] M. Ain, A. Menelle, B. M. Wanklyn, and E. F. Bertaut, Journal of Physics: Condensed Matter **4**, 5327 (1992).
- [59] R. Villarreal et al., Physical Review Letters **109**, 167206 (2012).
- [60] M. Ain, W. Reichardt, B. Hennion, G. Pepy, and B. M. Wanklyn, Physica C: Superconductivity **162-164**, 1279 (1989).
- [61] A. T. Boothroyd et al., Physica B: Condensed Matter **234-236**, 731 (1997).
- [62] T. Shimizu et al., Physical Review B **68**, 224433 (2003).
- [63] D. A. Yablonskii, Physica C: Superconductivity **171**, 454 (1990).
- [64] A. Junod, D. Eckert, G. Triscone, J. Müller, and W. Reichardt, Journal of Physics: Condensed Matter **1**, 8021 (1989).

- [65] J. W. Loram, K. A. Mirza, C. P. Joyce, and A. J. Osborne, *Europhysics Letters (EPL)* **8**, 263 (1989).
- [66] E. Gmelin, U. Köbler, W. Brill, T. Chattopadhyay, and S. Sastry, *Bulletin of Materials Science* **14**, 117 (1991).
- [67] A. M. Shuvaev et al., *Physical Review B* **82**, 174417 (2010).
- [68] K. Cao, F. Giustino, and P. G. Radaelli, *Physical Review Letters* **114**, 197201 (2015).
- [69] D. H. Auston and P. R. Smith, *Applied Physics Letters* **43**, 631 (1983).
- [70] D. H. Auston, K. P. Cheung, J. a. Valdmanis, and D. a. Kleinman, *Physical Review Letters* **53**, 1555 (1984).
- [71] N. M. Burford and M. O. El-Shenawee, *Optical Engineering* **56**, 010901 (2017).
- [72] M. Awad, M. Nagel, H. Kurz, J. Herfort, and K. Ploog, *Applied Physics Letters* **91**, 181124 (2007).
- [73] G. Rodriguez and A. J. Taylor, *Optics Letters* **21**, 1046 (1996).
- [74] D. S. Kim and D. S. Citrin, *Applied Physics Letters* **88**, 161117 (2006).
- [75] A. Dreyhaupt, S. Winnerl, T. Dekorsy, and M. Helm, *Applied Physics Letters* **86**, 1 (2005).
- [76] A. Dreyhaupt, S. Winnerl, M. Helm, and T. Dekorsy, *Optics Letters* **31**, 1546 (2006).
- [77] M. Beck et al., *Optics Express* **18**, 9251 (2010).
- [78] J. R. Freeman, H. E. Beere, and D. A. Ritchie, *Terahertz Spectroscopy and Imaging*, Springer Berlin Heidelberg, London, 2013.
- [79] T. Yajima and N. Takeuchi, *Japanese Journal of Applied Physics* **9**, 1361 (1970).
- [80] K. H. Yang, *Applied Physics Letters* **19**, 320 (1971).

- [81] B. B. Hu, X.-C. Zhang, D. H. Auston, and P. R. Smith, *Applied Physics Letters* **56**, 506 (1990).
- [82] R. L. Sutherland, *Handbook of Nonlinear Optics*, Dekker, New York, 2nd edition, 2003.
- [83] A. Nahata, A. S. Weling, and T. F. Heinz, *Applied Physics Letters* **69**, 2321 (1996).
- [84] T. Löffler, T. Hahn, M. Thomson, F. Jacob, and H. Roskos, *Optics Express* **13**, 5353 (2005).
- [85] N. C. J. van der Valk, W. A. M. van der Marel, and P. C. M. Planken, *Opt. Lett.* **30**, 2802 (2005).
- [86] P. C. M. Planken, H.-K. Nienhuys, H. J. Bakker, and T. Wenckebach, *Journal of the Optical Society of America B* **18**, 313 (2001).
- [87] L. Zhang, H. Zhong, C. Deng, C. Zhang, and Y. Zhao, *Applied Physics Letters* **211106** (2009).
- [88] N. Yasumatsu and S. Watanabe, *Review of Scientific Instruments* **83**, 023104 (2012).
- [89] N. C. J. van der Valk, T. Wenckebach, and P. C. M. Planken, *Journal of the Optical Society of America B* **21**, 622 (2004).
- [90] M. van Exter, C. Fattinger, and D. Grischkowsky, *Optics Letters* **14**, 1128 (1989).
- [91] L. Duvillaret, F. Garet, and J.-L. Coutaz, *IEEE Journal of Selected Topics in Quantum Electronics* **2**, 739 (1996).
- [92] L. Duvillaret, F. Garet, and J.-L. Coutaz, *Applied Optics* **38**, 409 (1999).
- [93] T. D. Dorney, R. G. Baraniuk, and D. M. Mittleman, *Journal of the Optical Society of America A* **18**, 1562 (2001).
- [94] R. M. A. Azzam, N. M. Bashara, and S. S. Ballard, *Physics Today* **31**, 72 (1978).

- [95] H. Fujiwara, *Spectroscopic ellipsometry : principles and applications*, John Wiley & Sons, 2007.
- [96] Y. Kim, M. Yi, B. G. Kim, and J. Ahn, *Applied Optics* **50**, 2906 (2011).
- [97] C. M. Morris, R. V. Aguilar, A. V. Stier, and N. P. Armitage, *Optics Express*, Vol. 20, Issue 11, pp. 12303-12317 **20**, 12303 (2012).
- [98] T. Nagashima, M. Tani, and M. Hangyo, *Journal of Infrared, Millimeter, and Terahertz Waves* **34**, 740 (2013).
- [99] P. Kuhne et al., *IEEE Transactions on Terahertz Science and Technology* **8**, 257 (2018).
- [100] I. Yamada, K. Takano, M. Hangyo, M. Saito, and W. Watanabe, *Optics Letters* **34**, 274 (2009).
- [101] O. Morikawa et al., *Journal of Applied Physics* **100**, 033105 (2006).
- [102] O. Morikawa et al., *Applied Physics Letters* **75**, 3387 (1999).
- [103] E. D. Palik and J. K. Furdyna, *Reports on Progress in Physics* **33**, 307 (1970).
- [104] E. Castro-Camus et al., *Applied Physics Letters* **86**, 3 (2005).
- [105] E. Castro-Camus et al., *Optics Express* **15**, 7047 (2007).
- [106] H. Makabe, Y. Hirota, M. Tani, and M. Hangyo, *Opt. Express* **15**, 11650 (2007).
- [107] M. Neshat and N. P. Armitage, *Optics Letters* **37**, 1811 (2012).
- [108] M. Neshat and N. P. Armitage, *Journal of Infrared, Millimeter, and Terahertz Waves* **34**, 682 (2013).
- [109] E. Castro-Camus, *J. Infrared Millim. Terahertz Waves* **33**, 418 (2012).
- [110] A. Filin, M. Stowe, and R. Kersting, *Optics Letters* **26**, 2008 (2001).
- [111] Y. Nakata, Y. Taira, T. Nakanishi, and F. Miyamaru, *Optics Express* **25**, 2107 (2017).

- [112] L. Cong et al., Applied Physics Letters **103**, 171107 (2013).
- [113] Y. Z. Cheng et al., Applied Physics Letters **105**, 181111 (2014).
- [114] L. Cong, N. Xu, J. Han, W. Zhang, and R. Singh, Advanced Materials **27**, 6630 (2015).
- [115] Y. Kawada et al., Optics Letters **39**, 2794 (2014).
- [116] H. Wen and A. M. Lindenberg, Physical Review Letters **103**, 023902 (2009).
- [117] J. Van Rudd, J. L. Johnson, and D. M. Mittleman, Journal of the Optical Society of America B **18**, 1524 (2001).
- [118] Y. Kim, J. Ahn, B. G. Kim, and D.-S. Yee, Japanese Journal of Applied Physics **50**, 030203 (2011).
- [119] S. A. Hayward et al., Physical Review B **72**, 054110 (2005).
- [120] J. Serrano et al., Physical Review B **81**, 174304 (2010).
- [121] G. Gallot, J. Zhang, R. W. McGowan, T.-I. Jeon, and D. Grischkowsky, Applied Physics Letters **74**, 3450 (1999).
- [122] R. Brazis and D. Nausewicz, Optical Materials **30**, 789 (2008).
- [123] M. Born and E. Wolf, *Principles of Optics*, Cambridge University Press, 7th editio edition, 2006.
- [124] E. Castro-Camus and M. Alfaro, Photonics Research **4**, A36 (2016).
- [125] S. Winnerl, B. Zimmermann, F. Peter, H. Schneider, and M. Helm, Optics Express **17**, 1571 (2009).
- [126] K. Kan et al., Applied Physics Letters **102**, 0 (2013).
- [127] S. Waselikowski, C. Fischer, J. Wallauer, and M. Walther, New Journal of Physics **15**, 75005 (2013).
- [128] M. J. Cliffe, A. Rodak, D. M. Graham, and S. P. Jamison, Applied Physics Letters **105**, 191112 (2014).

- [129] Y. Hirota, R. Hattori, M. Tani, and M. Hangyo, *Opt. Express* **14**, 4486 (2006).
- [130] C. D. W. Mosley, M. Failla, D. Prabhakaran, and J. Lloyd-Hughes, *Scientific Reports* **7**, 12337 (2017).
- [131] W. L. Stutzman and G. A. Thiele, *Antenna Theory and Design*, John Wiley & Sons, 2012.
- [132] N. Froberg, Bin Bin Hu, Xi-Cheng Zhang, and D. Auston, *IEEE Journal of Quantum Electronics* **28**, 2291 (1992).
- [133] C. W. Berry, M. R. Hashemi, and M. Jarrahi, *Applied Physics Letters* **104**, 081122 (2014).
- [134] T. Hattori, K. Egawa, S.-i. Ookuma, and T. Itatani, *Japanese Journal of Applied Physics* **45**, L422 (2006).
- [135] Merck Performance Materials GmbH, AZ 5214 E Image Reversal Photoresist.
- [136] S. E. Ralph and D. Grischkowsky, *Applied Physics Letters* **59**, 1972 (1991).
- [137] I. Gregory et al., *IEEE Journal of Quantum Electronics* **41**, 717 (2005).
- [138] E. Castro-Camus, J. Lloyd-Hughes, and M. B. Johnston, *Physical Review B* **71**, 195301 (2005).
- [139] J. Dai, J. Zhang, W. Zhang, and D. Grischkowsky, *Journal of the Optical Society of America B* **21**, 1379 (2004).
- [140] D. J. Aschaffenburg et al., *Applied Physics Letters* **100**, 241114 (2012).
- [141] S. B. Roy, *Journal of Physics: Condensed Matter* **25**, 183201 (2013).
- [142] S. B. Roy and P. Chaddah, *physica status solidi (b)* **251**, 2010 (2014).
- [143] A. Soibel et al., *Nature* **406**, 282 (2000).
- [144] A. B. Harris, *Physical Review B* **76**, 054447 (2007).

- [145] M. L. Plumer, Physical Review B **78**, 094402 (2008).
- [146] G. Quirion and M. L. Plumer, Physical Review B **87**, 174428 (2013).
- [147] Y. Imry and M. Wortis, Physical Review B **19**, 3580 (1979).
- [148] S. L. Johnson et al., Physical Review Letters **108**, 037203 (2012).
- [149] J. Hellsvik et al., Physical Review B **90**, 014437 (2014).
- [150] D. Hone, P. A. Montano, T. Tonegawa, and Y. Imry, Physical Review B **12**, 5141 (1975).
- [151] C. L. Henley, Physical Review Letters **62**, 2056 (1989).
- [152] J.-P. Zhou, Y.-X. Zhang, Q. Liu, and P. Liu, Acta Materialia **76**, 355 (2014).
- [153] S. Ishiwata et al., Physical Review B **81**, 100411 (2010).
- [154] Z. Wang et al., Nature Communications **7**, 10295 (2016).
- [155] S. Wang et al., Proceedings of the National Academy of Sciences of the United States of America **112**, 15320 (2015).
- [156] Y. Mukai, H. Hirori, and K. Tanaka, Physical Review B **87**, 201202 (2013).
- [157] B. Ewers et al., Physical Review B **85**, 075307 (2012).
- [158] W. Kuehn et al., Physical Review Letters **104**, 146602 (2010).
- [159] P. Bowlan et al., Physical Review Letters **107**, 256602 (2011).
- [160] F. H. Su et al., Optics Express **17**, 9620 (2009).
- [161] L. Razzari et al., Physical Review B **79**, 193204 (2009).
- [162] J. Hebling, M. C. Hoffmann, H. Y. Hwang, K.-L. Yeh, and K. A. Nelson, Physical Review B **81**, 035201 (2010).
- [163] M. C. Hoffmann, J. Hebling, H. Y. Hwang, K.-L. Yeh, and K. A. Nelson, Journal of the Optical Society of America B **26**, A29 (2009).
- [164] I.-C. Ho and X.-C. Zhang, Applied Physics Letters **98**, 241908 (2011).



- [165] S. Tani, F. Blanchard, and K. Tanaka, *Physical Review Letters* **109**, 166603 (2012).
- [166] H. J. Shin, V. L. Nguyen, S. C. Lim, and J.-H. Son, *Journal of Physics B: Atomic, Molecular and Optical Physics* **51**, 144003 (2018).
- [167] S. Watanabe, N. Minami, and R. Shimano, *Optics Express* **19**, 1528 (2011).
- [168] I. Katayama et al., *Physical Review Letters* **108**, 097401 (2012).
- [169] M. Kozina et al., *Structural Dynamics* **4**, 054301 (2017).
- [170] R. Matsunaga and R. Shimano, *Physical Review Letters* **109**, 2 (2012).
- [171] A. Dienst et al., *Nature Materials* **12**, 535 (2013).
- [172] Z. Wang et al., *Journal of Applied Physics* **103**, 123905 (2008).
- [173] C. Vicario et al., *Nature Photonics* **7**, 720 (2013).
- [174] T. Kampfrath et al., *Nature Photonics* **5**, 31 (2011).
- [175] K. Yamaguchi, M. Nakajima, and T. Suemoto, *Physical Review Letters* **105**, 3 (2010).
- [176] Z. Jin et al., *Physical Review B* **87**, 094422 (2013).
- [177] H. Hamster and R. W. Falcone, *Ultrafast Phenomena VII*, volume 53 of *Springer Series in Chemical Physics*, Springer Berlin Heidelberg, Berlin, Heidelberg, 1990.
- [178] H. Hamster, A. Sullivan, S. Gordon, W. White, and R. W. Falcone, *Physical Review Letters* **71**, 2725 (1993).
- [179] H. Hamster, A. Sullivan, S. Gordon, and R. W. Falcone, *Physical Review E* **49**, 671 (1994).
- [180] M. D. Thomson, M. Kreß, T. Löffler, and H. G. Roskos, *Laser and Photonics Reviews* **1**, 349 (2007).
- [181] T. Löffler, F. Jacob, and H. G. Roskos, *Applied Physics Letters* **77**, 453 (2000).

- [182] T. Löffler and H. G. Roskos, *Journal of Applied Physics* **91**, 2611 (2002).
- [183] M. Kreß et al., *Nature Physics* **2**, 327 (2006).
- [184] D. J. Cook and R. M. Hochstrasser, *Optics Letters* **25**, 1210 (2000).
- [185] K.-Y. Kim, J. H. Glowina, A. J. Taylor, and G. Rodriguez, *Optics Express* **15**, 4577 (2007).
- [186] N. Karpowicz, X. Lu, and X.-C. Zhang, *Journal of Modern Optics* **56**, 1137 (2009).
- [187] T. Seifert et al., *Applied Physics Letters* **110**, 252402 (2017).
- [188] M. T. Hibberd et al., *Applied Physics Letters* **114**, 031101 (2019).
- [189] B. Monoszlai, C. Vicario, M. Jazbinsek, and C. P. Hauri, *Optics Letters* **38**, 5106 (2013).
- [190] C. Vicario et al., *Optics Express* **23**, 4573 (2015).
- [191] J. Hebling, G. Almasi, I. Kozma, and J. Kuhl, *Optics Express* **10**, 1161 (2002).
- [192] S. S. Dhillon et al., *Journal of Physics D: Applied Physics* **50**, 043001 (2017).
- [193] D. Shao et al., *Nanotechnology* **29**, 145203 (2018).
- [194] M. G. Burdanova et al., *ACS Photonics* **6**, 1058 (2019).
- [195] K. P. Marshall et al., *Materials Chemistry Frontiers* **2**, 1515 (2018).
- [196] R. L. Milot et al., *Advanced Materials* **30**, 1804506 (2018).
- [197] M. Monti et al., *The Journal of Physical Chemistry C* **122**, 20669 (2018).
- [198] J. Lloyd-Hughes et al., *Nano Letters* **17**, 2506 (2017).
- [199] D. Kleinman and D. Auston, *IEEE Journal of Quantum Electronics* **20**, 964 (1984).
- [200] J. A. Fülöp, L. Pálfalvi, G. Almási, and J. Hebling, *Optics Express* **18**, 12311 (2010).

- [201] J. A. Fülöp et al., *Optics Express* **22**, 20155 (2014).
- [202] L. Pálfalvi, J. A. Fülöp, G. Almási, and J. Hebling, *Applied Physics Letters* **92**, 171107 (2008).
- [203] H. Hirori and K. Tanaka, *Journal of the Physical Society of Japan* **85**, 082001 (2016).
- [204] J. Hebling, A. Stepanov, G. Almási, B. Bartal, and J. Kuhl, *Applied Physics B: Lasers and Optics* **78**, 593 (2004).
- [205] C. L. Littler and D. G. Seiler, *Applied Physics Letters* **46**, 986 (1985).
- [206] S. Adachi, Indium Antimonide (InSb), in *Optical Constants of Crystalline and Amorphous Semiconductors*, pages 268–278, Springer US, Boston, MA, 1999.
- [207] D. L. Rode, *Physical Review B* **3**, 3287 (1971).
- [208] S. Ilani and P. L. McEuen, *Annual Review of Condensed Matter Physics* **1**, 1 (2010).
- [209] A. R. Amori, Z. Hou, and T. D. Krauss, *Annual Review of Physical Chemistry* **69**, 81 (2018).
- [210] M. F. L. De Volder, S. H. Tawfick, R. H. Baughman, and A. J. Hart, *Science (New York, N.Y.)* **339**, 535 (2013).
- [211] D. Suzuki, S. Oda, and Y. Kawano, *Nature Photonics* **10**, 809 (2016).
- [212] R. R. Hartmann, J. Kono, and M. E. Portnoi, *Nanotechnology* **25**, 322001 (2014).
- [213] R. Wang, L. Xie, S. Hameed, C. Wang, and Y. Ying, *Carbon* **132**, 42 (2018).
- [214] T. Morimoto et al., *ACS Nano* **8**, 9897 (2014).
- [215] J. L. Blackburn et al., *ACS Nano* **2**, 1266 (2008).
- [216] K. Mustonen et al., *Beilstein journal of nanotechnology* **3**, 692 (2012).

- [217] O. A. Bârsan, G. G. Hoffmann, L. G. J. van der Ven, and G. de With, *Advanced Functional Materials* **26**, 4377 (2016).
- [218] C. Zhang et al., *New Journal of Physics* **15**, 055017 (2013).
- [219] A. G. Nasibulin, A. Moisala, D. P. Brown, H. Jiang, and E. I. Kauppinen, *Chemical Physics Letters* **402**, 227 (2005).
- [220] L. Yang, M. P. Anantram, J. Han, and J. P. Lu, *Physical Review B* **60**, 13874 (1999).
- [221] S. Gyungseon et al., *CNTbands*, 2006.
- [222] A. Chanthbouala et al., *Nature Materials* **11**, 860 (2012).
- [223] S. Fusil, V. Garcia, A. Barthélémy, and M. Bibes, *Annual Review of Materials Research* **44**, 91 (2014).
- [224] E. Beaurepaire, J.-C. Merle, A. Daunois, and J.-Y. Bigot, *Physical Review Letters* **76**, 4250 (1996).
- [225] A. Kirilyuk, A. V. Kimel, and T. Rasing, *Reviews of Modern Physics* **82**, 2731 (2010).
- [226] J. Stein et al., *Journal of Physics: Condensed Matter* **27**, 446001 (2015).